

# Cohesive Zone Modelling in Adhesively Bonded Joints

Analysis on crack propagation in adhesives and adherends

D.C. Noorman

Technical University of Delft



# COHESIVE ZONE MODELLING IN ADHESIVELY BONDED JOINTS

ANALYSIS ON CRACK PROPAGATION IN ADHESIVES AND  
ADHERENDS

by

**D.C. Noorman**

in partial fulfillment of the requirements for the degree of

**Master of Science**  
in Mechanical Engineering

at the Delft University of Technology,  
to be defended in September, 2014.

Student number:	1309153	
Supervisor:	Dr. M. Calomfirescu,	Airbus Defence and Space
	Prof. dr. ir. A. van Keulen,	TU Delft
Thesis committee:	Prof. dr. ir. A. van Keulen,	TU Delft
	Ir. A. van Beek,	TU Delft
	Ir. C. Ayas,	TU Delft

An electronic version of this thesis is available at <http://repository.tudelft.nl/>.

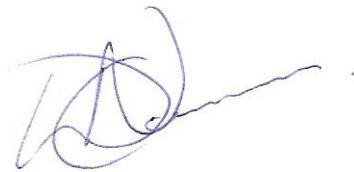


# PREFACE

This Master's thesis is for those interested in the structural mechanics and finite element analysis of composite laminated bonded joints. Cracks, or damage growth, within the adhesives and adherends are analysed using a technique called cohesive zone modelling. This thesis assumes that the reader possesses a basic understanding of structural mechanics, finite element analyses and laminated composites beforehand, as the contents of this thesis expands on these topics.

The thesis was written as the final examination of the track Solid and Fluid Mechanics, in the Master of Science programme of Mechanical Engineering at the Technical University of Delft. The thesis was performed and written within and for the department of Air Systems of Cassidian, which is now Airbus Defence and Space (Manching, Germany).

During the thesis, I was supported by numerous people. I would personally like to thank my supervisor at Airbus Defence and Space, Mircea Calomfirescu, who granted me this thesis and guided me throughout. Also, I would like to thank the department of Air Systems for their financial support and the knowledge they shared with me. I also wish to thank Prof. Dr. Ir. Fred van Keulen for being my supervisor on the university and accepting this thesis as the final examination of my Master's programme, together with Anton van Beek and Can Ayas. And finally, I would like to thank my parents, brothers, sister and friends who have supported me throughout my thesis.



*D.C. Noorman  
Leiden, 8<sup>th</sup> of August, 2014*



# ABSTRACT

Laminated composites is a material that is rapidly being adapted in the aircraft industry and new joining techniques are being researched for new structural designs. One such technique is adhesive bonding, which can result in decreased weight, fuel saving and improved strength of aircraft components. Robust strength and failure analysis methods are required to assess new designs beforehand. One of these methods is cohesive zone modelling. Cohesive zone modelling is a technique based on cohesive forces and energy within a material or interface region which keeps material together. Damage can be tracked progressively along a region with cohesive elements and damage propagation can be monitored in a structure. This thesis work relies on cohesive zone modelling to monitor damage propagation of the bondline and in between plies of simple bonded joints, together with progressive failure criteria to assess any failure within the plies of a joint.

A composite Cracked Lap Shear (CLS) specimen was tested with results of a possible crack jump from bondline to adherend. The objective of this thesis was to assess and recreate damage propagation and the possibility of a jump of damage growth from bondline to adherend in the CLS specimen. This was done by using cohesive zone modelling and progressive failure criteria with the finite element package MSC.Mentat and its solver MSC.Marc. A validation with another test report on mixed-mode bending and interlaminar failure was performed using a cohesive zone model with the settings MSC.Marc has to offer. This yielded accurate results in terms of loading and damage. With the aid of this validation, the options within the cohesive zone model which had the best results in the validation were used for simulations of the CLS specimen. Cohesive zone elements representing the bondline and the adhesive within the laminate adherends in the CLS model are used to assess cohesive and interlaminar failure, while progressive failure criteria are used to assess intralaminar failure. The results of the current simulation setups were unsatisfying as the failure load and strain results had large errors. Further detailed analyses will be needed to recreate the multiple failure modes in the CLS specimen in MSC.Marc with acceptable results. On the other hand, the thesis has proven that MSC.Marc and its own cohesive zone model perform well enough for mixed-mode bending and interlaminar failure in simple geometries.



# LIST OF FIGURES

1.1	Building block approach in the aircraft industry. . . . .	3
2.1	Overview of common bonded joints. Taken from ESA [1], Zwinderman [2]. . . . .	5
2.2	A stress distribution curve using analytical methods for different overlap lengths in a single lap joint. Stress peaks at the ends decrease the longer the overlap length becomes. Taken from Kelly [3]. . . . .	6
2.3	Different types of tapered ends to reduce stress peaks. Taken from Gleich <i>et al.</i> [4]. . . . .	6
2.4	Generalised depictions of stress peaks at adhesive and adherend interfaces at the joint end, denoted by strength presence. Taken from da Silva and Campilho [5]. . . . .	7
2.5	Tapers and roundings at joint ends and their influences on stress peaks and distribution. Smaller angled tapers result in lower stresses throughout the joint and larger roundings result in a more spread out stress distribution at the joint ends. . . . .	7
2.6	Correct and incorrect designs of composite bonded joints with optimal fibre orientation depending on different shear and tensile loads. Taken from ESA [1]. . . . .	8
2.7	Cohesive failure modes in bonded joints. . . . .	9
2.8	Adhesive failure modes in bonded joints. . . . .	10
2.9	Adherend failure modes in bonded joints. . . . .	10
2.10	Overview of failure modes within composite material. Fracture resistance denotation ( $R$ ), fibre failure ( $FF$ ) or inter fibre failure ( $IFF$ ), normal fracture ( $NF$ ) or shear fracture ( $SF$ ), tension ( $t$ ) or compression ( $c$ ) and parallel ( $\parallel$ ) or perpendicular ( $\perp$ ) loading to fibres. See Table 2.3 for a tabular overview. Taken from Cuntze [6]. . . . .	11
2.11	Stress singularities at crack tips and material interfaces. Taken from da Silva and Campilho [5]. . . . .	12
2.12	Contour of the J-integral around a crack tip. The contour encloses the crack tip where plasticity occurs. . . . .	14
2.13	Depiction of the virtual crack closure technique. Left figure depicts a global system while the right figure shows the local system where the virtual work takes place. Taken from Krueger [7]. . . . .	14
2.14	3D coordinate system $(x_1, x_2, x_3)$ of UD composite element, with fibre direction $x_1$ , laminate mid-surface $x_2$ and thickness direction $x_3$ . Rotation failure plane angle $\theta_{fp}$ results in coordinate system $(x_1, x_n, x_t)$ , with fibre direction $x_1$ , normal direction to failure plane $x_n$ and tangential direction to failure plane $x_t$ . Normal stresses $\sigma_{ii}$ are noted as $\sigma_i$ and shear stress $\sigma_{ij}$ as $\tau_{ij}$ . Taken from Puck and Schürmann [8]. . . . .	20
2.15	Fracture envelope for Puck's matrix failure modes A, B and C, depicting the different fracture resistances and positions of the failure modes on the stress coordinate system. Taken from Puck and Schürmann [8]. . . . .	20
2.16	Angle $\theta_{fp}$ representation in Puck's criterion in MSC.Marc. . . . .	24
3.1	Simple illustrations of a cohesive zone element resembling a simplified spring-damper configuration and the deformation of a cohesive zone element. Taken from Kregting [9] and Bosch <i>et al.</i> [10]. . . . .	28
3.2	Position of relative displacement between opposing point pairs of a loaded bonded joint in the traction law. Example of a bonded joints in continuum approach. Taken from Khoramishad <i>et al.</i> [11]. . . . .	29
3.3	Reversible and irreversible behaviour and the effect of elastic and plastic loading and reloading. . . . .	29
3.4	An example of a bilinear traction law. Code found in Appendix D. . . . .	31
3.5	An example of a trapezoidal traction law. Code found in Appendix D. . . . .	31
3.6	An example of an exponential traction law. Code found in Appendix D. . . . .	32
3.7	A 3D cohesive zone element in a reference and local coordinate system. . . . .	33
3.8	The three different fracture modes: tensile (Mode I), shear (Mode II) and tear (Mode III). . . . .	34

3.9	3D view of a mixed-mode exponential traction law based on Ye's criterion. Any moment in mixed-mode loading can be traced to a point on the surface of the 3D graph. Code found in Appendix D. . . . .	35
3.10	Influence of maximum traction and critical energy release rate. . . . .	36
3.11	3D interface element with a reference system based on an integration point. Taken from Marc 2010 Volume A: Theory and User Information [12]. . . . .	37
3.12	MSC.Marc's three built-in traction laws: Bilinear (left), exponential (middle), linear-exponential (right). . . . .	38
3.13	Example of MSC.Marc's built in mixed-mode calculation between pure Modes I and II for an exponential traction law. Code found in Appendix D. . . . .	39
3.14	3D view of a mixed-mode exponential traction law based on MSC.Marc's algorithm. The relations $\beta_1$ and $\beta_2$ are highlighted as red arrows to distinguish their influence in the mixed-mode surface graph. Code found in Appendix D. . . . .	39
4.1	MMB test setups. Taken from Turon <i>et al.</i> [13]. . . . .	42
4.2	Simplified model of MMB specimen with length $x$ , width $y$ , total thickness $2z$ , adhesive region $a$ and initial crack region $a_0$ . . . . .	42
4.3	Graphical overview of numerical and experimental results of all five setups. Taken from Turon <i>et al.</i> [13]. . . . .	43
4.4	MSC.Marc model of the 0% fracture mode, or DCB, setup. . . . .	46
4.5	MSC.Marc model of the 50% fracture mode setup. Lever length $c$ differs for 20% and 80% fracture mode ratios. . . . .	47
4.6	MSC.Marc model of the 100% fracture mode, or ENF, setup. . . . .	48
4.7	MSC.Marc model of the 0% fracture mode, or DCB, setup. . . . .	50
4.8	MSC.Marc model of the 50% fracture mode setup. Lever length $c$ differs for 20% and 80% fracture mode ratios. . . . .	51
4.9	MSC.Marc model of the 100% fracture mode, or ENF, setup. . . . .	52
4.10	Damage levels in first CZEs. . . . .	54
4.11	Damage and traction in a CZE. . . . .	55
5.1	Simple drawing of CLS specimen, with strap (1), bondlines (2), lap (3), foot (4), clamps (5), strain gauges (6) and trigger (7). . . . .	59
5.2	Real life specimen with strain gauges (orange), bottom view. Foot is located on the right, and two of the three strain gauges can be seen. . . . .	60
5.3	Traction laws of the cohesive properties of the adhesives. Note that the laminate adhesive is stronger in both modes than the bondline adhesive. . . . .	61
5.4	Simplified drawing of CLS specimen with strain gauges: strap top gauge (1), strap bottom gauge (2) and lap gauge (3). . . . .	61
5.5	Real life CLS experiment results, retrieved with data from the strain gauges and the loading mechanism. . . . .	62
5.6	Model views of the CLS specimen. . . . .	63
5.7	View of strap with reduced element size to highlight the CZE (blue) between the plies and bulk region (purple) in the strap adherend. . . . .	64
5.8	Close-up side view of constraints on both ends. . . . .	64
5.9	View of trigger resting on lap. Strap is made invisible. Note that the trigger symbolises the initial crack region $a_0$ . . . . .	65
5.10	Strain-Load results of Puck model. The drop in strain of the lap gauge indicates the failure load. . . . .	69
A.1	Contact Table Properties for 2D and 3D models. . . . .	77
A.2	Rigid lever as in the 50% mode ratio simulations. Grey circle (1) is the node with displacement. Blue circles (2) are nodes that are tied. Green circles (3) are nodes that share DOF. The red lines on the model are nodes that are tied by DOF to the middle nodes. . . . .	79
A.3	3D models in deformed shape. . . . .	80
A.4	Results of the 0% fracture mode setup for 2D simulations 1 through 8 with varying cohesive zone model settings. . . . .	81
A.5	Results of the 0% fracture mode setup for 2D simulations 1 through 14. . . . .	82

A.6	Results of the 0% fracture mode setup for 3D simulations 1 through 8 with varying cohesive zone model settings. . . . .	83
A.7	Results of the 0% fracture mode setup for 3D simulations 1 through 14 with varying cohesive zone model settings. . . . .	84
A.8	Results from the 0% fracture mode for 3D simulations 15 through 20 with varying time step sizes. . . . .	85
A.9	Results of the 0% fracture mode setup for 3D simulations 21 through 28 with varying $G_{c,I}$ and $G_{c,II}$ . . . . .	86
A.10	Results of the 0% fracture mode setup for 3D simulations 29 through 36 with varying $T_{m,I}$ and $T_{m,II}$ . . . . .	87
A.11	Results of the 20% fracture mode setup for 2D simulations 1 through 8 with varying cohesive zone model settings. . . . .	88
A.12	Results of the 20% fracture mode setup for 2D simulations 1 through 14 with varying cohesive zone model settings. . . . .	89
A.13	Results of the 20% fracture mode setup for 3D simulations 1 through 8 with varying cohesive zone model settings. . . . .	90
A.14	Results of the 20% fracture mode setup for 3D simulations 1 through 14 with varying cohesive zone model settings. . . . .	91
A.15	Results from the 20% fracture mode for 3D simulations 15 through 20 with varying time step sizes. . . . .	92
A.16	Results of the 50% fracture mode setup for 2D simulations 1 through 8 with varying cohesive zone model settings. . . . .	93
A.17	Results of the 50% fracture mode setup for 2D simulations 1 through 14 with varying cohesive zone model settings. . . . .	94
A.18	Results of the 50% fracture mode setup for 3D simulations 1 through 8 with varying cohesive zone model settings. . . . .	95
A.19	Results of the 50% fracture mode setup for 3D simulations 1 through 14 with varying cohesive zone model settings. . . . .	96
A.20	Results from the 50% fracture mode for 3D simulations 15 through 20 with varying time step sizes. . . . .	97
A.21	Results of the 80% fracture mode setup for 2D simulations 1 through 8 with varying cohesive zone model settings. . . . .	98
A.22	Results of the 80% fracture mode setup for 2D simulations 1 through 14 with varying cohesive zone model settings. . . . .	99
A.23	Results of the 80% fracture mode setup for 3D simulations 1 through 8 with varying cohesive zone model settings. . . . .	100
A.24	Results of the 80% fracture mode setup for 3D simulations 1 through 14 with varying cohesive zone model settings. . . . .	101
A.25	Results from the 80% fracture mode for 3D simulations 15 through 20 with varying time step sizes. . . . .	102
A.26	Results of the 100% fracture mode setup for 2D simulations 1 through 8 with varying cohesive zone model settings. . . . .	103
A.27	Results of the 100% fracture mode setup for 2D simulations 1 through 14 with varying cohesive zone model settings. . . . .	104
A.28	Results of the 100% fracture mode setup for 3D simulations 1 through 8 with varying cohesive zone model settings. . . . .	105
A.29	Results of the 100% fracture mode setup for 3D simulations 1 through 14 with varying cohesive zone model settings. . . . .	106
A.30	Results from the 100% fracture mode for 3D simulations 15 through 20 with varying time step sizes. . . . .	107
A.31	Results of the 100% fracture mode setup for 3D simulations 21 through 28 with varying $G_{c,I}$ and $G_{c,II}$ . . . . .	108
A.32	Results of the 100% fracture mode setup for 3D simulations 29 through 36 with varying $T_{m,I}$ and $T_{m,II}$ . . . . .	109
B.1	Contact table for CLS specimen. . . . .	111
B.2	Technical drawing of CLS specimen. . . . .	112

B.3	Material property defining of a composite region. . . . .	113
B.4	Properties of the laminates of the CLS specimen. . . . .	114
B.5	Comparison of time step sizes. . . . .	115
B.6	First few CZE disappearing, or failing, in the bondline. . . . .	116
B.7	The strain and load results of the simulation without failure criteria. . . . .	117
B.8	The strain and load results of the simulation with Tsai-Wu failure criterion. . . . .	118
B.9	The strain and load results of the simulation with Hashin failure criterion. . . . .	119
B.10	The strain and load results of the simulation with Puck failure criterion. . . . .	120
B.11	The strain and load results at the gauges for all models and real CLS. . . . .	121
B.12	The highest failure index results in the single ply region of the Tsai-Wu model at $F = 25.6kN$ ( $t = 0.3395$ ). . . . .	122
B.13	The highest failure index results in the single ply region of the Tsai-Wu model at $F = 55kN$ ( $t = 0.9245$ ). . . . .	123
B.14	The highest failure index results in the single ply region of the Hashin model at $F = 25.6kN$ ( $t = 0.3395$ ). . . . .	124
B.15	The highest failure index results in the single ply region of the Puck model at $F = 55kN$ ( $t = 0.9245$ ). . . . .	125
B.16	The highest failure index results in the single ply region of the Puck model at $F = 25.6kN$ ( $t = 0.3395$ ). . . . .	126
B.17	The highest failure index results in the single ply region of the Puck model at $F = 55kN$ ( $t = 0.9245$ ). . . . .	127
B.18	The highest damage results in the single ply region of the Tsai-Wu model at $F = 55kN$ ( $t = 0.9245$ ). . . . .	128
B.19	The highest damage results in the single ply region of the Puck model at $F = 55kN$ ( $t = 0.9245$ ). . . . .	129
B.20	The highest damage results in the single ply region of the Puck model at $F = 55kN$ ( $t = 0.9245$ ). . . . .	130
C.1	Mentat GUI windows for defining cohesive properties. . . . .	132
C.2	Material property window for solids in Mentat. . . . .	133
C.3	Loadcase property with solution control. . . . .	133
C.4	Loadcase property with convergence testing. . . . .	134

# LIST OF TABLES

2.1	Advantages and disadvantages of mechanical fasteners [1]. . . . .	8
2.2	Overview of popular analytical methods for forces and stresses in a 2D single-lap joint. Taken from da Silva <i>et al.</i> [14]. . . . .	9
2.3	Tabular overview of Figure 2.10. . . . .	11
2.4	Comparison table for the different failure analysis approaches and their advantages and disadvantages. . . . .	17
2.5	Recurring material properties in failure criteria discussed in the remainder of this thesis. . . . .	18
4.1	Tabular overview of material properties of Turon's specimen. . . . .	42
4.2	Tabular overview of specimen properties per fracture mode ratio; 0% denoting pure Mode I and 100% pure Mode II. . . . .	42
4.3	Numerical and experimental results for the five setups. Taken from Turon <i>et al.</i> [13]. . . . .	43
4.4	Adherend material property conversion to MSC.Marc. See Figure C.2 for the GUI input view. . . . .	44
4.5	Bondline material property conversion to MSC.Marc. See Figure C.1a for the GUI input view. . . . .	45
4.6	Simulation setup for 2D and 3D models. . . . .	45
4.7	Additional simulation setup for 3D models. These simulations all use one fixed time step size as noted, Gaussian integration scheme, tangent stiffness matrix solving method, deactivated CZE and no viscosity. . . . .	49
5.1	Dimensions of CLS specimen components. Technical drawing of the specimen can be found in Appendix B.2. . . . .	60
5.2	Laminate material properties. Taken from Figure B.4. . . . .	60
5.3	Cohesive material properties. . . . .	60
5.4	Strain gauge results at 25.6 kN. . . . .	62
5.5	Laminate material property conversion to MSC.Marc. Taken from Figure B.4. See Figure C.2 for the GUI input parameters and view. . . . .	66
5.6	Laminate failure criteria conversion to MSC.Marc. Taken from Figure B.4. See Figure C.5a, Figure C.5b and Figure C.5c for the GUI input parameters and view. All other input parameters are with default value. . . . .	66
5.7	Laminate cohesive material property conversion to MSC.Marc. See Figure C.1a for the GUI view. All other input parameters are with default value. . . . .	67
5.8	Bondline material property conversion to MSC.Marc. See Figure C.1a for the GUI input view. All other input parameters are with default value. . . . .	67
5.9	Simulation setup for CLS model. . . . .	67
5.10	Simulation times for CLS model. . . . .	68
5.11	Strain gauge results of the simulations at 25.6 kN, compared to the experiment results. . . . .	68
5.12	Failure load results of the simulations, compared to the experiment results. . . . .	69
5.13	Failure indices of single modelled plies as taken at increment where bondline failure occurred first ( $t = 0.3395$ s) (FI = Failure Index). . . . .	70
5.14	Damage levels of single modelled plies as taken at increment where $F = 55000$ N ( $t = 0.9245$ s) (FI = Failure Index). . . . .	70
A.1	Element information. . . . .	77
A.2	Tabular overview of lever length $c$ per fracture mode ratio. . . . .	78
A.3	Results from the 0% fracture mode ratio for 2D simulations 1 through 14 with varying cohesive zone model settings. . . . .	81
A.4	Results from the 0% fracture mode ratio for 3D simulations 1 through 14 with varying cohesive zone model settings. . . . .	83

A.5	Results from the 0% fracture mode ratio for 3D simulations 15 through 36 with varying time step sizes, $G_{c,I}$ , $G_{c,II}$ , $T_{m,I}$ and $T_{m,II}$ .	85
A.6	Results from the 20% fracture mode ratio for 2D simulations 1 through 14 with varying cohesive zone model settings.	88
A.7	Results from the 20% fracture mode ratio for 3D simulations 1 through 14 with varying cohesive zone model settings.	90
A.8	Results from the 20% fracture mode ratio for 3D simulations 15 through 20 with varying time step sizes.	92
A.9	Results from the 50% fracture mode ratio for 2D simulations 1 through 14 with varying cohesive zone model settings.	93
A.10	Results from the 50% fracture mode ratio for 3D simulations 1 through 14 with varying cohesive zone model settings.	95
A.11	Results from the 50% fracture mode ratio for 3D simulations 15 through 20 with varying time step sizes.	97
A.12	Results from the 80% fracture mode ratio for 2D simulations 1 through 14 with varying cohesive zone model settings.	98
A.13	Results from the 80% fracture mode ratio for 3D simulations 1 through 14 with varying cohesive zone model settings.	100
A.14	Results from the 80% fracture mode ratio for 3D simulations 15 through 20.	102
A.15	Results from the 100% fracture mode ratio for 2D simulations 1 through 14 with varying cohesive zone model settings.	103
A.16	Results from the 100% fracture mode ratio for 3D simulations 1 through 14 with varying cohesive zone model settings.	105
A.17	Results from the 100% fracture mode ratio for 3D simulations 15 through 36 with varying time step sizes, $G_{c,I}$ , $G_{c,II}$ , $T_{m,I}$ and $T_{m,II}$ .	107
B.1	Element information.	111
B.2	Simulation setup for CLS model.	113

# CONTENTS

<b>Abstract</b>	<b>v</b>
<b>List of Figures</b>	<b>vii</b>
<b>List of Tables</b>	<b>xi</b>
<b>1 Introduction</b>	<b>1</b>
1.1 Background	1
1.2 Objective and Approach	3
1.3 Outline	4
<b>2 Literature Research</b>	<b>5</b>
2.1 Adhesively Bonded Joints	5
2.1.1 Joint Design and Types	5
2.1.2 Advantages and Disadvantages	7
2.1.3 General Analytical Methods of Single-lap Joints	9
2.2 Failure Modes within Bonded Joints	9
2.2.1 Cohesive Failure	9
2.2.2 Adhesive Failure	10
2.2.3 Adherend Failure	10
2.3 Approaches to Crack Failure Analyses	11
2.3.1 Continuum Mechanics	11
2.3.2 Fracture Mechanics	13
2.3.3 Extended Finite Element Method	14
2.3.4 Damage Mechanics	15
2.3.5 Comparison Summary and Choice	16
2.4 Analysis of Failure Modes	18
2.4.1 Failure Criteria	18
2.4.2 Failure criteria in MSC.Marc	22
<b>3 Cohesive Zone Modelling</b>	<b>27</b>
3.1 Theory	27
3.1.1 Traction Laws	27
3.1.2 Cohesive Zone Elements	33
3.1.3 Fracture Modes	34
3.1.4 Influences on a Cohesive Zone Model	36
3.2 MSC.Marc	36
3.2.1 Theory	37
3.2.2 Input	40
<b>4 Validation of MSC.Marc</b>	<b>41</b>
4.1 Turon's Model	41
4.1.1 Turon's Model Properties	41
4.1.2 Turon's Load-Displacement Results	43
4.2 2D MSC.Marc Models	44
4.2.1 Model Properties	44
4.3 3D Models	48
4.3.1 Model Properties	48

4.4	Evaluation . . . . .	52
4.4.1	Load-Displacement Results . . . . .	52
4.4.2	Damage and Traction Results . . . . .	54
4.4.3	Time Step Dependency Results . . . . .	56
4.4.4	Range of Different $G_C$ and $T_m$ Results . . . . .	56
4.4.5	Discussion . . . . .	57
<b>5</b>	<b>Cracked Lap Shear Test and Simulation</b>	<b>59</b>
5.1	CLS specimen . . . . .	59
5.1.1	Properties . . . . .	59
5.1.2	Experiment Results . . . . .	61
5.2	CLS Specimen in MSC.Marc . . . . .	62
5.2.1	FE Model . . . . .	62
5.2.2	Material and Geometric Properties . . . . .	65
5.2.3	Simulations . . . . .	67
5.3	Evaluation . . . . .	68
5.3.1	Strain and failure load results . . . . .	68
5.3.2	Damage results . . . . .	69
5.3.3	Discussion . . . . .	71
<b>6</b>	<b>Conclusion and Recommendations</b>	<b>73</b>
6.1	Conclusion . . . . .	73
6.2	Recommendations . . . . .	74
<b>A</b>	<b>MSC.Marc Validation with Turon's Experiment</b>	<b>77</b>
A.1	Full Details Modelling . . . . .	77
A.2	Rigid Lever for MMB simulation . . . . .	78
A.2.1	Analysis . . . . .	78
A.2.2	Modelling . . . . .	78
A.3	Tables and Figures of Results . . . . .	79
<b>B</b>	<b>CLS Model &amp; Simulations</b>	<b>111</b>
B.1	Full Details Modelling . . . . .	111
B.2	Time Step Evaluation . . . . .	111
B.3	Figures of Results . . . . .	113
<b>C</b>	<b>GUI of MSC.Marc Windows and Options</b>	<b>131</b>
<b>D</b>	<b>MatLab Codes</b>	<b>137</b>
<b>E</b>	<b>Recommendations for when using MSC.Marc</b>	<b>147</b>
<b>F</b>	<b>Used Software and Hardware</b>	<b>149</b>
	<b>Bibliography</b>	<b>151</b>

# 1

## INTRODUCTION

### 1.1. BACKGROUND

In recent years, composite material is being applied more extensively in the aerospace industry. The Airbus Group company currently applies composite material in the design and manufacture of aircraft components, and it is seeing an increased use in fuselage design. The main reasons for the application of this material, is that they are capable of supporting large loads, are lightweight and are more reliable with a longer lifespan than other traditional metallic materials. In turn, this reduces aircraft maintenance, costs, and frequency of inspections during service.

The increased application of composite material calls for efficient and robust joining techniques when designing new primary structures as well as performing repairs. Currently, conventional mechanical fastening, such as riveting and bolting, is the favoured joining technique for primary composite structures. This traditional joining technique usually results in the cutting and interruptions of fibres and thus introduces large stress concentrations, reducing structural integrity. An alternative joining technique would be adhesive bonding for primary composite structures, which reduces detrimental stress concentrations by better load and stress distributions along its area [15] and without the need of fibre cuts meant for fastener holes. This can result that bonded joints can be stronger than the ultimate strength of many metals that are in common use for aircraft construction today. Rivet- and bolt-free joining would also considerably contribute to weight and cost reduction of primary aerospace structures. Still, this alternative joining technique suffers from certification issues and airworthiness requirements regarding undetectability of manufacturing flaws within adhesively bonded structures, which does not provide absolute assurance of bond integrity and could lead to premature failure of purely bonded joints. This is the main reason why mechanical fastening is still preferred over adhesive bonding.

While improvements and developments on manufacturing processes and non-destructive techniques for weak bond inspection are being made, it remains desirable to look into the implementation of adhesive bonding as the joining technique in primary composite structures, due to its advantages over conventional mechanical fastening. The Boltless Assembling of Primary Aerospace Composite Structures (BOPACS) project selects target applications that are commonly used in today's primary aerospace structures where adhesive bonding might advantageously replace the conventional riveting and fastening. While BOPACS is not focussing on improvement of manufacturing processes and non-destructive inspection techniques, it instead proposes a different road map to certification and requirement fulfilment by developing Means of Comply based on:

- Thorough research, beyond the state of the art, into crack growth and disbond extension mechanisms in adhesively bonded joints.
- Research and development on different categories of crack stopping design features to prevent or arrest crack growth and ultimately failure of joints.

BOPACS considers this topic to be breakthrough technology: the features mentioned above secure structural integrity of the bond line in bonded joints throughout the entire service life. There are still several issues and

topics that are unresolved within the research of BOPACS. The thesis will concentrate on a topic within the first point mentioned in the road map.

One of the main research fields of BOPACS is failure in adhesively bonded joints. In order to understand and improve adhesively bonded joints, damage and failure in these structures must first be understood. Failure in bonded joints can be classified in three basic categories [16]:

1. Failure within one of the adherends that is technically outside the joint
2. Failure throughout the adhesive layer, also known as cohesive failure
3. Failure at the interface between the adhesive and one of the adherend, also known as adhesive failure

The first option is the ideal form of failure, which proves that the joint has given its maximum performance and had not failed. It is desirable to have only the first option as failure, since it may reduce the testing required for structural certification. Currently, research is put into understanding and preventing cohesive and adhesive failure, in order to perfect the bond line itself and prevent it from failing as much as possible.

Next to the possibility of failure within joints, be it in the bond line itself or in the interface, failure can also occur in the adherends near the bond line. The most common damage type in composite structures and laminates is delamination, due to relatively weak interlaminar strengths [17]. Delamination is the process whereby the laminate layers within composites separate. Global structural failure from delamination is usually attributed to the evolution of damage, referred to as crack growth, created in local zones in the structure. In these local zones, micro-cracks and voids may grow in size and result into macroscopic cracks, which eventually will lead to global failure.

Most contemporary methods to investigate debonding and delamination come from a fracture mechanics point of view, which incorporates damage evolution on a micro scale. Within fracture mechanics, many techniques and methods are used to determine crack growth, with different failure criteria. Methods based on Linear Elastic Fracture Mechanics (LEFM) has proven to be effective once non-linearities can be neglected. In the case that non-linearities cannot be neglected, well-known techniques in elastic-plastic fracture mechanics, such as the J-integral method and Virtual Crack Closure Technique, are used. But these well-proven methods have their shortcomings. For instance, LEFM needs the presence of an initial crack before it is applicable and is dependent on the size of the non-linear zone ahead of the crack tip. The other techniques like VCCT and J-integral method have encountered difficulties when used in finite element codes [5].

To overcome the limitations of the previously mentioned methods, cohesive zone modelling (CZM) is proposed to simulate and analyse damage initiation and propagation in bonded joints and their laminates. The concept dates back to the previous century, when it was introduced by Dugdale and Barenblatt in the sixties [18, 19]. In their models, the concept of a yield stress was introduced, a thin plastic zone is generated in front of the notch and that cohesive forces are present to solve the problem of equilibrium in elastic bodies with cracks. It was subsequently improved by Hillerborg in a modified model with the concept of tensile strength, initiation of new cracks and allowing existing cracks to grow [20].

BOPACS uses a building block approach as in Figure 1.1 and is performing tests on coupon level to understand composite bonded joints. One of their aims is recreating these joints and there experiments in finite element packages with accurate results. Recent Cracked Lapped Shear (CLS) tests in BOPACS have given results that were unexpected. In some cases, the CLS specimen showed initial cohesive failure in the bondline which was expected, but then abruptly stopped and failure was continued by only delamination or intralaminar failure in the adherend. The crack, or damage propagation was thus shifted from the bondline to inbetween laminates in one of the adherend. It is still unknown how this jump occurred, even with the aid of NDTs. A possible and probable explanation behind this damage propagation jump is the influence of the 90° ply, which is the weakest ply when it comes to Mode I fracture due to its low matrix tensile strength, and the direct influence of first ply next to the bondline showing intralaminar failure. A closer inspection on this phenomenon is wanted to fully understand if and why the jump occurs, what parameters are of major influence in this and how to model and simulate this phenomenon is a finite element package with the aid of CZM. The objective of this thesis will concentrate on this.

For the Defence and Space department, a subdivision of Airbus Group and the provider of the Eurofighter, it is of high interest to investigate the use of CZM in structural analysis in adhesively bonded assemblies and repairs, and in the design and creation of crack stopping features. It can be of use for military and civil aircraft

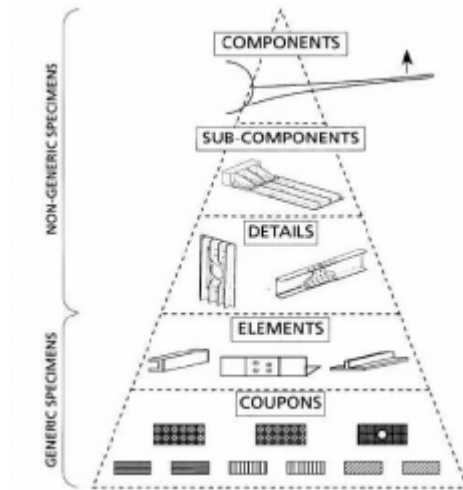


Figure 1.1: Building block approach in the aircraft industry.

that Airbus Group offers in the competitive aircraft industry. Currently, Airbus Group resides over a licence for the commercial finite element analysis tool MSC.Mentat, a pre- and postprocessing tool, and its solver MSC.Marc, which has the possibility to analyse and solve simulations using CZM.

## 1.2. OBJECTIVE AND APPROACH

The objective of the research work in this thesis is the validation and evaluation of the capabilities to predict failure loads, damage onset and damage growth with cohesive zone modelling in composite bonded joints on coupon level using the finite element package MSC.Marc. To do this, three research questions are devised to understand the problem that occurred in the CLS specimen that BOPACS is currently researching and how to recreate this problem accurately to make future predictions on varying material properties:

- First research question: What parameters and material properties of a cohesive model are of influence in damage onset and growth?
  - Determine the influence of the critical energy release rate.
  - Determine the influence of the maximum traction allowed of the adhesive.
- Second research question: Is ply failure or delamination present and does this failure cause damage growth to physically jump from the bondline to the adherend in the CLS specimen?
  - If there is a jump in damage growth, what cohesive parameters are of influence to prevent or induce this?
- Third research question: How accurate can you model (the jump of) damage growth progressively of a coupon level test specimen in the finite element package MSC.Marc?
  - Determine the accuracy of the solver's own cohesive zone model.
  - Determine the accuracy of the progressive failure within the adherends of the CLS specimen.

To help answer the above questions and have a background understanding on the subject, the thesis covers a general review on bonded joints and failure analysis approaches, the main theoretical and analysis aspects of CZM and variable mode ratio testing in a literature review study. Validation tests will be performed with MSC.Mentat and MSC.Marc on coupon level first and compared to previously performed experiments from a test report. This is done to become familiar with the package and to make sure it's compatible for simulating 3D variable mode ratio tests with CZM. With these validation tests, the parameter settings and options of MSC.Mentat will also be explored and evaluated for optimal use in the CLS experiment.

For the first question, a fundamental understanding of cohesive zone models is needed which then can be applied to the simulations. The literature review will help a lot in this.

For the second and last question, the modelling options such as progressive failure criteria and cohesive zone elements will be explored to optimally simulate the real life CLS specimen and experiment in MSC.Marc. The matter whether failure in one of the plies is of influence on a potential jump will be explored via this. An optimal model which gives the best results will be designed for this. For the last question, the accuracy can be determined by the use of a cohesive zone model and failure criteria in the simulations and by relating the results to the real life experiment.

### 1.3. OUTLINE

The research was started by performing a preliminary literature study on the subject of adhesively bonded joints and failure analyses. In Chapter 2, a small study concerning the basic understanding of adhesively bonded joints has been performed and a general study has been performed on failure analyses, in particular why CZM was chosen. In Chapter 3, an extended study has been performed on CZM, regarding theories and the implementation in MSC.Marc. A validation of MSC.Marc's home settings and options was performed in Chapter 4 on a mixed-mode bending test based on another research paper to assess the accuracy of MSC.Marc's settings to that of analytical and experimental results and what difficulties were encountered. Chapter 5 covers the CLS experiment and simulations and their results.

Both Chapter 4 and Chapter 5 are built in the same manner. The first section is an explanation on the experiment performed and the experimental results are shown. The following sections describe the models and simulation setups that are to be run within MSC.Marc. In the last section of those chapters, an evaluation follows, detailing the results and showing a discussion about the outcome of the simulations and what it means for the research questions.

Using the evaluation sections of Chapter 4 and Chapter 5 results in Chapter 6, which ultimately provides the conclusions to this research. In this chapter, the three previously formulated research questions are answered, followed by recommendations on future research on this topic.

# 2

## LITERATURE RESEARCH

A literature research was conducted prior to the evaluation of the main subject, to get a better understanding of bonded joints and the theories behind failure analysis, and why cohesive zone modelling was chosen as the method of analysing damage propagation. Chapter 2.1 is dedicated to some general information regarding bonded joints, their designs and their advantages and disadvantages over mechanical fasteners. Chapter 2.2 explains the failure modes of bonded joints. Chapter 2.3 explains the most well-known methods for crack analyses and an argumentation why continuum damage mechanics and CZM are used in this thesis. Chapter 2.4 then explains the theories behind several failure criteria that will be used, and their implementation in MSC.Marc.

### 2.1. ADHESIVELY BONDED JOINTS

#### 2.1.1. JOINT DESIGN AND TYPES

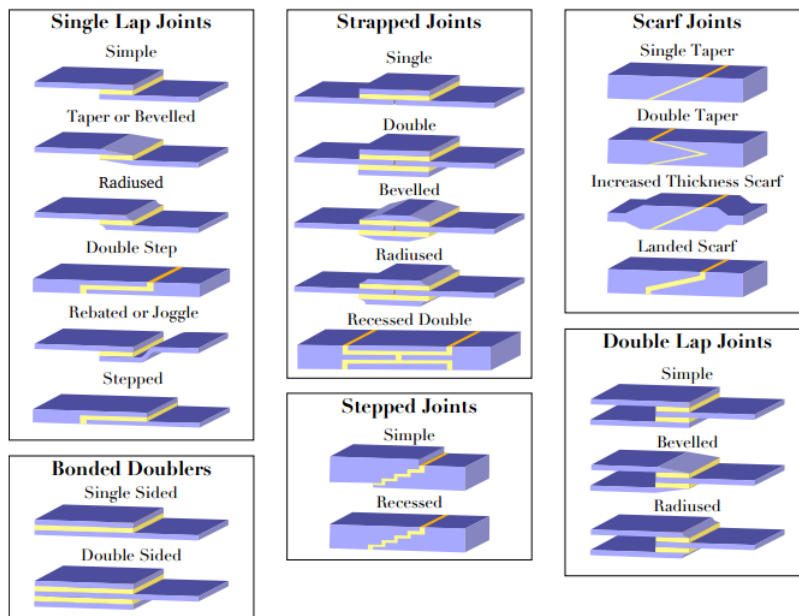


Figure 2.1: Overview of common bonded joints. Taken from ESA [1], Zwinderman [2].

There are many joint designs that are used. Each has certain characteristics coming with the design to cope with a type of load case. Single-lap joints for instance are easy to produce, to inspect, and to analyse. Double-lap joints are more resistant to peel stresses. Corner and T-joints are also common, for example in aircraft

tails. The CLS specimen that is evaluated later on is a single-sided bonded doubler. An overview of common bonded joints can be found in Figure 2.1. The strength of a bonded joint is dependent on several important properties. The adhesive and adherend thickness are often of crucial importance. For adherend thickness, there is a critical thickness dependant on the load case to make sure that failure should or should not occur in the adherend part of the bonded joint, which would not lead or lead to failure in the adhesive [21]. For adhesive thickness, experimental results have made manufacturers recommend a thickness range between 0.1 – 0.2 mm for maximum joint strength [4]. Experimental results depict a contradiction with analytical results, derived from analytical methods such as Goland-Reissner's and Hart-Smith's, whereby increasing adhesive thickness gives lower failure loads, which wasn't expected [22]. This is due to stress singularities at the interface corners of the adhesive and adherend which are caused by the mismatch in stiffness due to material discontinuity. These singularities indicate that the stress has an infinite value according to continuum mechanics. A typical stress distribution for single-lap joints as in Figure 2.2 shows the spikes at the ends of the adhesive using analytical methods.

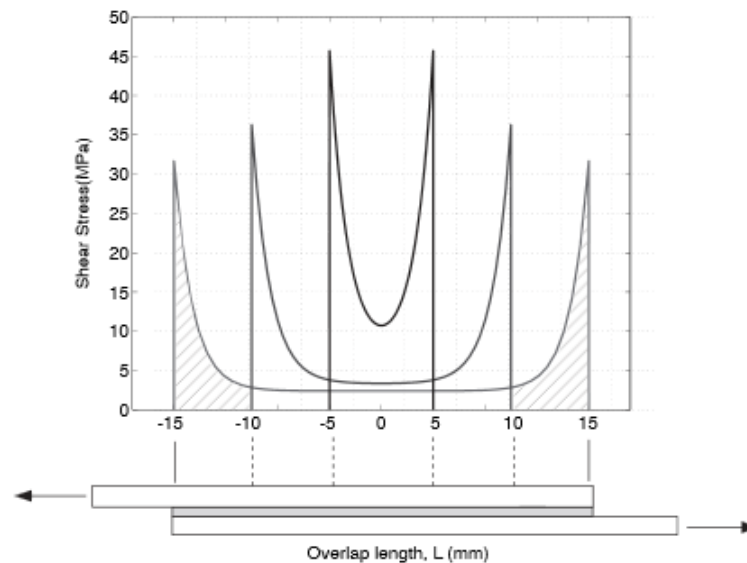


Figure 2.2: A stress distribution curve using analytical methods for different overlap lengths in a single lap joint. Stress peaks at the ends decrease the longer the overlap length becomes. Taken from Kelly [3].

The stress singularities can be reduced and minimised by the addition of taper or rounding of both adhesive and adherends, but still cannot be fully removed. Studies have concentrated on this tapering with results that a small taper angle and large roundings can reduce stress significantly at the end of the adhesive [23, 24], see Figure 2.5. A few examples of tapered joint designs are given in Figure 2.3 and locations of stress singularities even in tapered joints in Figure 2.4.

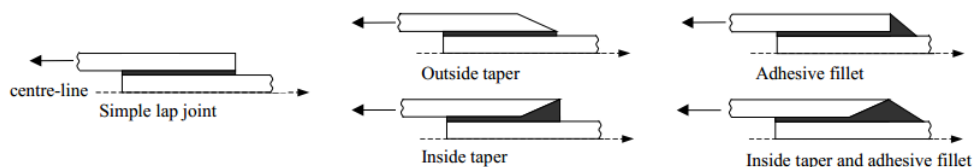


Figure 2.3: Different types of tapered ends to reduce stress peaks. Taken from Gleich *et al.* [4].

When composite laminate adherends are used, design should incorporate effective fibre orientation due to the differing strength properties of each different orientated ply for a given load case. Often the shear load transfer in the main load direction is engineered to coincide with the fibre orientation of the first ply in a unidirectional laminate, due to the suitable strength properties. A weak ply in a laminate is often the 90° ply because of its low tensile and shear strength and strain to failure of the resin-to-fibre interface within the

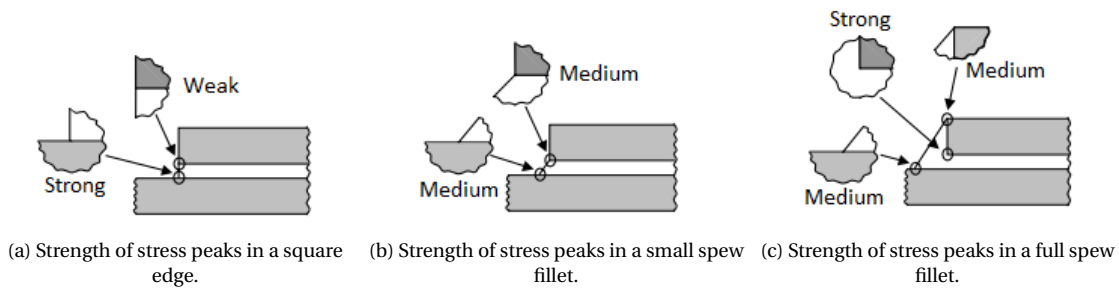
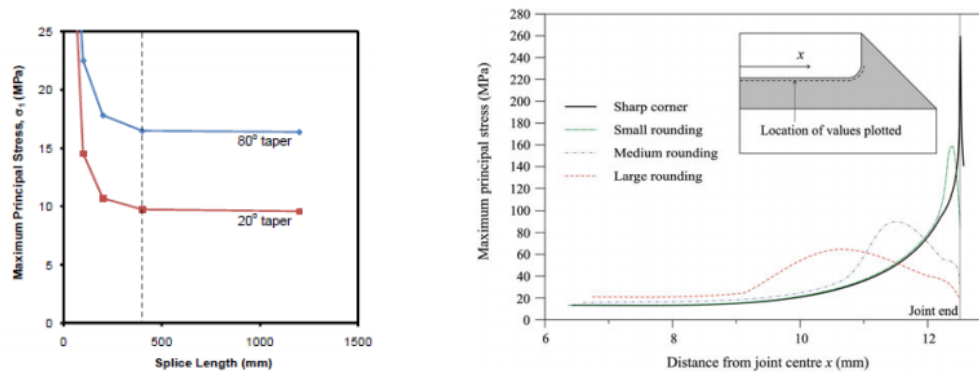


Figure 2.4: Generalised depictions of stress peaks at adhesive and adherend interfaces at the joint end, denoted by strength presence. Taken from da Silva and Campilho [5].



(a) Influence of tapered ends. Taken from Dawood [23]. (b) Influence of rounded ends. Taken from Zhao *et al.* [24].

Figure 2.5: Tapers and roundings at joint ends and their influences on stress peaks and distribution. Smaller angled tapers result in lower stresses throughout the joint and larger roundings result in a more spread out stress distribution at the joint ends.

structure. It is also the case that the matrix resin strength properties are significantly lower than those of the adhesive. It is therefore desirable to minimise usage of 90° plies in order to obtain a specific bonded joint with predictable and reproducible strength, since these plies cause a weakness in strength in bonded joints, which could lead to early failure in the composite adherend. Ultimately, this means that it is preferred to have a cohesive failure rather than an adherend failure for composite bonded joints [1]. Figure 2.6 depicts a series of fibre orientation choices for several joint design subjected to shear loads.

### 2.1.2. ADVANTAGES AND DISADVANTAGES

To choose between adhesive bonded joints and mechanically fastened ones comes a lot of advantages and disadvantages. Mechanical fasteners are still widely used in aircraft production, even though they carry large disadvantages like introducing stress concentrations around the fastener holes which can initiate cracks and lead to failure. Yet they also have advantages which justify their usage. A list of advantages and disadvantages for mechanically fastened joints is given as follows in Table 2.1.

With the current increase of composite material being used in aircraft, the disadvantages on mechanical fastening are more evident in this type of material. According to research, a 60% decrease of the in-plane properties of laminated composite structures takes place when fasteners are used as the joining method in joints [25]. Therefore, it is highly desirable to incorporate adhesive bonding as fasteners and their holes are not present and thus do not reduce the strength of a composite structure. There are more numerous advantages to bonded joints, but also disadvantages. A summary of advantages and disadvantages for adhesively bonded joints can also be found in Table 2.1.

For both mechanically fastened and adhesively bonded joints, many advantages and disadvantages have to be taken into account. Yet experience has shown that adhesive bonding for laminated composite joints has proven to be above all stronger, lighter and cheaper than their mechanically fastened counterpart [1, 15, 25].

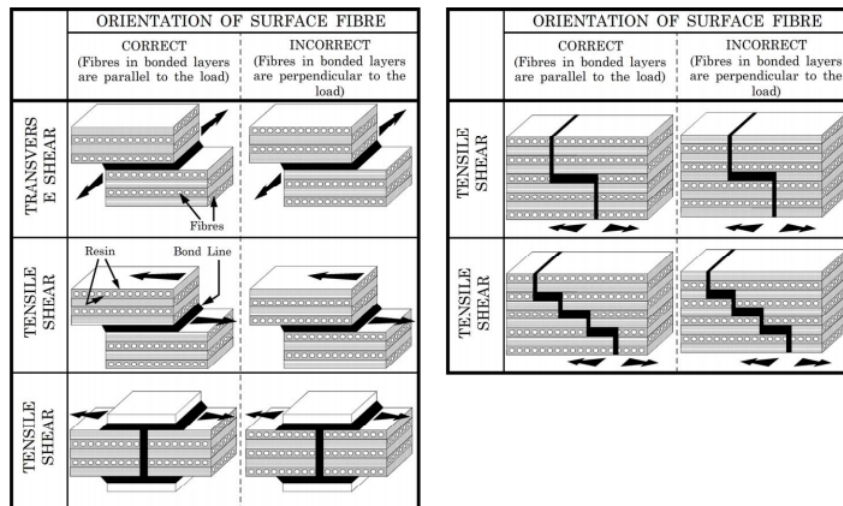


Figure 2.6: Correct and incorrect designs of composite bonded joints with optimal fibre orientation depending on different shear and tensile loads. Taken from ESA [1].

#### *Advantages:*

#### *Disadvantages:*

##### Mechanical fasteners

- No special surface preparation needed
- Strength not affected by thermal cycling or high humidity
- Presents no unusual inspection problems for joint quality
- Can be quickly and easily disassembled and reassembled, without destruction of the adherends

- Weakening of the composite adherends due to holes
- Stress concentrations near holes which can initiate failure
- Not generally as strong as bonded joints unless joining thick laminates
- Fasteners increase the overall weight
- Protruding fasteners can disrupt aerodynamic surfaces

##### Adhesive bonding

- Reduced average stress and stress concentration due to more equal load distribution over its area
- No machining on adherends
- Weight addition is minimum with only adhesives
- Bonded joints show less permanent set after first loading
- Smooth aerodynamic surfaces remain
- Good elevated temperature creep resistance
- Creates integrally sealed joints with low sensitivity to crack propagation
- Large areas of bonded joints cost less than mechanical fastened joints
- Corrosive resistant
- Enables the assembly of dissimilar materials prone to galvanic corrosion

- Difficulty with accurate non-destructive testing
- Impurities or non-uniformity of composite adherend and bondline material can give inaccurate strengths
- Careful design needed for peel loadings
- Special surface preparation needed on adherends for adhesives
- Permanent, allowing for no or very difficult disassembling
- Patch repairs are difficult
- Accurate mating and fit of adherends needed
- Thermal cycling and high humidity can affect strength

Table 2.1: Advantages and disadvantages of mechanical fasteners [1].

### 2.1.3. GENERAL ANALYTICAL METHODS OF SINGLE-LAP JOINTS

The single-lap joint is often taken as its the easiest and simplest joint. Many researchers have created analytical equations based on the single-lap joint that incorporate certain properties like material linearity, type of adherends, stress etc. to study and understand the forces and stresses in a single-lap joint. An overview can be found in Table 2.2.

	Material linearity		Adherends				Adhesive stresses			Solution				
	Adhesive		Adherend		Isotropic	Composite	Similar	Dissimilar		$\sigma_x$	$\sigma_y$	$\tau_{xy}$	Closed-form	Numerical
	Linear	Nonlinear	Linear	Nonlinear				Thickness	Material					
Volkersen [1]	X		X		X		X	X			X	X		
Goland and Reissner [2]	X		X		X		X			X	X	X		
Wah [21]	X		X		X	X	X	X			X	X	X	X
Hart-Smith [13,50]	X	X	X		X		X				X	X	X	
Pirvics [22]	X		X		X		X	X	X	X	X	X		X
Grimes and Greimann [58]	X	X	X	X	X	X	X	X	X	X	X	X		X
Renton and Vinson [23-24]	X		X		X	X	X	X	X	X	X	X		
Srinivas [25]	X		X		X	X	X	X	X	X	X	X	X	
Allman [18]	X		X		X	X	X			X	X	X	X	
Ojalvo and Eidinoff [16]	X		X		X	X	X	X	X	X	X	X	X	
Delale et al. [32]	X	X	X		X	X	X	X	X	X	X	X	X	
Bigwood and Crocombe [12]	X		X		X		X	X	X	X	X	X		X
Bigwood and Crocombe [51]	X	X	X		X		X	X	X	X	X	X	X	
Cheng et al. [26]	X		X		X		X	X	X	X	X	X		X
Crocombe and Bigwood [59]	X	X	X	X	X		X	X	X	X	X	X		X
Adams and Mallick [31]	X	X	X		X	X	X	X	X	X	X	X	X	
Tong [54]	X	X	X		X		X			X	X	X	X	
Yang and Pang [27]	X		X		X	X	X	X	X	X	X	X		X
Frostig et al. [48]	X		X		X	X	X	X	X	X	X	X		X
Sawa et al. [28]	X		X		X		X	X	X	X	X	X		X
Mortensen and Thomsen [33]	X	X	X		X	X	X	X	X	X	X	X		
Adams et al. [61]	X	X	X	X	X		X			X	X	X	X	
Wang et al. [60]	X	X	X	X	X		X	X	X	X	X	X		X
Smeltzer and Klang [56]	X	X	X	X	X	X	X	X	X	X	X	X		X

Table 2.2: Overview of popular analytical methods for forces and stresses in a 2D single-lap joint. Taken from da Silva *et al.* [14].

The methods in Table 2.2 are only meant for single-lap joints. Bonded joints are so complex and unique, that there are no general analytical equations and equations that are able to give the full stress distributions throughout the full joint thickness. Calculations further on in this thesis, in particular for the CLS specimen, will thus be trusted to the finite element package MSC.Marc.

## 2.2. FAILURE MODES WITHIN BONDED JOINTS

A bonded joint can fail in many ways. In general, as noted in Chapter 1, failure in bonded joints is often placed in three categories: cohesive, adhesive and adherend failures.

### 2.2.1. COHESIVE FAILURE

Cohesive failure takes place within the adhesive, with clear presence of adhesive on both adherends once fractured. Cohesive failure often occurs with shear load, although peel stresses or a combination of may also result in cohesive failure. Poor joint design such as insufficient overlap length is a typical cause for cohesive failure. Excessive porosity can also result in cohesive failure [16].

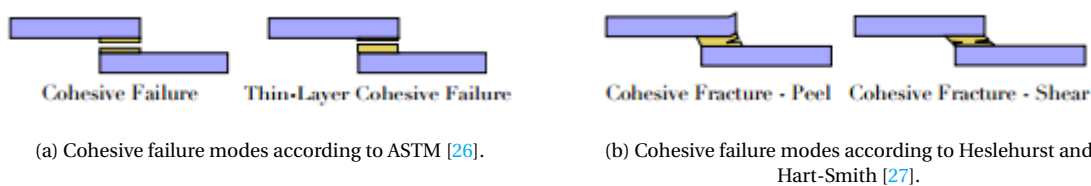
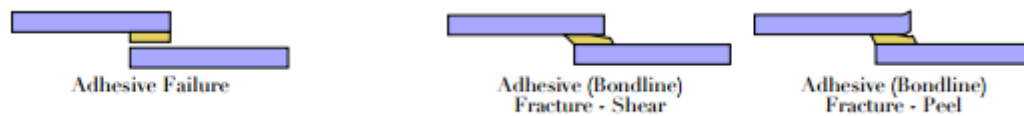


Figure 2.7: Cohesive failure modes in bonded joints.

Figure 2.7 gives two interpretations of cohesive failure modes within composite bonded joints. ASTM [26] approaches the failure modes as it would look like after testing while Heslehurst and Hart-Smith [27] approaches failure modes more based on the load cases.

### 2.2.2. ADHESIVE FAILURE

Adhesive failure takes place on the interface of the adherend and adhesive. Adhesive failure is often commonly called disbonding. Common causes are improper manufactured and contaminated surfaces, surfaces that are not properly resistant to hydration and adhesive curing that took place before the bonding. A mixed failure mode of adhesive and cohesive failure can occur. Such a mix is still classified as an adhesive failure when the adherend surface is visible and the adhesive fractured close to the surface. Figure 2.8 gives two interpretations of cohesive and adherend failure modes within composite bonded joints. ASTM [26] approaches the failure modes as it would look like after testing while Heslehurst and Hart-Smith [27] approaches failure modes more based on the load cases.

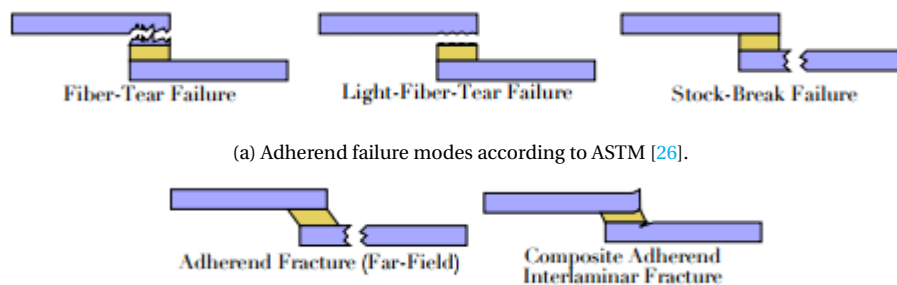


(a) Adhesive failure modes according to ASTM [26]. (b) Adhesive failure modes according to Heslehurst and Hart-Smith [27].

Figure 2.8: Adhesive failure modes in bonded joints.

### 2.2.3. ADHEREND FAILURE

Adherend failure takes place anywhere in the adherend of the bonded joint. A common cause for adherend failure would be faulty ply matrices or improper curing of plies. Figure 2.9 gives two interpretations of adherend failure modes within composite bonded joints. ASTM [26] approaches the failure modes as it would look like after testing while Heslehurst and Hart-Smith [27] approaches failure modes more based on the load cases.



(a) Adherend failure modes according to ASTM [26].

(b) Adherend failure modes according to Heslehurst and Hart-Smith [27].

Figure 2.9: Adherend failure modes in bonded joints.

For composite adherends, there are multiple failure modes to be taken into account due to the complexity of composite materials [26–28]. There exist three special types of failure modes in the adherends: interlaminar failure, intralaminar failure and fibre failure. Interlaminar failure happens between plies, intralaminar failure within plies and failure directly in the fibres of the plies. Interlaminar failure is delamination, which is separation at the interface between plies. For fibre and intralaminar failure, there are five types of fracture that have been recognized [6, 29]:

- Tensile fiber fracture
- Compressive fiber fracture, also known as kinking
- Tensile matrix failure

- Compressive matrix failure
- Shear matrix failure

A visualisation and overview of these fractures can be found in Figure 2.10 and Table 2.3.

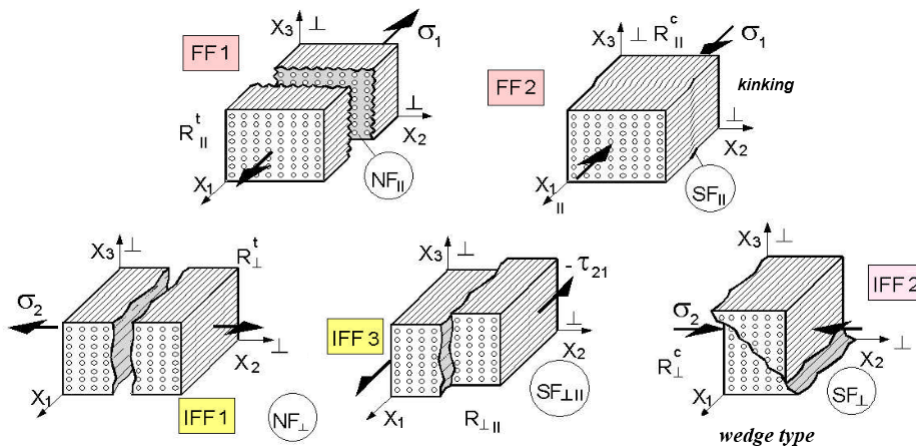


Figure 2.10: Overview of failure modes within composite material. Fracture resistance denotation ( $R$ ), fibre failure ( $FF$ ) or inter fibre failure ( $IFF$ ), normal fracture ( $NF$ ) or shear fracture ( $SF$ ), tension ( $t$ ) or compression ( $c$ ) and parallel ( $\parallel$ ) or perpendicular ( $\perp$ ) loading to fibres. See Table 2.3 for a tabular overview. Taken from Cuntze [6].

Failure Mode	Driving failure stress	Stress type	Fracture Resistance
Tensile fiber fracture (FF1)	$\sigma_1$	$NF_{\parallel}$	$R_{\parallel}^t$
Compressive fiber fracture (FF2)	$-\sigma_1$	$SF_{\parallel}$	$R_{\parallel}^c$
Tensile matrix failure (IFF1)	$\sigma_2$	$NF_{\perp}$	$R_{\perp}^t$
Compressive matrix failure (IFF2)	$\sigma_2$	$SF_{\perp}$	$R_{\perp}^c$
Shear matrix failure (IFF3)	$-\tau_{21}, \tau_{23}$	$SF_{\parallel\perp}, SF_{\perp\perp}$	$R_{\parallel\perp}, R_{\perp\perp}$

Table 2.3: Tabular overview of Figure 2.10.

## 2.3. APPROACHES TO CRACK FAILURE ANALYSES

When it comes to failure, cracks are the most common defects in joints and composite laminates. They cause fracture, delamination and debonding. The emphasis in this literature research is put on crack failure in and around an adhesively bonded joint. Research on cracks have been extensive and have resulted in many models and failure criteria. Finite element methods have become the preferred method for analysis on bonded joints. Several reasons for this include that joint rotation and plasticity in both adherend and adhesive are easier to treat with the finite element method [30]. There are four well-known approaches to failure analysis that are based on finite element method: continuum mechanics, fracture mechanics, extended finite element method and damage mechanics [5]. A brief general description on the four most popular methods is given together with the advantages and disadvantages they bring.

### 2.3.1. CONTINUUM MECHANICS

The most common and well-known approach for material failure analysis is via continuum mechanics. Approaches based on continuum mechanics use the maximum values of stress, strain or strain energy resulting from finite element analyses, against a chosen failure criterion which uses the critical values of the material and indicates if a material has failed. Examples of such failure criteria are Von Mises and Drucker-Prager. Using continuum mechanics in failure analysis has proven successful and are still used today, although it has a shortcomings when applied to bonded joints.

Within cracks, a stress discontinuity exist at the beginning of the crack tip. Figure 2.11a shows a model with a crack tip in a planar plate problem, derived from a continuum mechanics approach. In reality, the  $y$ -stresses at the crack tip are actually finite instead of infinite as derived by continuum mechanics. Further along the crack towards the end, the  $y$ -stresses are zero, due to free surfaces where crack propagation has already occurred. This creates a discontinuity between the head of the crack and the remaining crack length. In both case of Figure 2.11a and Figure 2.11b, the stresses are required to be continuous, and so the stresses at the crack tip are not defined, being infinite. This is called a singularity. These singularities are always present in crack angles smaller than 180 degrees [31]. A singularity is also presented between two bonded materials, with a stress jump at the interface, as in Figure 2.11b.

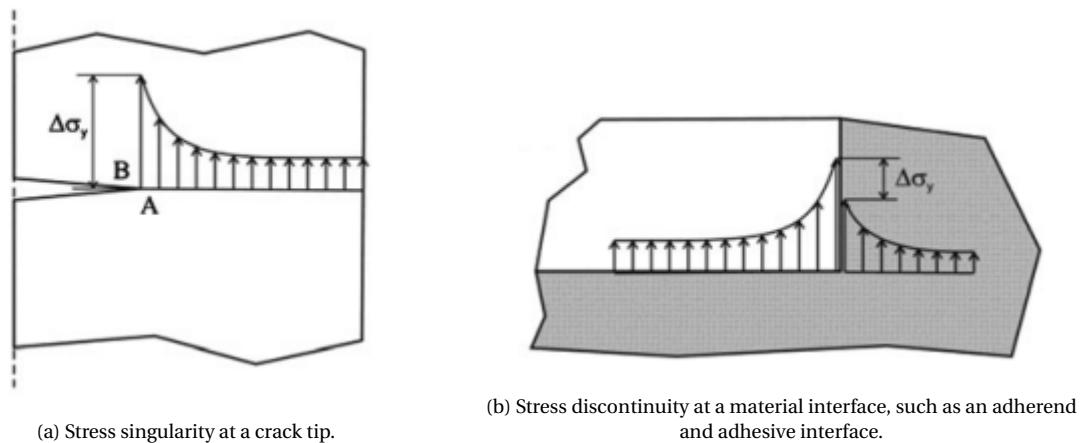


Figure 2.11: Stress singularities at crack tips and material interfaces. Taken from da Silva and Campilho [5].

Due to the singularity of stress at re-entrant corners of joints, the stresses depend on the mesh size and the proximity of the stress taken to the singularities, so care must be taken when using critical maximum values as failure criteria, such as maximum principal stresses. Using these stresses as a criterion is often applied to brittle materials [32, 33]. Several models have had some success with predicting failure. Clarke and McGregor [34] used maximum principal stress as a failure criterion, relating it to the maximum uniaxial stress in bulk adhesives over a certain length normal to the direction of the maximum principal stresses. Shear stresses are also often used as failure criteria and to predict joint strength [35–37]. Using shear stresses as criteria has its limitations. It ignores normal stresses and overestimates the joint strength, and articles have shown that the criterion is only valid for brittle adhesives and short overlaps [14, 38]. Clarke and McGregor [39] used critical peel stress at a certain distance from the stress singularity as a failure criterion in mixed-mode loading. The drawback was that the distance from the singularity differed in mixed-mode loading due to the constant change in plastic zone size. The stress based criteria don't have any physical justification when it comes to critical distances from the stress singularities and are largely dependent on mesh sizes and other physical parameters such as adhesive thickness and adherend rounding.

Stress based criteria are suitable for brittle materials, but not for ductile materials because joints can still sustain large loads during adhesive yielding. So for ductile materials, strain based failure criteria are used, with much success [15, 30, 40, 41]. The drawback with this type of criteria suffers from the same effects as stress based criteria.

Other failure criteria include the use of plastic energy density in the plastic part of deformation, which is based on total strain energy. Total strain energy takes account for all stress and strain components. Using an average plastic energy density as failure criteria has shown promising results for ductile adhesives [24, 42]. Other special criteria have been developed for specific situation, for example very ductile adhesives which caused severe yielding before failure. These are again limited to ductile adhesives and to lap joints [32, 39]. Yield criteria such as Von Mises' criterion have also been used as a failure criterion, although this is more applicable to material failure than strength failure and disbonding in joints.

The criteria based on the continuum approach are best limited to continuous structures only. They have difficulty when defects such as cracks or multiple materials are present like in bonded joints, due to stresses

and strains not being well defined at singular points.

### 2.3.2. FRACTURE MECHANICS

Because of the stress discontinuity in cracks and re-entrant corners, continuum mechanics is not a suitable approach as this approach requires that the structure and its material should be continuous. The stress singularity in the continuum mechanics approach results in infinity, which is physically not true. To still effectively study crack propagation and failure, studies were dedicated to this and the field of fracture mechanics was introduced. Fracture mechanics can be divided in Linear Elastic Fracture Mechanics (LEFM) and Elasto-Plastic Fracture Mechanics (EPFM). LEFM neglects non-linearity while EPFM takes non-linearity and plasticity into account.

#### Linear Elastic Fracture Mechanics

LEFM was the first introduced form of fracture mechanics and is still used today. As the name suggests, it assumes linear elastic behaviour in brittle materials up till the point of failure and uses simple failure criteria to indicate crack growth once reached, such as Griffith's criterion and Irwin's modification of Griffith's criterion [43]. Irwin also followed with a method to predict fracture initiation with a so-called stress intensity factor [44], which is based on the stress field of the crack tip within a radius and involves a small surrounding volume of the crack tip, and was widely adapted. A disadvantage when using the stress intensity factor is that the factor itself is not easily determinable when cracks grow near or at an interface. To counter this, methods were introduced using the strain energy release rate and critical value of fracture toughness and applied to laminates or bonded joints [45–48]. Another method that was to improve the use of stress intensity factors was the generalised stress intensity factor. This improved version was able to predict damage initiation for bonded joints at interface corners [49, 50] and for a variety of adhesive thickness [4]. These methods work well enough for standard simple joints, although they are questionable for more complex geometries and joints. Even though LEFM has its limits, it still has success the aircraft industry, where the damage tolerance design concept, which is based on linear elastic fracture mechanics, is widely used.

#### Elasto-Plastic Fracture Mechanics

LEFM is not applicable for ductile material as these materials tend to plastically deform before fracturing and thus rendering the assumption of linearity untrue. To analyse ductile material, or material subject to plastic deformation before failure, EPFM was introduced. The first theories to incorporate plasticity in crack behaviour were using the crack tip opening displacement as an important parameter and a plastic radial or spherical zone which incorporated the crack [51]. Modifications and improvements were made to improve the method by correcting the actual crack length, plastic zone and assumption that the stress is not singular at the boundaries but zero [18]. Although the method took care of the stress singularity, a strain singularity is still invoked for ductile materials.

A breakthrough was made within non-linear fracture mechanics with the introduction of the J-integral [52]. The J-integral is used as an energy contour line integral, and the independent integral path can be used to travel from one crack surface to another and encloses the crack tip. In each point of the contour, it calculates the current specific elastic energy stress and strain states. Due to the path independency of the integral, the contour can be chosen as circular and can be related to the stress intensity factor and the energy release rate, which then can be used in failure criteria. A simple visualisation of the J-integral can be found in Figure 2.12.

A modified version of the J-integral is the Hutchinson, Rice and Rosengren solution, applied to material that behave according to the Ramberg-Osgood relation [53, 54]. The J-integral has given good results in cracked bonded joints [55–57], although the J-integral comes with disadvantages. Even though the integral itself is path-independent, it is limited by joint geometry. The development of the plastic zone field is limited by the adherends and the interfaces, seeing as the adhesive is often very thin in bonded joints. This ultimately makes the fracture toughness dependent of the geometry of the joint and interface length [58]. Because of this, the integral must be extrapolated against interface length whereby a mesh refinement is required, which increases computational time. Also, since the adherends are close to each other because of the thin bond-line, the interference of the closely situated singular sources in each adherend cause difficulty for numerical extrapolation. If a contour included both adherends, problems in accuracy will arise because the interfering singular sources will offset each other. These problems result in the J-integral being unsuitable as a strength criterion in uncracked bonded joints with ductile adhesives. An initial crack tip should be present in the

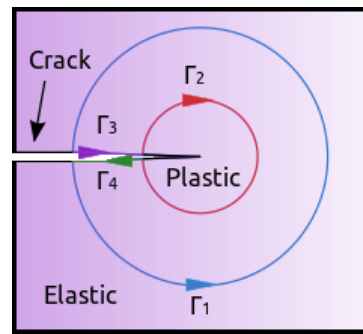


Figure 2.12: Contour of the J-integral around a crack tip. The contour encloses the crack tip where plasticity occurs.

structure if J-integral is used. Aside from this, the J-integral also has some issues when applied in finite element codes regarding crack propagation. Nodal variable and topological information from the nodes ahead and behind the crack front are required for the calculation of fracture parameters, such as the energy release rates or stress factors, and these calculations can be difficult when these codes are applied to progressive crack propagation [13].

Another method that is popular to use in fracture mechanics is the Virtual Crack Closure Technique (VCCT). It is based on the assumption that when a crack extends, the energy that was released during this is also the virtual work required to close the crack back to its original state [7]. It works with energy release rates and its critical value, or fracture toughness, which once reached indicates crack propagation by splitting coincident nodes, see Figure 2.13. VCCT uses nodal forces and displacements in a finite element model to calculate the current energy release rate for a particular mode, which is thus the same energy or work that is required to close the crack tip. The sum of all current energy release rates is the total energy release rate. Once the total energy release rate is equal to the critical energy release rate, crack propagation has occurred. A drawback of the method is that it assumes that nodal forces at nodes along a crack tip path are equal, which makes that crack initiation and propagation of short crack cannot be predicted [59]. It also suffers from the same drawbacks as the J-integral when implemented and used in finite element tools.

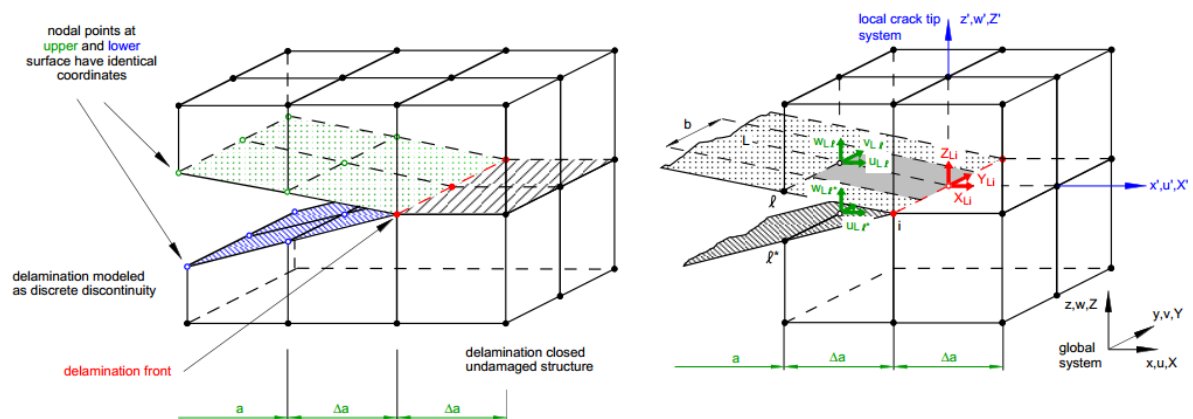


Figure 2.13: Depiction of the virtual crack closure technique. Left figure depicts a global system while the right figure shows the local system where the virtual work takes place. Taken from Krueger [7].

### 2.3.3. EXTENDED FINITE ELEMENT METHOD

A very recent development that has taken place in the field of crack propagation is the use of extended finite element method (XFEM) for modelling crack growth. Although the first theories of XFEM were introduced in 1999 [60], it is now gradually being adopted in finite element tools. Since its introduction, it has been improved over the years to accommodate 3D damage simulation [61], intersecting cracks with multiple branches [62], improvement to basis function to incorporate singularities in EPFM [63], crack propagation in

concrete [64], frictional contact modelling [65, 66], incorporating geometrical non-linearities [67] and fatigue applications in pure modes [68].

XFEM applies an initial linear elastic behaviour in the materials. For damage initiation and propagation, it uses criteria and damage laws respectively, which in turn are based on bulk strength values of materials and strain, between the real nodes and so-called phantom nodes of cracked elements. The damage initiation criteria can be based on principal stresses or strains, while the damage laws can be based on averaged fracture toughnesses, or energy release rates in this case, in finite regions following a linear or exponential behaviour. Once damage initiation occurs, so-called phantom nodes that were constrained to existing nodes start to separate, subdividing the elements that are cut by a crack and simulating separation between two newly created subelements. The phantom and real node then follow a damage law up until damage propagation. This technique ensures that cracks don't require a predefined path. Thus, XFEM has the major advantage that it can grow arbitrary cracks on its own without any crack tip or predefined crack path and does not require remeshing for crack propagation because of the averaging of the fracture toughness [69]. XFEM can be readily implemented in standard finite elements via the introduction of local enrichment functions for nodal displacements close to the crack to allow damage propagation and separation.

Because of XFEM being a fairly new concept, especially in finite element tools, not many applications and simulations have been performed regarding XFEM and bonded joints. Campilho *et al.* [70] ran two DCB simulations with XFEM to model and analyse crack propagation in 2D, in the finite element tool Abaqus. One DCB test involved steel adherends with a brittle adhesive inbetween, the other carbon-epoxy adherends with a ductile adhesive inbetween. Both tests had a crack tip with predefined crack path along the bond line and used a triangular shaped damage law to simulate damage initiation and propagation. The DCB testing is commonly performed to analyse pure tensile loading, also called pure mode I loading. Results were based on load-displacement curves and were found to have a good approximation in comparison with the experimental tests.

Another 2D simulation by Campilho *et al.* [71] on single and double lapped joints with aluminium adherends, a brittle adhesive and a range of overlap lengths. It used a principal strain failure criterion for damage initiation and estimation of crack growth direction. These tests were performed to analyse the tensile and shear load capabilities. Results showed that damage propagated towards and eventually in the aluminium adherend due to the corresponding direction of principal strains at the crack tip. This behaviour in the type of adherend is not supposed to reflect the experiments, and therefore damage propagation along the bond line was deemed unfeasible with XFEM by the authors. The reason behind this is that the XFEM algorithm will always search for maximum stresses or stress around the crack tip, giving the possibility for cracks to propagate in any adjacent element, regardless of bond line or material restriction. Another problem with these tests is that the use of one maximum principal strain criterion is only valid for brittle adhesives, as ductile adhesives deform plastically before damage propagation. Another issue was that the type of damage initiation criterion is subjected to mesh sensitivity as well. In the end, the result produced fair estimations compared to the experimental data.

Although XFEM has some major advantages, its current drawbacks can be problematic. The current implementation of XFEM in finite element tools such as Abaqus limits the use of the method. Damage in bonded joints differs from standard bulk material due to geometry, multiple materials and interfaces between materials. Due to XFEM's algorithm in tools like Abaqus and its reliance on one maximum principal stress and strain criterion, it is not possible to analyse mixed-mode loading for tensile and shear properties properly. The other downside was the current implementation which bases crack propagation on the failure criteria in any element around the crack tip, regardless of interface or material, that can give unfeasible results. This brings another problem, that when there is no initial crack, XFEM tends to find the maxima in any part of the structure, be it adherend or adhesive, to start a crack based on solely one single criterion. Even if XFEM was only restricted in the adhesive material, cracking still initiates orthogonally to the direction of the principal stresses or strains, which automatically specifies the direction of crack propagation. This works fine in situations like the DCB tests, but in bonded joints like lap joints, the crack will run up to the adherend interface and will halt crack propagation, as seen in Campilho *et al.* [71]. As it stands currently, XFEM methods are limited in finite element tools for multi material structures.

#### 2.3.4. DAMAGE MECHANICS

Failure of a material or cracks can also be perceived as damage in a material: creation and growth of microvoids and microcracks which are discontinuities in a medium considered as continuous on a macro scale

[72]. Damage mechanics follow cracks, or damage, progressively in a finite region, starting at an arbitrary point or a pre-defined crack, up to complete structural failure. This technique monitors and allows damage growth progressively while taking continuous stiffness degradation into account, from damage initiation till propagation [28, 72–74]. Damage models incorporate a so-called damage variable  $D$  or tensor  $\mathbf{D}$ , which decreases the stiffness properties in elements. These damage variables and tensor, or collectively called damage laws, can be expressed in many ways and be dependent on a variety of material properties such as moduli, strain, strain rates, stresses, Poisson ratios and more [72]. Damage laws are often expressed as ratios to indicate damage in the element, ranging from  $[0, 1]$  with 0 indicating no damage and 1 full damage and thus failure, reducing the stiffness properties to zero. Continuum damage mechanics can be seen as damage variables incorporated in continuum mechanics approaches. These mechanics can thus also use failure criteria such as Tsai-Wu, Puck or Hashin combined with damage laws.

A unique damage model is cohesive zone modelling. It can be divided into two approaches: local and continuum approach. In the local approach, damage in a finite element region is confined to a zero volume or zero surface area, which allows simulation of interfacial failure between materials in 3D or 2D respectively. In the continuum approach, the damage is modelled over a finite element region, non-zero volume or surface area elements. The elements used in both approaches that are subjected to damage mechanics can use the theories of Dugdale, Barenblatt and Hillerborg [18–20], and are called cohesive elements. CZM works with the strain energy release rate, which acts as the fracture toughness, and the cohesive traction in an element as a function of the relative displacement of opposing nodes. This function is called a constitutive relation, or separation-traction law, whereby the area of the function is the fracture toughness. The traction law starts with reversible or elastic behaviour, allowing no penalty to its stiffness for unloading and reloading, and after the maximum traction has been reached it shows irreversible or softening behaviour, lowering the stiffness for unloading and reloading after the maximum traction. A critical value for the fracture toughness is assigned, and once reached, indicates that the cohesive zone has reached full damage and is destroyed, and damage propagation occurs. The theory of CZM will be explained more in detail in Chapter 3.

CZM has started to become a favoured method in predicting static or fatigue damage and damage propagation, especially since the recent advances in finite element codes. Since the early nineties, the first applications of CZM were done in a local approach in brittle materials [75, 76]. The first applications of CZM on composites were performed in the last decade around the turn of the new millennia, with the advances in finite element software packages contributing a major part around half the decade [77–81]. CZM and its implementation in finite element codes have since then proven to be a successful new way of monitoring and analysing damage growth in bonded joints [79, 82–86]. It is versatile in both local and continuum approaches. Several examples are the ability to analyse delamination in a local approach [59, 87, 88], and bond line fracture in a continuum approach [11, 89, 90].

The benefits of CZM are numerous. CZM incorporates damage initiation and propagation in the same model, making it easy to analyse damage tolerances and strength altogether in one model [59, 87]. It follows damage progressively in an element, allowing a detailed capture of the damage evolution and the amount of damage an element has undergone up to its complete failure [5, 91]. The separation-traction law is simple in nature and has reversible and irreversible behaviour, allowing damage in non-destroyed elements to be retained during cyclic loading [11]. Due to the nature of damage mechanics and cohesive elements, CZM does not need an initial crack for damage propagation in a region. A crack in CZM can start arbitrarily within a region or on an interface. This means that a crack path does not necessarily have to be predefined, multiple crack paths can occur and uncracked structures can be analysed [92].

Drawbacks of CZM are its sensitivity to mesh sizes, which trades accuracy for additional computational time. The finer a mesh of a structures, the more accurate one can pinpoint where damage can originate and will propagate to. Another drawback are the traction laws which CZM is dependent on. Some traction laws are more suitable for ductile or materials, others for composites, and others for particular failure modes.

### 2.3.5. COMPARISON SUMMARY AND CHOICE

A comparison summary between the failure analysis approaches can be made and is found in Table 2.4. With the aid of Table 2.4, the choice has fallen on CZM to approach damage propagation in the bondline and delamination within the adherends in the CLS specimen. To approach the failure modes and ultimately damage propagation in the plies itself, progressive failure criteria based within continuum damage mechanics will be chosen to indicate whether there is intralaminar or fibre failure. The reason why failure criteria are used for

intralaminar and fibre failure is because of the multiple failure modes that can occur; there are failure criteria which have the ability to distinguish fibre and matrix failure within composites. CZM and their corresponding element types and material in MSC.Marc cannot support the possible complex failure modes in composite plies.

Table 2.4: Comparison table for the different failure analysis approaches and their advantages and disadvantages.

*Advantages:*

*Disadvantages:*

Continuum Mechanics approach:

- |   |   |
|---|---|
| <ul style="list-style-type: none"> <li>• Simple and easy to use criteria</li> <li>• Very suitable for brittle materials</li> <li>• Less information needed for criteria due to dependency on one or few parameters</li> </ul> | <ul style="list-style-type: none"> <li>• Not suitable for discontinuous structures</li> <li>• Not suitable for ductile materials</li> <li>• Sensitive to stress singularities</li> <li>• Can be inaccurate and give overestimation due to use of only one or few variables</li> <li>• Mesh sensitive, which can increase computational time for accuracy</li> <li>• Can't grow cracks without an initial crack tip</li> </ul> |
|---|---|

Fracture Mechanics approach:

- |   |   |
|---|---|
| <ul style="list-style-type: none"> <li>• Can be used for brittle and ductile materials, e.g. LEFM and EPFM</li> <li>• Suitable for multiple material structures like joints</li> <li>• Good accuracy</li> </ul> | <ul style="list-style-type: none"> <li>• Limited by joint geometry</li> <li>• Does not take care of strain singularity in ductile materials</li> <li>• Mesh sensitive, which can increase computational time for accuracy</li> <li>• Multiple singular sources close to each other can cause difficulty</li> <li>• Difficult numerical implementation for progressive crack propagation in finite element packages</li> <li>• Can't grow cracks without an initial crack tip</li> </ul> |
|---|---|

XFEM approach:

- |   |  |
|---|--|
| <ul style="list-style-type: none"> <li>• Can be used for brittle and ductile materials, e.g. LEFM and EPFM</li> <li>• Can incorporate singularities</li> <li>• Good accuracy</li> <li>• Can grow cracks without an initial crack tip</li> <li>• Doesn't require remeshing for increased accuracy</li> </ul> | <ul style="list-style-type: none"> <li>• XFEM is not yet well implemented and very limited in finite element packages</li> <li>• Mesh sensitive, which can increase computational time for accuracy</li> <li>• Current criteria don't distinguish between different materials or region, which can result in unfeasible crack paths and origins</li> </ul> |
|---|--|

Damage mechanics approach:

- |   |  |
|---|--|
| <ul style="list-style-type: none"> <li>• Can be used for brittle and ductile materials</li> <li>• Good accuracy</li> <li>• Can grow cracks without an initial crack tip</li> <li>• Can monitor crack propagation progressively for any element</li> <li>• Can be applied as bulk or interface elements</li> <li>• Reversible and irreversible behaviour taken into account</li> </ul> | <ul style="list-style-type: none"> <li>• Mesh sensitive, which can increase computational time for accuracy</li> <li>• CZM: Traction laws dependent on material types and failure modes</li> </ul> |
|---|--|

## 2.4. ANALYSIS OF FAILURE MODES

To examine the failure modes that occur in the CLS specimen, several methods are chosen. For cohesive and adhesive failure, CZM is chosen. This method is explained in detail in Chapter 3. For adherend failure, failure criteria in continuum damage mechanics are chosen. The theory behind several of these criteria will be explained in Chapter 2.4.1. The implementation of these criteria in MSC.Marc is explained in Chapter 2.4.2.

### 2.4.1. FAILURE CRITERIA

The failure modes encountered in composites were previously described as interlaminar failure, intralaminar failure and fibre failure. For intralaminar and fibre failure, failure criteria will be the preferred method to appropriately distinguish the type of failure. Failure criteria that can distinguish tensile and compressive fibre fracture and tensile and compressive matrix failure should be used to assess the CLS specimen on its failure modes. A selection has been made on several failure criteria, based on the World-Wide Failure Exercises (WWFE) [93, 94] and research extensions [95, 96]. Within the WWFE, the Puck failure criterion demonstrated as one of the most reliable with good results, with Hashin and Tsai-Wu failure criteria having above average results. These failure criteria will be used in the CLS specimen to assess the intralaminar and fibre failure modes. They will be explained in this section.

Several recurring material properties are frequently used within these criteria. These are listed in Table 2.5.

Material Property	Description
$x, y, z$	Global coordinate system with x being fibre direction
$X_T$	Tensile strength of ply in fibre direction
$X_C$	Compressive strength of ply in fibre direction
$Y_T, Z_T$	Tensile strength of ply in matrix direction
$Y_C, Z_C$	Compressive strength of ply in matrix direction
$S_{12}$	In-plane shear strength of ply
$S_{23}$	Transverse shear strength of ply

Table 2.5: Recurring material properties in failure criteria discussed in the remainder of this thesis.

#### Tsai-Wu

A well known failure criterion used for failure analysis in composites is the Tsai-Wu criterion [97], as seen in Eq. 2.1. It uses linear and quadratic polynomial terms of in-plane stress components, combining fibre and matrix failure modes in one equation. The use of only one equation has the advantage of having lower computational times for failure analyses.

$$f_i \sigma_i + f_{ij} \sigma_i \sigma_j = 1 \quad \text{for } i, j = 1, \dots, 6 \quad (2.1)$$

with

$$\begin{aligned}
 f_1 &= \left( \frac{1}{X_T} - \frac{1}{X_C} \right) & f_{11} &= \frac{1}{X_T X_C} & f_{44} &= \frac{1}{S_{12}^2} & f_{12} &= -\frac{1}{2} \sqrt{f_{11} f_{22}} \\
 f_2 &= \left( \frac{1}{Y_T} - \frac{1}{Y_C} \right) & f_{22} &= \frac{1}{Y_T Y_C} & f_{55} &= \frac{1}{S_{23}^2} & f_{23} &= -\frac{1}{2} \sqrt{f_{22} f_{33}} \\
 f_3 &= \left( \frac{1}{Z_T} - \frac{1}{Z_C} \right) & f_{33} &= \frac{1}{Z_T Z_C} & f_{66} &= \frac{1}{S_{13}^2} & f_{13} &= -\frac{1}{2} \sqrt{f_{11} f_{33}}
 \end{aligned}$$

The linear shear terms are reduced to zero because of symmetry in orthotropic material and the shear strength being independent of the sign in shear stress and like-wise the shear-normal coupling terms are not present due to the multiplying coefficients to these terms can be shown to vanish [28, 97], e.g.  $f_4$  and  $f_{14}$  etc. are obsolete. Shear strengths are all uncoupled as well for orthotropic materials, which reduces  $f_{45}$  and similar terms to zero [97].

### Hashin

Hashin and Rotem [98] proposed a criterion for unidirectional fibre composites in terms of quadratic stress polynomials. Hashin assumes four failure modes to be analysed: tensile fibre mode, compressive fiber mode, tensile matrix mode and compressive matrix node, with each mode being assigned a failure criterion, respectively Eq. 2.2 - Eq. 2.5.

$$\frac{\sigma_x}{X_T} \geq 1 \quad \text{for } \sigma_x > 0 \quad (2.2)$$

$$\frac{\sigma_x}{X_C} \geq 1 \quad \text{for } \sigma_x < 0 \quad (2.3)$$

$$\left( \frac{\sigma_{22} + \sigma_{33}}{Y_T} \right)^2 + \frac{\sigma_{23}^2 - \sigma_{22}\sigma_{33}}{S_{23}^2} + \frac{\sigma_{12}^2 + \sigma_{13}^2}{S_{12}^2} = 1 \quad \text{for } \sigma_{22} + \sigma_{33} > 0 \quad (2.4)$$

$$\left( \frac{\sigma_{22} + \sigma_{33}}{Y_C} \right)^2 + \frac{\sigma_{23}^2 - \sigma_{22}\sigma_{33}}{S_{23}^2} + \frac{\sigma_{12}^2 + \sigma_{13}^2}{S_{12}^2} = 1 \quad \text{for } \sigma_{22} + \sigma_{33} < 0 \quad (2.5)$$

With initial success, an improvement was made later on the failure modes for fibre tension and matrix compression [99]. It is based on stress invariants for transversely isotropic symmetry, making the assumption of the cross-sectional plane within a unidirectional fibre composite isotropic. The improved criteria can be found as Eq. 2.6 - Eq. 2.9

$$\left( \frac{\sigma_{11}}{X_T} \right)^2 + \frac{\sigma_{12}^2 + \sigma_{13}^2}{S_{12}^2} = 1 \quad \text{for } \sigma_{11} > 0 \quad (2.6)$$

$$\left( \frac{\sigma_{11}}{X_C} \right)^2 = 1 \quad \text{for } \sigma_{11} < 0 \quad (2.7)$$

$$\left( \frac{\sigma_{22} + \sigma_{33}}{Y_T} \right)^2 + \frac{\sigma_{23}^2 - \sigma_{22}\sigma_{33}}{S_{23}^2} + \frac{\sigma_{12}^2 + \sigma_{13}^2}{S_{12}^2} = 1 \quad \text{for } \sigma_{22} + \sigma_{33} > 0 \quad (2.8)$$

$$\left( \frac{\sigma_{22} + \sigma_{33}}{2S_{23}} \right)^2 + \left[ \left( \frac{Y_C}{2S_{23}} \right)^2 - 1 \right] \frac{\sigma_{22} + \sigma_{33}}{Y_C} + \frac{\sigma_{23}^2 - \sigma_{22}\sigma_{33}}{S_{23}^2} + \frac{\sigma_{12}^2 + \sigma_{13}^2}{S_{12}^2} = 1 \quad \text{for } \sigma_{22} + \sigma_{33} < 0 \quad (2.9)$$

### Puck

The Puck failure criterion works with an action plane to distinguish several matrix failure modes next to fibre failure modes [8]. This action plane occurs at a so-called failure, or fracture, plane angle  $\theta_{fp}$ . It represents the angle at which its stress plane  $\theta$  exhibits the global maximum of risk of fracture. The action plane is shown in Figure 2.14, together with the transformed coordinate system to the failure plane angle.

With the transformation of the coordinate system, transformation rules for the stresses are also introduced. The state of plane stresses are transformed according to Eq. 2.10 to stresses on the failure plane.

$$\begin{aligned} \sigma_{11} &= \sigma_{11} \\ \sigma_n &= \sigma_{22} \cos^2 \theta \\ \tau_{nt} &= -\sigma_{22} \sin \theta \cos \theta \\ \tau_{n1} &= \tau_{21} \cos \theta \end{aligned} \quad (2.10)$$

The fibre failure modes are seen in Eq. 2.11 and Eq. 2.12 and are independent on the failure plane.

$$\frac{\sigma_{11}}{X_T} = 1 \quad \text{for } \sigma_{11} > 0 \quad (2.11)$$

$$\frac{\sigma_{11}}{X_C} = 1 \quad \text{for } \sigma_{11} < 0 \quad (2.12)$$

Puck's inter fibre, or matrix, fracture modes are represented by three different modes, denoted A, B and C. Mode A and B are a result from tensile and compressive matrix and shear fracture, whilst Mode C is a result from in-plane shear and compressive matrix fracture. All three modes can be divided in the fracture envelope

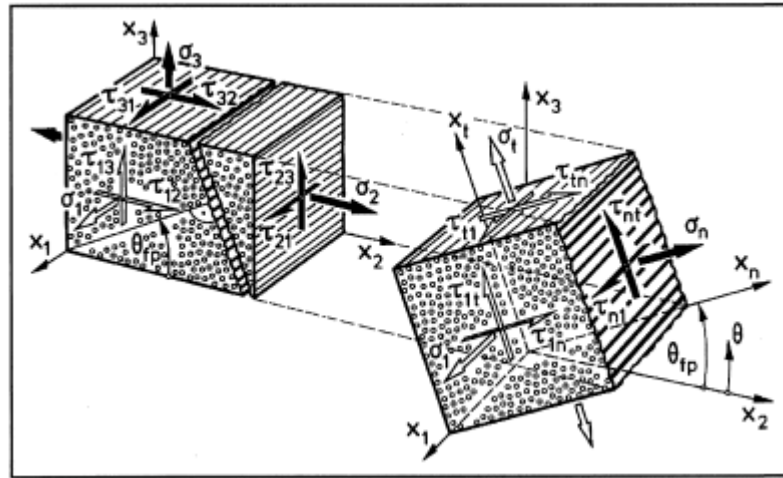


Figure 2.14: 3D coordinate system  $(x_1, x_2, x_3)$  of UD composite element, with fibre direction  $x_1$ , laminate mid-surface  $x_2$  and thickness direction  $x_3$ . Rotation failure plane angle  $\theta_{fp}$  results in coordinate system  $(x_1, x_n, x_t)$ , with fibre direction  $x_1$ , normal direction to failure plane  $x_n$  and tangential direction to failure plane  $x_t$ . Normal stresses  $\sigma_{ij}$  are noted as  $\sigma_i$  and shear stress  $\sigma_{ij}$  as  $\tau_{ij}$ . Taken from Puck and Schürmann [8].

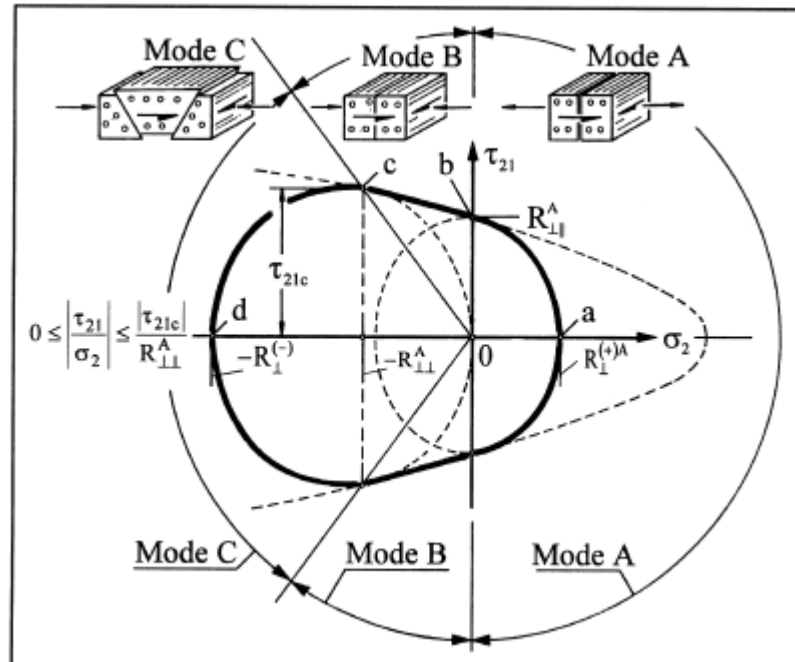


Figure 2.15: Fracture envelope for Puck's matrix failure modes A, B and C, depicting the different fracture resistances and positions of the failure modes on the stress coordinate system. Taken from Puck and Schürmann [8].

of Puck, see Figure 2.15. Mode A describes a plane stress  $(\sigma_{22}, \sigma_{21})$  condition, with  $\sigma_{22} \geq 0$ , rendering the fracture with a failure plane angle  $\theta_{fp} = 0^\circ$  [8]. The failure criterion for Mode A is expressed in Eq. 2.13. Mode B describes the same plane stress condition, but with  $\sigma_{22} < 0$ , rendering only a part of the fracture envelope with a failure plane angle  $\theta_{fp} = 0^\circ$ . The failure criterion for Mode B is expressed in Eq. 2.14.

$$\sqrt{\left(\frac{\sigma_{12}}{S_{12}^A}\right)^2 + \left(1 - \frac{p_{\perp\parallel}^{(+)}}{S_{12}^A} Y_T^A\right)^2 \left(\frac{\sigma_{22}}{Y_T^A}\right)^2} + \frac{p_{\perp\parallel}^{(+)}}{S_{12}^A} \sigma_{22} = 1 \quad \text{for } \sigma_{22} \geq 0, \theta_{fp} = 0^\circ \quad (2.13)$$

$$\sqrt{\left(\frac{\sigma_{12}}{S_{12}^A}\right)^2 + \left(\frac{p_{\perp\parallel}^{(-)}}{S_{12}^A}\right)^2 \sigma_{22}^2} + \left(\frac{p_{\perp\parallel}^{(-)}}{S_{12}^A}\right) \sigma_{22} = 1 \quad \text{for } \sigma_{22} < 0, \theta_{fp} = 0^\circ \quad (2.14)$$

with  $p_{\perp\parallel}^{(+)}$  being the slope of the  $(\sigma_n, \tau_{n1})$  fracture envelope at  $\sigma_n = 0$  for  $\sigma_n \geq 0$  and  $p_{\perp\parallel}^{(-)}$  being the slope of the  $(\sigma_n, \tau_{n1})$  fracture envelope at  $\sigma_n = 0$  for  $\sigma_n \leq 0$ .

Fracture tests with uniaxial transverse compressive loads have often shown fracture angles around  $\theta_{fp} = \pm 45^\circ$ , which may lead to the remainder of the fracture envelope in Figure 2.15, where  $\sigma_{22} < 0$  and  $\theta_{fp} \neq 0^\circ$  and thus failure Mode C. To find  $\theta_{fp}$ , the risk of fracture value can be used. The risk of fracture is expressed as the angle-dependent effort  $f_E(\theta)$  for a any given stress state for  $-90^\circ \leq \theta \leq +90^\circ$ . The angle-dependent effort  $f_E(\theta)$  is a reciprocal value of the so-called reserve factor  $f_r(\theta)$ , with  $f_r(\theta_{fp})$  and  $f_E(\theta_{fp})$  being the point where fracture is expected. The reserve factor is in fact a factor all existing stresses have to be multiplied with in order to achieve fracture. The maximum of  $f_E(\theta)$  can be calculated with its derivative, which then leads to the failure plane angles  $\theta_{fp}$ , one being the trivial  $\theta_{fp} = 0^\circ$  and the other being the unique solution. The unique solution is seen as Eq. 2.15 and  $f_E(\theta_{fp})$  in Eq. 2.16.

$$\theta_{fp} = \arccos \sqrt{\frac{f_w S_{23}^A}{-\sigma_{22}}} \quad (2.15)$$

$$f_E(\theta_{fp}) = \sqrt{\left(\frac{\sigma_{12}}{S_{23}^A}\right)^2 + \left(\frac{\sigma_{23}}{S_{13}^A}\right)^2 + \left(\frac{p_{\perp\parallel}^{(-)}}{S_{12}^A}\right)^2 \sigma_n^2 + \left(\frac{p_{\perp\parallel}^{(-)}}{S_{12}^A}\right) \sigma_n} \quad (2.16)$$

$$f_E(\theta_{fp}) = f_w = 1 - \frac{\sigma_{11}}{\sigma_{11D}} \quad \text{for } \sigma_n < 0$$

with  $p_{\perp\perp}^{(-)}$  being the slope of the  $(\sigma_n, \tau_{n1})$  fracture envelope at  $\sigma_n = 0$  for  $\sigma_n \leq 0$ , weakening factor  $f_w$  and  $\sigma_{11D}$  being the stress value for linear degradation:  $\sigma_{11D} > 0$  for  $\sigma_{11} > 0$  and  $\sigma_{11D} < 0$  for  $\sigma_{11} < 0$ . A coupling relation exists between the slopes of the fracture envelopes: This is expressed in Eq. 2.17.

$$\frac{p_{\perp\parallel}^{(-)}}{S_{12}^A} = \frac{p_{\perp\perp}^{(-)}}{R_{\perp\perp}^A} = \text{const.} \quad (2.17)$$

with

$$R_{\perp\perp}^A = \frac{Y_C}{2(1 + p_{\perp\perp}^{(-)})}$$

and  $p_{\perp\perp}^{(-)}$  being the slope of the  $(\sigma_n, \tau_{n1})$  fracture envelope for  $\sigma_n \leq 0$  at  $\sigma_n = 0$ .

With the help of Eq. 2.15, the failure criterion for Mode C is expressed in Eq. 2.18.

$$\frac{1}{2 \left[ 1 + \left(\frac{p_{\perp\parallel}^{(-)}}{S_{12}^A}\right) R_{\perp\perp}^A \right]} \left[ \left(\frac{\sigma_{12}}{S_{12}^A}\right)^2 + \left(\frac{\sigma_{22}}{R_{\perp\perp}^A}\right)^2 \right] \frac{R_{\perp\perp}^A}{(-\sigma_{22})} + \frac{\sigma_{11}}{\sigma_{11D}} = 1 \quad \text{for } \sigma_{22} < 0, \theta_{fp} = \arccos \sqrt{\frac{f_w S_{23}^A}{-\sigma_{22}}} \quad (2.18)$$

### 2.4.2. FAILURE CRITERIA IN MSC.MARC

Cassidian has a licence on the finite element package of the pre- and postprocessor MSC.Mentat and the solver MSC.Marc. It is capable of handling non-linear simulations and has the ability to implement failure criteria in a progressive manner, to apply continuum damage mechanics. The criteria that are chosen for the CLS specimen will be explained in short how they work in MSC.Marc, together with the progressive failure mechanics behind them. For more information, see Marc 2010 Volume A: Theory and User Information [12].

#### Tsai-Wu Failure Criterion

Tsai-Wu is a failure criterion designed to attend to a more global form of failure. It does not make distinction between different failure modes, yet has proven to be accurate when any form of failure occurs. Therefore, Tsai-Wu only has one failure index, which is seen in

$$FI_1 = \left[ \left( \frac{1}{X_T} - \frac{1}{X_C} \right) \sigma_1 + \left( \frac{1}{Y_T} - \frac{1}{Y_C} \right) \sigma_2 + \left( \frac{1}{Z_T} - \frac{1}{Z_C} \right) \sigma_3 + \frac{\sigma_1^2}{X_T X_C} + \frac{\sigma_2^2}{Y_T Y_C} + \frac{\sigma_3^2}{Z_T Z_C} \right] / F$$

$$+ \left[ \frac{\sigma_{12}^2}{S_{12}^2} + \frac{\sigma_{23}^2}{S_{23}^2} + \frac{\sigma_{13}^2}{S_{13}^2} + 2F_{12}\sigma_1\sigma_2 + 2F_{23}\sigma_2\sigma_3 + 2F_{13}\sigma_1\sigma_3 \right] / F \quad (2.19)$$

with maximum allowable stresses in tension  $X_t$ ,  $Y_t$ ,  $Z_t$  and compression  $X_c$ ,  $Y_c$ ,  $Z_c$  in 1-, 2- and 3-direction respectively, shear stresses  $\sigma_{ij}$ , principal stresses  $\sigma_i$ , maximum allowable shear stresses  $S_{ij}$ , failure index  $F$  and interactive strength constants for the 12  $F_{12}$ , 23  $F_{23}$ , and 31  $F_{13}$  plane.

The input parameters within MSC.Marc are the following, see also Figure C.5a:

- Max Tensile Stress X
- Max Compressive Stress X
- Max Tensile Stress Y
- Max Compressive Stress Y
- Max Tensile Stress Z
- Max Compressive Stress Z
- Max Shear Stress XY
- Max Shear Stress YZ
- Max Shear Stress ZX
- Failure Index. Default value is 1.
- Interactive Strength Tensor XY. Default value is 0.
- Interactive Strength Tensor YZ. Default value is 0.
- Interactive Strength Tensor ZX. Default value is 0.

Additional settings include:

- Progressive failure model: Selective Gradual Degradation, Selective Immediate Degradation and Original Marc Method.
- Deactivation of elements upon failure for: fibre tension, fibre compression, matrix tension and matrix compression.

#### Hashin Failure Criterion

The Hashin failure criterion is designed to distinguish fibre and matrix failure. Failure indices are implemented to respond to tension and compressive fibre modes, respectively Eq. 2.20 and Eq. 2.21, and to tension and compression matrix modes, respectively Eq. 2.22 and Eq. 2.23.

$$FI_1 = \left( \frac{\sigma_{11}}{X_t} \right)^2 + \frac{1}{S_{12}^2} (\sigma_{12}^2 + \sigma_{13}^2) \quad \text{for } \sigma_1 > 0 \quad (2.20)$$

$$FI_2 = \frac{|\sigma_{11}|}{X_c} \quad \text{for } \sigma_1 < 0 \quad (2.21)$$

$$FI_3 = \frac{1}{Y_t^2} (\sigma_2 + \sigma_3)^2 + \frac{1}{S_{23}^2} (\sigma_{23}^2 - \sigma_2\sigma_3) + \frac{1}{S_{12}^2} (\sigma_{12}^2 + \sigma_{23}^2) \quad \text{for } \sigma_2 + \sigma_3 > 0 \quad (2.22)$$

$$\begin{aligned}
FI_4 = \frac{1}{Y_c} \left( \left( \frac{Y_c}{2S_{23}} \right)^2 - 1 \right) (\sigma_2 + \sigma_3) + \frac{1}{4S_{23}^2} (\sigma_2 + \sigma_3)^2 \\
+ \frac{1}{S_{23}^2} (\sigma_{23}^2 - \sigma_2\sigma_3) + \frac{1}{S_{12}^2} (\sigma_{12}^2 + \sigma_{23}^2)
\end{aligned}
\quad \text{for } \sigma_2 + \sigma_3 < 0 \quad (2.23)$$

with maximum allowable stresses in tension  $X_t, Y_t, Z_t$  and compression  $X_c, Y_c, Z_c$  in 1-, 2- and 3-direction respectively, shear stresses  $\sigma_{ij}$ , principal stresses  $\sigma_i$  and maximum allowable shear stresses  $S_{ij}$ .

The input parameters within MSC.Marc are the following, see also Figure C.5c:

- Max Fibre Tension
- Max Fibre Compression
- Max Matrix Tension
- Max Matrix Compression
- Layer Shear Strength
- Transverse Shear Strength
- Slope  $P_{12C}$  of Fracture Envelope
- Slope  $P_{12T}$  of Fracture Envelope
- Slope  $P_{23C}$  of Fracture Envelope
- Slope  $P_{23T}$  of Fracture Envelope
- Residual Stiffness Factor. Default value is 0.01.
- Matrix Compression Factor. Default value is 0.
- Shear Stiffness Factor. Default value is 0.
- $E_{33}$  Reduction from Fibre Failure Factor. Default value is 0.
- Shear Reduction from Fibre Failure Factor. Default value is 0.

Additional settings include:

- Progressive failure: the use of the Residual Stiffness, Matrix Compression, Shear Stiffness,  $E_{33}$  Reduction from Fibre Failure and Shear Reduction from Fibre Failure factors.
- Progressive failure model: Selective Gradual Degradation, Selective Immediate Degradation and Original Marc Method.
- Deactivation of elements upon failure for: fibre tension, fibre compression, matrix tension and matrix compression.

### Puck Failure Criterion

The Puck failure criterion is designed to distinguish fibre and matrix failure. This criterion uses the concept of a fracture failure angle. This angle represents the angle of the fracture that is made by matrix failure. The angle is shown graphically in a coordinate system in Figure 2.16.

Failure indices are implemented to respond to tension and compressive fibre modes, respectively Eq. 2.24 and Eq. 2.25, and to plane stress cases, respectively Eq. 2.26, which is Mode A fracture, Eq. 2.27, which is Mode B fracture, and Eq. 2.28, which is Mode C fracture.

$$FI_1 = \frac{\sigma_1}{X_t} \quad \text{for } \sigma_1 > 0 \quad (2.24)$$

$$FI_2 = \frac{|\sigma_1|}{X_c} \quad \text{for } \sigma_1 < 0 \quad (2.25)$$

$$FI_3 = \sqrt{\left( \frac{\sigma_{12}}{S_{12}} \right)^2 + \left( 1 - p_{12t} \frac{Y_t}{S_{12}} \right)^2 \left( \frac{\sigma_2}{Y_t} \right)^2} + p_{12t} \frac{\sigma_2}{S_{12}} \quad \text{for } \sigma_2 > 0, \theta_{fp} = 0^\circ \quad (2.26)$$

$$FI_4 = \frac{1}{S_{12}} \left( \sqrt{\sigma_{12}^2 + (p_{12c}\sigma_2)^2} + p_{12c}\sigma_2 \right) \quad \text{for } \sigma_2 < 0, 0 \leq \left| \frac{\sigma_2}{\sigma_{12}} \right| \leq \frac{R^A}{\sigma_{21c}}, \theta_{fp} = 0^\circ \quad (2.27)$$

$$FI_5 = \left( \left( \frac{\sigma_{12}}{2(1 + p_{23c}S_{12})} \right)^2 + \left( \frac{\sigma_2}{Y_c} \right)^2 \right) \frac{Y_c}{|\sigma_2|} \quad \text{for } \sigma_2 < 0, 0 \leq \left| \frac{\sigma_{12}}{\sigma_2} \right| \leq \frac{\sigma_{21c}}{R^A} \quad (2.28)$$

with

$$R^A = \frac{Y_c}{2(1 + p_{23c})} \quad (2.29)$$

$$\sigma_{21c} = S_{12} \sqrt{1 + 2p_{23c}} \quad (2.30)$$

$$\cos^2 \theta_{fp} = \frac{1}{2(1 + p_{23c})} \left( \left( \frac{\sigma_{12}}{\sigma_2} \right)^2 \left( \frac{R^A}{S_{12}} \right)^2 + 1 \right) \quad (2.31)$$

and with maximum allowable stresses in tension  $X_t$ ,  $Y_t$  and compression  $X_c$ ,  $Y_c$  in 1-, 2-direction respectively, shear stresses  $\sigma_{ij}$ , principal stresses  $\sigma_i$ , maximum allowable shear stresses  $S_{ij}$ , fracture failure angle as in in Figure 2.16 and slope parameters of the failure envelop  $p_{12c}$ ,  $p_{12t}$ ,  $p_{23c}$  and  $p_{23t}$ . Eq. 2.31 is available as a sixth failure index only in postprocessing.

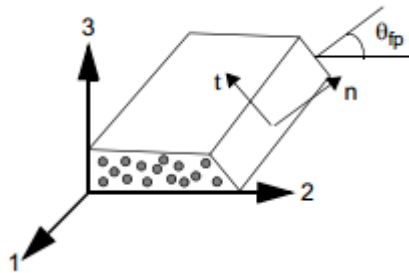


Figure 2.16: Angle  $\theta_{fp}$  representation in Puck's criterion in MSC.Marc.

The input parameters within MSC.Marc are the following, see also Figure C.5b:

- Max Fibre Tension
- Max Fibre Compression
- Max Matrix Tension
- Max Matrix Compression
- Layer Shear Strength
- Slope  $P_{12C}$  of Fracture Envelope
- Slope  $P_{12T}$  of Fracture Envelope
- Slope  $P_{23C}$  of Fracture Envelope
- Slope  $P_{23T}$  of Fracture Envelope
- Residual Stiffness Factor. Default value is 0.01.
- Matrix Compression Factor. Default value is 0.
- Shear Stiffness Factor. Default value is 0.
- $E_{33}$  Reduction from Fibre Failure Factor. Default value is 0.
- Shear Reduction from Fibre Failure Factor. Default value is 0.

Additional settings include:

- Progressive failure: the use of the Residual Stiffness, Matrix Compression, Shear Stiffness,  $E_{33}$  Reduction from Fibre Failure and Shear Reduction from Fibre Failure factors
- Progressive failure model: Selective Gradual Degradation, Selective Immediate Degradation and Original Marc Method.
- Deactivation of elements upon failure for: fibre tension, fibre compression, matrix tension, matrix compression (Mode B) and matrix compression (Mode C)

### Progressive Failure

MSC.Marc has three types of progressive failure models that are maintained in the failure criteria. The type that is chosen is a model that uses a selective degradation of the elastic and shear moduli. These moduli decrease gradually when failure occurs. When a failure index  $FI$  gets larger than one, so-called stiffness reduction factors  $r_i$  are re-calculated to change the moduli in each increment. The relationship of a re-calculated

modulus can be seen for all cases in Eq. 2.32. The smallest reduction factor is taken as the damage parameter  $D = 1 - r_i$ , from 0 being no damage to  $1 - a_1$  being full damage.

$$\begin{aligned} E_{11}^{new} &= r_1 E_{11}^{orig} & G_{12}^{new} &= r_4 G_{12}^{orig} \\ E_{22}^{new} &= r_2 E_{22}^{orig} & G_{23}^{new} &= r_5 G_{23}^{orig} \\ E_{33}^{new} &= r_3 E_{33}^{orig} & G_{31}^{new} &= r_6 G_{31}^{orig} \end{aligned} \quad (2.32)$$

The Poisson ratios are scaled in the same way as the re-calculated shear moduli. For Hashin and Puck failure criteria, distinctions are made between  $r_i$  for fibre and matrix failure:

- $r_1$  and  $r_3$  depend on the first and second failure index, signifying fibre failure. Uses the highest failure index of the two.
- $r_2, r_4, r_5$  and  $r_6$  depend on the third, fourth and fifth failure index, signifying matrix failure. Uses the highest failure index of the three.

The default incremental change in stiffness reduction factors is noted in a general fashion for all  $r_i$  in Eq. 2.33, based on a failure index  $FI$ .

$$\Delta r_i = - (1 - e^{1-FI}) \quad \text{if } FI > 1 \quad (2.33)$$

For Puck and Hashin failure criteria, Eq. 2.33 can be altered with the use and addition of five extra parameters:

$a_1$  - *Residual Stiffness factor*: The moduli are never reduced to less than this value.

$a_2$  - *Matrix Compression factor*:  $\Delta r_2$  is able to reduce less due to matrix compression failure, resulting in slower degrading for  $r_2$ . Certain types of material have a slower degradation of stiffness in compression than in tension [100]. This results in Eq. 2.34, with  $FI_{MC}$  denoting the failure index used for matrix compression. The higher index is used.

$$\Delta r_2 = - (1 - a_2) (1 - e^{1-FI_{MC}}) \quad \text{if } FI_{MC} > 1 \quad (2.34)$$

$a_3$  - *Shear Stiffness factor*: The shear stiffness  $G_{12}$ , dependent on  $r_4$ , has the possibility to reduce less than matrix stiffness  $E_{22}$ . This results in Eq. 2.35, with  $FI_M$  denoting the failure index for matrix tensile or compression failure. The higher index is used.  $a_2$  can also be taken into account for matrix compression failure, and results in Eq. 2.36.

$$\Delta r_4 = - (1 - a_3) (1 - e^{1-FI_M}) \quad \text{if } FI_M > 1 \quad (2.35)$$

$$\Delta r_4 = - (1 - a_2) (1 - a_3) (1 - e^{1-FI_{MC}}) \quad \text{if } FI_{MC} > 1 \quad (2.36)$$

$a_4$  -  *$E_{33}$  Reduction from Fibre Failure factor*:  $\Delta r_3$  is able to reduce less due to fibre and matrix failure, resulting in slower degrading for  $r_3$ . This results in Eq. 2.37, with  $FI_M$  denoting the failure index for matrix tensile or compression failure and  $FI_F$  denoting the failure index for fibre tensile or compression failure. The higher index is used.

$$\Delta r_3 = - (1 - a_4) (1 - e^{1-FI_F}) - a_4 (1 - e^{1-FI_M}) \quad \text{if } FI_M, FI_F > 1 \quad (2.37)$$

$a_5$  - *Shear Reduction from Fibre Failure factor*:  $\Delta r_4, \Delta r_5$  and  $\Delta r_6$  are now able to reduce less due to fibre failure as well, resulting in slower degrading for  $r_4, r_5$  and  $r_6$ . This reduction can be changed to vary linearly with both fibre and matrix failure. This results in Eq. 2.38, with  $FI_M$  denoting the failure index for matrix tensile or compression failure and  $FI_F$  denoting the failure index for fibre tensile or compression failure. The higher index is used.

$$\Delta r_4 = \Delta r_5 = \Delta r_6 = - (1 - a_5) (1 - e^{1-FI_M}) - a_5 (1 - e^{1-FI_F}) \quad \text{if } FI_M, FI_F > 1 \quad (2.38)$$

Note that not using parameters  $a_2$  through  $a_5$  results in the usage of Eq. 2.33. The material also does not 'heal'; it will retain the degraded properties after unloading.

Two other models are also available regarding progressive failure: Selective Immediate Degradation and Original Marc Method. Selective Immediate Degradation changes the stiffness values abruptly to the Residual Stiffness factor when failure occurs. The Original Marc Method used the following for certain materials:

- For orthotropic materials, the moduli at the integration points are set to the smallest of the original moduli, and the smallest to 10% of the original upon failure.
- For isotropic materials, the moduli are set to 10% of the original moduli upon failure.
- For material types that only require one modulus, the modulus is set to 10% of the original upon failure.

These remaining two progressive failure models will not be used since studies have shown a more gradual degradation of stiffness properties in composites [100, 101].

# 3

## COHESIVE ZONE MODELLING

Cohesive zone modelling will be used to analyse cohesive and adhesive failure in the debonding and delamination in the remainder of the thesis. The analytical theories behind CZM are explained in Chapter 3.1, which covers the fundamental understanding and the types of CZ models that are used today. As the solver MSC.Marc is the only tool Cassidian has to solve non-linear CZM problems, Chapter 3.2 is dedicated to explain the theory behind the programme regarding CZM.

### 3.1. THEORY

CZM has been introduced in the early sixties as an effort to analyse damage under static loading beyond the crack tip [18, 19]. CZM relates the relative displacement of two opposing associated points in a finite region to the force per unit of area, also known as traction. In cohesive elements, the relative displacement is often expressed as changes in surface normals and the traction as a function of the displacement with a stiffness tensor. Cohesive zone elements do not necessarily have to represent any physical material, yet they still describe the cohesive forces that exists when material elements separate from each other. Cohesive zone elements can also be modelled with an initial zero-thickness. This means that they can be used as a bulk element or as an interface element between bulk elements. A more fundamental background will be given on cohesive elements, relating to their traction forces and displacements. A simple illustration on the cohesive elements and forces can be found in Figure 3.1. CZM projects all damage mechanisms in and around a crack tip, leading to a constitutive relation, or cohesive zone law. There are many ways to define the criteria and laws for a cohesive zone model: the most common will be briefly discussed. The different load cases, or fracture modes, will also be discussed.

#### 3.1.1. TRACTION LAWS

A cohesive zone law, also known as a traction-separation law, describes the constitutive behaviour between the relative displacement  $\delta$  between two points and traction  $T$  as a curve. There are many varieties of traction laws, with the majority of them being piece-wise linear or non-linear and continuous or discontinuous.

A traction law can be divided into two parts. The first part is the interval between zero displacement and traction up till the damage initiation criterion. The damage initiation criterion is where maximum traction of a mode at a certain displacement occurs. The interval can be seen as an initial stiffness which the structure possesses. The damage initiation criterion is described as the maximum traction  $T_{max}$  or the displacement at the maximum traction  $\delta_c$  of a pure mode, based on known material properties. Once the damage initiation criterion has been reached and displacement increases, damage starts to occur and the initial elastic behaviour disappears, and the behaviour goes into the second part of the traction law. This part is the interval between the damage initiation criterion and the damage propagation criterion. The damage propagation criterion is described as a critical energy release rate  $G_c$ . The energy release rate, often called cohesive energy, is in fact the area between the traction law curve and  $y = 0$ , governed by the simple integral for a pure mode

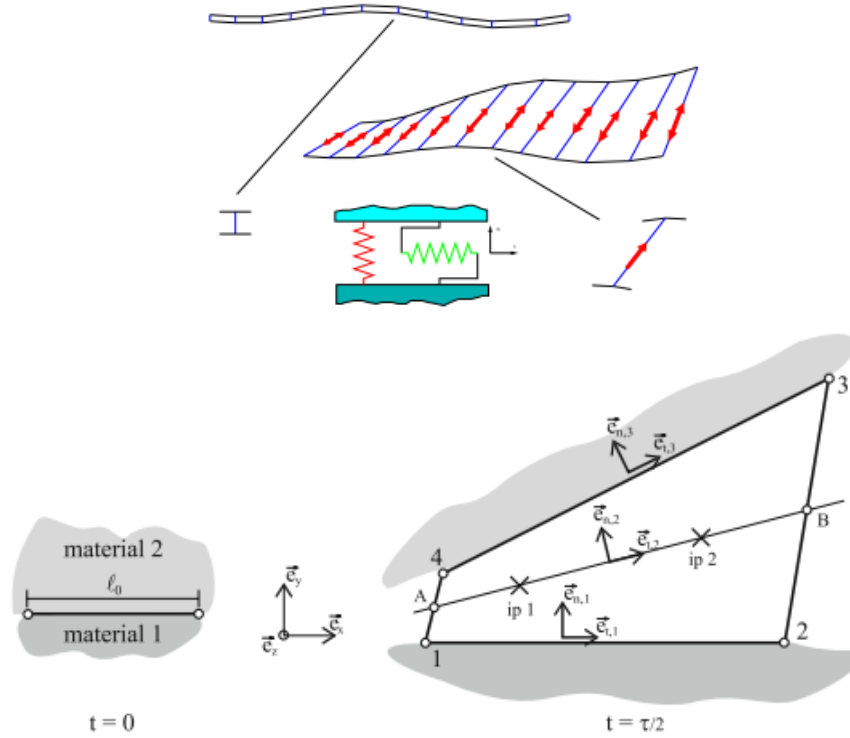


Figure 3.1: Simple illustrations of a cohesive zone element resembling a simplified spring-damper configuration and the deformation of a cohesive zone element. Taken from Kregting [9] and Bosch *et al.* [10].

fracture  $i$ :

$$G_i = \int T_i d\delta_i \quad (3.1)$$

$$G_{c,i} = \int_0^{T_i \rightarrow 0} T_i d\delta_i \quad (3.2)$$

with boundary conditions:

$$\frac{dG_i}{d\delta_i} \Big|_{\delta_i = \delta_{c,i}} = 0 \quad (3.3)$$

$$T_i(\delta_{c,i}) = T_{m,i} \quad (3.4)$$

and critical energy release rate  $G_c$ , max traction  $T_m$ , energy release rate  $G$  and opening displacement  $\delta$ . The critical energy release rate is often based on pure mode fracture, such as tension or shear. When the critical energy release rate is reached, it coincides with zero or near-zero traction. By then, full damage has been achieved, the cohesive zone disappears and crack growth occurs, hence the traction being reduced to zero as no cohesive forces are available to keep the material together. For a pre-determined crack path that has been designated as a cohesive zone, every opposing point or node pair along the interface or bulk material will find itself at a certain point on the traction law, depending on the relative displacement between the opposing points. Figure 3.2 illustrates these positions of random opposing point or node pairs along the cohesive zone in the traction law.

The first part up to damage initiation shows reversible behaviour, e.g. it can be seen as elastic behaviour. The second part from damage initiation to propagation shows irreversible behaviour, subjecting the cohesive zone to different behaviour under loading-unloading cycles and consequently to forced discontinuity. This behaviour can come in two forms: elastically and plastically damaged reloading. Elastically damaged

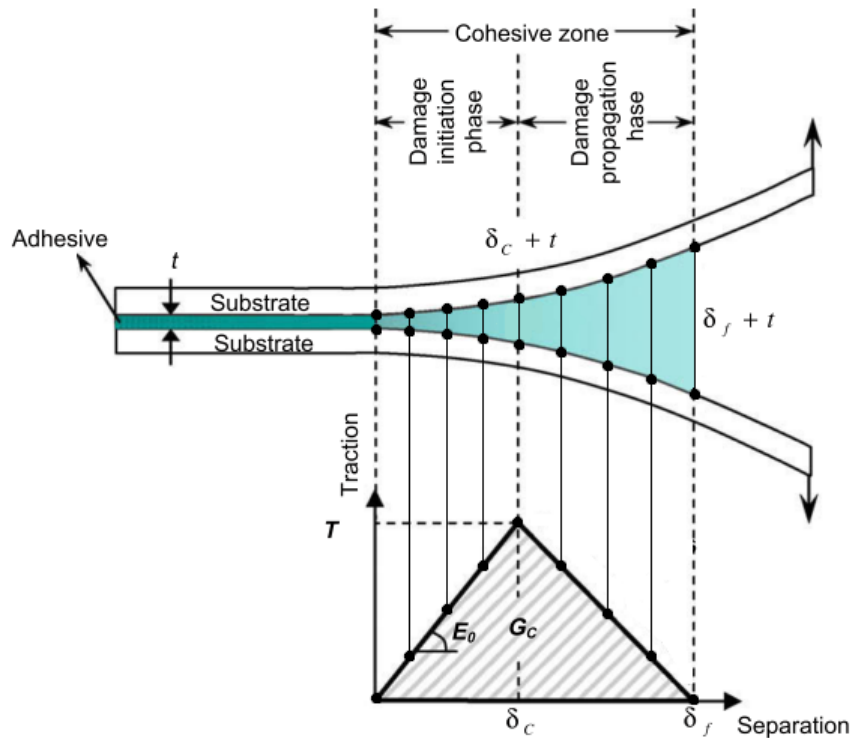
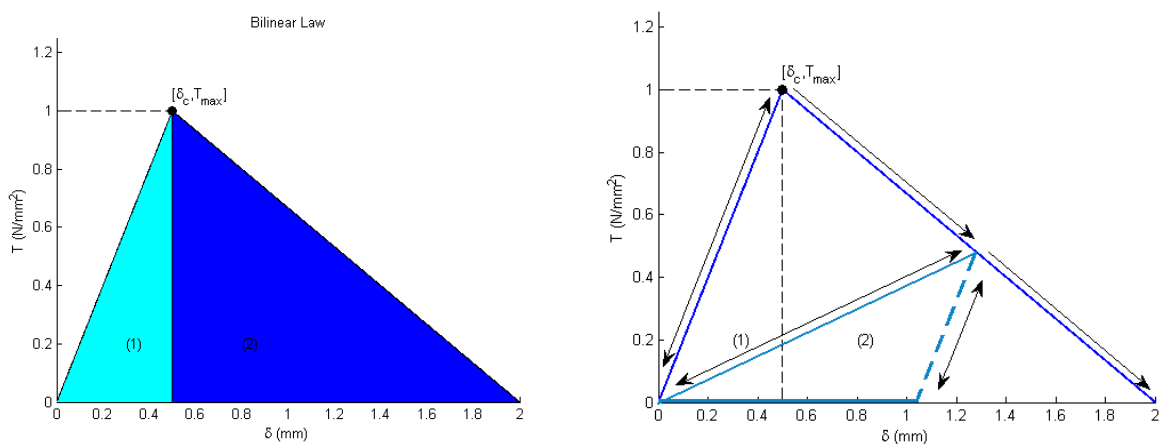


Figure 3.2: Position of relative displacement between opposing point pairs of a loaded bonded joint in the traction law. Example of a bonded joints in continuum approach. Taken from Khoramishad *et al.* [11].

reloading behaviour incorporates stiffness degradation of the cohesive zone, weakening the zone for repeated loading and unloading in a linear behaviour to and from the origin of the traction law. Plastically damaged reloading behaviour is reminiscent to material yielding in metals for the 0.2% strain proof: it retains the initial stiffness from the origin [91]. Figure 3.3 illustrates this in a traction law. In many papers, experiments and finite element packages, elastically damaged reloading behaviour is considered.



(a) Elastically damaged behaviour (1) in the reversible part and plastically damaged behaviour (2) in the irreversible part of a bilinear traction law.

(b) Reversible behaviour up to the critical opening displacement showing elasticity and irreversible behaviour with elastic (full line) and plastic (dotted line) damaged reloading between the critical and maximum opening displacement.

Figure 3.3: Reversible and irreversible behaviour and the effect of elastic and plastic loading and reloading.

The damage variable can be applied within traction laws. The damage remains zero in the part with reversible behaviour, see Figure 3.3, or in other words, until the damage initiation criterion  $\delta_c$  or  $T_{max}$ . Within the irreversible damaged part, damage starts to become non-zero and increases till the value of 1, indicating damage propagation and thus failure in the element. The damage law can be expressed in many forms to attain a damage model. To relate to Figure 3.3 and a more general form for other traction laws, a damage variable can be set up as a scalar function ranging from 0 to 1, see Eq. 3.5.

$$D(\delta) = \frac{G(\delta) - G_{\delta=\delta_c}}{G_c - G_{\delta=\delta_c}} \quad (3.5)$$

Most common used traction laws in literature and experimental validation are the bilinear law, the trapezoidal law and the exponential law [102]. The selection of traction law is dependent on the type of experiment, geometry and material. A bilinear model is often preferred for brittle materials and delamination [59], which offers a good compromise between numerical performance, computational cost and accuracy of results. For ductile adhesives, a trapezoidal law is preferred [103]. In simple coupon tests like a double cantilever beam test, the exponential law offers the most accurate results at the expense of computational cost [102].

### Bilinear Law

The bilinear, or triangular, traction law is a popular choice because of its simplicity. The bilinear law was redesigned from a simple rigid linear softening relationship to include an initial stiffness [76, 104]. The shape as it suggests is triangular and the function is piece-wise linear and discontinuous. It is described by the following uncoupled relation:

$$T_i = \begin{cases} \frac{T_{m,i}}{\delta_{c,i}} \delta_i & \text{if } 0 \leq \delta_i \leq \delta_{c,i} \\ \frac{T_{m,i}}{\delta_{c,i} - \delta_{m,i}} (\delta_i - \delta_{m,i}) & \text{if } \delta_{c,i} < \delta_i \leq \delta_{m,i} \\ 0 & \text{if } \delta_i > \delta_{m,i} \end{cases} \quad (3.6)$$

with max traction  $T_m$ , max and critical displacement  $\delta_m$  and  $\delta_c$  and relative displacement  $\delta$ . Using Eq. 3.2, the energy release rate and critical energy release rate can also be calculated:

$$G_i = \begin{cases} \frac{1}{2} \frac{T_{m,i}}{\delta_{c,i}} \delta_i^2 & \text{if } 0 \leq \delta_i \leq \delta_{c,i} \\ \frac{1}{2} T_{m,i} \left( \delta_{c,i} + (\delta_{m,i} - \delta_{c,i}) + \frac{(\delta_i - \delta_{m,i})^2}{\delta_{c,i} - \delta_{m,i}} \right) & \text{if } \delta_{c,i} < \delta_i \leq \delta_{m,i} \\ \frac{1}{2} T_{m,i} \delta_{m,i} & \text{if } \delta_i > \delta_{m,i} \end{cases} \quad (3.7)$$

$$G_c = \frac{1}{2} T_{m,i} \delta_{m,i} \quad (3.8)$$

Due to the amount of unknown parameters, the initial stiffness  $T_m/\delta_c$  is often chosen and described as a very high value to assume a stiff connection between an opposing point or node pair before damage occurs. This is called the penalty stiffness  $K$ , and is usually around a value of  $10^6 \text{ N/mm}^3$ , which was proven successfully in Gonçalves *et al.* [105] and Camanho *et al.* [106]. The shape of the bilinear law can be seen in Figure 3.4.

### Trapezoidal Law

Another often used model is the trapezoidal law. This function is also piece-wise linear and discontinuous. Tvergaard and Hutchinson [107] introduced it first. It is described by the following uncoupled relation for fracture mode  $i$ :

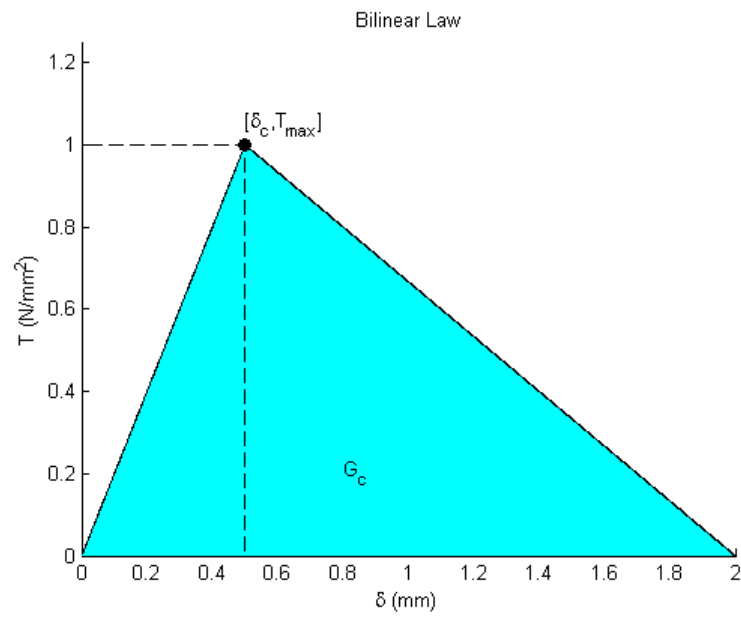


Figure 3.4: An example of a bilinear traction law. Code found in Appendix D.

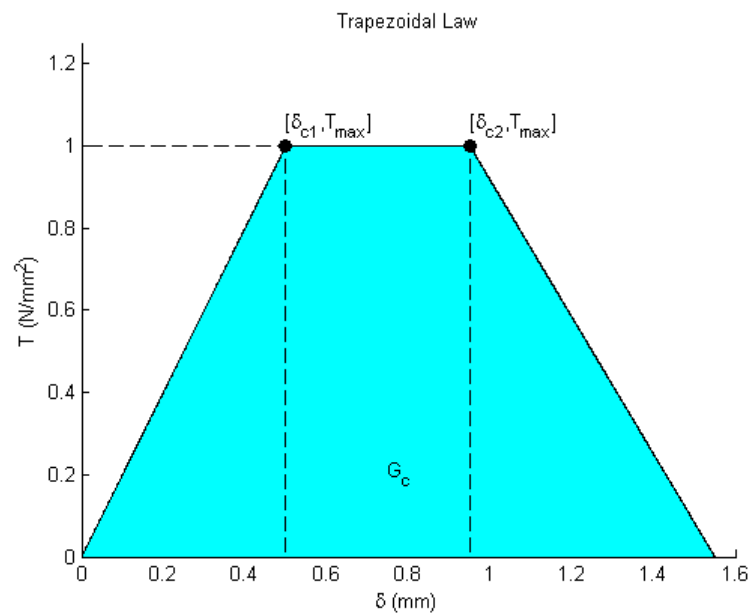


Figure 3.5: An example of a trapezoidal traction law. Code found in Appendix D.

$$T_i = \begin{cases} \frac{T_{m,i}}{\delta_{cI,i}} \delta_i & \text{if } 0 \leq \delta_i \leq \delta_{cI,i} \\ T_{m,i} & \text{if } \delta_{cI,i} < \delta_i \leq \delta_{cII,i} \\ \frac{T_{m,i}}{\delta_{cII,i} - \delta_{m,i}} (\delta_i - \delta_{m,i}) & \text{if } \delta_{cII,i} < \delta_i \leq \delta_{m,i} \\ 0 & \text{if } \delta_i > \delta_{m,i} \end{cases} \quad (3.9)$$

with max traction  $T_m$ , max and critical displacements  $\delta_m$ ,  $\delta_{cI}$  and  $\delta_{cII}$  and relative displacement  $\delta$ . Using Eq. 3.2, the energy release rate and critical energy release rate can also be calculated:

$$G_i = \begin{cases} \frac{1}{2} \frac{T_{m,i}}{\delta_{c,i}} \delta_i^2 & \text{if } 0 \leq \delta_i \leq \delta_{c,i} \\ T_{m,i} \left( \frac{1}{2} \delta_{cI,i} + (\delta_i - \delta_{cI,i}) \right) & \text{if } \delta_{cI,i} < \delta_i \leq \delta_{cII,i} \\ \frac{1}{2} T_{m,i} \left( \delta_{cI,i} + 2(\delta_i - \delta_{cI,i}) + (\delta_{m,i} - \delta_{cII,i}) + \frac{(\delta_i - \delta_{m,i})}{\delta_{cII,i} - \delta_{m,i}} \right) & \text{if } \delta_{cII,i} < \delta_i \leq \delta_{m,i} \\ \frac{1}{2} T_{m,i} (\delta_{cI,i} + 2(\delta_{cII,i} - \delta_{cI,i}) + (\delta_{m,i} - \delta_{cII,i})) & \text{if } \delta_i > \delta_{m,i} \end{cases} \quad (3.10)$$

$$G_c = \frac{1}{2} \frac{T_{m,i}}{\delta_{m,i}} \quad (3.11)$$

The shape of the trapezoidal law can be seen in Figure 3.5.

### Exponential Law

The exponential law is also used often. This function is continuous and smooth. It was first introduced by Xu and Needleman [75].

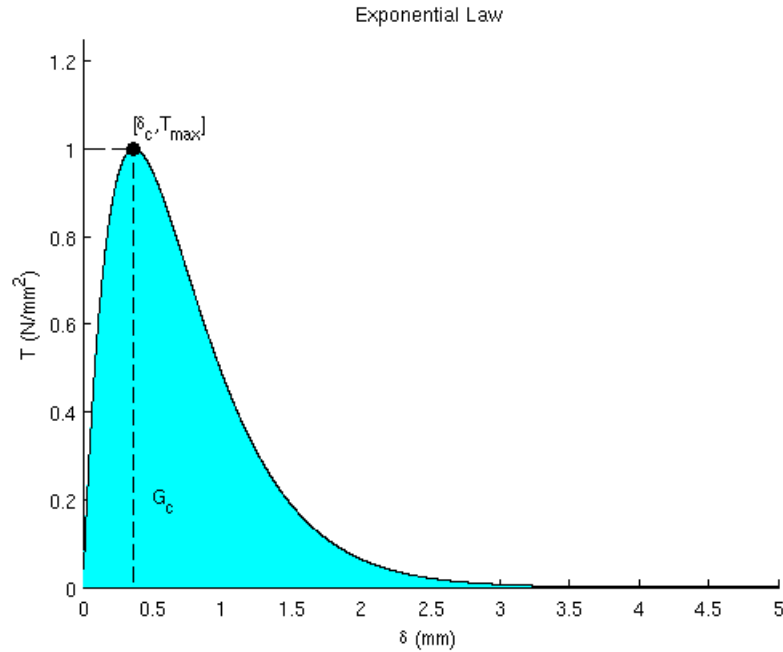


Figure 3.6: An example of an exponential traction law. Code found in Appendix D.

Their relation includes coupling and calculates directly with the energy release rates, equalising modes II and III:

$$T_I = G_{c,I} \frac{\delta_I}{\delta_{c,I}^2} e^{-\frac{\delta_I}{\delta_{c,I}}} \quad (3.12)$$

$$T_{II} = G_{c,II} \frac{\delta_{II}}{\delta_{c,II}^2} e^{-\left(\frac{\delta_{II}}{\delta_{c,II}}\right)^2} \quad (3.13)$$

with:

$$G_{c,I} = e T_{m,I} \delta_{c,I} \quad (3.14)$$

$$G_{c,II} = \sqrt{\frac{1}{2}} e T_{m,II} \delta_{c,II} \quad (3.15)$$

with max traction  $T_m$ , critical energy release rates  $G_c$ , critical opening displacement  $\delta_c$ , traction  $T$  and opening displacement  $\delta$ .

The shape of the exponential law can be seen in Figure 3.6.

### 3.1.2. COHESIVE ZONE ELEMENTS

As previously mentioned, a cohesive zone elements can be modelled as a flat interface element, having no volume in 3D or no surface in 2D, or bulk element, having a finite volume in 3D or finite surface in 2D. As a flat interface element, they are still modelled as a 3D eight-noded element in 3D or as a 2D four-noded element in 2D for example. A cohesive zone element can be approach analytically and be related to its traction, volume and body forces [10]. The weak form of the weighted residual integral of the equilibrium equation can be formulated as follows:

$$\int_V (\nabla \mathbf{w})^c : \mathbf{S} dV = \int_V \mathbf{w} \cdot \mathbf{q} dV + \int_A \mathbf{w} \cdot \mathbf{t} dA \quad \forall \mathbf{w}(\mathbf{x}) \quad (3.16)$$

with gradient operator  $\nabla$ , stress tensor  $\mathbf{S}$  body forces  $\mathbf{q}$ , boundary traction  $\mathbf{t}$  and arbitrary continuous weighing function  $\mathbf{w}$ . The left side of Eq. 3.16 represents the internal force which expresses the virtual work of the internal stresses and the cohesive tractions, while the right side represent the external forces on the element. Together with Gauss' theorem and the relation  $\mathbf{t} = \mathbf{S} \cdot \mathbf{n}$ , Eq. 3.16 can be rewritten to:

$$f_i(\mathbf{w}, \mathbf{S}) = f_e(\mathbf{w}, \mathbf{t}, \mathbf{q}) \quad \forall \mathbf{w} \quad (3.17)$$

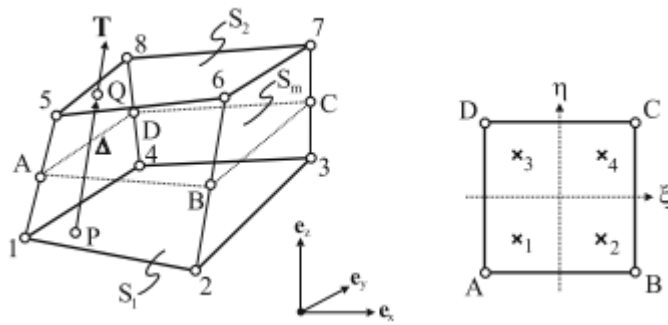


Figure 3.7: A 3D cohesive zone element in a reference and local coordinate system.

Using a 3D reference  $\mathbf{e}$  and local coordinate system  $[\eta, \xi]$  with range  $[-1, 1]$  and traction  $\mathbf{T}$  which connects original opposing points P and Q in the deformed state, see Figure 3.7, the internal forces can be expressed as:

$$f_i = \int_A \Delta \mathbf{w} \cdot \boldsymbol{\sigma} dA \quad (3.18)$$

$$f_i = \int_{A_0} \Delta \mathbf{w} \cdot \mathbf{T} dA_0 \quad (3.19)$$

with Cauchy traction vector  $\sigma$  and first Piola-Kirchhoff traction vector  $\mathbf{T}$ . Eq. 3.18 refers to the deformed state and Eq. 3.19 to the undeformed state. The weighing function  $\mathbf{w}$  is chosen to be a function of the local coordinate  $\eta$ , and together with traction  $\mathbf{T}$  can result into:

$$\underline{f}_i = \frac{A_0}{4} \int_{-1}^1 \int_{-1}^1 \underline{P}^T \underline{N}^T(\xi, \eta) \underline{T}(\xi, \eta) d\xi d\eta \quad (3.20)$$

with an operator matrix  $\underline{P} = [-\underline{I}_{12} \ \underline{I}_{12}]$ ,  $\underline{I}_{12}$  being a  $12 \times 12$  unity matrix and matrix  $\underline{N}$  containing the interpolation functions:

$$\underline{N}^T(\xi, \eta) = \begin{bmatrix} \psi_1 & 0 & 0 & \psi_2 & 0 & 0 & \psi_3 & 0 & 0 & \psi_4 & 0 & 0 \\ 0 & \psi_1 & 0 & 0 & \psi_2 & 0 & 0 & \psi_3 & 0 & 0 & \psi_4 & 0 \\ 0 & 0 & \psi_1 & 0 & 0 & \psi_2 & 0 & 0 & \psi_3 & 0 & 0 & \psi_4 \end{bmatrix} \quad (3.21)$$

where the shape functions  $\psi_i$  are associated with points A, B, C, and D in Figure 3.7:

$$\begin{aligned} \psi_1 &= \frac{1}{4}(1-\xi)(1-\eta) & \psi_2 &= \frac{1}{4}(1+\xi)(1-\eta) \\ \psi_3 &= \frac{1}{4}(1+\xi)(1+\eta) & \psi_4 &= \frac{1}{4}(1-\xi)(1+\eta) \end{aligned} \quad (3.22)$$

With an iterative procedure, one can approximate the integral in Eq. 3.20 and create the incremental value of the internal forces and element stiffness matrix:

$$\underline{f}_i^* = \frac{A_0}{4} \sum_{i=1}^4 [\underline{P}^T \underline{N}^T(\xi, \eta) \underline{T}^*(\xi, \eta)]^i \quad (3.23)$$

$$\underline{K}^* = \frac{A_0}{4} \sum_{i=1}^4 [\underline{P}^T \underline{N}^T(\xi, \eta) \underline{M}(\xi, \eta) \underline{N}(\xi, \eta) \underline{P}]^i \quad (3.24)$$

with cohesive tangent operator  $\underline{M}$ . This leads up to the iterative equation:

$$\underline{K}^* \delta \underline{u} = \underline{f}_e - \underline{f}_i^* \quad (3.25)$$

Eq. 3.25 can then be used in an iterative increment scheme like Newton-Raphson.

### 3.1.3. FRACTURE MODES

Traction occurs in normal and shear direction. Tensile stresses occur in mode I delamination, and shear stresses occur in mode II and mode III delamination. Figure 3.8 shows the different modes that are distinguished in pure form.

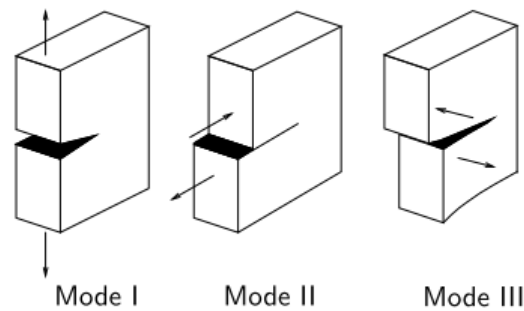


Figure 3.8: The three different fracture modes: tensile (Mode I), shear (Mode II) and tear (Mode III).

Mixed-mode loading is a combination of normal, shear and tear loading. Relations between the different modes can be found within a traction law. Most models which describe the behaviour between modes are often based on Ye's criterion, which is a quadratic interaction, relating to damage initiation:

$$\left(\frac{T_I}{T_{m,I}}\right)^2 + \left(\frac{T_{II}}{T_{m,II}}\right)^2 + \left(\frac{T_{III}}{T_{m,III}}\right)^2 = 1 \quad (3.26)$$

with max tractions and tractions for all modes  $T_m$  and  $T$ .

The energy release rate for mixed-mode is often described as a function of the pure mode energy release rates and is used as the damage propagation criterion. A popular criterion for calculating the energy release rates and subsequent failure criterion in mixed-mode loading is the power law criterion, shown in Eq. 3.27, but also other criteria have been used depending on the material [78], such as the Benzeggagh and Kenane criterion, as shown in Eq. 3.28:

Power Law: 
$$\left(\frac{G_I}{G_{c,I}}\right)^m + \left(\frac{G_{II}}{G_{c,II}}\right)^n + \left(\frac{G_{III}}{G_{c,III}}\right)^p = 1 \quad (3.27)$$

Benzeggagh and Kenane: 
$$\frac{G_I + G_{II} + G_{III}}{G_{c,I} + (G_{c,II} - G_{c,I}) \left(\frac{G_{II} + G_{III}}{G_I + G_{II} + G_{III}}\right)^\eta} = 1 \quad (3.28)$$

with energy release rates  $G$  and critical energy release rates  $G_c$  for modes I, II and III and empirical factor parameters  $m$ ,  $n$ ,  $p$  and  $\eta$ .

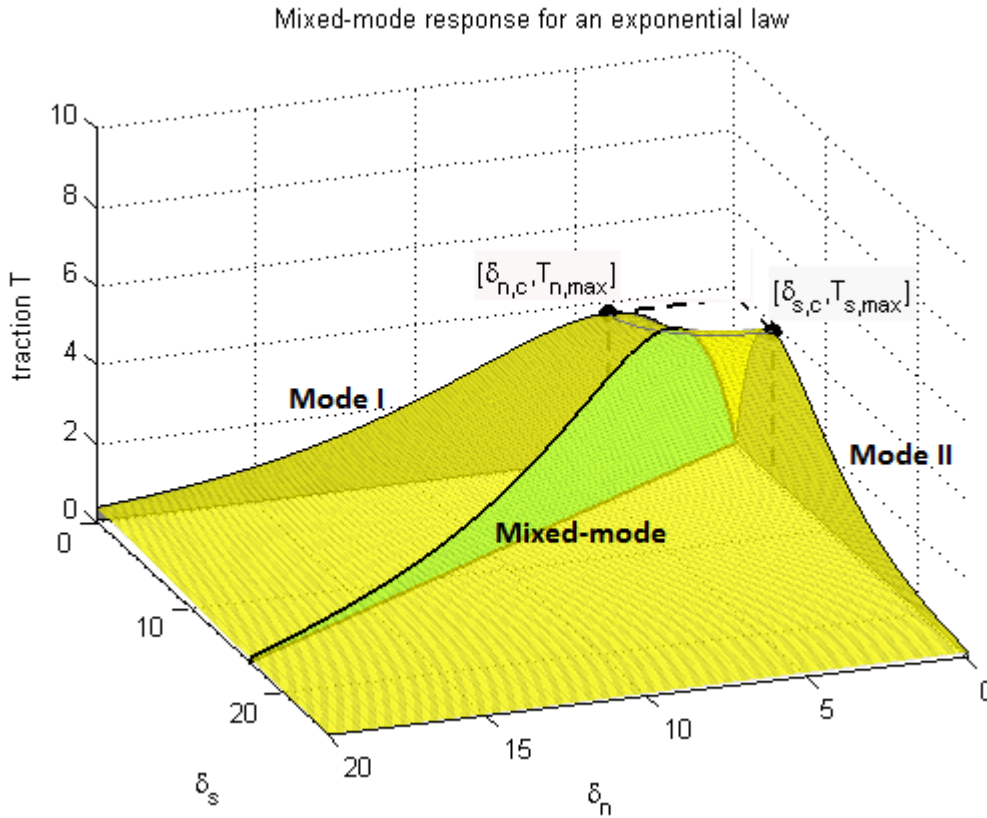


Figure 3.9: 3D view of a mixed-mode exponential traction law based on Ye's criterion. Any moment in mixed-mode loading can be traced to a point on the surface of the 3D graph. Code found in Appendix D.

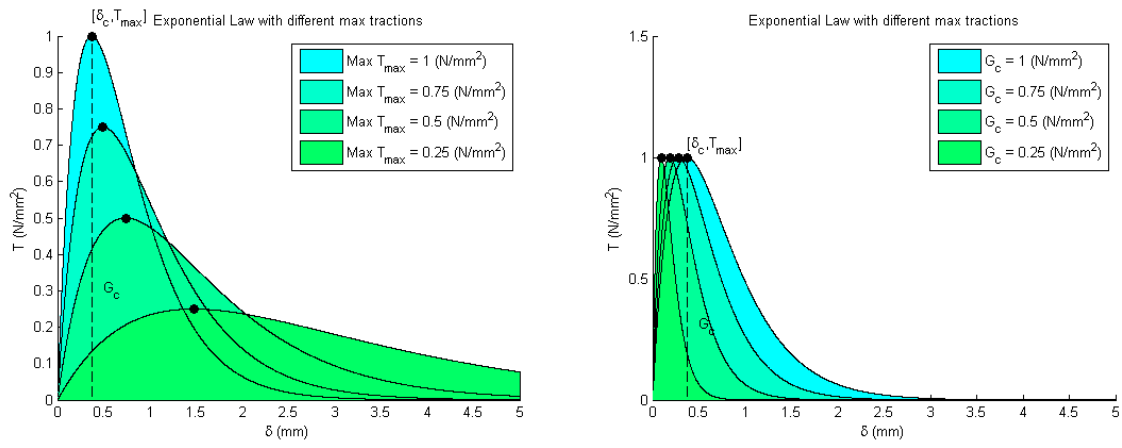
Using one of these relations that describe mixed-mode behaviour, for example Ye's criterion and the Power Law, one can visualise the mixed-mode response as a 3D surface graph, encompassing any mixed-mode ratio of loading between pure mode I and pure mode II, see Figure 3.9. On curve anywhere on this surface represents a mixed-mode traction law.

### 3.1.4. INFLUENCES ON A COHESIVE ZONE MODEL

So what can influence a cohesive zone model? Using the theories noted in the previous subsections, one can sum up the properties which have a big impact upon crack propagation.

Firstly, the traction law is a big influence. It determines the behaviour of how a cohesive element should behave: an elastic first part and plastic second part. It also indicated the impact of traction on the element. For example, a trapezoidal law compared to an exponential law has the ability to sustain a large traction for a significant longer amount of displacement. This has its advantages [103], and its situational in terms of material properties.

Second, the maximum traction has a large influence. It controls the slope of traction in the irreversible part since it will need to compensate of the fixed critical energy release rate, which was the area under a traction law and subsequently the amount of energy a CZE needs to get fully damaged. This makes a requirement for the type of adhesive, brittle or ductile. The critical opening displacement increases in a decreasing  $T_m$ , requiring a physically larger distance between nodes for a CZE to initiate damage. See Figure 3.10a for an example.



(a) Influence of a maximum traction on an exponential law. The critical opening displacement increases when the maximum traction decreases.

(b) Influence of a critical energy release rate on an exponential law. The critical opening displacement increases when the critical energy release rate also increases.

Figure 3.10: Influence of maximum traction and critical energy release rate.

Thirdly, the critical opening displacement and the critical energy release rate play a significant role if the initial stiffness and thus reversible part of the cohesive element: is it more stiff or more elastic? A decrease in critical energy release rate automatically decreases the critical opening displacement, without a change in max traction. This results in steeper or gradual decay of a CZE and physically requires a smaller distance between nodes for a CZE to initiate damage. An increase in critical energy release rate would require a physically larger opening displacement to fully damage a CZE. The effect of having a large critical opening displacement may have its advantages in fatigue loading.

Another parameter that seems to be of influence are the shear components of the critical energy release rate and max traction. This relates to mixed-mode loading and how well a traction law will perform in it. Several criteria relating to mixed-mode ratios were already explained in the previous chapter. Some adhesives have better shear properties while some have better tensile properties. The adhesive used in the CLS specimen for the bondline for example has a lower max shear traction than tensile traction, while it's the opposite way around for the adhesive in the laminates. This can give completely opposite mixed-mode cohesive zone models, and may be crucial in determining what failure may occur first.

## 3.2. MSC.MARC

MSC.Marc is capable of handling non-linear simulations and also has the ability to implement CZM. The theory behind CZM is explained in Chapter 3.2.1. A small explanation of the input parameters follows in

Chapter 3.2.2.

### 3.2.1. THEORY

The CZM algorithm in MSC.Marc is based on the tractions being a function of the relative displacements of the top and bottom edges or surfaces of a 2D or 3D element respectively. See Figure 3.11. The relative displacements are divided into a normal and two shear direction. Each relative displacement is expressed in the distance between the centres of the top and bottom element faces or edges. The effective opening displacement is then expressed as a simple Pythagorean relation:

$$\delta_n = u_1^{top} - u_1^{bottom} \quad (3.29a)$$

$$\delta_s = u_2^{top} - u_2^{bottom} \quad (3.29b)$$

$$\delta_t = u_3^{top} - u_3^{bottom} \quad (3.29c)$$

$$\delta = \sqrt{\delta_n^2 + \delta_s^2 + \delta_t^2} \quad (3.29d)$$

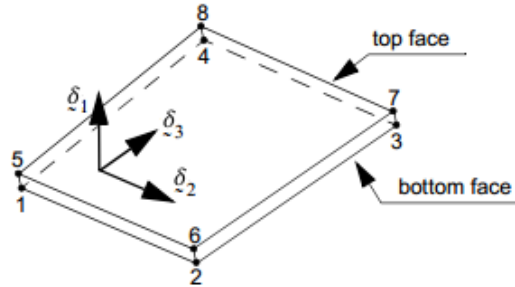


Figure 3.11: 3D interface element with a reference system based on an integration point. Taken from Marc 2010 Volume A: Theory and User Information [12].

with displacements  $u$ , relative displacements in normal  $\delta_n$ , shear  $\delta_s$  and tear  $\delta_t$ . Compressive loading is also taken into account. The normal component of Eq. 3.29d is changed to the following for compressive loading, so loading still remains physically possible and realistic:

$$\delta = \sqrt{[\max(\delta_n, 0)]^2 + \delta_s^2 + \delta_t^2} \quad (3.30)$$

The cohesive zone element is able to withstand compressive loading since interpenetration is prohibited in MSC.Marc, although it is possible to make the stiffness in compression a function of the corresponding (negative) opening displacement.

The effective traction is expressed as a function of the effective relative displacement. The effective traction is also characterised by having a reversible behaviour before and an irreversible behaviour after the critical effective opening displacement  $\delta_c$ . The irreversible behaviour in postprocessing is characterised by an increasing damage law value from 0, being damage initiation, to 1, being damage propagation. The damage law is according to Eq. 3.5. The damage law value can be used as a postprocessing parameter. MSC.Marc adopts elastically damaged reloading behaviour, e.g. when reloading, it uses a newly calculated stiffness from the origin to the last point the element was on the traction law.

MSC.Marc has three built-in traction laws to choose from: bilinear, exponential and linear-exponential. They are governed by the following functions respectively:

$$\text{Bilinear: } T = \begin{cases} \frac{2G_c}{\delta_m} \frac{\delta}{\delta_c} & \text{if } 0 \leq \delta \leq \delta_c \\ \frac{2G_c}{\delta_m} \frac{\delta_m - \delta}{\delta_m - \delta_c} & \text{if } \delta_c < \delta \leq \delta_m \\ 0 & \text{if } \delta > \delta_m \end{cases} \quad (3.31)$$

Exponential: 
$$T = G_c \frac{\delta}{\delta_c^2} e^{-\delta/\delta_c} \quad (3.32)$$

Linear-Exponential: 
$$T = \begin{cases} \frac{2G_c}{\delta_m} \frac{\delta}{\delta_c} & \text{if } 0 \leq \delta \leq \delta_c \\ \frac{2qG_c}{\delta_c(q+2)} e^{q(1-\delta/\delta_c)} & \text{if } \delta > \delta_c \end{cases} \quad (3.33)$$

with traction  $T$ , effective relative displacement  $\delta$ , critical energy release rate  $G_c$ , critical opening displacement  $\delta_c$ , maximum effective opening displacement  $\delta_m$  for the bilinear model and exponential decay factor  $q$  for the linear-exponential model. A general depiction can be found in Figure 3.12. Note the irreversible behaviour and initial stiffness change after the critical opening displacement has been reached, for cyclic loading.

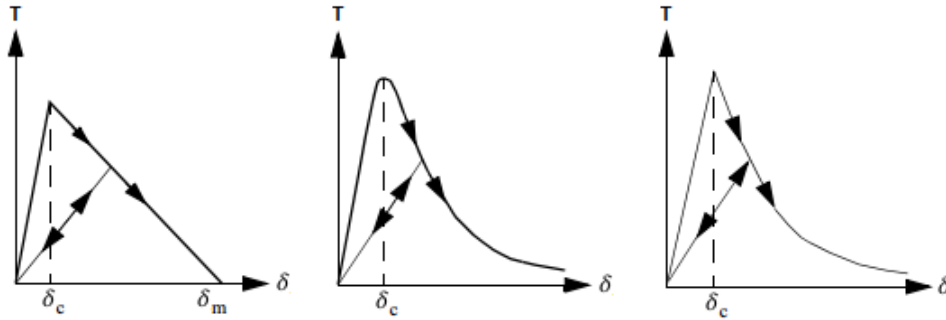


Figure 3.12: MSC.Marc's three built-in traction laws: Bilinear (left), exponential (middle), linear-exponential (right).

The critical opening displacement can be calculated from the critical energy release rate and the maximum traction for Mode I fracture, which are known material properties for a composite structure or adhesive bond line.

Mixed-mode fractures are also taken into account in the software package. Mode II and III are both treated as a shear stress and are treated the same way with a traction law. A normal to shear traction ratio and Mode I to Mode II energy release rate ratio govern a mixed-mode fracture automatically for any arbitrary simulation. The ratio is based in a similar way as in Camacho and Ortiz [76]. MSC.Marc actually approaches fracture analysis in every simulation as mixed-mode: it depends on the definition and modelling of the loading which determines to what mode or combination the fracture is related to. The relation between normal and shear is the following for traction and energy release rate respectively:

$$T_{II} = \beta_1 T_I \quad (3.34)$$

$$G_{c,II} = \beta_2 G_{c,I} \quad (3.35)$$

with shear traction  $T_{II}$ , normal traction  $T_I$ , normal-shear stress ratio  $\beta_1$ , energy release rate in shear direction  $G_{c,II}$ , energy release rate in normal direction  $G_{c,I}$  and normal-shear energy release ratio  $\beta_2$ . Figure 3.13 shows an example with  $\beta_1 = 0.6$  and  $\beta_2 = 0.9$ , illustrating the difference between pure Mode I and pure Mode II. The relation between normal and shear traction gives the following 3D interpretation of mixed mode fracture, see Figure 3.14.

Damping can be introduced as viscous energy dissipation. Damping can help the convergence rate in the simulation and prevent instability. The viscous contribution term that is added is governed by the following equation:

$$T^{vis} = \frac{\zeta T_c \dot{\delta}}{\dot{\delta}_r} \quad (3.36)$$

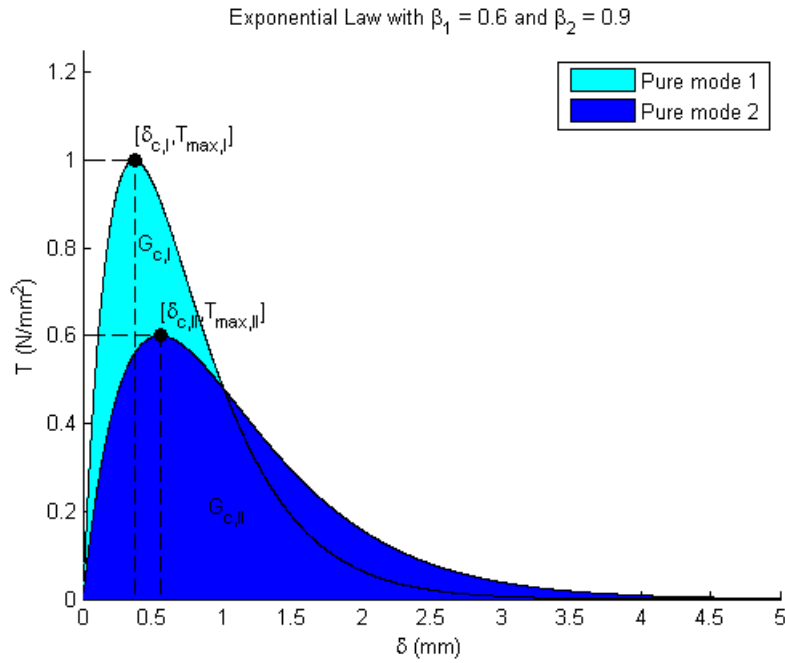


Figure 3.13: Example of MSC.Marc's built in mixed-mode calculation between pure Modes I and II for an exponential traction law. Code found in Appendix D.

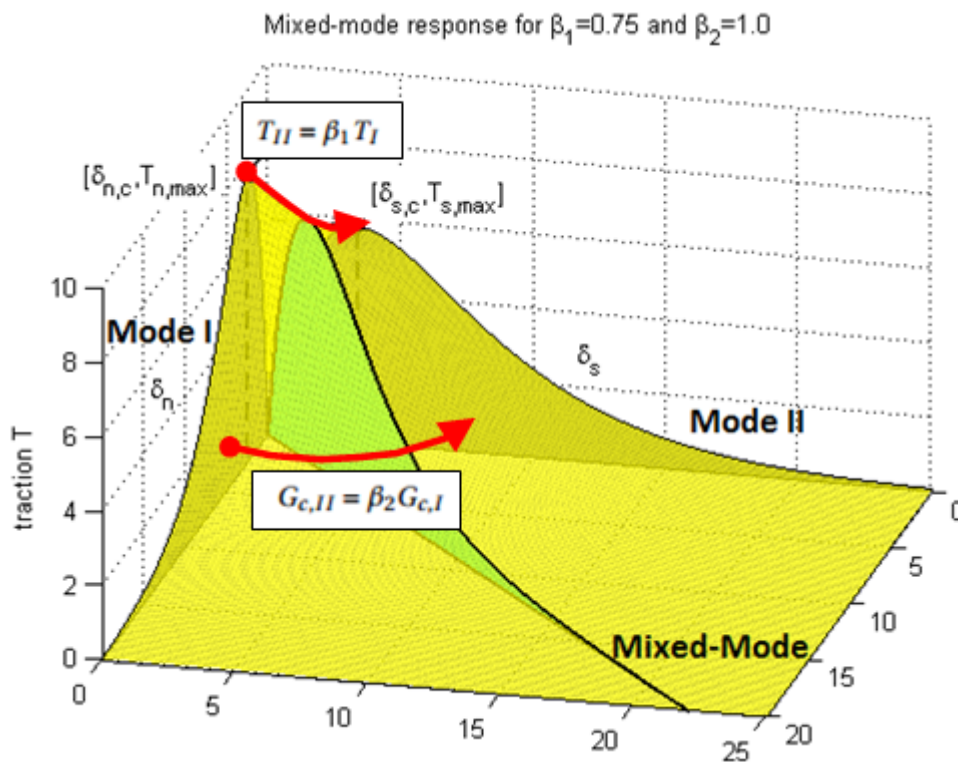


Figure 3.14: 3D view of a mixed-mode exponential traction law based on MSC.Marc's algorithm. The relations  $\beta_1$  and  $\beta_2$  are highlighted as red arrows to distinguish their influence in the mixed-mode surface graph. Code found in Appendix D.

with viscous traction contribution  $T^{vis}$ , maximum traction  $t_c$ , viscous energy factor  $\zeta$ , effective opening displacement rate  $\dot{\delta}$  and reference value of effective opening displacement rate  $\dot{\delta}_0$ .

### 3.2.2. INPUT

MSC.Marc needs input parameters to model the cohesive zone elements. A cohesive material and geometric property have to be assigned to an element of correct class and type. Element classes include triangular and quad elements for 2D and pentahedron and hexahedron elements for 3D, with various multiple noded element types. A geometric property is directly linked to the modelled element, and for cohesive elements contain the thickness direction and what integration points need to be taken. Two types of integration points for the integration scheme can be chosen from: Gaussian points resulting in a Gauss integration scheme or the nodes directly which result in a Newton-Cotes integration scheme, as seen in the GUI window in Figure C.1a.

A material property for the cohesive zone elements needs to be assigned also. The following parameters are required for a cohesive material property as seen in the GUI window in Figure C.1b:

- Traction law: bilinear, exponential, linear-exponential law.
- Secant or tangent solving method of stiffness matrix.
- Critical energy release rate  $G_{c,I}$  for Mode I.
- Critical opening displacement  $\delta_c$  for Mode I.
- Maximum opening displacement  $\delta_m$  for Mode I, only for bilinear law.
- Exponential decay factor  $q$  for Mode I, only for linear-exponential law.
- Shear to normal stress ratio  $\beta_1$ , as indicated in Eq. 3.34.
- Shear to normal energy release ratio  $\beta_2$ , as indicated in Eq. 3.35.
- Stiffening factor for compression. Default value is 0.
- Optional input: viscous energy factor for damping  $\zeta$ .
- Optional input: reference value of effective opening displacement rate  $\dot{\delta}_0$ .
- Optional input: deactivate fully damaged elements so they will not partake in any structural analysis in the simulation further, but will remain in the post file. Left unchecked means that CZE will still partake in the analyses despite their damage level.
- Optional input: remove deactivated fully damaged elements so they will not partake in the simulation further, and will be removed from the post file the instance full damage has been attained.

An error will appear if a cohesive zone element has not yet been assigned a geometric and material property and a simulation is run. For further information regarding the input commands and code structure of the CZM of MSC.Marc, see Marc 2010 Volume C: Program Input [108].

# 4

## VALIDATION OF MSC.MARC

A quick validation is performed with MSC.Marc to see how accurate the options and settings regarding CZM within MSC.Marc are. The already performed experiment by Turon *et al.* [13] and its load-displacement results will be used to compare to the ones from the MSC.Marc simulations. Also, stress and strain properties will be explored within the cohesive zone elements to understand the behaviour. The experiment and simulation done in Turon *et al.* [13] was a mixed-mode bending (MMB) test reproduced in the finite element package Abaqus, using a custom made algorithm for the cohesive zone model. The mode-I/II ratios tested in the MMB tests are 0%, 20%, 50%, 80% and 100%, with 0% signifying pure tensile loading and 100% pure shear loading. Chapter 4.1 will summarise Turon's experiment and his model. Chapter 4.2 will explore simple 2D models of the MMB tests while Chapter 4.3 will explore 3D models. Additionally in Chapter 4.3, extra simulations will be carried out to mark the influence of different time steps, critical energy release rates  $G_c$  and maximum tractions  $T_m$ . In both sections, several options and settings found within the default MSC.Marc cohesive zone models will also be explored, and all simulation results will be evaluated in Chapter 4.4. Stress, strain and damage properties of a cohesive element will be evaluated in Chapter 4.4 as well. Finally, a discussion on the outcome of the simulations follows together with a decision on what MSC.Marc options to use for further research in this document.

### 4.1. TURON'S MODEL

#### 4.1.1. TURON'S MODEL PROPERTIES

Within the simulations of Turon *et al.* [13], user-defined algorithms were used for solving the stiffness matrix equation and for traction laws. The traction law was bilinear, similar to the one in Ch. 3.1.1. The damage propagation criterion is based on Benzeggagh and Kenane, Eq. 3.28, while the damage initiation criterion is calculated with a penalty stiffness  $K$  and the critical energy release rate  $G_c$ , whereby for an arbitrary fracture mode, a user-defined relation is formed which is slightly more accurate than Ye's criterion:

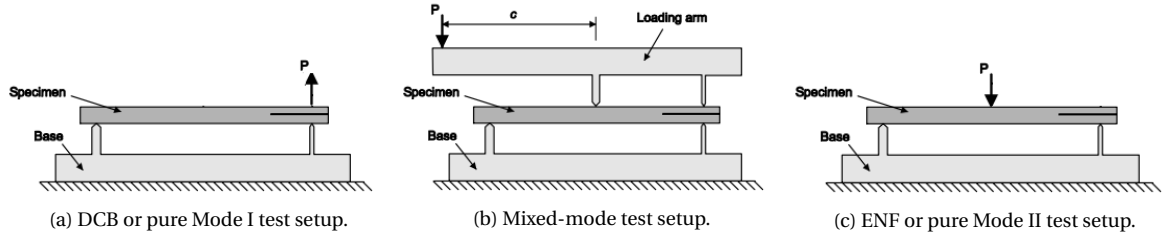
$$T_m^2 = T_{m,I}^2 + \left( \tau_{c, shear}^2 - T_{m,I}^2 \right) [B]^\eta \quad (4.1)$$

$$\delta_c^2 = \delta_{c,I}^2 + \left( \delta_{c, shear}^2 - \delta_{c,I}^2 \right) [B]^\eta \quad (4.2)$$

$$[B] = \frac{G_{II} + G_{III}}{G_I + G_{II} + G_{III}} = \frac{G_{shear}}{G_T} \quad (4.3)$$

with  $\eta = 2.284$ . More information regarding the theory behind Turon's mathematical models and relations can be found in Turon *et al.* [13], Turon [59], Turon *et al.* [81].

Turon compared his simulation with load-displacement curves to the real experiment, which used the MMB test method as in Figure 4.1. The MMB test setup is able to reproduce any variable fracture mode ratio test from 0% being pure tensile to 100% being pure shear. A 0% fracture mode is consistent to a standard double cantilever beam (DCB) or a pure Mode I test, while a 100% fracture mode is consistent to an end notch flexure (ENF) or pure Mode II test.

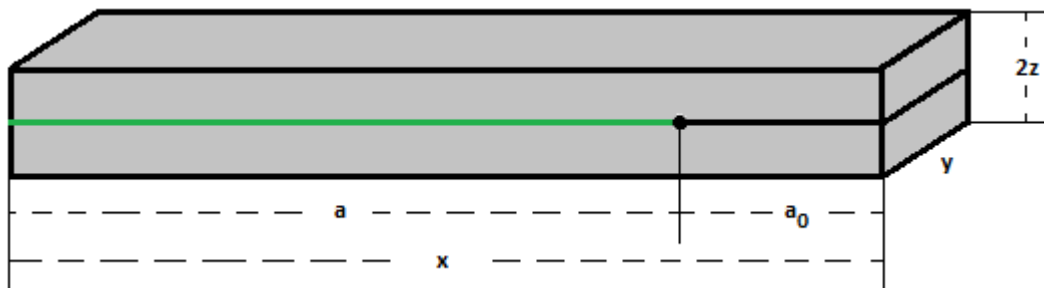
Figure 4.1: MMB test setups. Taken from Turon *et al.* [13].

The specimen is a unidirectional AS4/PEEK carbon-fibre reinforced composite, comprising of the following dimensions and properties found in Table 4.1. The fibres are conveniently aligned along the length  $x$  of the adherends.

Length $x$		Width $y$	Thickness $2z$	
102 mm		25.4 mm	2 x 1.56 mm	
$E_{11}$	$E_{22} = E_{33}$	$G_{12} = G_{13}$	$G_{23}$	$\nu_{12} = \nu_{13}$
122.7 GPa	10.1 GPa	5.5 GPa	3.7 GPa	0.25
$\nu_{23}$	$G_{c,I}$	$G_{c,II}$	$T_{m,I}$	$T_{m,II} = T_{m,III}$
0.45	0.969 kJ/m <sup>2</sup>	1.719 kJ/m <sup>2</sup>	80 MPa	100 MPa

Table 4.1: Tabular overview of material properties of Turon's specimen.

A specimen or model consists of three parts: two adherends and a bondline. The adherends are modelled as 3D solids and the bondline as 3D flat interface elements, as in a local approach. The adherends are modelled as 150 elements in length  $x$ , four elements in the width  $y$  and one element in thickness  $z$ . An initial crack length  $a_0$  has been taken into consideration to make the crack more manageable and predictable. The bondline is modelled in a similar way as the adherends up to the  $a_0$ . The  $a_0$  region is modelled as dummy cohesive elements with no strength properties, only being present for the user-defined algorithm while region  $a$  contains the material properties as in Table 4.1. Figure 4.2 mirrors a simplified drawing of the MMB specimen. There are five specimens subjected to tests from pure Mode I to pure Mode II. All specimens are of same length  $x$ , width  $y$  and thickness  $2z$  but with different initial crack lengths  $a_0$  and critical energy rates  $G_c$  with respect to their fracture mode ratio  $G_{II}/G_T$ . An overview of the five specimens concerning the latter two properties can be found in Table 4.2.

Figure 4.2: Simplified model of MMB specimen with length  $x$ , width  $y$ , total thickness  $2z$ , adhesive region  $a$  and initial crack region  $a_0$ .

$G_{II}/G_T$	0%	20%	50%	80%	100%
$G_c$ [kJ/m <sup>2</sup> ]	0.969	1.103	1.131	1.376	1.719
$a_0$ [mm]	32.9	33.7	34.1	31.4	39.2
$a$ [mm]	69.1	68.3	67.9	70.6	62.8

Table 4.2: Tabular overview of specimen properties per fracture mode ratio; 0% denoting pure Mode I and 100% pure Mode II.

### 4.1.2. TURON'S LOAD-DISPLACEMENT RESULTS

Turon compared the load results of the simulation to the real experiment using an error based on load difference percentage as in Eq. 4.4. An overview of the top loads in each experiment can be found in Table 4.3, with a graphical comparison in Figure 4.3. The 20% ratio test scores the largest deviation from the real experiment, which is expected [78].

$$Error = \frac{F_{Predicted} - F_{Experimental}}{F_{Experimental}} \cdot 100\% \quad (4.4)$$

$G_{II}/G_T$	Predicted [N]	Experimental [N]	Error (%)
0%	152.4	147.5	3.4
20%	99.3	108.1	-8.1
50%	263.9	275.3	-4.2
80%	496.9	518.7	-4.2
100%	697.1	748.4	-6.9

Table 4.3: Numerical and experimental results for the five setups. Taken from Turon *et al.* [13].

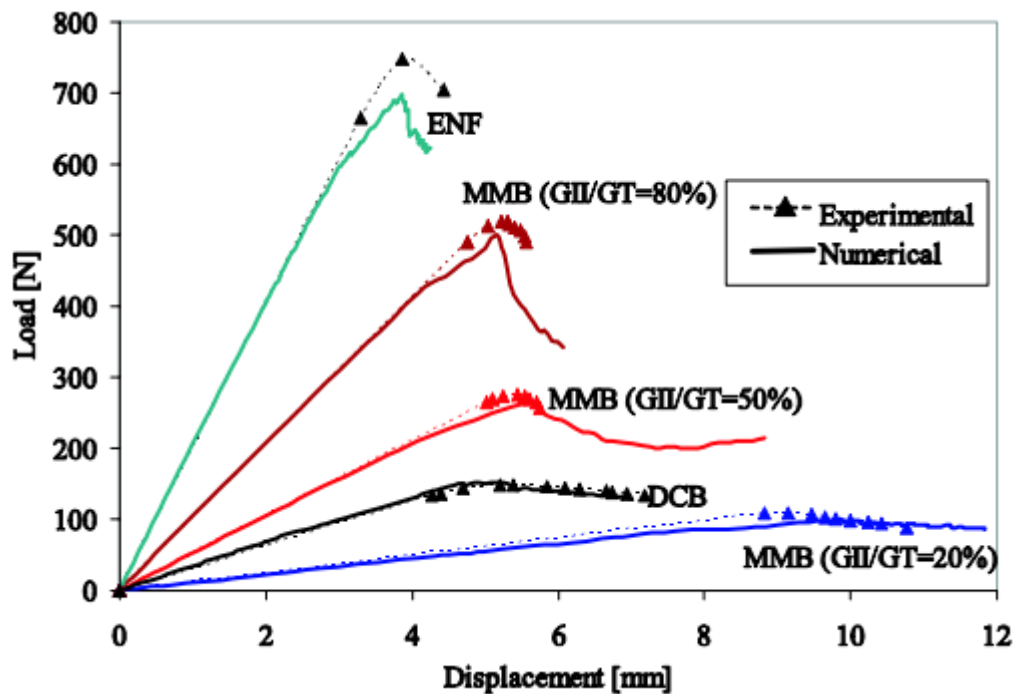


Figure 4.3: Graphical overview of numerical and experimental results of all five setups. Taken from Turon *et al.* [13].

## 4.2. 2D MSC.MARC MODELS

### 4.2.1. MODEL PROPERTIES

The first models to be created and tested are 2D ones due to their simplicity and very short calculation times. For all models the following can be assumed:

- Dimensions and material properties according to Table 4.1 and Table 4.2.
- The models work in a coordinate system where the x-axis is the length and the y-axis the thickness of the specimen. The width is in-plane and is utilised as a fixed value when defining the geometry properties.
- Adherends consisting of 150 by 1 quadrilateral four-noded 2D elements with orthogonal material properties.
- Bondline consisting of quadrilateral four-noded interface, or cohesive, elements with zero initial thickness, filling the region  $a$  according to Figure 4.2 while  $a_0$  remains empty to simulate the initial crack. Contact bodies with touch properties are established to prevent accidental intertwining of adherend elements.
- MSC.Marc's exponential law is used, as it is dependent on the least amount of input parameters and its good spread of accuracy and computational time [102].
- A normal-to-plane thickness value for both adherend and bondline geometric properties of 25.4 mm is used.
- All models use a fixed time-step of 0.01 seconds in a total simulation time of 1 second for their prescribed displacement.
- The value for Residual Force Tolerance is decreased to 0.01 instead of the default value 0.1 for better accuracy. See Figure C.4.
- Remaining default options of MSC.Marc are used.

Concerning the element characteristics, one is referred to Table A.1. The conversion of the given material properties to input parameters can be seen in Table 4.4. The conversion on the given bondline properties to input parameters can be seen in Table 4.5. The conversion in MSC.Marc is done according to the input parameter windows as in Figure C.2 and Figure C.1a.

Property	Value	Equivalent property MSC.Marc	Value MSC.Marc	Comment
$E_{11}$	122.7 GPa	$E_1$	122700	
$E_{22}$	10.1 GPa	$E_2$	10100	
$E_{33}$	10.1 GPa	$E_3$	10100	
$\nu_{12}$	0.25	$\nu_{12}$	0.25	
$\nu_{23}$	0.45	$\nu_{23}$	0.45	
$\nu_{13}$	0.25	$\nu_{31}$	0.020579	Use orthotropic relation $E_{11}\nu_{31} = E_{33}\nu_{13}$ .
$G_{12}$	5.5 GPa	$G_{12}$	5500	
$G_{23}$	3.7 GPa	$G_{23}$	3700	
$G_{13}$	5.5 GPa	$G_{31}$	5500	Use orthotropic relation $G_{13} = G_{31}$ .

Table 4.4: Adherend material property conversion to MSC.Marc. See Figure C.2 for the GUI input view.

In the MSC.Marc simulations, various options within the cohesive properties will be explored to determine what CZM settings to use best for the CLS specimen. The following options will be tested:

- Stiffness matrix solving method: Secant or tangent
- Integration point location scheme: Gaussian or Newton-Cotes
- Viscous damping
- Fully damaged CZE: Keep or Deactivate

For the theory behind the working of the stiffness matrix solving methods or the integration schemes, one is referred to Marc 2010 Volume A: Theory and User Information [12]. The simulations with the different options for each of the five fracture modes can be found in Table 4.6.

Property	Value	Equivalent property MSC.Marc	Value MSC.Marc	Comment
$G_{c,I}$	0.969 kJ/m <sup>2</sup>	Cohesive Energy $G_c$	0.969	
$G_{c,II}$	1.719 kJ/m <sup>2</sup>	Shear/Normal Coefficients: Cohesive Energy $\beta_2$	1.77399	Use Eq. 3.35.
$T_{m,I}$	80 MPa	Critical Opening Displacement $\delta_c$	0.004456	Use Eq. 3.32.
$T_{m,II}$	100 MPa	Shear/Normal Coefficients: Maximum Stress $\beta_1$	1.25	Use Eq. 3.34.
$T_{m,III}$	100 MPa	Shear/Normal Coefficients: Maximum Stress $\beta_1$	1.25	Use Eq. 3.34.
-	-	Stiffening Factor in Compression	1	Default value.

Table 4.5: Bondline material property conversion to MSC.Marc. See Figure C.1a for the GUI input view.

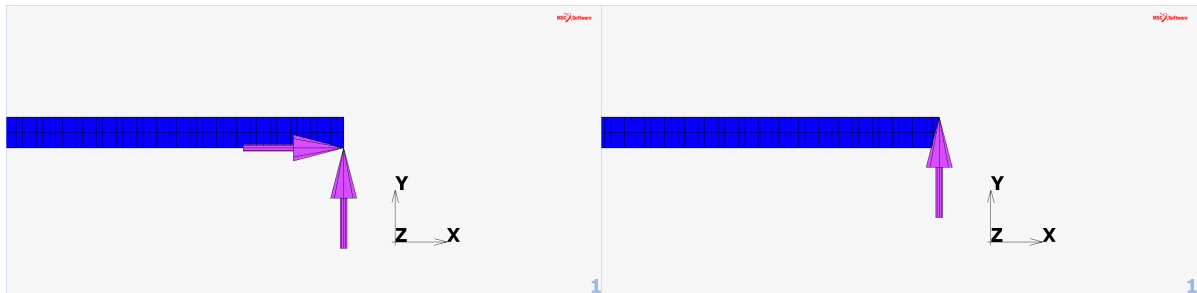
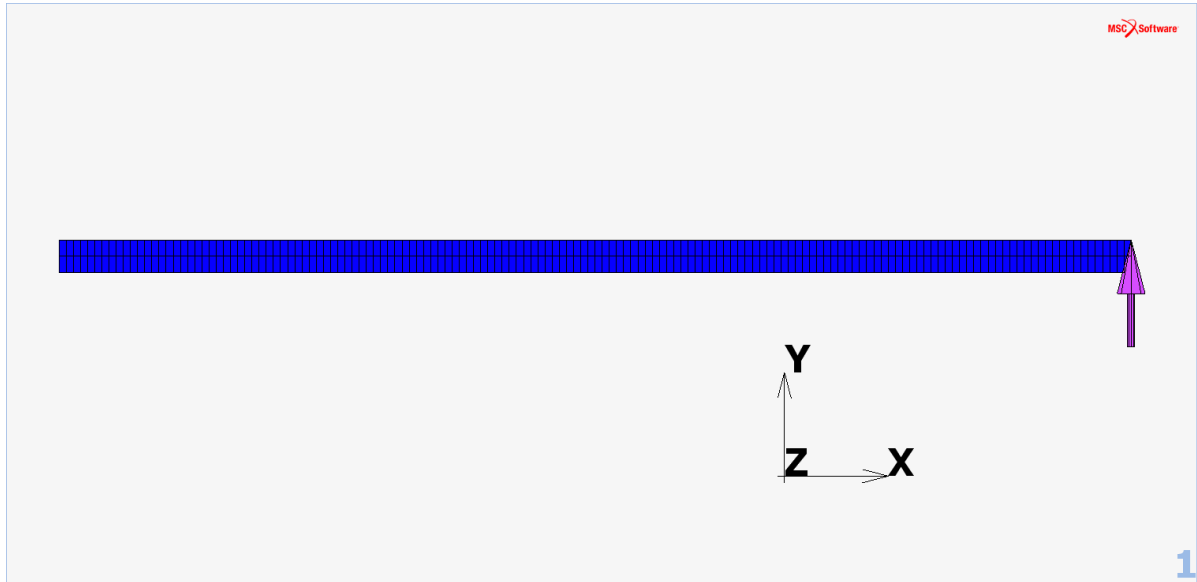
Sim	Integration Scheme	Stiffness Matrix Method	CZE Deactivated/Kept	Viscosity Factor
1	Gaussian	Secant	Kept	-
2	Gaussian	Secant	Deactivated	-
3	Gaussian	Tangent	Kept	-
4	Gaussian	Tangent	Deactivated	-
5	Newton-Cotes	Secant	Kept	-
6	Newton-Cotes	Secant	Deactivated	-
7	Newton-Cotes	Tangent	Kept	-
8	Newton-Cotes	Tangent	Deactivated	-
9	Gaussian	Tangent	Deactivated	0.05
10	Gaussian	Tangent	Deactivated	0.01
11	Gaussian	Tangent	Deactivated	0.005
12	Gaussian	Tangent	Deactivated	0.001
13	Gaussian	Tangent	Deactivated	0.0005
14	Gaussian	Tangent	Deactivated	0.0001

Table 4.6: Simulation setup for 2D and 3D models.

**Mixed-mode ratio: 0%**

In the 0% fracture mode, or DCB mode, the model has certain constraints on several nodes. A full model view can be seen in Figure 4.4a. On the far bottom right corner, the node is constrained and fixed in the first and second degree of freedom (DOF), which correspond to x- and y-direction, as can be seen in Figure 4.4b. The prescribed displacement in the y-direction is placed on the upper right corner node and is constrained and fixed in the x-direction as in Figure 4.4c. The prescribed displacement is 7 mm upwards in the y-direction.

(a) Complete view of 2D model with prescribed displacement on far right top node.



(b) Bottom right node fixed in x- and y-direction.

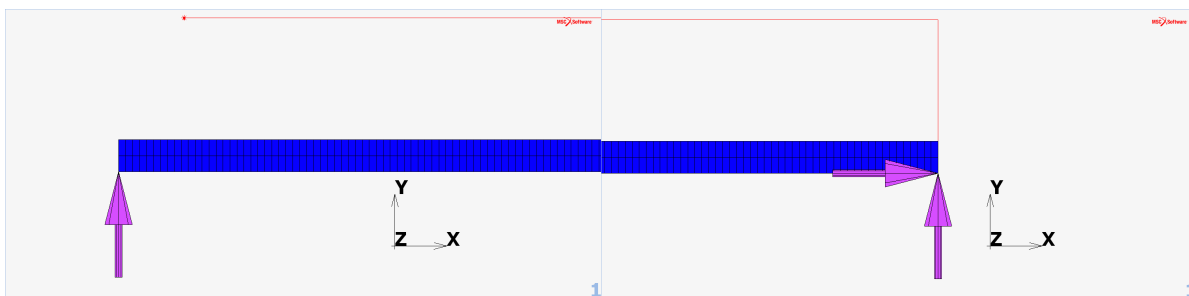
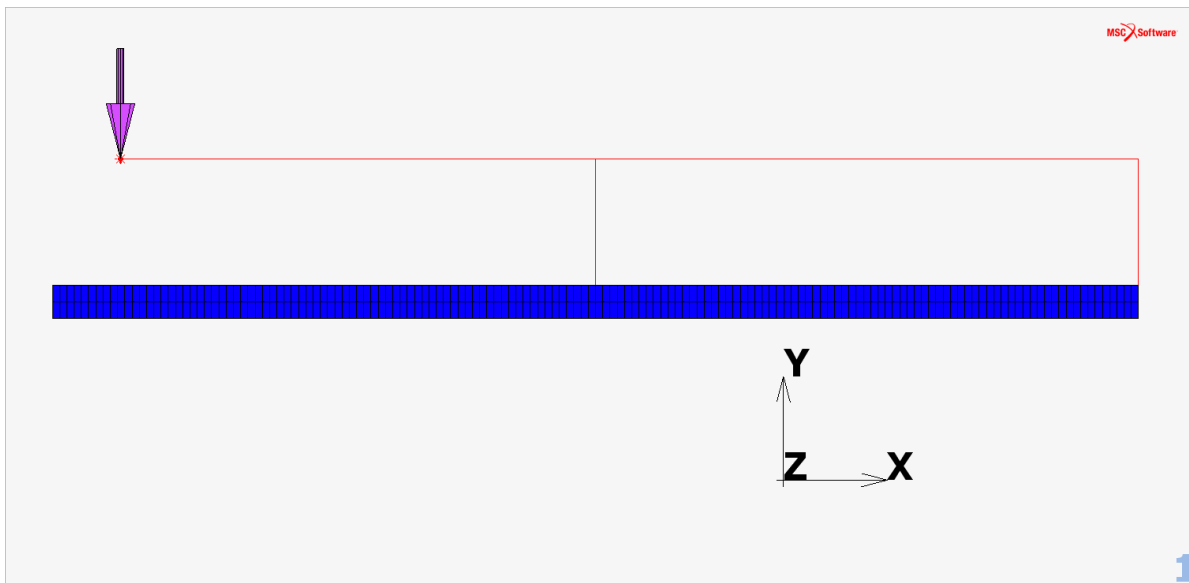
(c) Top right node with prescribed displacement.

Figure 4.4: MSC.Marc model of the 0% fracture mode, or DCB, setup.

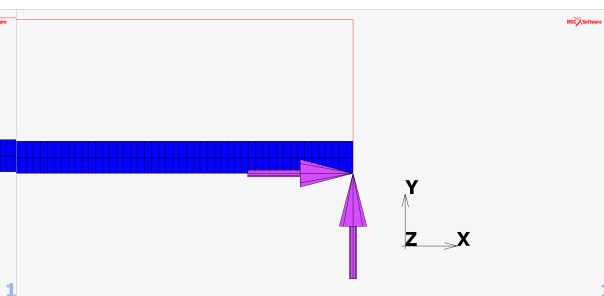
**Mixed-mode ratio: 20%, 50% and 80%**

For the 20%, 50% and 80%, special links must be added to the model to simulate the correct amount of tensile pulling at the far right end and the shear effect in the middle. A rigid 'lever' is modelled for this, which uses rigid links and bars relating a given amount of DOFs of a single node to another node. In this case, the centre top node and top right corner node of the specimen are dependent on the displacement of the lever. To distinguish the different fracture mode ratios, the length of the lever  $c$  as in Figure 4.1 is recalculated and remodelled. Explanation and calculations behind the rigid links and modelling of can be found in Appendix A.2. An example of the lever can be found in Figure 4.5a for the 50% mode ratio model. Constraints are placed on both bottom ends: The right bottom corner node is fixed in x- and y-direction as in Figure 4.5c and the left bottom corner node is fixed in y-direction as in Figure 4.5b. The prescribed displacement in the y-direction is placed on the node which symbolises the lever end as in Figure 4.5a. The prescribed displacement is 12 mm downwards in the y-direction for the 20% mode ratio and 7 mm downwards in the y-direction for the 50% and 80% mode ratio.

(a) Complete view of 2D model with prescribed displacement on the lever (red) for the 50% ratio setup.



(b) Bottom left node fixed in the y-direction.



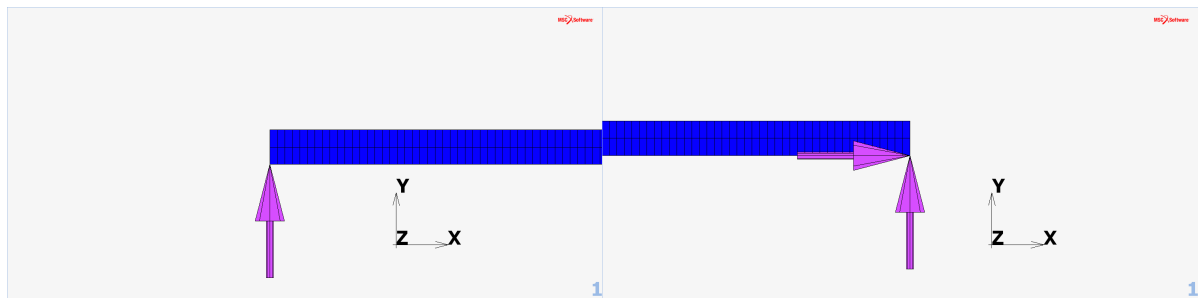
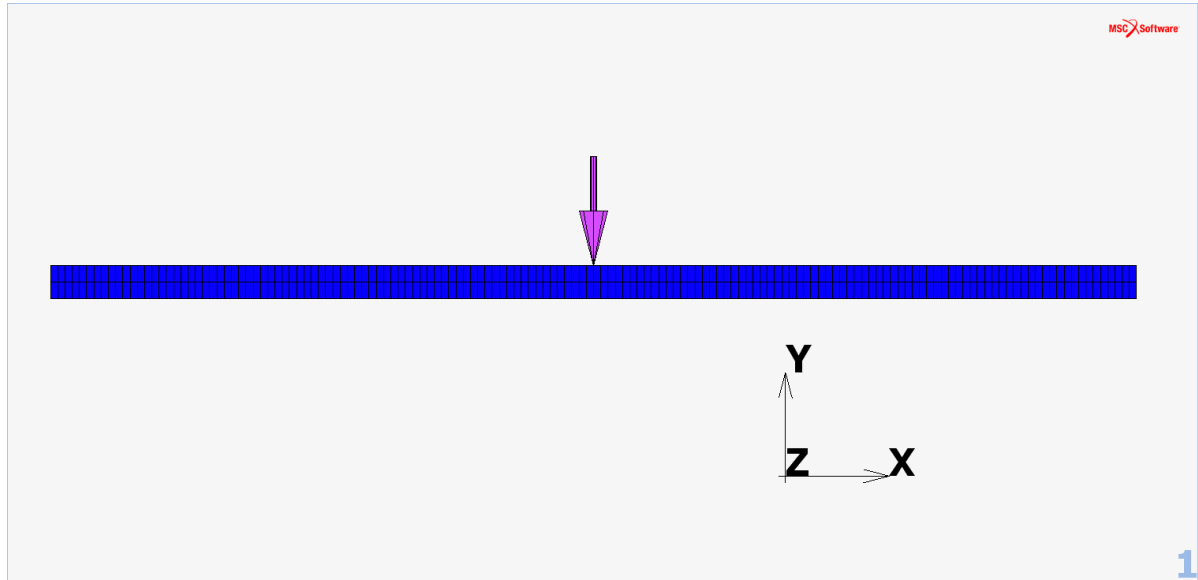
(c) Bottom right node fixed in x- and y-direction.

Figure 4.5: MSC.Marc model of the 50% fracture mode setup. Lever length  $c$  differs for 20% and 80% fracture mode ratios.

**Mixed-mode ratio: 100%**

For the 100% ratio mode, or ENF mode, the constraints are simple. Constraints are placed on both bottom ends: The right bottom corner node is fixed in x- and y-direction as in Figure 4.6b and the left bottom corner node is fixed in y-direction as in Figure 4.6c. The prescribed displacement in the y-direction is placed on the centre top node as in Figure 4.6a. The prescribed displacement is 5 mm downwards in the y-direction.

(a) Complete view of 2D model with prescribed displacement on the middle top node.



(b) Bottom right node fixed in x- and y-direction.

(c) Bottom left node fixed in the y-direction.

Figure 4.6: MSC.Marc model of the 100% fracture mode, or ENF setup.

### 4.3. 3D MODELS

#### 4.3.1. MODEL PROPERTIES

For all 3D models, the following can be assumed.

- Dimensions and material properties according to Table 4.1 and Table 4.2.
- The models work in a coordinate system where the x-axis is the length, y-axis the width and z-axis the thickness of the specimen.
- Adherends consisting of 150 by 4 by 1 hexagonal eight-noded 3D elements with orthotropic material properties.
- Bondline consisting of hexagonal eight-noded interface, or cohesive, elements with zero initial thickness, filling the region  $a$  according to Figure 4.2 with four elements in width while  $a_0$  remains empty to simulate the initial crack.
- MSC.Marc's exponential law is used, as it is dependent on the least amount of input parameters and its good spread of accuracy and computational time [102].

- All models in the simulation setup of Table 4.6 use a simulation time of 1 second, but have the simulation split in two parts: first part has a fixed time-step of 0.02 and the second part a fixed time-step of 0.005 for more accuracy. The different time steps are done since for the first few millimeters of loading the specimen acts linear and just before point of failure it acts non-linear. This non-linear part needs a small time step to be able to get accurate results. The time step for the both parts are also the same ones used in Turon [59]. Length of parts varies per model.
- The value for Residual Force Tolerance is decreased to 0.01 instead of the default value 0.1 for better accuracy and the option of Non-Positive Definite matrix in the solution control is checked to solve non-positive definite systems which could halt the simulations.. See Figure C.3 and Figure C.4.
- Remaining default options of MSC.Marc are used.

Concerning the 3D element characteristics, one is referred again to Table A.1. As with the 3D models, the conversion of the given material properties to input parameters can be seen in Table 4.4, and for the conversion on the given bondline properties to input parameters, Table 4.5. The 3D models will follow the same set of simulations as in Table 4.6 and also additional ones in Table 4.7. The extra simulations carried out in Table 4.7 are performed to distinguish a time step,  $G_c$  and  $T_m$  influence. Simulations 15 through 18 will be performed for all mode ratios while 19 through 34 only for the 0% and 100% mode ratios to assess the direct influence in pure mode I and II on the maximum load required to damage the MMB specimen.

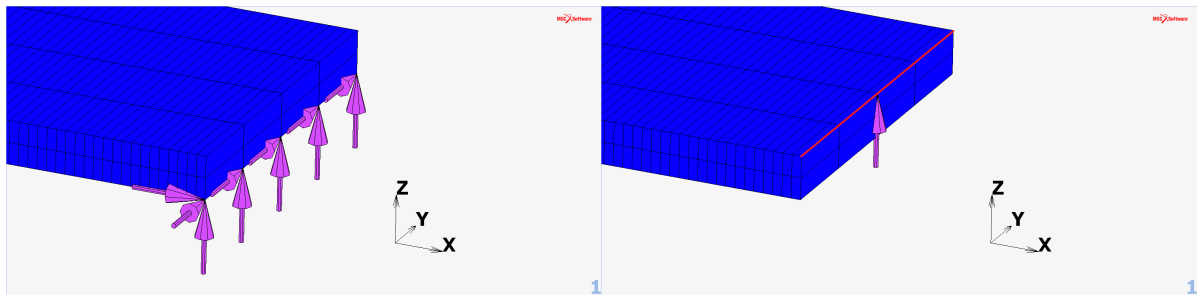
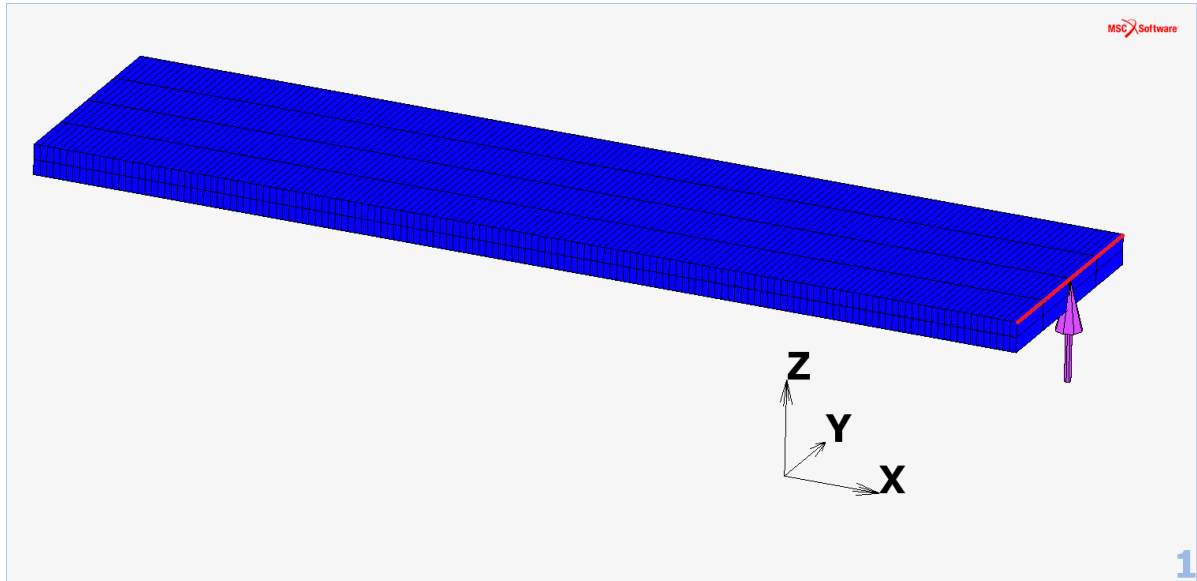
Sim	Time Step Size [s]	$G_{c,I}$ [kJ/m <sup>2</sup> ]	$G_{c,II}$ [kJ/m <sup>2</sup> ]	$T_{m,I}$ [MPa]	$T_{m,II}$ [MPa]
15	0.05	0.969	1.719	80	100
16	0.01	0.969	1.719	80	100
17	0.005	0.969	1.719	80	100
18	0.001	0.969	1.719	80	100
19	0.0005	0.969	1.719	80	100
20	0.0001	0.969	1.719	80	100
21	0.001	0.500	1.719	80	100
22	0.001	1.000	1.719	80	100
23	0.001	1.500	1.719	80	100
24	0.001	2.000	1.719	80	100
25	0.001	0.969	1.250	80	100
26	0.001	0.969	1.750	80	100
27	0.001	0.969	2.250	80	100
28	0.001	0.969	2.750	80	100
29	0.001	0.969	1.719	60	100
30	0.001	0.969	1.719	80	100
31	0.001	0.969	1.719	100	100
32	0.001	0.969	1.719	120	100
33	0.001	0.969	1.719	80	80
34	0.001	0.969	1.719	80	100
35	0.001	0.969	1.719	80	120
36	0.001	0.969	1.719	80	140

Table 4.7: Additional simulation setup for 3D models. These simulations all use one fixed time step size as noted, Gaussian integration scheme, tangent stiffness matrix solving method, deactivated CZE and no viscosity.

#### Mixed-mode ratio: 0%

For the 3D model, it has certain extra constraints on several nodes compared to its 2D counterpart. A full view of the model can be found in Figure 4.7a. On the far bottom corner nodes at the start of the initial crack, all are constrained and fixed in the first, second and third DOE, which correspond to x-, y- and z-direction, as can be seen in Figure 4.7b. The prescribed displacement in the z-direction is placed on the middle upper node at the start of the initial crack and is constrained and fixed in the x- and y-direction as in Figure 4.7c. To keep consistent to the test setup, its neighbouring nodes along the width are linked in z-direction so they follow the point of loading in the z-direction. The prescribed displacement is 7 mm upwards in the z-direction. The displacement is split in two parts: the first part up to 40% of the load with a time-step of 0.02 seconds and the second part from 40% of the load with a time-step of 0.005 seconds.

(a) Complete view of 3D model with prescribed displacement at the start of the initial crack. Red line indicates nodes that have tied DOF to the load node.



(b) Bottom corner nodes at start of initial crack fixed in x-, y- and z-direction.

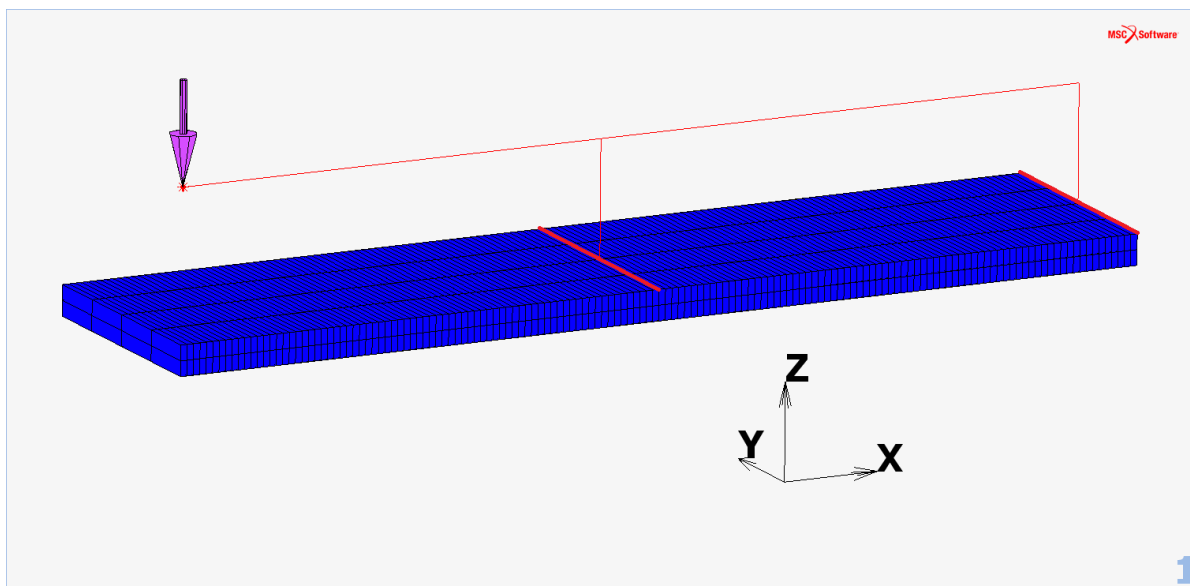
(c) Top middle node with prescribed displacement with neighbouring nodes linked in z-direction.

Figure 4.7: MSC.Marc model of the 0% fracture mode, or DCB, setup.

**Mixed-mode ratio: 20%, 50% and 80%**

For the 20%, 50% and 80% in 3D models, the rigid lever concept is maintained. In this case, the centre top node in the middle and top middle corner node at the start of the crack on the specimen are dependent on the displacement of the lever, which is modelled with rigid links and bars. Their neighbouring nodes along the width of the specimen are linked to the centre nodes in the z-direction. To distinguish the different fracture mode ratios, the length of the lever  $c$  as in Figure 4.1 is recalculated and remodelled. Explanation and calculations behind the rigid links and bars and modelling of can be found in Appendix A.2. Constraints are placed on both bottom corner ends: The bottom corner nodes at the crack start are fixed in x-, y- and z-direction as in Figure 4.8b and the opposite bottom corner nodes are fixed in z-direction as in Figure 4.8c. The prescribed displacement in z-direction is placed on the node which symbolises the lever end as in Figure 4.8a. The prescribed displacement is 12 mm downwards in the z-direction for the 20% mode ratio and 7 mm downwards in the z-direction for the 50% and 80% mode ratio. The displacement for the 20%, 50% and 80% mode ratio is split in two parts: the first part up to 66% of the load with a time-step of 0.02 seconds and the second part from 66% of the load with a time-step of 0.005 seconds.

(a) Complete view of 3D model with prescribed displacement on the lever (red) for 50% ratio. Red line on the specimen indicates nodes that have tied DOF to the centre nodes.



(b) Bottom corner nodes at start of initial crack fixed in x-, y- and z-direction.

(c) Bottom corner nodes opposite of initial crack fixed in z-direction.

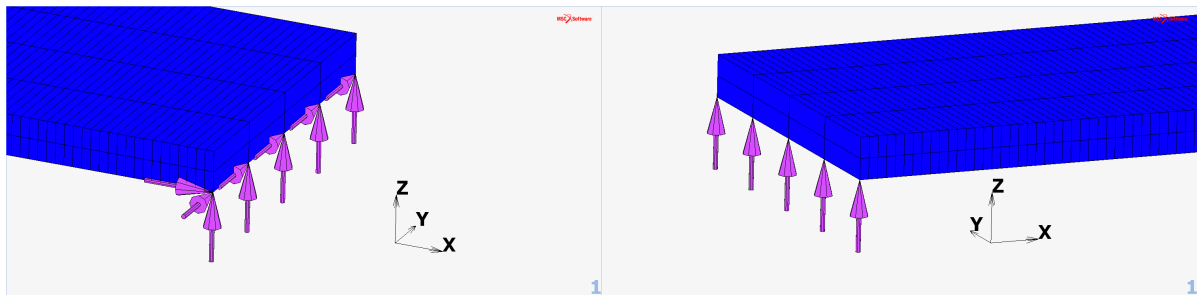
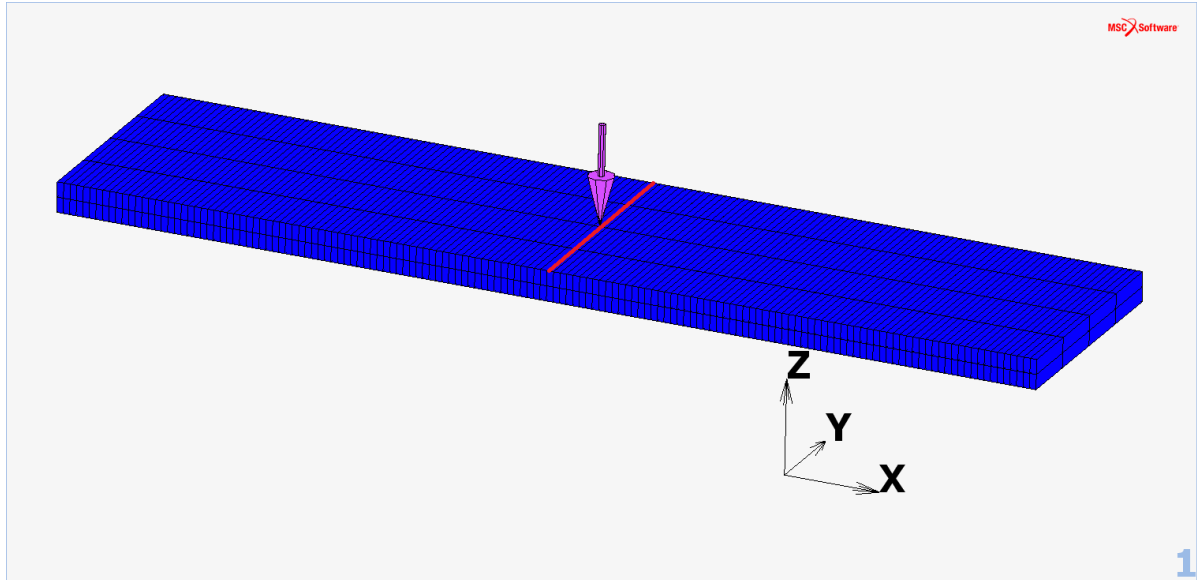
Figure 4.8: MSC.Marc model of the 50% fracture mode setup. Lever length  $c$  differs for 20% and 80% fracture mode ratios.

**Mixed-mode ratio: 100%**

For the 100% ratio mode in 3D, the constraints are similar to the 20%, 50% and 80% modes. Constraints are placed on both bottom corner ends: The bottom corner nodes at the crack start are fixed in x-, y- and z-direction as in Figure 4.9b and the opposite bottom corner nodes are fixed in z-direction as in Figure 4.9c. The prescribed displacement in z-direction is placed on the center top node in the middle of the specimen's

length, with its neighbouring nodes along the width linked to the load node in the z-direction as in Figure 4.9a. The prescribed displacement is 5 mm downwards in the z-direction. The displacement is split in two parts: the first part up to 40% of the load with a time-step of 0.02 seconds and the second part from 40% of the load with a time-step of 0.005 seconds.

- (a) Complete view of 2D model with prescribed displacement in the middle. Red line indicates nodes that have tied DOF to the load node.



(b) Bottom right node fixed in x- and y-direction.

(c) Bottom left node fixed in the y-direction.

Figure 4.9: MSC.Marc model of the 100% fracture mode, or ENE, setup.

## 4.4. EVALUATION

A short evaluation on the behaviour of the cohesive zone elements is given. The results from the simulations will be used to analyse the different options MSC.Marc has to offer on cohesive geometry and material properties and the cohesive zone elements. Additionally, a discussion on the outcome of the simulations will be made. All simulations were performed with the software and hardware listed in Appendix F.

### 4.4.1. LOAD-DISPLACEMENT RESULTS

The load displacement of the 2D and 3D results for the different options and setting the models have according to Table 4.6 will be listed here. A decision to what options to use for the CLS specimen will be based on these results.

#### Mixed-mode ratio: 0%

For the 0% fracture mode simulations, the 2D model results can be found in Table A.3, Figure A.4 and Fig-

ure A.5. All 2D models seem to reach their maximum loads sooner than the real experiment, although the maximum loads that used a Gaussian integration scheme come closer to the real experimental maximum load than the ones that used a Newton-Cotes integration scheme or even Turon's model. The option to keep or deactivate cohesive zone elements seem to have no effect on the results, even hardly in computational time. A secant method for solving the stiffness matrix seems to have a large overshoot for Newton-Cotes integration schemes, resulting in a large max load error.

For the 3D models, the results can be found in Table A.4, Figure A.6 and Figure A.7. All 3D models seem to reach their maximum loads sooner than the real experiment. The option to keep or deactivate cohesive zone elements seem to have no effect on the results, even hardly in computational time. The load error is slightly more accurate than Turon's. Computational times are of the same magnitude and near each other. The accuracy remains fairly consistent amongst all model settings. The viscosity factor has a large influence as well. Large values tend to be highly inaccurate, such as the value in model 9 and 10. A value around 0.005 and 0.001 seems to be well suited to smooth out the oscillations and have a better accuracy and reduce computational time. A deformed shape of the simulation can be found in Figure A.3a.

#### **Mixed-mode ratio: 20%, 50% and 80%**

For the 20% fracture mode simulations, the 2D model results can be found in Table A.6, Figure A.11 and Figure A.12. All models seem to reach their maximum loads later than the real experiment, with the maximum loads having a high deviation from the real experiment maximum load, which was to be expected [78]. The ones with the Gaussian schemes seems to have a much longer computational time than the ones with a Newton-Cotes scheme, but atleast finish the simulation: all models with either Newton-Cotes and/or secant seem to suffer too many cutbacks and end their simulations prematurely. Again, the option to keep or deactivate cohesive zone elements seem to have no effect on the results.

For the 3D models, the results can be found in Table A.7, Figure A.13 and Figure A.14. Also here the models seem to reach their maximum loads later than the real experiment, with the maximum loads having a high deviation from the real experiment maximum load, although the load errors are more close to each other and Turon's model than they were in the 2D models. The difference in computational time between the different integration schemes, as in the 2D models, seems to have vanished. Again, the option to keep or deactivate cohesive zone elements seem to have no effect on the results. The viscosity factor has a large influence again. Several of the larger values, models 9 through 11, don't seem to reach a maximum for its prescribed displacement. A value around 0.005 and 0.001 seems to be well suited to smooth out the oscillations and reduce computational time. A deformed shape of the simulation can be found in Figure A.3b.

For the 50% fracture mode simulations, the 2D model results can be found in Table A.9, Figure A.16 and Figure A.17. All models seem to reach their maximum loads later than the real experiment, with the maximum loads of models using Newton-Cotes schemes with a secant solving method deviating the most, also computational-wise. Gaussian schemes give the most accurate results with only small load errors, although the initial loading stiffness deviates from the real experiment. Again, the option to keep or deactivate cohesive zone elements seem to have no effect on the results.

For the 3D models, the results can be found in Table A.10, Figure A.18 and Figure A.19. Most models suffer to many time step cutbacks and the simulations halt prematurely. Models using Newton-Cotes schemes with a secant solving method seem to deviate the most and ending prematurely. Gaussian schemes give the most accurate results, with the tangent solving method having the best computational time. Again, the option to keep or deactivate cohesive zone elements seem to have no effect on the results. Also here the load errors are small for the Gaussian schemes. For the viscosity factor, several of the larger values, models 9 through 11, don't seem to reach a maximum for its prescribed displacement. A value below 0.0005 seems to be well suited to smooth out the oscillations and reduce computational time. A deformed shape of the simulation can be found in Figure A.3c.

As for the 80% fracture mode simulations, the 2D model results can be found in Table A.12, Figure A.21 and Figure A.22. Almost all models, 1 through 8, seem to have near-identical results, with the Gaussian scheme using a tangent solving method having the advantage of lower computational time. Again, the option to keep or deactivate cohesive zone elements seem to have no effect on the results. All model settings have an error close to each other and is slightly less accurate than Turon's model.

As for the 3D models, the results can be found in Table A.13, Figure A.23 and Figure A.24. Also here, all models, 1 through 8, are close together, with the Gaussian scheme using a tangent solving method having

the advantage of lower computational time. Models with the secant solving method have very high computational time and have larger errors. Again, the option to keep or deactivate cohesive zone elements seem to have no effect on the results. The load errors for the Gaussian schemes are nearly the same as those found in the 2D models. For the viscosity factor, several of the larger values, such as models 9 and 10, seem to deviate heavily from the real experiment and don't reach their maximum within the prescribed displacement. A value below 0.001 seems to be well suited to smooth out the oscillations, have a better accuracy and reduce computational time. A deformed shape of the simulation can be found in Figure A.3d.

#### Mixed-mode ratio: 100%

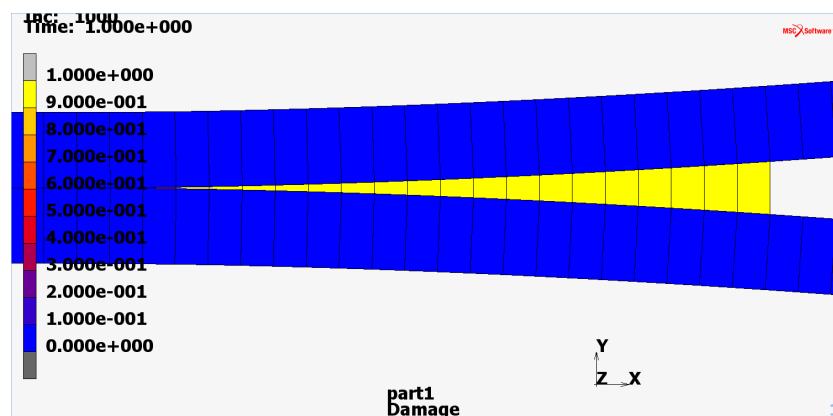
As for the 100% fracture mode simulations, the 2D model results can be found in Table A.15, Figure A.26 and Figure A.27. Almost all models, 1 through 8, seem to have near-identical results, and again models with the Gaussian scheme using a tangent solving method having a major advantage of low computational time. Again, the option to keep or deactivate cohesive zone elements seem to have no effect on the results. The load errors are all close to each other, and slightly better than Turon's model.

As for the 3D models, the results can be found in Table A.16, Figure A.28 and Figure A.29. Also here, all models, 1 through 8, have near same results, and again models with the Gaussian scheme have the advantage of lower computational time and tend to be the most accurate. Again, the option to keep or deactivate cohesive zone elements seem to have nearly no effect on the results. The load errors for the Gaussian schemes are lower than its 2D counterparts and Turon's Model. For the viscosity factor, for large values such as model 9, it seems to deviate heavily from the real experiment. A value below 0.01 seems to be well suited for a better accuracy in terms of maximum load and a decrease in computational time. A deformed shape of the simulation can be found in Figure A.3e.

#### 4.4.2. DAMAGE AND TRACTION RESULTS

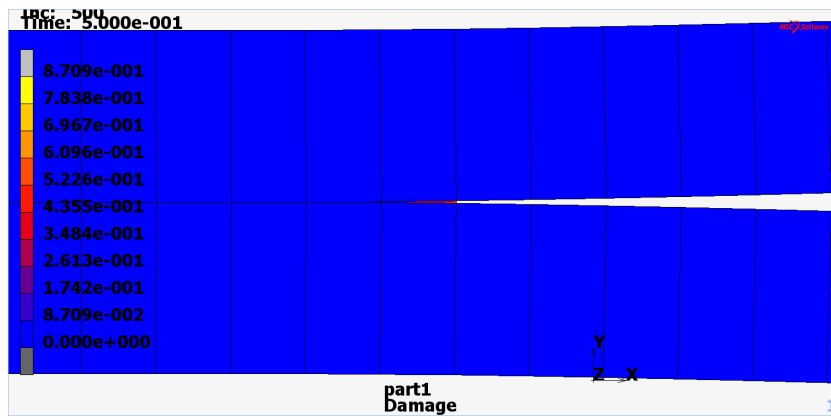
The damage levels in the CZE element can be followed within the postprocessor. Taking one of the 2D models as example, it is seen that damaged CZE have the damage value of 1, see Figure 4.10. Subsequently, all strain increases are halted and stresses are reduced to zero. Because MSC.Marc calculates the traction separately and is combined with to a global output of stress parameters for a node or element, it is difficult to assess the traction quality of a CZE. There is also no separate output parameter regarding only the traction that comes from the CZE. The best way to assess how much failure a CZE has is by damage level as in Figure 4.10, with the additional aid of visually removing the CZE in the postprocessor.

To be able to see the traction behaviour of the CZE element, one can model only the CZE and prescribe it a force or displacement. A single CZE with the same properties as in Table 4.5 is prescribed a small displacement good enough to 'destroy' the element in a tensile loading, or mode I loading. A damage value output and traction output are given in Figure 4.11. In this CZE simulation, the CZE is eliminated completely once it has reached a damage level of 0.99 for the exponential traction law.



(a) Close-up damaged CZE. Yellow indicates an element having a damage value of 1, resulting in the deactivation of that element.

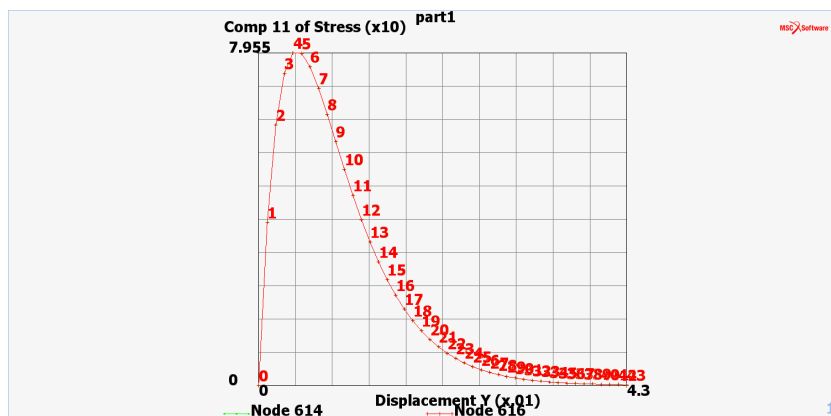
Figure 4.10: Damage levels in first CZEs.



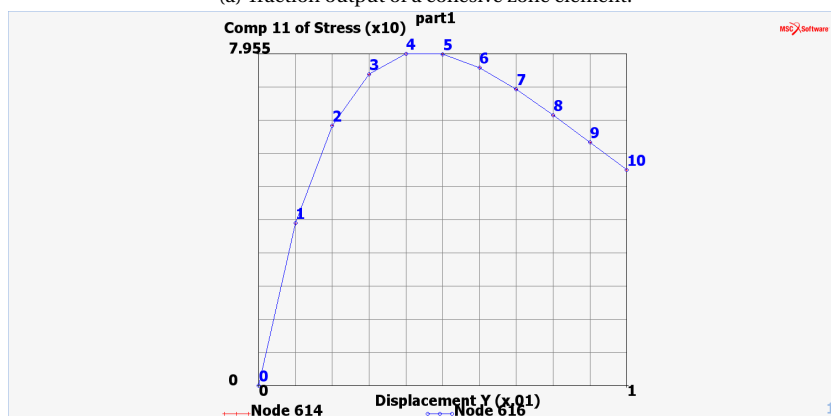
(b) Close-up of first CZE getting damaged.

Figure 4.10: Damage levels in first CZE (cont.).

It thus has a tolerance of 0.01 since the exponential law in theory never reaches zero traction, which should denote the the CZE has debonded from it neighbouring material. The traction law is well represented as its maximum of 80 MPa on the critical opening displacement. Note that the damage output only increases once the critical opening displacement has been reached, see also Figure 4.11.

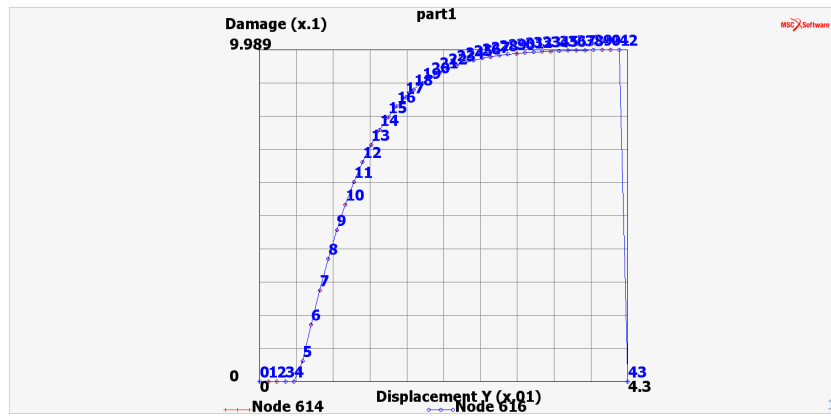


(a) Traction output of a cohesive zone element.

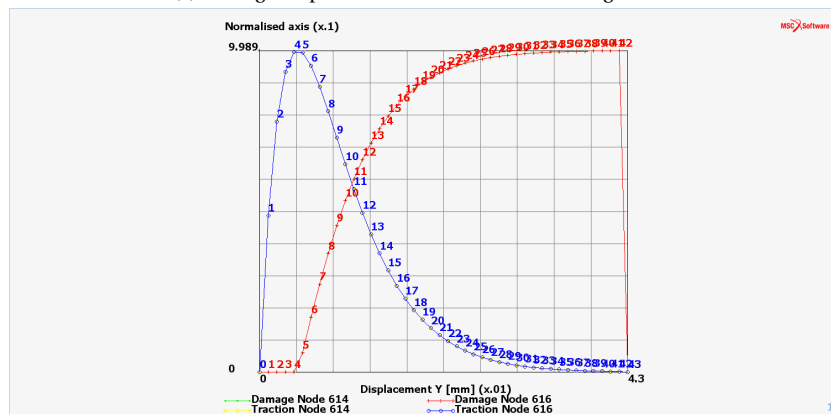


(b) Close-up of traction law. The critical opening displacement of 0.004456 mm with a traction of  $\pm 80$  MPa is evident.

Figure 4.11: Damage and traction in a CZE.



(c) Damage output with a tolerance of 0.01 damage value.



(d) Traction law scaled to damage law. Note the start of damage only at the critical opening displacement.

Figure 4.11: Damage and traction in a CZE (cont.).

#### 4.4.3. TIME STEP DEPENDENCY RESULTS

A range of time steps was considered from simulations 15 through 20 in Table 4.7. The results for the 0% ratio can be found in Table A.5 and Figure A.8, for the 20% ratio in Table A.8 and Figure A.15, for the 50% ratio in Table A.11 and Figure A.20, for the 80% in Table A.14 and Figure A.25 and for the 100% ratio in Table A.17 and Figure A.30.

For all ratios, a large step size is unwanted since it can be inaccurate and miss the maximum load, like the 0.05 s time step. A step size of magnitude  $10^{-3}$  is accurate enough compared to a magnitude lower, and saves more computational time.

#### 4.4.4. RANGE OF DIFFERENT $G_c$ AND $T_m$ RESULTS

A range of critical energy release rates was simulated for the 0 and 100% ratios. The results can be found in Table A.5 and Table A.17, along with paring graphs Figure A.9, Figure A.10, Figure A.31 and Figure A.32.

For the 0% ratio, a significant change can be witnessed in the altering of its  $G_{c,I}$  property and to a lesser extent its  $T_{m,I}$  property. An increasing maximum load is needed the higher these properties become. Alterations in  $G_{c,II}$  and  $T_{m,II}$  have no effect, which is logical for this type of bending.

For the 100% ratio, a significant change can be witnessed in the range of its  $G_{c,II}$  property and to a lesser extent in its  $T_{m,II}$  property. An increasing maximum load is needed the higher these properties becoming. As with the 0% ratio, this was expected since these two properties are directly related to this pure mode bending. Alterations in  $G_{c,I}$  and  $T_{m,I}$  have no effect as expected again.

#### 4.4.5. DISCUSSION

The results from the validation with Turon's work give promise. The results from the different critical energy release rates and maximum traction show that there is indeed an influence, mainly in different failure loads as would be expected. This was expected since these two properties are directly related to pure mode bending and the formulas of the traction laws as given in Chapter 3. Another observation is that the stiffness remains the same in the range of different  $G_c$  and  $T_m$ , although the traction law used in the CZE changes in shape and thus also the stiffness of the CZE. This keeping of linear behaviour could be attributed to the adherend properties which are also decisive in the stiffness of the structure and the fact that the minute difference in stiffnesses and critical opening displacements of the traction law happens on a micro scale. This could be neglected against the much larger stiffness of the adherends. The  $G_c$  is of larger influence than  $T_m$  due to the area a CZE needs to cover to get fully damaged. A larger area under the traction law requires a larger critical opening displacement to ensure damage initiation. Ultimately, a larger area also requires a larger physical displacement in the end to fully damage a CZE compared to a change in  $T_m$ , which in terms requires only a larger load on the structure itself to initiate damage. This was also clearly related to Figure 3.10a and Figure 3.10b. This information can be used to answer the first research question in Chapter 6.

The best errors were kept in a order of magnitude  $10^0$  with certain CZM options used. This leads to the use of a CZM with a Gaussian integration scheme and a tangent solving method for the CLS specimen. Secant solving methods are to be avoided due to large errors and overshoots of failure loads. Newton-Cotes integration schemes are also avoided because of the many cutbacks and premature endings of simulations. The deactivation of CZE has no influence on the load-displacement and damage results. Nevertheless, for the CLS specimen a choice is made to deactivate the elements for the bondline and between the laminates once they are fully damaged. This is close to what physically happens: pure interfacial separation, meaning that the adhesive is destroyed or split and not physically contributing to the structural loading. The CLS specimen is also mostly based on shear loading; it will be hard to set a viscosity factor for the simulations. For a 50% mode ratio a factor of 0.0005 would suffice, while for a 100% mode ratio a factor of 0.01 would suffice and a factor between 0.01 and 0.005 would already be disastrous for a 50% and 80% mode ratio. The range to choose from is still very large and can have large consequences. For the time steps, accuracy and computational time need to be taken into account. The trade-off for a higher accuracy is a longer computational time and shorter computational times often result in lower accuracy. Comparing this to Turon's work, a time step equal of the same magnitude suffices for the MMB tests. This however, does not mean it would suffice for the CLS specimen due to the different dimensions of the specimen, mesh sizes and the presence of a bond line. Therefore, a separate time step study should be performed for the CLS specimen to see what magnitude would suffice and also would not be computationally too expensive.

Regarding Turon's results, it appears that his user-defined CZE has the advantage of predicting the displacement at the failure load very near to the one of the real experiment. The same goes for the initial stiffness until the model begins to fail. His maximum loads are often close or better than the loads predicted by MSC.Marc. To compensate for the initial stiffness, one can use a finer mesh or time step in MSC.Marc at the cost of computational time. Another alternative is to recreate the CZE model of Turon, or to create one's own user-defined CZE model, but this is out of the scope of this thesis work due to financial and time constraints.

#### **CZM options for CLS Specimen**

Using the previous discussion, a summary of what options to be used for the cohesive properties for the exponential traction law in the CLS simulations can be made.

The integration scheme to be used is the Gaussian scheme. In all simulations with exception of the 2D 20% mixed-mode models, the Gaussian scheme is the most accurate with the lowest computational time.

The stiffness matrix solving method to be used is the tangent method. Especially combined with the Gaussian integration scheme, the tangent solving method has the lowest computational times.

The option whether to keep cohesive zone elements in the structural analysis or to deactivate them has no distinguishable results. Still, the option to deactivate them is chosen to simulate the real life situation as much as possible. Additionally, for the bondline in the CLS specimen, the elements are removed from postprocessing to have a better view of the deformation.

Finally, no viscosity factor will be used unless there would be convergence problems within the simulations.



# 5

## CRACKED LAP SHEAR TEST AND SIMULATION

The CLS experiment together with its simulation is the main subject of the thesis. Progressive failure criteria and cohesive zone modelling will be used in the CLS simulations to detect damage initiation and growth. A real CLS specimen was tested at the site in Manching, where the CLS specimen is based on. A detailed description of the specimen is given in Ch. 5.1. What is suspected in the CLS specimen is a cohesive or adhesive failure, with the possibility of adherend failure as was described in Chapter 2.2. The CLS specimen has strain gauges attached to extract results, also noted in Ch. 5.1. The FE model of the CLS specimen will be explained in Ch. 5.2. These results of the real experiment and the simulations are listed and will be compared with the simulations in Ch. 5.3. A discussion then follows on the outcome of the simulations.

### 5.1. CLS SPECIMEN

An explanation on the real life specimen is given, together with the results from the strain gauges, which will be compared eventually to the simulation results.

#### 5.1.1. PROPERTIES

A CLS specimen consists of mainly out of three parts: the strap, the lap and the bondline. Figure 5.1 shows a simple drawing of the CLS specimen with its laminates and Figure 5.2 shows the real life CLS specimen. In the case of the tested specimen, an additional part is added, called the foot, for clamping reasons. The initial crack  $a_0$  is modelled as a so-called trigger, which is a saw-like pattern of bondline adhesive in the  $a_0$  region, to guide the crack more steadily and gradually as previous experiments have suffered from sudden and quick crack propagation which lead to faulty and unreliable results.

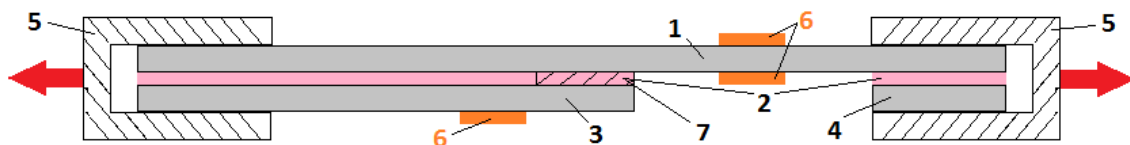


Figure 5.1: Simple drawing of CLS specimen, with strap (1), bondlines (2), lap (3), foot (4), clamps (5), strain gauges (6) and trigger (7).

The technical drawing of the tested CLS specimen can be found in Appendix B.2. The CLS specimen that is tested has the following dimensions in Table 5.1, using the same coordinate system as in Chapter 4.

#### Material

The material of the laminates is the composite CFRP prepreg Hexcel IM7/8552 and the adhesive used for the

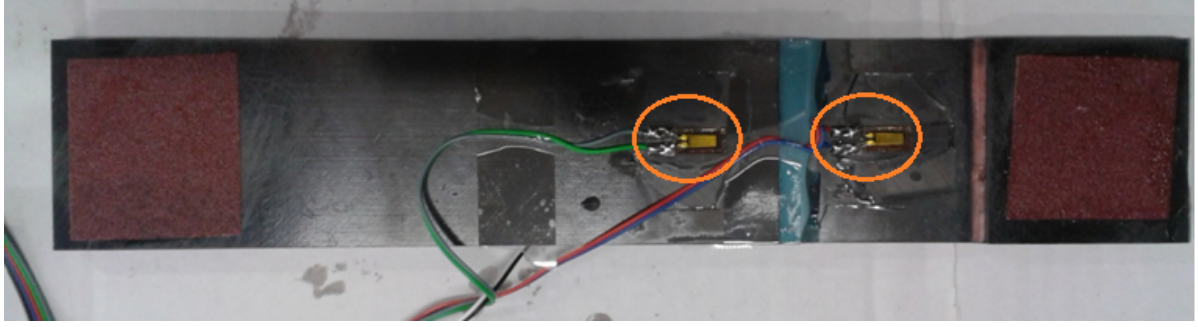


Figure 5.2: Real life specimen with strain gauges (orange), bottom view. Foot is located on the right, and two of the three strain gauges can be seen.

Part of Model	Length $x$ [mm]	Width $y$ [mm]	Thickness $z$ [mm]	Comment
Strap	275	50	3	
Lap	175	50	3	
Bondline (Strap - Lap)	175	50	0.3	Bondline between strap and lap
Bondline (Trigger)	10	50	0.3	Signifies initial crack
Bondline (Strap - Foot)	50	50	0.3	Bondline between strap and foot
Foot	50	50	3	

Table 5.1: Dimensions of CLS specimen components. Technical drawing of the specimen can be found in Appendix B.2.

Property	Value	Property	Value
$E_{11}$	160000 MPa	Tensile Strength $F_{11,t}$	2500 MPa
$E_{22}$	9000 MPa	Compression Strength $F_{11,c}$	2000 MPa
$E_{33}$	9000 MPa	Tensile Strength $F_{22,t}$	65 MPa
$\nu_{12}$	0.32	Compression Strength $F_{22,c}$	285 MPa
$\nu_{23}$	0.4	Shear Strength in-plane $\tau_{12}$	85 MPa
$\nu_{13}$	0.32	Shear Strength transverse $\tau_{23}, \tau_{13}$	50 MPa
$G_{12}$	4500 MPa		
$G_{23}$	3215 MPa		
$G_{13}$	4500 MPa		

Table 5.2: Laminate material properties. Taken from Figure B.4.

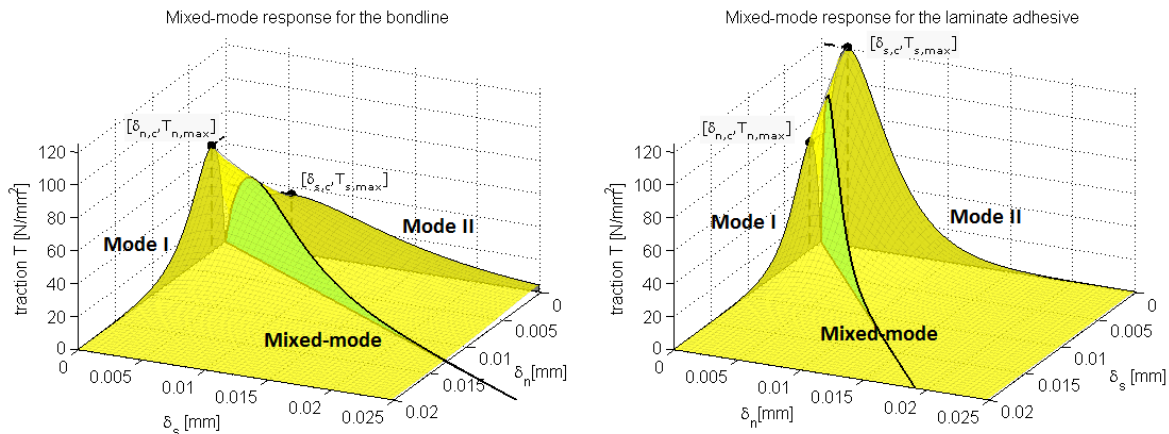
Property	Value	Property	Value
$G_{c,I}$	0.26477 kJ/m <sup>2</sup>	$G_{c,I}$	0.328 kJ/m <sup>2</sup>
$G_{c,II}$	0.6911 kJ/m <sup>2</sup>	$G_{c,II}$	0.5 kJ/m <sup>2</sup>
Tensile Strength $F_{22,t}, T_{m,I}$	65 MPa	$T_{m,I}$	64 MPa
Shear Strength 0° ILS, $T_{m,II}$	120 MPa	$T_{m,II}$	35 MPa
Shear Strength 0° ILS, $T_{m,III}$	120 MPa	$T_{m,III}$	35 MPa

(a) Laminate cohesive material properties.

(b) Bondline material properties.

Table 5.3: Cohesive material properties.

bondline is "Mojo-Mix", which is a mixture of 80% Henkel Hysol EA9395 and 20% Henkel Hysol EA9696. All laminates, strap, lap and foot, consist out of 24 plies of each 0.125 mm thick. The stacking sequence of the plies in the composite laminates is  $((0/45/90/135)_3)_s$ . The material properties of the laminates are given as follows in Table 5.2 and Table 5.3a and the material properties of the bondline is given in Table 5.3b. Using the cohesive properties, one can set up the mixed-mode behaviour of the two adhesives. The mixed mode behaviour in an exponential traction law can be found in Figure 5.3. With taking a look at the traction laws with the properties, there can be made the assumption that cohesive failure in the bondline would occur sooner than interlaminar failure in the strap or lap due to a higher maximum shear traction of the laminate adhesive.



(a) Traction law of the bondline. Note that the adhesive has a higher tensile maximum than shear maximum. (b) Traction law of the laminate adhesive. Note that the adhesive has a higher shear maximum than tensile maximum.

Figure 5.3: Traction laws of the cohesive properties of the adhesives. Note that the laminate adhesive is stronger in both modes than the bondline adhesive.

### Gauges

The CLS specimen also has three strain gauges attached to it: Two on the strap, one on the lap. All strain gauges were placed in the middle of the width. The locations are highlighted in Figure 5.1 and Figure 5.4. The exact centre locations of the gauges can be found in the technical drawing, Appendix B.2. The strain gauges are of type "LY11-6/120", and are 6 mm in length by 2.8 mm in width. The strain gauges are supposed to measure the strain  $\epsilon_{11}$ , which is in the length direction  $x$  of the specimen. The gauges are branded as "Strap Top", "Strap Bottom" and "Lap" gauge.

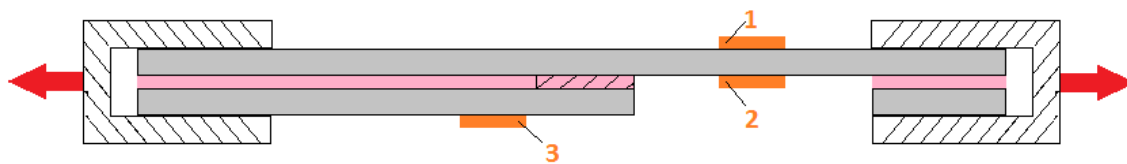


Figure 5.4: Simplified drawing of CLS specimen with strain gauges: strap top gauge (1), strap bottom gauge (2) and lap gauge (3).

### 5.1.2. EXPERIMENT RESULTS

#### Strain Gauges

The CLS specimen has three strain gauges to extract results from during the loading. This is to track the strain in the  $x$  direction. At a certain point, the force was also measured against the current strain: this can be found in Table 5.4. The graphic result of the data of all gauges are found in Figure 5.5a. The specimen ultimately fails at 55 kN.

	Load	Strap Top Gauge	Strap Bottom	Lap Gauge
Measured Strain [ $\mu\epsilon$ ]	25.6 kN	2222	3000	364

Table 5.4: Strain gauge results at 25.6 kN.

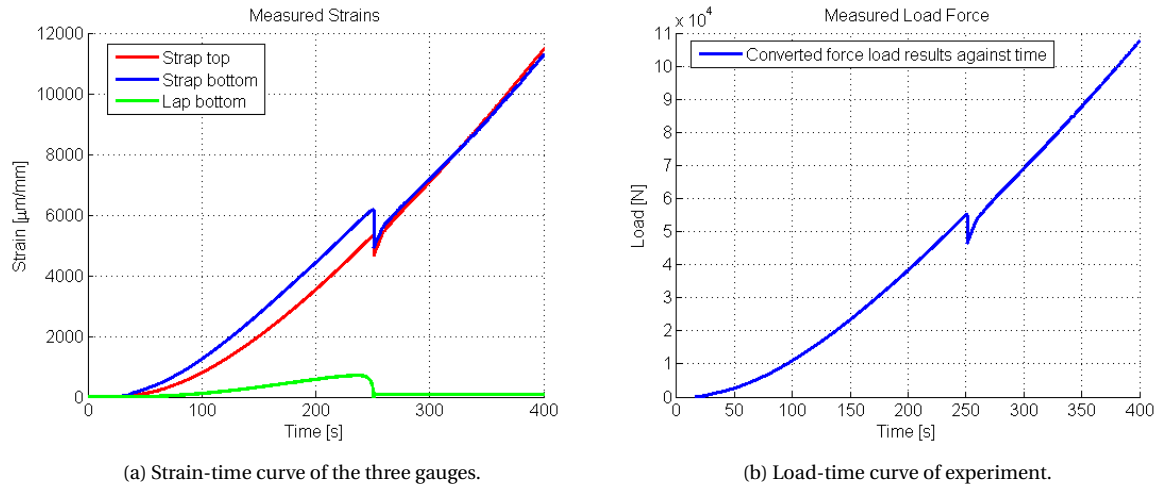


Figure 5.5: Real life CLS experiment results, retrieved with data from the strain gauges and the loading mechanism.

### Force load

The CLS specimen had its driving force of the clamp measured as well against the displacement of the machine. With some fitting and interpolation with the strain curves, the displacement, which was deemed unreliable, has been converted to the load time. The conversion is found in Appendix D. The graphic result of the force load can be found in Figure 5.5b.

## 5.2. CLS SPECIMEN IN MSC.MARC

An explanation on the model and its properties will be given, as well as the setup of simulations.

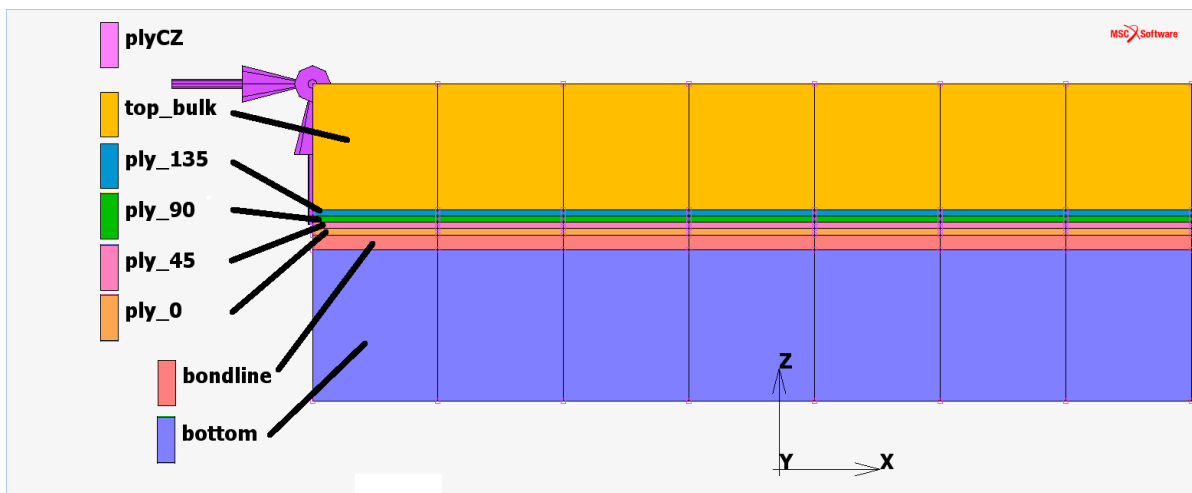
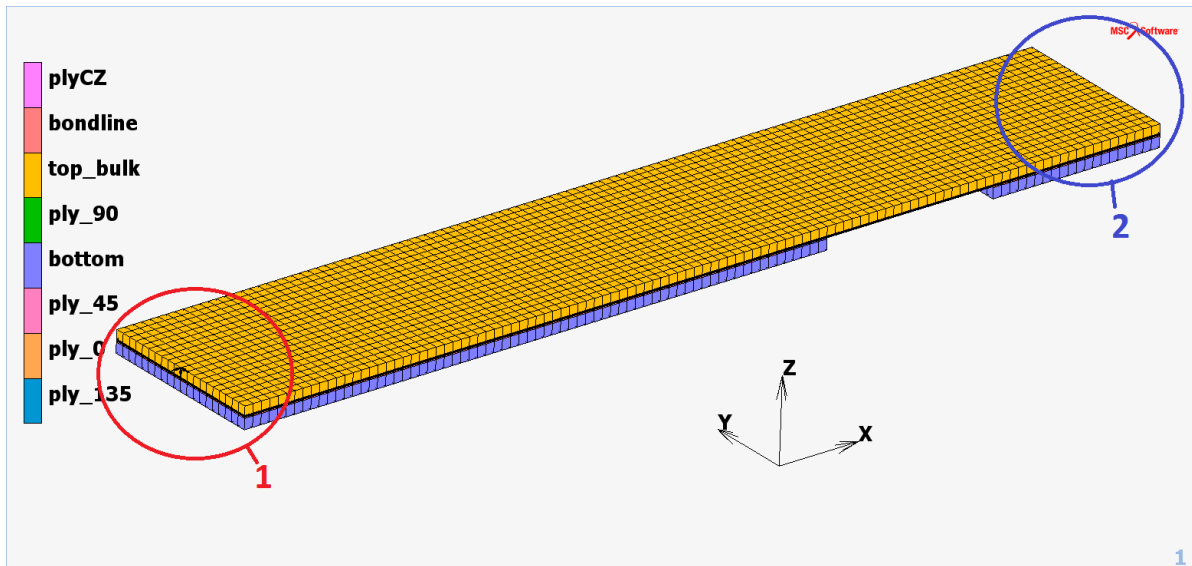
### 5.2.1. FE MODEL

There are a single FE model that will be worked with. The lap and foot will be modelled as one region, consisting of composite solid elements of 2.5 by 2.5 by 3 mm. The bondline will be modelled as another region, consisting of cohesive zone elements of 2.5 by 2.5 by 0.3 mm, as in the continuum approach described in Ch. 2.3. The strap will be split up into five regions: one region contains the first 20 plies and the other regions will be single plies, e.g. the remaining four close to the bondline for there was reason to believe that one of these four plies would fail. This means that the region with 20 plies, or 'bulk' region, will consist of 2.5 by 2.5 by 2.5 mm composite solid elements and the single ply region composite solid elements will consist of 2.5 by 2.5 by 0.125 mm. The lap and bulk region can be defined as a composite multi-ply region, defining an  $x$  number of orientated plies in the thickness direction within the material property of the region, which in turn can be assigned to an element. This can be seen in Figure B.3. The single plies that will be modelled separately, from bondline to bulk region, are the  $0^\circ$ ,  $45^\circ$ ,  $90^\circ$  and  $135^\circ$  plies. Between the single plies and the bulk region, layers of CZE are implemented, each 2.5 by 2.5 by 0 mm, as in the local approach, to distinguish and catch delamination between the plies. Figure 5.6a shows the complete model and Figure 5.6b the different modelled regions that represent the laminates, plies and bondline. For further information regarding element attributed, see Table B.1.

The CZE within the laminates have a zero thickness and will be modelled in between the single ply regions and bulk region, meaning that there will be four layers of CZE in the strap throughout its entire length. Figure 5.7 highlights the present CZE within the strap in a modified view.

Figure 5.6: Model views of the CLS specimen.

(a) Complete view of 3D model. The left end of the specimen in this picture is the 'strap-lap' end (1), while the right end of the specimen is the 'strap-foot' end (2).



(b) Close-up side view of strap-lap end. All different regions of plies and adhesive can be found. The region known as 'top\_bulk' contains the remaining 20 plies of the upper adherend and the region known as 'bottom' contains all plies of the lap adherend. CZE in between plies are not visible since they have zero thickness and are labelled 'plyCZ'.

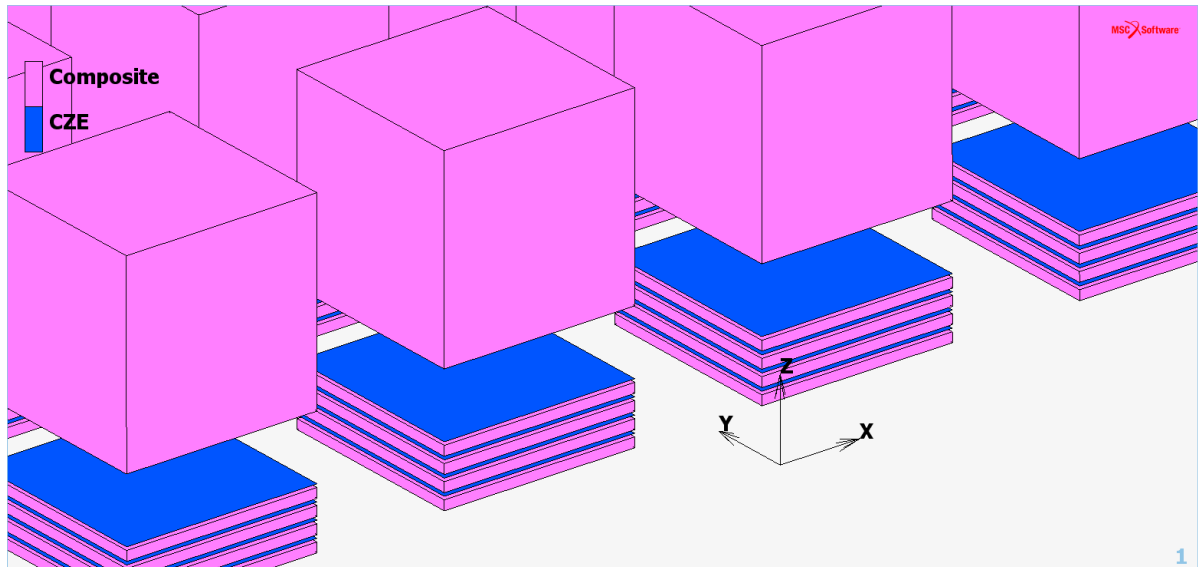
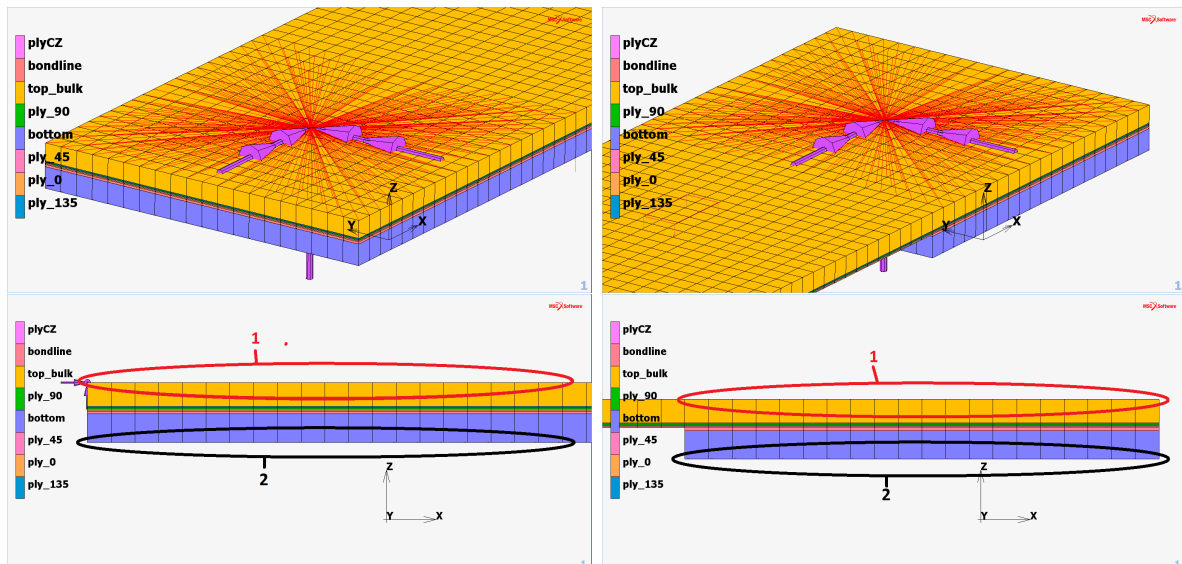


Figure 5.7: View of strap with reduced element size to highlight the CZE (blue) between the plies and bulk region (purple) in the strap adherend.

### Constraints

The constraints to be applied will be as realistic as possible to simulate the clamps like in Figure 5.1. This is done by constraining the first, second and third DOF of all outer surface nodes up to 50 mm of the strap to a master node on both ends. The master nodes are located on the exact centre top node within the 50 mm area of both strap ends as in Figure 5.8. Of the lap and foot end, the first DOF of all outer surface nodes up to 50 mm are also constrained to the master nodes located on the strap. Coincidentally, this contains the entire foot. The constraining is done with the aid of links, which tie DOFs. The strap-lap end is fixed, meaning a prescribed displacement of zero for all outer surface nodes of the strap within 50 mm of the end. The strap-foot end has the displacement load. The lap and foot nodes that are tied still have the freedom to move in the y- and z-direction to compensate for the Poisson ratio.



(a) Constraints on the strap-lap end, only the outer surface nodes up to 50 mm. Red circled nodes (1) mark first and third DOFs tied to the master node. Black circled nodes (2) mark the first DOF tied to the master node.

(b) Constraints on the strap-foot end, only the outer surface nodes up to 50 mm. Red circled nodes (1) mark first and third DOFs tied to the master node. Black circled nodes (2) mark the first DOF tied to the master node.

Figure 5.8: Close-up side view of constraints on both ends.

### Load

The 'load' is a prescribed displacement of 1.25 mm over 1 second, being pulled from the strap-foot end in the length  $x$  direction. Figure 5.8 shows the constraints on both ends. The prescribed displacement is split into three parts. The first part is from 0 to 2% of the load, with a time step of  $5 \cdot 10^{-4}$  seconds. This is done to take possible non-linearities into account at the beginning of the simulation due to bending and tension coupling. The second part is from 2% to 30% of the load, with a time step of  $5 \cdot 10^{-3}$ . This coarse time step is taken since this part is linear because of no failure occurring, and to save computational time. The third part is from 30% to 100% of the load, with a time step of  $5 \cdot 10^{-4}$  seconds. This is done because of the non-linearity during failure, and a smaller time-step would produce more accurate results. A time step evaluation for the CLS model was done in Appendix B.2.

### Contact bodies

For contact bodies, there are three bodies defined: entirety of the strap, lap and foot, and the bondline. This is done because of the trigger, which nodes do not coincide with the nodes of the  $0^\circ$  ply or the lap, see Figure 5.9. The bondline is therefore 'glued' on the other two contact bodies using the glue contact option which automatically adds rigid constraints between the opposite nodes of a common interface region. The contact table can be found in Figure B.1.

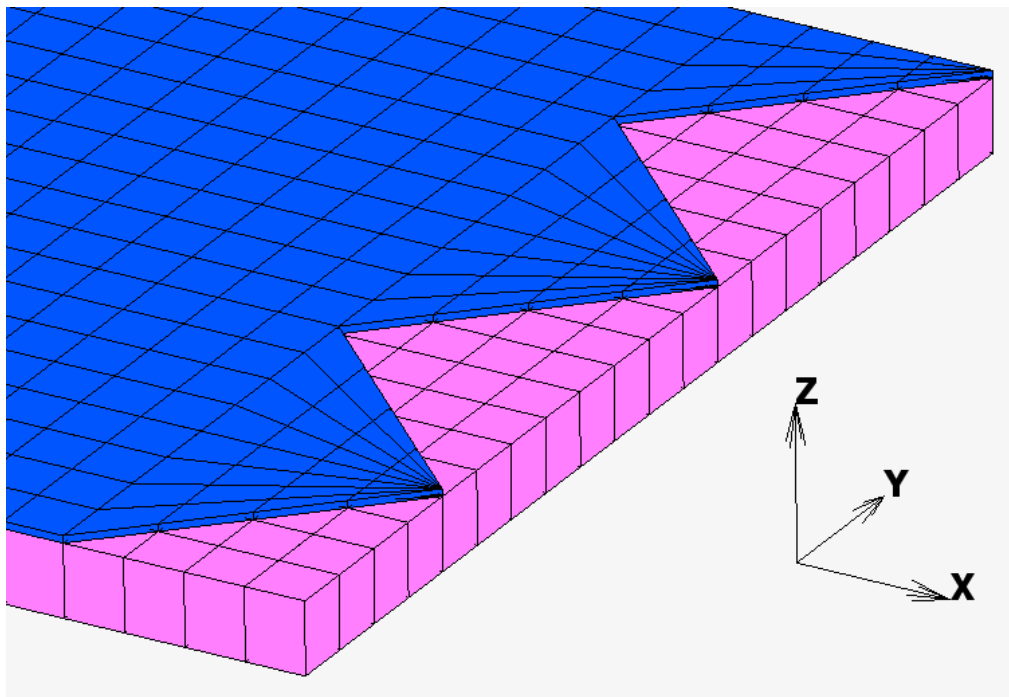


Figure 5.9: View of trigger resting on lap. Strap is made invisible. Note that the trigger symbolises the initial crack region  $a_0$ .

### 5.2.2. MATERIAL AND GEOMETRIC PROPERTIES

The material properties of the laminates are given as follows in Table 5.5 and Table 5.7 and the material properties of the bondline is given in Table 5.8, together with their conversion to MSC.Marc input parameters. The failure criteria properties are given in Table 5.6 together with their conversion to MSC.Marc input parameters. The composite material property has the input parameters used from Table 5.5 with the enabling of the failure criteria Tsai-Wu, Puck or Hashin, see also Figure C.5 for a GUI view of the input parameters. The cohesive material properties for the laminates and bondline use the exponential law and have a tangent solving method with deactivated elements for the interlaminar CZE and bondline CZE and with removal of fully damaged bondline CZE from postprocessing. It uses the input parameters from Table 5.7 and Table 5.8. Also, no viscosity factor is assigned. It further has the input parameters as in Table 5.5.

Property	Value	Equivalent property MSC.Marc	Value MSC.Marc	Comment
$E_{11}$	160000 MPa	$E_1$	160000	
$E_{22}$	9000 MPa	$E_2$	9000	
$E_{33}$	9000 MPa	$E_3$	9000	
$\nu_{12}$	0.32	$\nu_{12}$	0.32	
$\nu_{23}$	0.4	$\nu_{23}$	0.4	
$\nu_{13}$	0.32	$\nu_{31}$	0.018	Use orthotropic relation $E_{11}\nu_{31} = E_{33}\nu_{13}$ .
$G_{12}$	4500 MPa	$G_{12}$	4500	
$G_{23}$	3215 MPa	$G_{23}$	3215	
$G_{13}$	4500 MPa	$G_{31}$	4500	Use orthotropic relation $G_{13} = G_{31}$ .

Table 5.5: Laminate material property conversion to MSC.Marc. Taken from Figure B.4. See Figure C.2 for the GUI input parameters and view.

Property	Value	Equivalent property MSC.Marc	Value MSC.Marc	Comment
Tensile Strength $F_{11,t}$	2500 MPa	Max Fiber Tension / Max Tensile Stress X	2500	Equal to $X_T$ from Table 2.5. Used in all failure criteria.
Compression Strength $F_{11,c}$	2000 MPa	Max Fiber Compression / Max Compressive Stress X	2000	Equal to $X_C$ from Table 2.5. Used in all failure criteria.
Tensile Strength $F_{22,t}$	65 MPa	Max Matrix Tension / Max Tensile Stress Y & Z	65	Equal to $Y_T$ and $Y_C$ from Table 2.5. Used in all failure criteria.
Compression Strength $F_{22,c}$	285 MPa	Max Matrix Compression / Max Compressive Stress Y & Z	285	Equal to $Y_C$ and $Z_C$ from Table 2.5. Used in all failure criteria.
Shear Strength in-plane $\tau_{12}$	85 MPa	Layer Shear Strength / Max Shear Stress XY	85	Equal to $S_{12}$ from Table 2.5. Used in all failure criteria.
Shear Strength transverse $\tau_{23},$ $\tau_{13}$	50 MPa	Transverse Shear Strength / Max Shear Stress YZ & ZX	50	Equal to $S_{23}$ and $S_{13}$ from Table 2.5. Used in Hashin and Tsai-Wu failure crite- rion.
Slope of Fracture Envelope $p_{\perp\parallel}^{(-)}$	-	Slope P12C of Fracture Envelope	0.35	Rule of thumb. Used in Puck failure criterion.
Slope of Fracture Envelope $p_{\perp\parallel}^{(+)}$	-	Slope P12T of Fracture Envelope	0.3	Rule of thumb. Used in Puck failure criterion.
Slope of Fracture Envelope $p_{\perp\perp}^{(-)}$	-	Slope P23C of Fracture Envelope	0.25	Rule of thumb. Used in Puck failure criterion.
Slope of Fracture Envelope $p_{\perp\perp}^{(+)}$	-	Slope P23T of Fracture Envelope	0.25	Rule of thumb. Used in Puck failure criterion.

Table 5.6: Laminate failure criteria conversion to MSC.Marc. Taken from Figure B.4. See Figure C.5a, Figure C.5b and Figure C.5c for the GUI input parameters and view. All other input parameters are with default value.

Property	Value	Equivalent property MSC.Marc	Value MSC.Marc	Comment
$G_{c,I}$	0.26477 kJ/m <sup>2</sup>	Cohesive Energy $G_c$	0.26477	
$G_{c,II}$	0.6911 kJ/m <sup>2</sup>	Shear/Normal Coefficients:	2.6102	Use Eq. 3.35.
Tensile Strength $F_{22,t}, T_{m,I}$	65 MPa	Cohesive Energy $\beta_2$ Critical Opening Displacement $\delta_c$	0.0014985	Use Eq. 3.32.
Shear Strength 0° ILS, $T_{m,II}$	120 MPa	Shear/Normal Coefficients:	1.84615	Use Eq. 3.34.
Shear Strength 0° ILS, $T_{m,III}$	120 MPa	Maximum Stress $\beta_1$ Shear/Normal Coefficients:	1.84615	Use Eq. 3.34.
		Maximum Stress $\beta_1$		

Table 5.7: Laminate cohesive material property conversion to MSC.Marc. See Figure C.1a for the GUI view. All other input parameters are with default value.

Property	Value	Equivalent property MSC.Marc	Value MSC.Marc	Comment
$G_{c,I}$	0.328 kJ/m <sup>2</sup>	Cohesive Energy $G_c$	0.328	
$G_{c,II}$	0.5 kJ/m <sup>2</sup>	Shear/Normal Coefficients:	1.52439	Use Eq. 3.35.
$T_{m,I}$	64 MPa	Cohesive Energy $\beta_2$ Critical Opening Displacement $\delta_c$	0.0018854	Use Eq. 3.32.
$T_{m,II}$	35 MPa	Shear/Normal Coefficients:	0.546875	Use Eq. 3.34.
$T_{m,III}$	35 MPa	Maximum Stress $\beta_1$ Shear/Normal Coefficients:	0.546875	Use Eq. 3.34.
		Maximum Stress $\beta_1$		

Table 5.8: Bondline material property conversion to MSC.Marc. See Figure C.1a for the GUI input view. All other input parameters are with default value.

As for the geometric properties, the 3D composite geometric property uses classical laminate theory for analysing multi-orientated plies and the 3D cohesive geometric properties use a Gaussian integration scheme as determined in the previous chapter.

### 5.2.3. SIMULATIONS

A set of simulations is run, as in Table 5.9. They all share the same model, although they differ in what failure criteria is used.

Sim	Failure Criterion
1	None
2	Tsai-Wu
3	Hashin
4	Puck

Table 5.9: Simulation setup for CLS model.

All simulations now have the following in common:

- Dimensions and material properties according to Table 5.5, Table 5.6, Table 5.7 and Table 5.8.
- The model works in a coordinate system where the x-axis is the length, y-axis the width and z-axis the thickness of the specimen.
- Cohesive properties: MSC.Marc's exponential law, Gaussian integration scheme, tangent solving method, deactivate CZE once full damaged and removal of bondline CZE from postprocessing.
- Classical laminate theory enabled in the composite geometric property.

- All simulations use a simulation time of 1 second, but have the simulation split in three parts: first part up to 2% of the load, or 0.025 mm, consists of a time step of  $5 \cdot 10^{-4}$  s, the second part goes from 2% to 30% of the load, or from 0.025 to 0.375 mm, with a time step of  $5 \cdot 10^{-3}$  s and the third part goes from 30% to 100% s, or from 0.375 to 1.25 mm, with a time step of  $5 \cdot 10^{-4}$  s for more accuracy. This is due to non-linearity occurring near the moment of failure. A time step evaluation has been performed and can be found in Appendix B.2.
- The value for Residual Force Tolerance is decreased to 0.01 instead of the default value 0.1 for better accuracy and the option of Non-Positive Definite matrix in the solution control is checked to solve non-positive definite systems which could halt the simulations. See Figure C.3 and Figure C.4.
- Remaining default options of MSC.Marc are used.

### 5.3. EVALUATION

The CLS specimen had three strain gauges on it. With the real life results, the simulation results can be compared. Next to that, a look at the damage levels in the single plies and CZE inbetween will be looked at to assess any damage in the strap. The computational times are noted in Table 5.10. All simulations were performed with the software and hardware listed in Appendix F.

Sim	Failure Criterion	Comp. Time [s]
1	None	42412
2	Tsai-Wu	45246
3	Hashin	44974
4	Puck	56236

Table 5.10: Simulation times for CLS model.

It seems that the Puck failure criterion takes the most time to solve the analysis, which may be contributed by the amount of failure indices and calculations it has. The deformed shape can be witnessed in Figure B.6 from different angles. For all models, the deformed shape is identical by shape: the bondline has disappeared completely.

#### 5.3.1. STRAIN AND FAILURE LOAD RESULTS

The strain results of the four models can be viewed with curves and data points. The strains of the nodes that were on the designated area of a gauge were averaged all together and this strain result is the output and compared with the real strain results. The results can be found in Table 5.11. The failure load is either based on the moment the main part of the bondline without trigger starts to fail, a cohesive element in between the plies fails or a ply that reaches full failure via the criteria; in this case, the main part of the bondline. The result can be found in Table 5.12.

Sim	Failure Criterion	Strap Top Gauge		Strap Bottom Gauge		Lap Gauge		Comp. Time [s]
		$[\mu\epsilon]$	Error %	$[\mu\epsilon]$	Error %	$[\mu\epsilon]$	Error %	
Real CLS	-	2222	-	3000	-	364	-	-
1	None	2926	31.7	2891	-3.5	434	19.4	42412
2	Tsai-Wu	2926	31.7	2891	-3.5	434	19.4	45246
3	Hashin	2926	31.7	2891	-3.5	434	19.4	44974
4	Puck	2926	31.7	2891	-3.5	434	19.4	56236

Table 5.11: Strain gauge results of the simulations at 25.6 kN, compared to the experiment results.

The strain and load results are largely off. The CLS models had a much earlier failure than the real model. The bondline failed much sooner in the simulation than in real life. Since the data point is still in the linear loading part, all models despite their failure criterion have the same strains and load failure. A graph of the strain versus load of the Puck model can be found in Figure 5.10. All the strain, load and strain-load graphs of the other simulations can be found in Figure B.7, Figure B.8, Figure B.9 and Figure B.10. Even after the

Sim	Failure Criterion	Failure Load [N]	Load Error [%]	Comp. Time [s]
Real CLS	-	55000	-	-
1	None	28641	48	42412
2	Tsai-Wu	28641	48	45246
3	Hashin	28641	48	44974
4	Puck	28641	48	56236

Table 5.12: Failure load results of the simulations, compared to the experiment results.

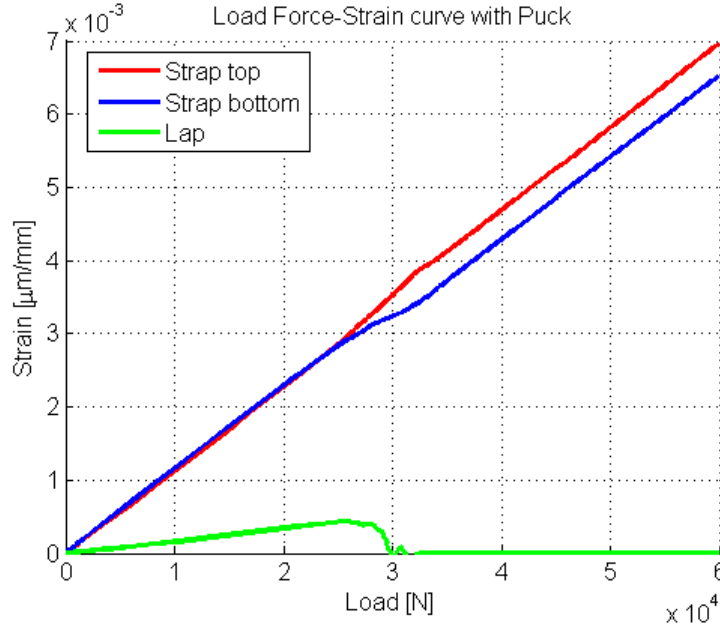


Figure 5.10: Strain-Load results of Puck model. The drop in strain of the lap gauge indicates the failure load.

cohesive failure, the graphs still largely coincide. This means that only cohesive failure should have occurred, for if complete ply failure would occur, there would be a difference in in the models with the failure criteria. A comparison between the strain-load graphs with the real experiment strain gauge results can be found in Figure B.11.

### 5.3.2. DAMAGE RESULTS

To be able to fully conclude that cohesive failure was the first failure to take place, a look can be taken at how far the single plies were damaged for interlaminar, intralaminar or fibre failure modes on the moment that damage of the bondline started to propagate. In the first simulation, no failure criteria was used, so no ply damages can be analysed. For all the other simulations, the damage can be monitored at the moment the real bondline starts failing, which is at simulation time  $t = 0.3395$  s. The damage is coupled to the reduction factors and failure indices of the failure criteria, as explained in Ch. 2.4.2. A table is set up with all the largest failure indices in each ply for each model to see what type of failure is the driving factor, see Table 5.13. The plies have suffered no damage at all at this time step, meaning that the failure occurring is not intralaminar. To see if interlaminar failure has occurred, the damage levels of the CZE between the plies can be analysed. For this time step, no damage was found in the CZE between the plies, ruling out interlaminar failure. The failure criteria Hashin and Puck point out that the plies are showing signs of tensile matrix failure at this stage, with no lasting damage.

A damage comparison can also be made if the failure would indeed occur at 55 kN just like in the experiment, to see whether or not damage occurred in the plies at that moment. The time step at which the load force was 55 kN is at  $t = 0.9245$  s. A second table is set up with all the largest failure indices in each ply for each model

Sim	Failure Criterion	Ply	Largest FI Value	FI No. in MSC.Marc	Type of Failure
2	Tsai-Wu	0° ply	0.5266	1	Not distinguishable
2	Tsai-Wu	45° ply	0.2811	1	Not distinguishable
2	Tsai-Wu	90° ply	0.4117	1	Not distinguishable
2	Tsai-Wu	135° ply	0.3963	1	Not distinguishable
3	Hashin	0° ply	0.2126	3	Tensile Matrix Failure
3	Hashin	45° ply	0.1811	3	Tensile Matrix Failure
3	Hashin	90° ply	0.2852	3	Tensile Matrix Failure
3	Hashin	135° ply	0.2453	3	Tensile Matrix Failure
4	Puck	0° ply	0.4480	3	Tensile Matrix Failure
4	Puck	45° ply	0.2977	3	Tensile Matrix Failure
4	Puck	90° ply	0.3817	3	Tensile Matrix Failure
4	Puck	135° ply	0.3210	3	Tensile Matrix Failure

Table 5.13: Failure indices of single modelled plies as taken at increment where bondline failure occurred first ( $t = 0.3395$  s) (FI = Failure Index).

to see what type of failure is the driving factor and to see how far damaged the ply is. The results can be found in Table 5.14. In all cases, the damage is either non-existent or not significant enough to cause intralaminar failure at 55 kN. For all plies excluding the 0° ply, tensile matrix failure seems to be occurring and for the 0° ply tensile fibre failure. For interlaminar failure, the damage levels in the CZE are again near zero, indicating no interlaminar failure.

Sim	Failure Criterion	Ply	Largest FI Value	FI No. in MSC.Marc	Damage Value	Type of Failure
2	Tsai-Wu	0° ply	0.3932	1	0.2088	Not distinguishable
2	Tsai-Wu	45° ply	0.5020	1	0.0989	Not distinguishable
2	Tsai-Wu	90° ply	0.5296	1	0.3373	Not distinguishable
2	Tsai-Wu	135° ply	0.5606	1	0.2777	Not distinguishable
3	Hashin	0° ply	0.1924	1	0.0000	Tensile Fibre Failure
3	Hashin	45° ply	0.2989	3	0.0000	Tensile Matrix Failure
3	Hashin	90° ply	0.5630	3	0.1567	Tensile Matrix Failure
3	Hashin	135° ply	0.4747	3	0.0000	Tensile Matrix Failure
4	Puck	0° ply	0.3959	1	0.0000	Tensile Fibre Failure
4	Puck	45° ply	0.3702	3	0.0000	Tensile Matrix Failure
4	Puck	90° ply	0.5250	3	0.0249	Tensile Matrix Failure
4	Puck	135° ply	0.4302	3	0.0000	Tensile Matrix Failure

Table 5.14: Damage levels of single modelled plies as taken at increment where  $F = 55000$  N ( $t = 0.9245$  s) (FI = Failure Index).

The Tsai-Wu model is starting to show signs of damage in most plies at the moment of initial bondline failure. Failure indices have moderate value at the spot where the bondline is supposed to fail, yet remain below 1 with no damage value, indicating no intralaminar failure. Sadly, no distinction can be made between the different failure modes. Figure B.12 displays the highest failure indices for each ply at  $t = 0.3395$  s. At  $F = 55000$  N, or  $t = 0.9245$  s, it seems that the 90° ply has started to show damage. The highest damage and failure indices levels at  $t = 0.9245$  s can be found in Figure B.18, Figure B.13 and Table 5.14. The 45° and 135° ply seem to have some slight damage spread out over the structure, yet all plies indicate no full intralaminar failure.

For the Hashin model, there doesn't appear to be any damage in the plies at  $t = 0.3395$  s, the moment the bondline starts damage propagation. Figure B.14 displays the highest failure indices levels for each ply at  $t = 0.3395$  s, where tensile matrix failure seems to be the acting failure type. The largest failure index still remains below 1 with no damage values in the plies, meaning that no intralaminar failure occurred. For  $t = 0.9245$  s, it seems that the expectation of the 90° ply being the most damaged is once again confirmed. The damage is of tensile matrix failure mode. The other plies show no signs of damage. Figure B.19, Figure B.15 and Table 5.14 displays the highest damage and failure indices levels for each ply at  $t = 0.9245$  s.

For the Puck model, all plies have no damage at  $t = 0.3395$  s. Figure B.16 displays the highest failure indices levels for each ply at  $t = 0.3395$  s, with all plies appearing to go for tensile matrix failure mode. Also with Puck's criterion, the largest failure index remains below 1 with no damage value in all plies, indicating no intralaminar failure. At  $t = 0.9245$  s the  $90^\circ$  ply remains the largest damaged ply in tensile matrix failure mode. The suspicion of a weakening  $90^\circ$  ply is once again confirmed. Figure B.17, Figure B.20 and Table 5.14 displays the highest failure indices and damage levels for each ply at  $t = 0.3395$  s.

The results have led for all models zero damage in the CZE and ply elements at  $t = 0.3395$  s and zero damage in the CZE and slight damage in the ply elements at  $t = 0.9245$  s. This means that no interlaminar or intralaminar failure occurred, and that the only failure that has been truly present in the model, was cohesive failure.

### 5.3.3. DISCUSSION

The remaining two research questions could now be answered as well with the aid of the CLS simulation results. These results have large errors on two of the three strain gauges and on the failure load. The only failure present was cohesive failure when also inter- or intralaminar failure was expected. This brings doubt in MSC.Marc's ability to accurately analyse combined failure modes. Several possibilities and factors can be mentioned for the inaccuracies.

The first would be wrong material properties and specimen build. During this thesis work, it has occurred numerous times that either the material properties of both adhesive and adherends were wrong and subsequently corrected, the lay-up and number of the plies were actually different, or that the entire dimensions of the specimen were different, meaning that the wrong specimen has been used. Deducing with the knowledge about cohesive zone modelling, were it that the bondline was in fact stronger, i.e. higher critical energy release rate and/or maximum traction in shear, there may have been the possibility of pre-emptive tensile matrix or even tensile fibre and interlaminar failure before complete cohesive failure in the bondline. In this case, most likely there would have been a jump in damage growth due to the progressive failure occurring in the strap and subsequently weakening it, allowing for stress discontinuities and concentrations, and thus damaging the strap ultimately before complete failure of the entire bondline. The same could also be said if the cohesive properties of the laminate adhesives were to be lower. This could be a way also to induce a damage growth jump from adhesive to adherend.

A second possibility would be the choice of solid elements. The single ply regions have a bad aspect ratio when it comes to solid element types dimension wise. This may yield inaccurate results, longer computational time and even errors. Yet in turn, many previous BOPACS project members have worked with similar mesh sizes on different studies like crack-stopping bonded joints, which had accurate results. These other studies did not use CZM but different failure criteria.

Another explanation would be the use of MSC.Marc's CZM with a continuum approach, i.e. using the CZM on cohesive zone elements with a finite thickness such as the bondline. Certain studies already have shown that the continuum approach is possible [11, 89, 90] and the lead developer of MSC.Marc had personally assured that a continuum approach can be used for small thicknesses. It could be an option to evaluate the continuum approach within a separate small study using a single lap joint for example, to confirm the ability to use this approach for MSC.Marc and to what range of thickness it remains reliable.

Another reason would be the cohesive zone model used, although this can be countered by the fact that MSC.Marc's exponential traction law performed well enough for the simple tests of Turon, and it would be highly unlikely for such a large error to occur only thanks to the cohesive model.

Another possibility would be the density of the mesh, which may be too coarse for this problem, although other BOPACS project members have used similar, larger and even solid element sizes for this problem.

Boundary conditions within the model can also be a factor, although they were adapted as realistic as possible compared to the real experiment. A follow-up on this research may keep a study in mind regarding different boundary conditions to assert and distinguish any large differences between boundary conditions.

What would have been a better experimental setup, was to test only the strap for static loading first and then the CLS specimen. This way the progressive failure criteria can be tested separately in order to assert their accuracy within MSC.Marc, and to confirm whether or not the right material properties and boundary conditions are used.



# 6

## CONCLUSION AND RECOMMENDATIONS

Now that the validation with Turon's work and the CLS specimen results have been processed and discussed, one can form the conclusion to the research question invoked in Chapter 1. The conclusion of this thesis is followed in Ch. 6.1. Several recommendations on this thesis work are given in Ch. 6.2.

### 6.1. CONCLUSION

The objective of this thesis work was guided with three questions which can now be answered thanks to the research performed. The first research question was as follows:

- What parameters and material properties of a cohesive model are of influence in damage onset and growth?
  - Determine the influence of the critical energy release rate.
  - Determine the influence of the maximum traction allowed of the adhesive.

With a fixed maximum traction, an increase in the critical energy release rate can make the damage initiation till propagation more gradual instead of sudden within the traction models for a traction law. A single CZE will then need a larger critical opening displacement and thus has a larger failure load, as seen in Figure 3.10b and Chapter 4.4.

With a fixed critical energy release rate, an increase in the maximum traction can in fact reduce the critical opening displacement needed as seen in Figure 3.10a. In turn, it makes the CZE stiffer and requires a larger failure load to start damaging the element. This is seen in Chapter 4.4.

Increasing critical energy release rate has a larger influence than the increase of maximum traction. This is due to the fact that traction law with a larger critical energy release rate has more area to cover and to fully damage a CZE, which is also related to the opening displacement between modes. This means that a larger gap is necessary to fully damage a CZE. This is confirmed in Chapter 3.1.4 and Chapter 4.4.4.

The second research question was as follows:

- Is ply failure or delamination present and does this failure cause damage growth to physically jump from the bondline to the adherend in the CLS specimen?
  - If there is a jump in damage growth, what cohesive parameters are of influence to prevent or induce this?

In the current simulations of the CLS specimen, no ply failure or delamination took place. The entire bondline is the first to fail, resulting in the CLS specimen being subjected to a cohesive failure. This is thanks to the low strength properties of the bondline material compared to the adhesive in the laminates.

To induce a jump in damage growth from adhesive to adherend, the critical energy release rates or maximum traction for shear mode of the bondline must be higher in order to let delamination occur during bondline failure, which causes a shift in damage growth. An alternative is that the rates and maximum traction for shear mode of the laminate adhesives must be lower to achieve the same result.

The third research question was as follows:

- How accurate can you model (the jump of) damage growth progressively of a coupon level test specimen in the finite element package MSC.Marc?
  - Determine the accuracy of the solver's own cohesive zone model.
  - Determine the accuracy of the progressive failure within the adherends of the CLS specimen.

The exponential law using a Gaussian integration scheme together with a tangent stiffness matrix solving method yields the most accurate results for damage onset and growth in mixed-mode experiments and interlaminar failure, as proven in Chapter 4. The validation based on Turon [59] yields accurate results, with most errors being kept under |10%| together with good computational times.

The CLS simulation results are not accurate enough to represent a feasible reconstruction of the CLS experiment. The largest errors are of magnitude  $10^1$  percentage. Analysing interlaminar failure in simple coupon level specimens yields good results, while analysing combined failure modes with the aid of progressive failure criteria in the CLS specimen is inaccurate for the current simulation setups. Cohesive failure is the only failure present in the simulations. With no real adherend failure occurring, the accuracy of progressive failure analysis for composite plies alone remains inconclusive.

## 6.2. RECOMMENDATIONS

The outlook of this research work and subject remains that an accurate way will be presented to simulate the CLS specimen. Despite this setback, for Airbus Group cohesive zone modelling still remains in interest due to successful application to simple coupon and delamination tests and new ways are now being explored and used to accurately assess this problem before moving on to real aircraft components. For example, currently, a new study has been connected to this thesis work by another person to continue the work on the CLS specimen with extensive use of shell elements.

Several recommendations and possible future research on this topic can be given in light of improving the subject and future work. The obstacles faced during the duration of this research made many of the possible options highlighted in this section not possible due to time constraints and technicalities. Specific recommendations on when using MSC.Marc can be found in Appendix E to help other people get over the primary 'teething troubles'. What follows now is a list of recommendation which may improve the research on CLS specimen and any future works afterwards.

### **Benchmarking with denser mesh and smaller time steps**

An option to improve the work in this thesis is to benchmark and test the density of the mesh together with lower time-steps. Taking a denser mesh is common to increase accuracy, and so are lower time steps. This is a costly recommendation though, since this increases computational time incredibly.

### **Continuum approach**

As previously mentioned, it may be worth performing a study around the continuum approach with MSC.Marc. This could be done to see up to what thickness cohesive zone elements are truly reliable for the CZM in MSC.Marc.

### **Shell elements**

The use of shell elements is an obvious one. A similar study was started by another person at a late stadium of this research work and is still currently being performed. The use of shell elements could significantly reduce the wall time of the simulations and could even be more accurate considering that the thickness of single modelled plies are very suitable for shells in finite element analysis. Another recommendation that can be combined with the use of shell elements is the remodelling of every ply in the strap. This may be tedious and computationally hard work, but it may yield accurate results.

### **User-Defined Cohesive Zone Elements**

Because of the limitation to MSC.Marc's home setting and CZE options, one can opt to applying a user-defined cohesive zone model. Turon [59] applied a user-defined model with the help of the Benzeggagh

and Kenane criterion, Eq. 3.28. His model proved to be even more accurate than MSC.Marc's exponential as was proven in Chapter 4. A similar study can be performed by making an even more accurate cohesive zone model in Python language and applying it in MSC.Marc, and to test it on the CLS specimen.

#### **P-FEM Analysis**

Another study that is being performed at the Defence and Space department of Airbus Group is P-FEM based analysis. P-FEM uses polynomials in shape functions to solve finite element analysis. Increasing the polynomial levels in the shape functions results in better accuracy while the elements stay the same size, meaning that more complex stress states can be analysed. Adapting P-FEM is already being done for coupon level based structures with the help of the P-FEM package StressCheck. StressCheck is still under development and does not support cohesive zone elements. It may take some time before it is applicable to many and all forms of structure, although it remains a future study for P-FEM to be tested on the CLS specimen with CZE.

#### **Element and sub-component level structures**

Advancement to element and even to sub-component level structures is a possible future study regarding adhesive bonded joints. The CLS specimen is a coupon level based structure which requires an extensive amount of understanding before moving onto complexer structures. Still, proper modelling techniques and preferably a standardised modelling methodology for FE analyses with composite adhesive bonded joints should be researched before one can validate and simulate sub-component level structures.



# A

## MSC.MARC VALIDATION WITH TURON'S EXPERIMENT

### A.1. FULL DETAILS MODELLING

Information regarding element types and sizes can be found in Table A.1.

Models	Part of Model	Element Size	No. Elements	Element Type	Element Class
All 2D MMB Models	Adherend	0.68 by 1.56	300	3	Quad 4 - Plane Stress Full Integration
2D 0% Model	Adhesive	0.68 by 0	102	186	Quad 4 - Interface
2D 20% Model	Adhesive	0.68 by 0	101	186	Quad 4 - Interface
2D 50% Model	Adhesive	0.68 by 0	101	186	Quad 4 - Interface
2D 80% Model	Adhesive	0.68 by 0	118	186	Quad 4 - Interface
2D 100% Model	Adhesive	0.68 by 0	92	186	Quad 4 - Interface
All 3D MMB Models	Adherend	0.68 by 6.35 by 1.56	1200	117	Hex 8 - Red. Integration type
3D 0% Model	Adhesive	0.68 by 6.35 by 0	408	188	Hex 8 - Interface
3D 20% Model	Adhesive	0.68 by 6.35 by 0	404	188	Hex 8 - Interface
3D 50% Model	Adhesive	0.68 by 6.35 by 0	404	188	Hex 8 - Interface
3D 80% Model	Adhesive	0.68 by 6.35 by 0	416	188	Hex 8 - Interface
3D 100% Model	Adhesive	0.68 by 6.35 by 0	368	188	Hex 8 - Interface

Table A.1: Element information.

Contact body used with default setting to compensate for intertwining of elements, see contact table in Table A.1.

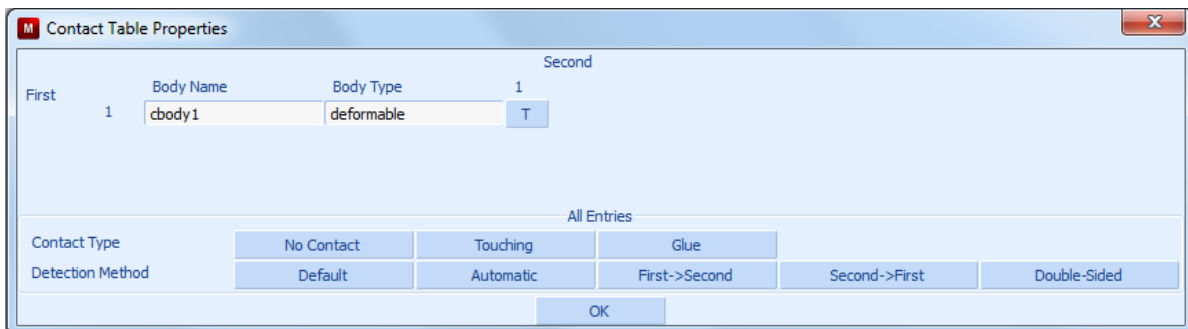


Figure A.1: Contact Table Properties for 2D and 3D models.

Nodal ties type 2 for 2D models and type 3 for 3D models and RBE2's used for both models to simulate rigid lever, see Ch. A.2.

## A.2. RIGID LEVER FOR MMB SIMULATION

An explanation is given here for the analysis theory behind the mixed-mode ratio calculation and how to attain a certain mixed-mode ratio. An explanation regarding the modelling of the rigid lever is also given.

### A.2.1. ANALYSIS

A formula can be set up to calculate the lever length  $c$ , as in Figure 4.1. A mode mixity ratio  $\kappa$  can be set up as a function of energy release rates of mode I and II:

$$\kappa = \frac{G_{II}}{G_I + G_{II}} \quad \therefore \quad \frac{G_I}{G_{II}} = \frac{1 - \kappa}{\kappa} \quad (\text{A.1})$$

Using a relation from Reeder and Crews [46]:

$$\frac{G_I}{G_{II}} = \frac{4}{3} \left( \frac{3c - l}{c + l} \right)^2 \quad \text{for } c \geq \frac{l}{3} \quad (\text{A.2})$$

with half the length of the specimen  $l$  and lever length  $c$ , one can combine both Eq. A.1 and Eq. A.2 to form:

$$c = \frac{l \left( \frac{1}{2} \sqrt{3 \left( \frac{1 - \kappa}{\kappa} \right) + 1} \right)}{3 - \frac{1}{2} \sqrt{3 \left( \frac{1 - \kappa}{\kappa} \right)}} \quad (\text{A.3})$$

Using the mixed-mode ratios, the lever lengths can be calculated, see Table A.2.

$G_{II}/G_T$	20%	50%	80%
$\kappa$	0.2	0.5	0.8
$c$ [mm]	109.89	44.60	28.47

Table A.2: Tabular overview of lever length  $c$  per fracture mode ratio.

### A.2.2. MODELLING

The modelling of the lever is done via links and a rigid bar. A visual explanation follows with the use of Figure A.2. The node that has the prescribed displacement, in the grey circle, is going to be called load node. The two nodes that are encircled by a red circle, are 'tied' to the load node, which is 'retained', to form a rigid structure. This is done with the option RBE2, under 'Links' tab in the GUI of MSC.Marc. Meanwhile, the nodes encircled by the green circles are linked to the red circle nodes and are tied in the z-direction, e.g. the green circle nodes are constrained to follow the red circle nodes in the z-direction.

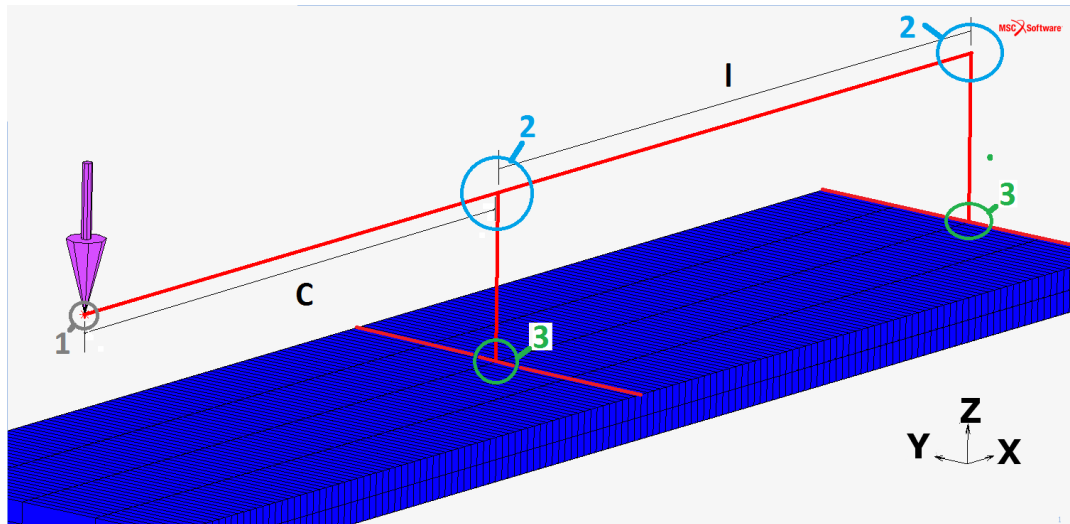
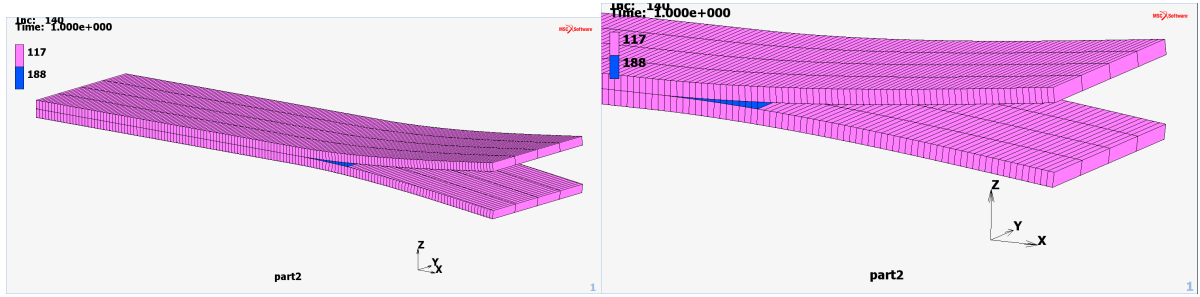
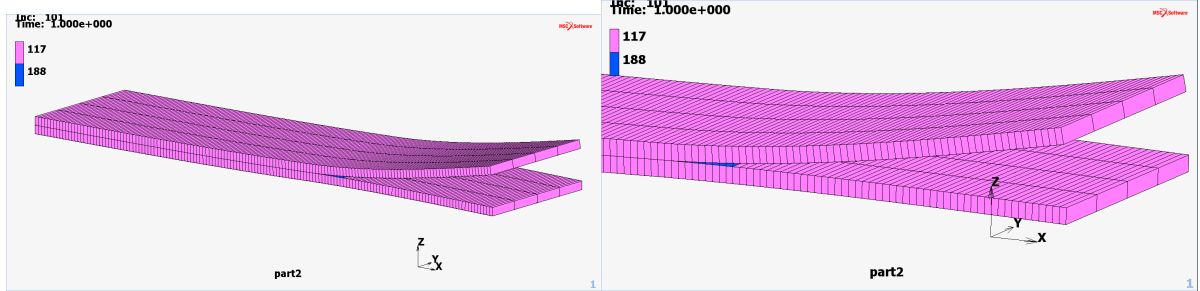


Figure A.2: Rigid lever as in the 50% mode ratio simulations. Grey circle (1) is the node with displacement. Blue circles (2) are nodes that are tied. Green circles (3) are nodes that share DOF. The red lines on the model are nodes that are tied by DOF to the middle nodes.

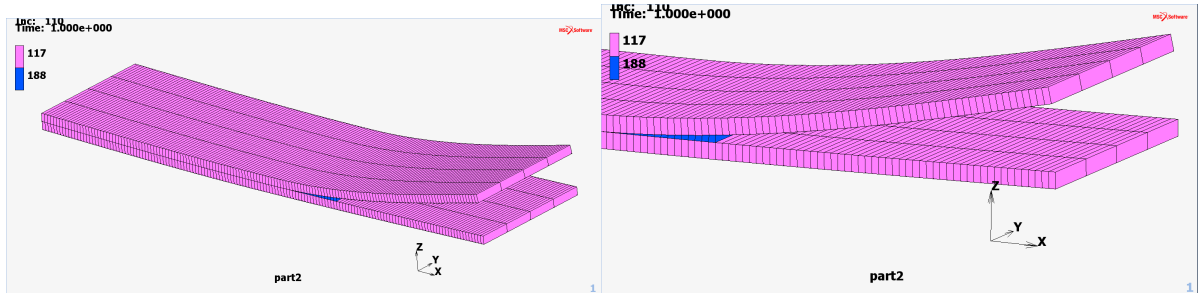
### A.3. TABLES AND FIGURES OF RESULTS



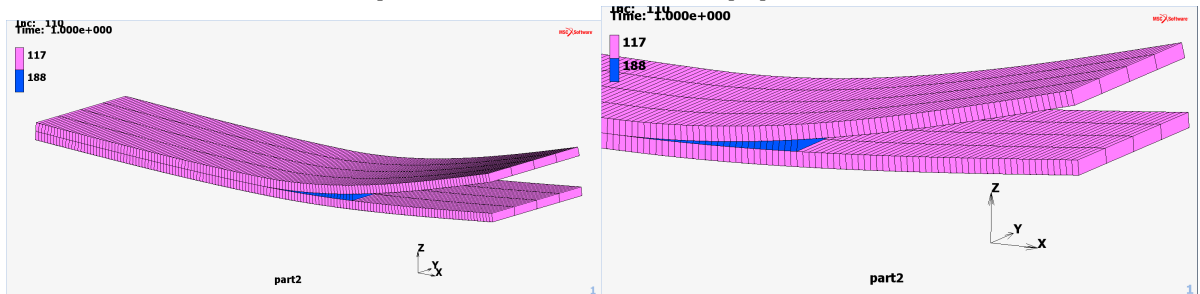
(a) Deformed shape of the 0% ratio. Bended adherends (purple) and bondline (blue).



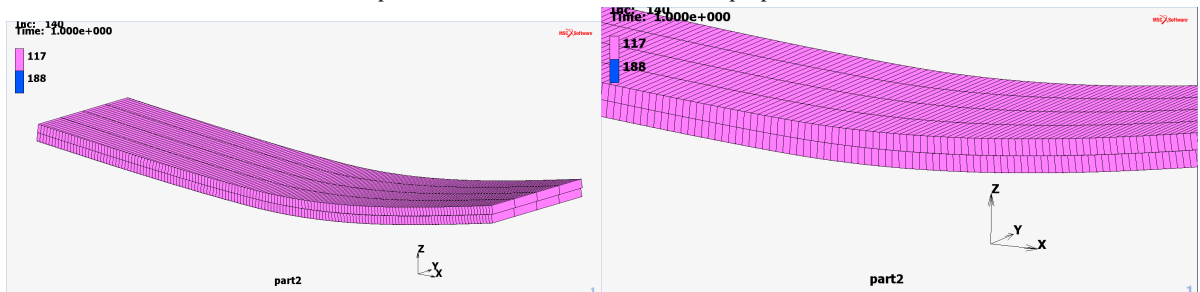
(b) Deformed shape of the 20% ratio. Bended adherends (purple) and bondline (blue).



(c) Deformed shape of the 50% ratio. Bended adherends (purple) and bondline (blue).



(d) Deformed shape of the 80% ratio. Bended adherends (purple) and bondline (blue).



(e) Deformed shape of the 100% ratio. Bended adherends (purple) and bondline (blue).

Figure A.3: 3D models in deformed shape.

Sim	Integ. Scheme	Stiffness Mtx. Method	CZE De-act./Kept	Visc. Factor	Max. Load [N]	Exp. Load [N]	Error [%]	Comp. Time [s]
Turon	G	T	-	-	152.4	147.5	3.32	-
1	G	S	K	-	146.4	147.5	-0.75	43
2	G	S	D	-	146.4	147.5	-0.75	43
3	G	T	K	-	146.4	147.5	-0.75	42
4	G	T	D	-	146.4	147.5	-0.75	52
5	NC	S	K	-	182.8	147.5	23.93	39
6	NC	S	D	-	182.8	147.5	23.93	36
7	NC	T	K	-	105	147.5	-28.81	43
8	NC	T	D	-	105	147.5	-28.81	44
9	G	T	D	0.05	(N/A)	147.5	-	15
10	G	T	D	0.01	173.1	147.5	17.36	17
11	G	T	D	0.005	158.7	147.5	7.59	18
12	G	T	D	0.001	148.3	147.5	0.54	22
13	G	T	D	0.0005	146.5	147.5	-0.68	24
14	G	T	D	0.0001	146.4	147.5	-0.75	34

Table A.3: Results from the 0% fracture mode ratio for 2D simulations 1 through 14 with varying cohesive zone model settings.

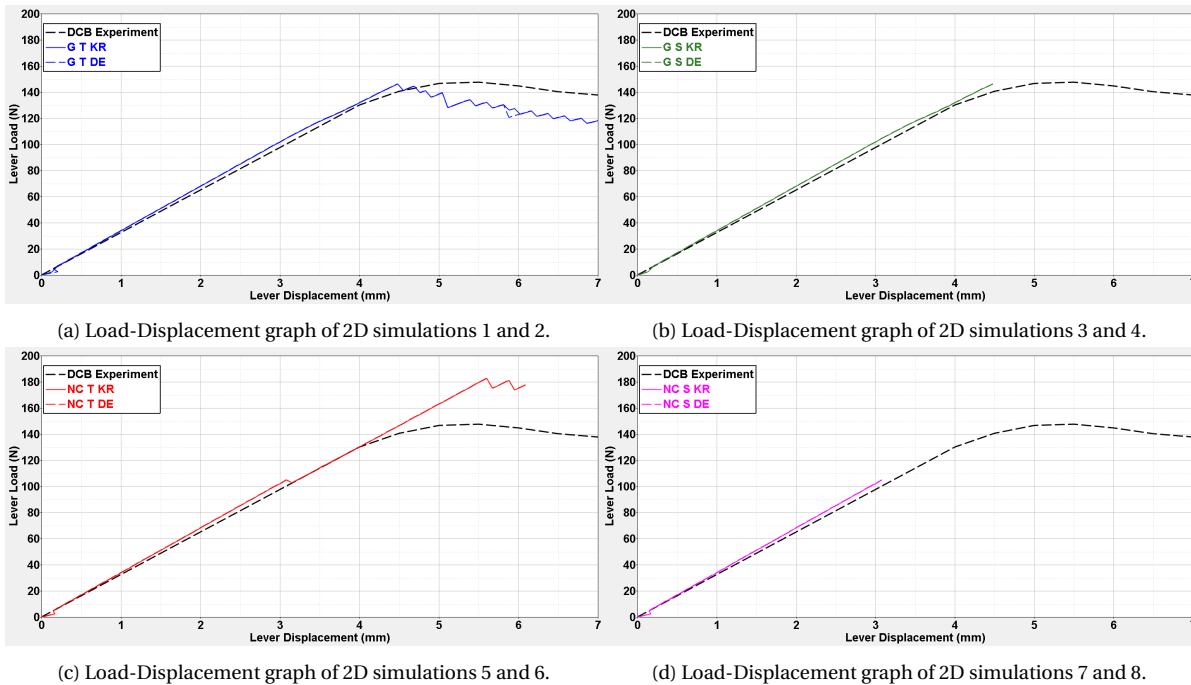
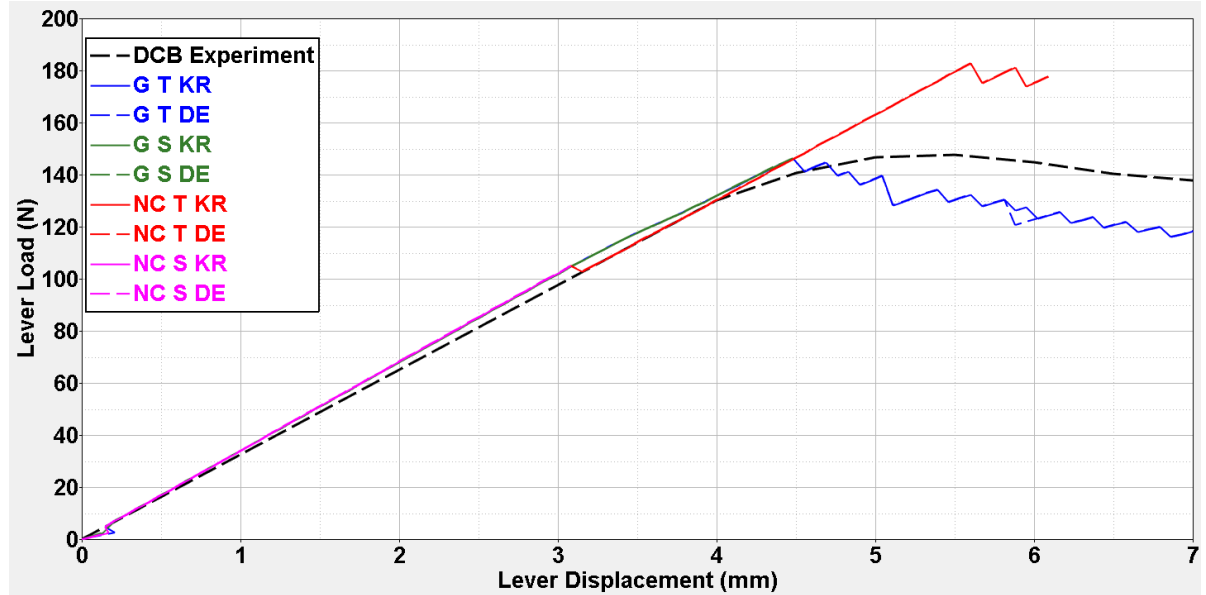
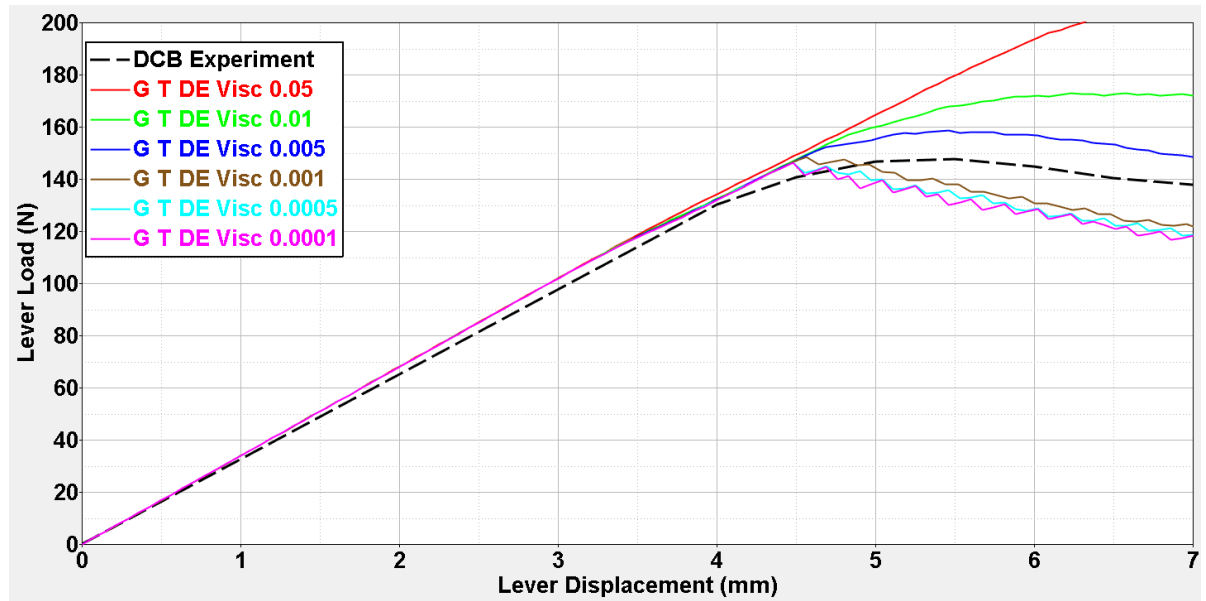


Figure A.4: Results of the 0% fracture mode setup for 2D simulations 1 through 8 with varying cohesive zone model settings.



(a) Load-Displacement graph of 2D simulations 1 through 8.



(b) Load-Displacement graph of 2D simulations 9 through 14: Viscosity factor results.

Figure A.5: Results of the 0% fracture mode setup for 2D simulations 1 through 14.

Sim	Integ. Scheme	Stiffness Mtx. Method	CZE De-act./Kept	Visc. Factor	Max. Load [N]	Exp. Load [N]	Error [%]	Comp. Time [s]
Turon	G	T	-	-	152.4	147.5	3.32	-
1	G	S	K	-	143.8	147.5	-2.51	362
2	G	S	D	-	143.8	147.5	-2.51	365
3	G	T	K	-	143.9	147.5	-2.44	345
4	G	T	D	-	143.9	147.5	-2.44	319
5	NC	S	K	-	144.5	147.5	-2.03	303
6	NC	S	D	-	144.5	147.5	-2.03	306
7	NC	T	K	-	144.5	147.5	-2.03	318
8	NC	T	D	-	144.5	147.5	-2.03	322
9	G	T	D	0.05	-	147.5	-	131
10	G	T	D	0.01	165.9	147.5	12.47	157
11	G	T	D	0.005	153.8	147.5	4.27	173
12	G	T	D	0.001	144.9	147.5	-1.76	222
13	G	T	D	0.0005	144.7	147.5	-1.90	235
14	G	T	D	0.0001	143.9	147.5	-2.44	288

Table A.4: Results from the 0% fracture mode ratio for 3D simulations 1 through 14 with varying cohesive zone model settings.

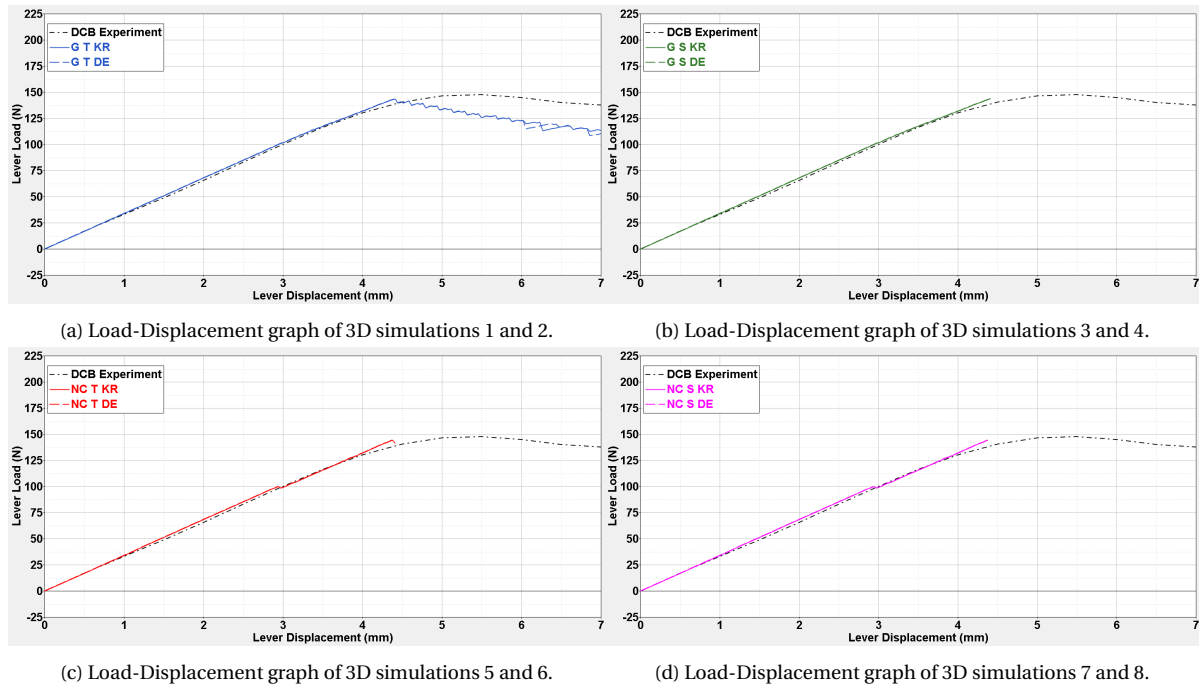
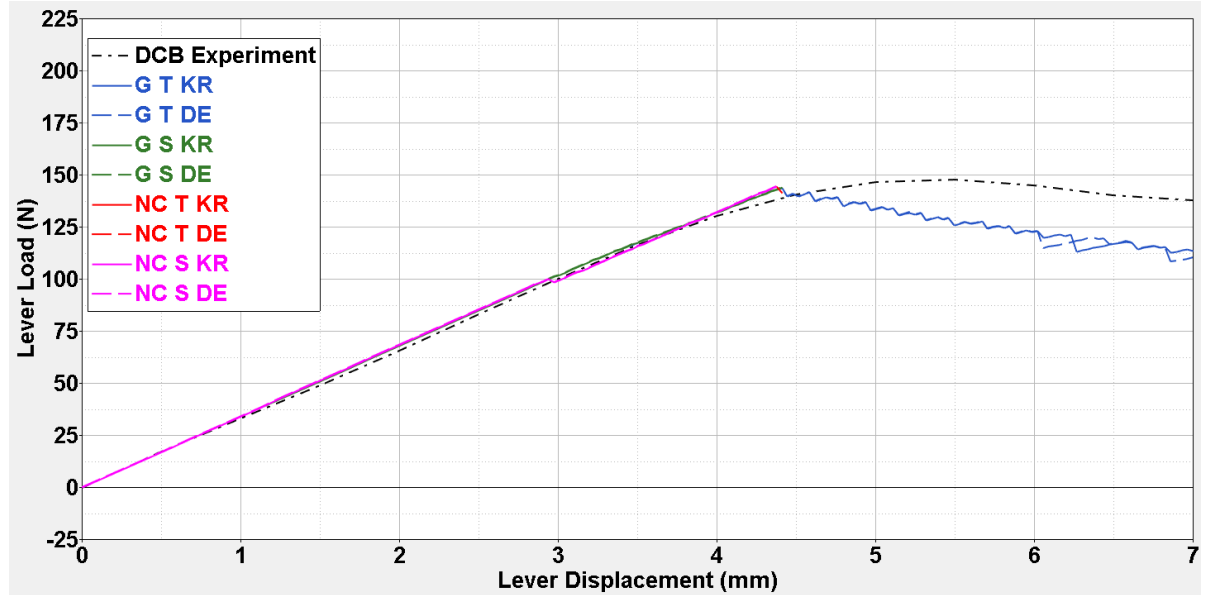
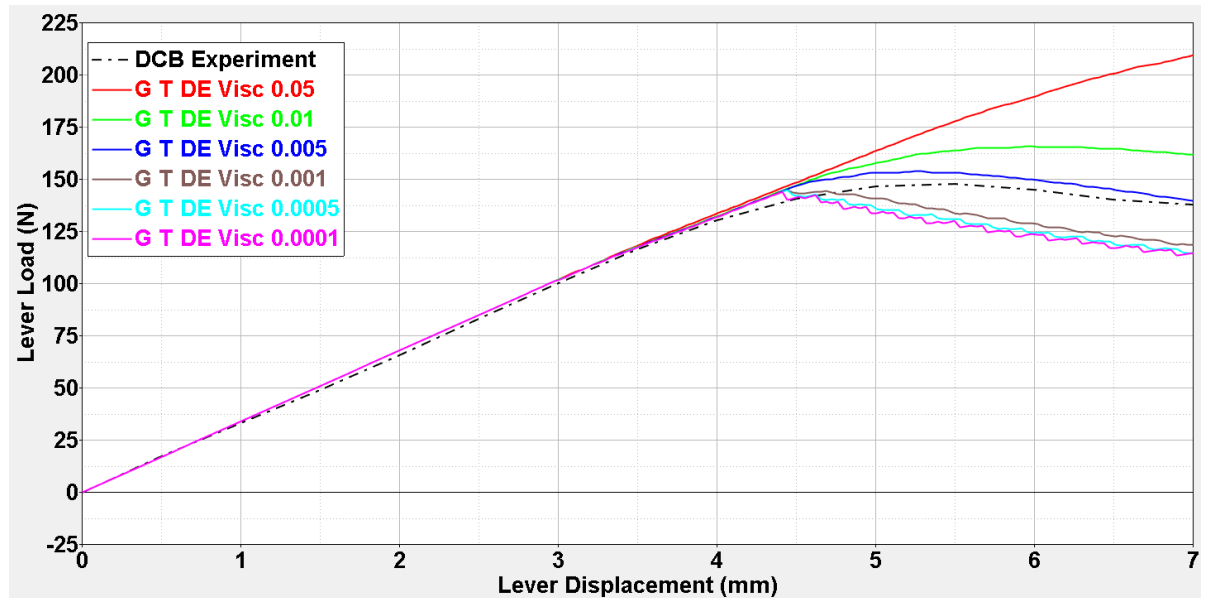


Figure A.6: Results of the 0% fracture mode setup for 3D simulations 1 through 8 with varying cohesive zone model settings.



(a) Load-Displacement graph of 3D simulations 1 through 8.



(b) Load-Displacement graph of 3D simulations 9 through 14: Viscosity factor results.

Figure A.7: Results of the 0% fracture mode setup for 3D simulations 1 through 14 with varying cohesive zone model settings.

Sim	Time Step Size [s]	$G_{c,I}$ [ $kJ/m^2$ ]	$G_{c,II}$ [ $kJ/m^2$ ]	$T_{m,I}$ [MPa]	$T_{m,II}$ [MPa]	Max. Load [N]	Exp. Load [N]	Error [%]	Comp. Time [s]
Turon	0.005	0.969	1.719	80	100	152.4	147.5	3.32	-
15	0.05	0.969	1.719	80	100	140.8	147.5	-4.54	96
16	0.01	0.969	1.719	80	100	143.9	147.5	-2.44	216
17	0.005	0.969	1.719	80	100	143.8	147.5	-2.51	248
18	0.001	0.969	1.719	80	100	144.0	147.5	-2.37	497
19	0.0005	0.969	1.719	80	100	144.1	147.5	-2.31	774
20	0.0001	0.969	1.719	80	100	144.1	147.5	-2.31	3132
21	0.001	0.500	1.719	80	100	111.1	147.5	-24.68	1932
22	0.001	1.000	1.719	80	100	145.8	147.5	-1.15	536
23	0.001	1.500	1.719	80	100	172.5	147.5	16.95	406
24	0.001	2.000	1.719	80	100	197.7	147.5	34.03	593
25	0.001	0.969	1.250	80	100	144	147.5	-2.37	604
26	0.001	0.969	1.750	80	100	144	147.5	-2.37	540
27	0.001	0.969	2.250	80	100	144	147.5	-2.37	528
28	0.001	0.969	2.750	80	100	144	147.5	-2.37	556
29	0.001	0.969	1.719	60	100	137.5	147.5	-6.78	498
30	0.001	0.969	1.719	80	100	144	147.5	-2.37	502
31	0.001	0.969	1.719	100	100	151.3	147.5	2.58	876
32	0.001	0.969	1.719	120	100	159.4	147.5	8.07	609
33	0.001	0.969	1.719	80	80	144	147.5	-2.37	533
34	0.001	0.969	1.719	80	100	144	147.5	-2.37	551
35	0.001	0.969	1.719	80	120	144	147.5	-2.37	575
36	0.001	0.969	1.719	80	140	144	147.5	-2.37	521

Table A.5: Results from the 0% fracture mode ratio for 3D simulations 15 through 36 with varying time step sizes,  $G_{c,I}$ ,  $G_{c,II}$ ,  $T_{m,I}$  and  $T_{m,II}$ .

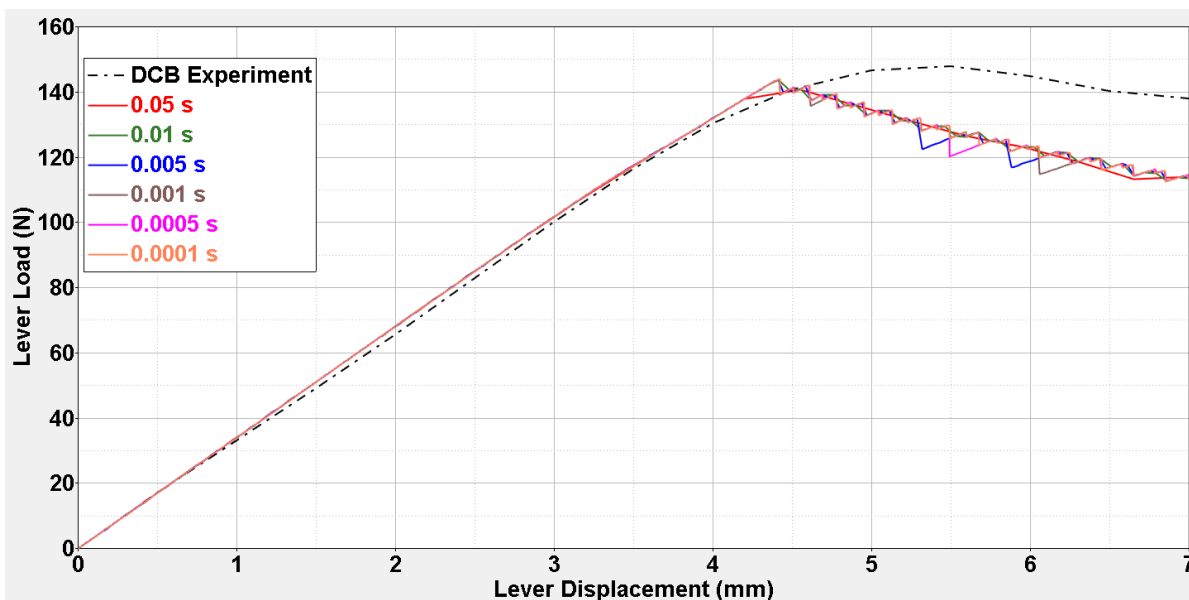
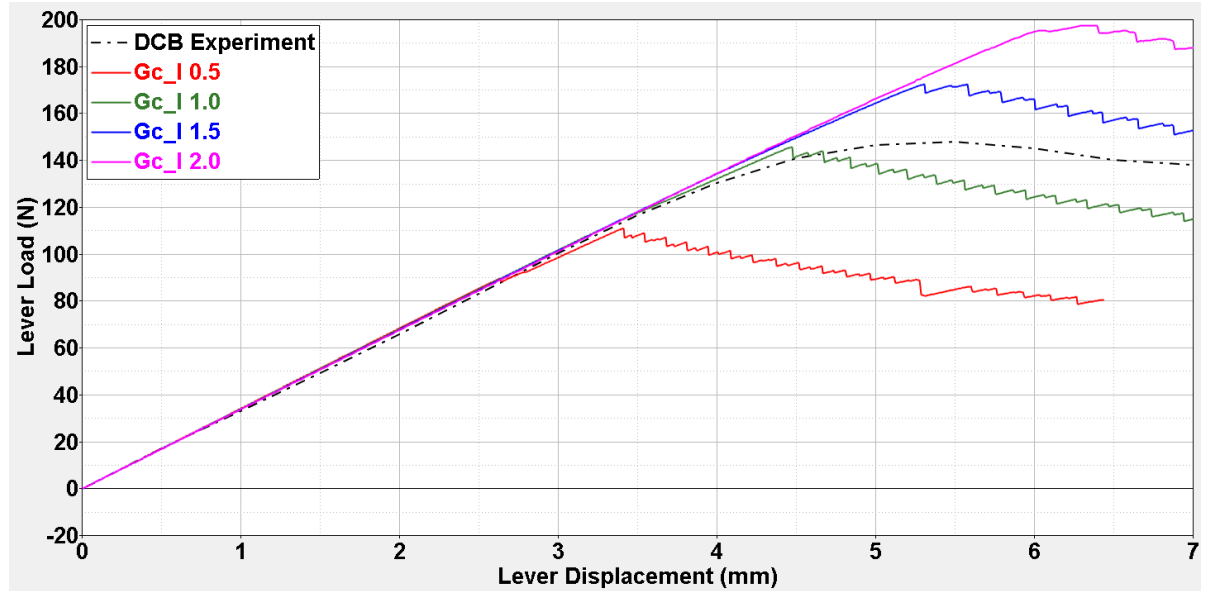
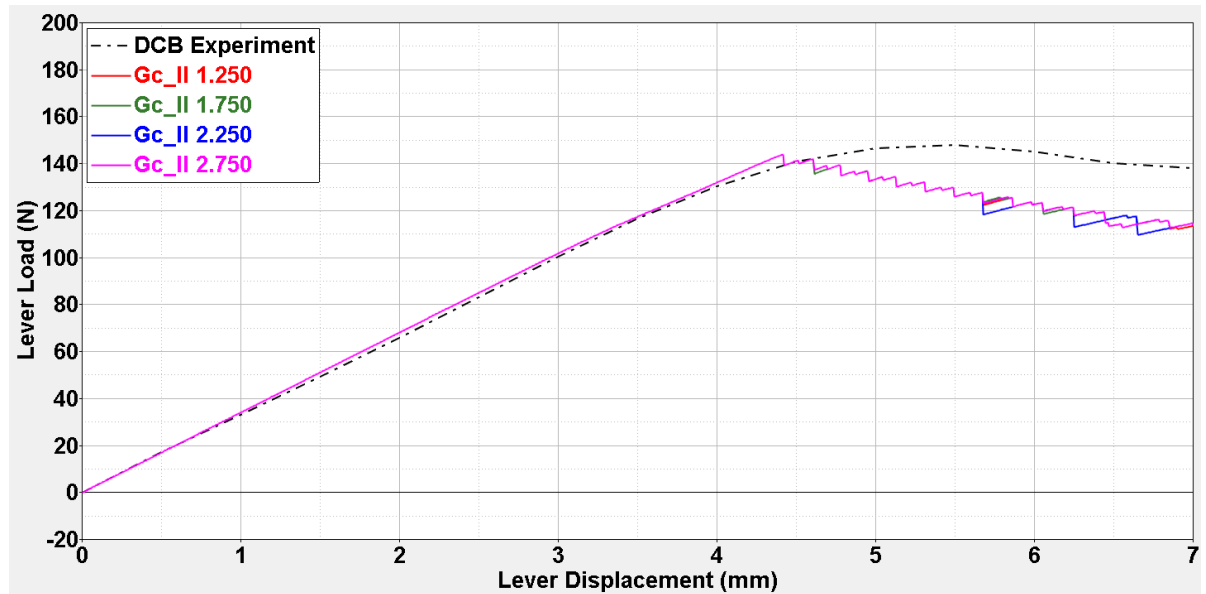


Figure A.8: Results from the 0% fracture mode for 3D simulations 15 through 20 with varying time step sizes.

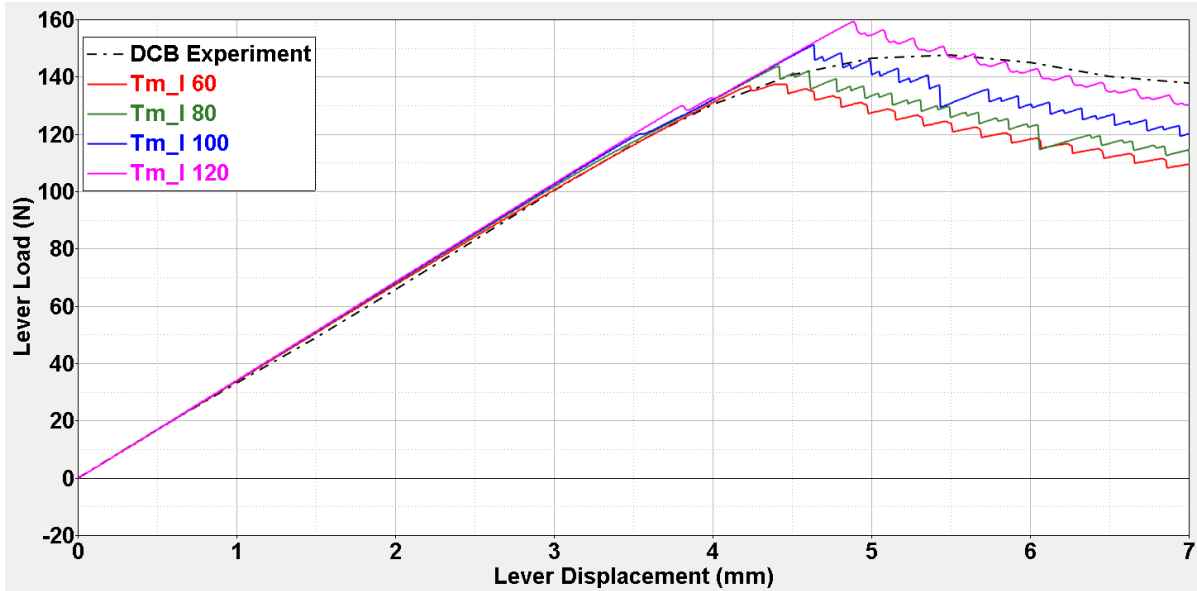


(a) Load-Displacement graph of 3D simulations 21 through 24.

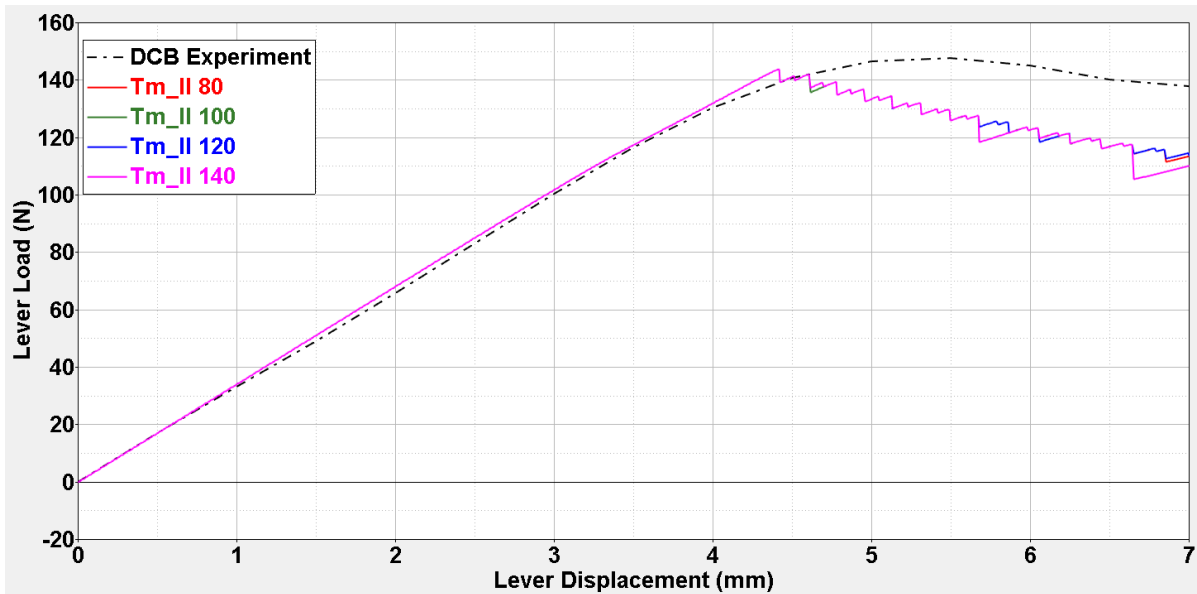


(b) Load-Displacement graph of 3D simulations 25 through 28.

Figure A.9: Results of the 0% fracture mode setup for 3D simulations 21 through 28 with varying  $G_{c,I}$  and  $G_{c,II}$ .



(a) Load-Displacement graph of 3D simulations 29 through 32.



(b) Load-Displacement graph of 3D simulations 33 through 36.

Figure A.10: Results of the 0% fracture mode setup for 3D simulations 29 through 36 with varying  $T_{m,I}$  and  $T_{m,II}$ .

Sim	Integ. Scheme	Stiffness Mtx. Method	CZE De-act./Kept	Visc. Factor	Max. Load [N]	Exp. Load [N]	Error [%]	Comp. Time [s]
Turon	G	T	-	-	99.3	108.1	-8.14	-
1	G	S	K	-	101.5	108.1	-6.11	336
2	G	S	D	-	101.5	108.1	-6.11	336
3	G	T	K	-	96.7	108.1	-10.55	343
4	G	T	D	-	96.7	108.1	-10.55	349
5	NC	S	K	-	119.4	108.1	10.45	72
6	NC	S	D	-	119.4	108.1	10.45	73
7	NC	T	K	-	116.3	108.1	7.59	84
8	NC	T	D	-	116.3	108.1	7.59	83
9	G	T	D	0.05	(N/A)	108.1	-	438
10	G	T	D	0.01	(N/A)	108.1	-	8
11	G	T	D	0.005	(N/A)	108.1	-	12
12	G	T	D	0.001	101.7	108.1	-5.92	40
13	G	T	D	0.0005	100.6	108.1	-6.94	63
14	G	T	D	0.0001	99.9	108.1	-7.59	123

Table A.6: Results from the 20% fracture mode ratio for 2D simulations 1 through 14 with varying cohesive zone model settings.

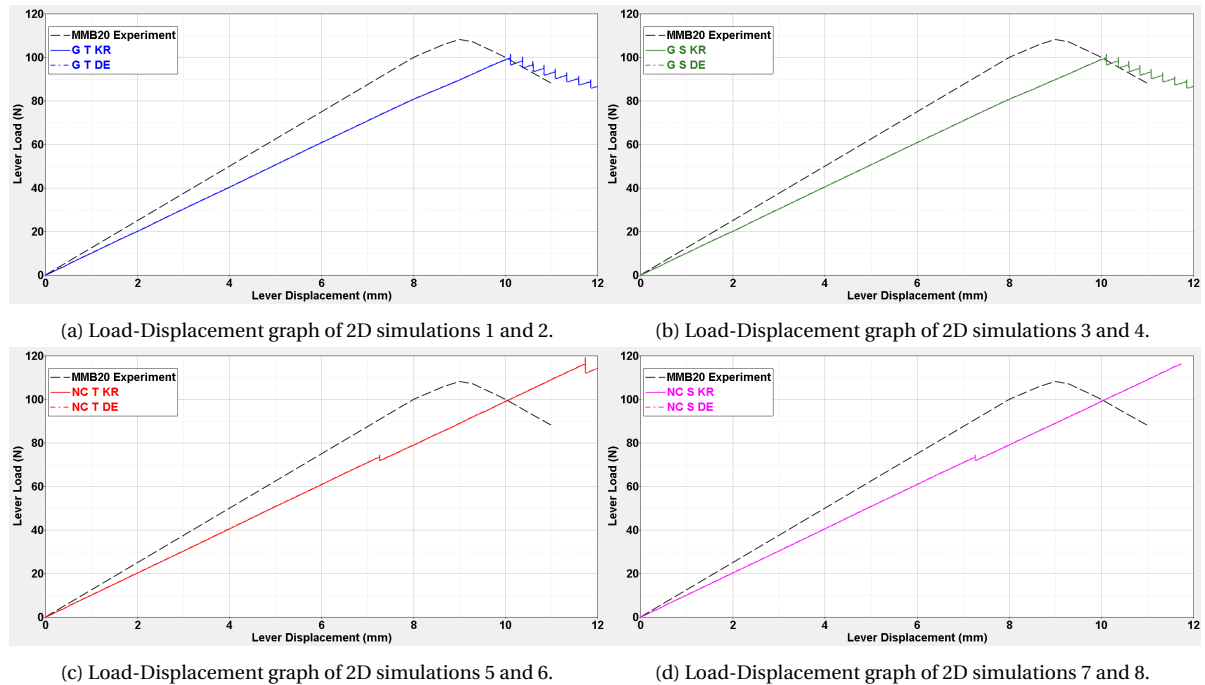
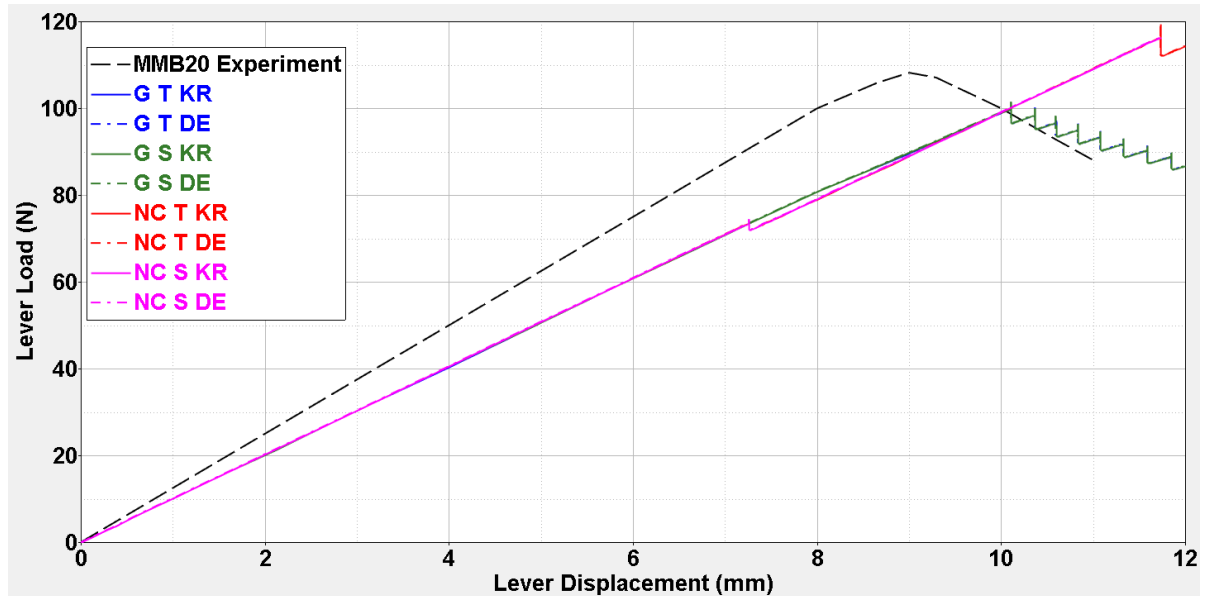
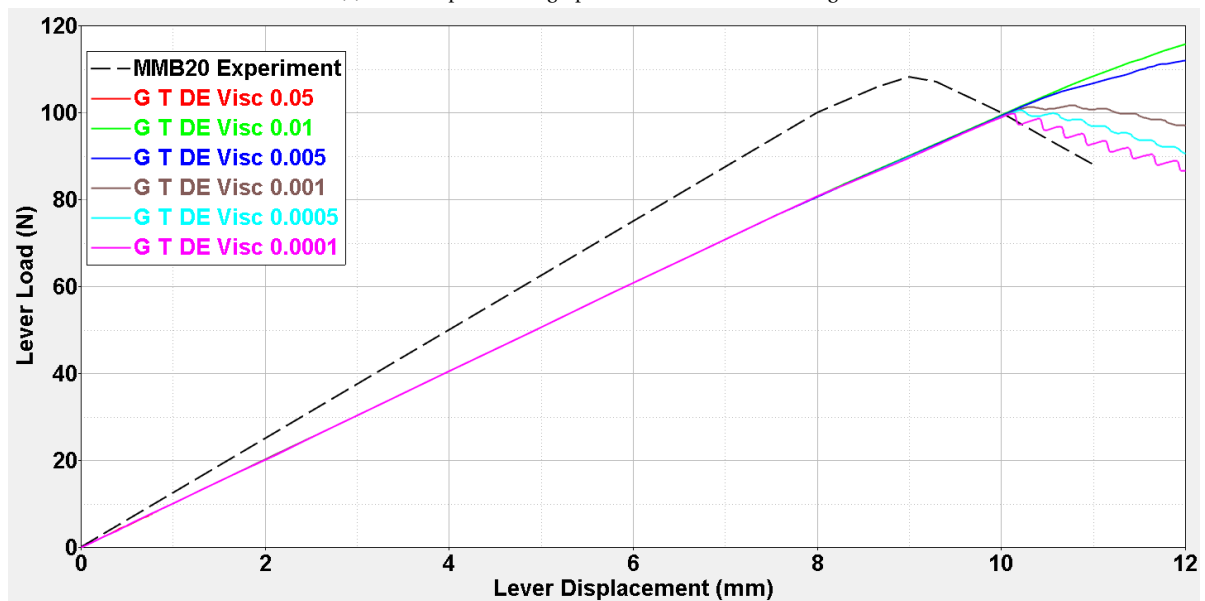


Figure A.11: Results of the 20% fracture mode setup for 2D simulations 1 through 8 with varying cohesive zone model settings.



(a) Load-Displacement graph of 2D simulations 1 through 8.



(b) Load-Displacement graph of 2D simulations 9 through 14: Viscosity factor results.

Figure A.12: Results of the 20% fracture mode setup for 2D simulations 1 through 14 with varying cohesive zone model settings.

Sim	Integ. Scheme	Stiffness Mtx. Method	CZE De-act./Kept	Visc. Factor	Max. Load [N]	Exp. Load [N]	Error [%]	Comp. Time [s]
Turon	G	T	-	-	99.3	108.1	-8.14	-
1	G	S	K	-	97.8	108.1	-9.53	465
2	G	S	D	-	97.8	108.1	-9.53	468
3	G	T	K	-	97.8	108.1	-9.53	370
4	G	T	D	-	97.8	108.1	-9.53	346
5	NC	S	K	-	98.4	108.1	-8.97	416
6	NC	S	D	-	99.2	108.1	-8.23	420
7	NC	T	K	-	94.1	108.1	-12.95	452
8	NC	T	D	-	94.1	108.1	-12.95	451
9	G	T	D	0.05	118	108.1	9.25	129
10	G	T	D	0.01	113.9	108.1	5.37	132
11	G	T	D	0.005	109.9	108.1	1.67	137
12	G	T	D	0.001	99.7	108.1	-7.77	176
13	G	T	D	0.0005	98.3	108.1	-9.07	195
14	G	T	D	0.0001	97.8	108.1	-9.53	236

Table A.7: Results from the 20% fracture mode ratio for 3D simulations 1 through 14 with varying cohesive zone model settings.

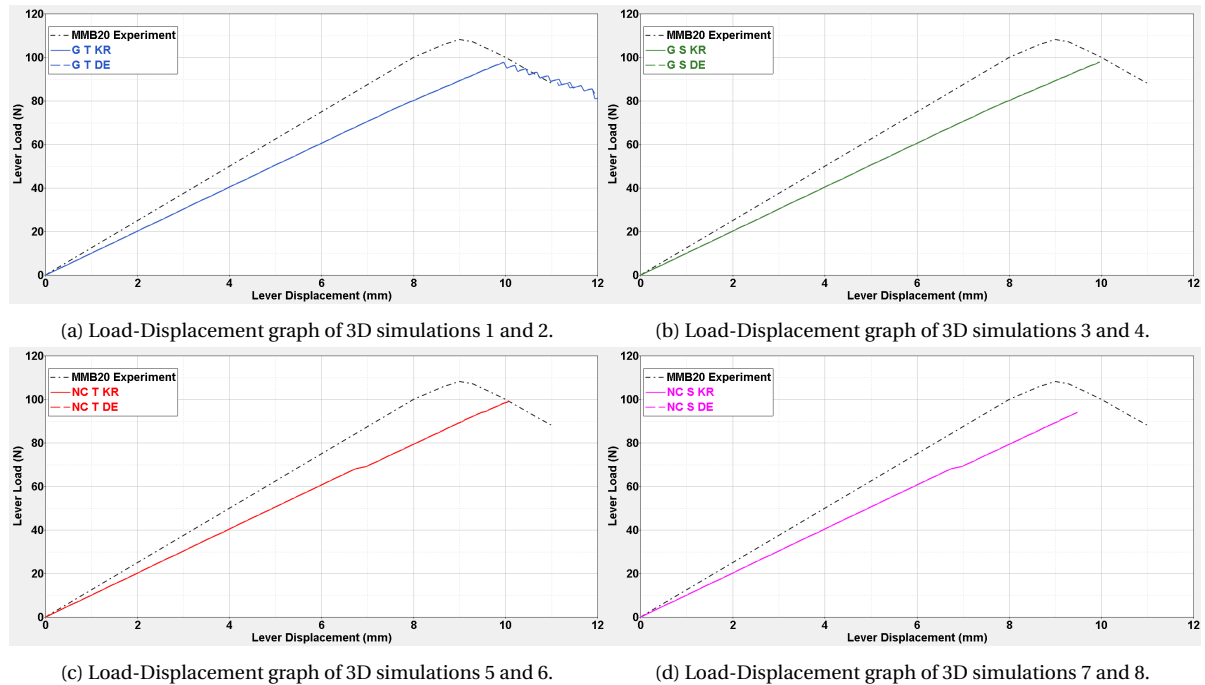
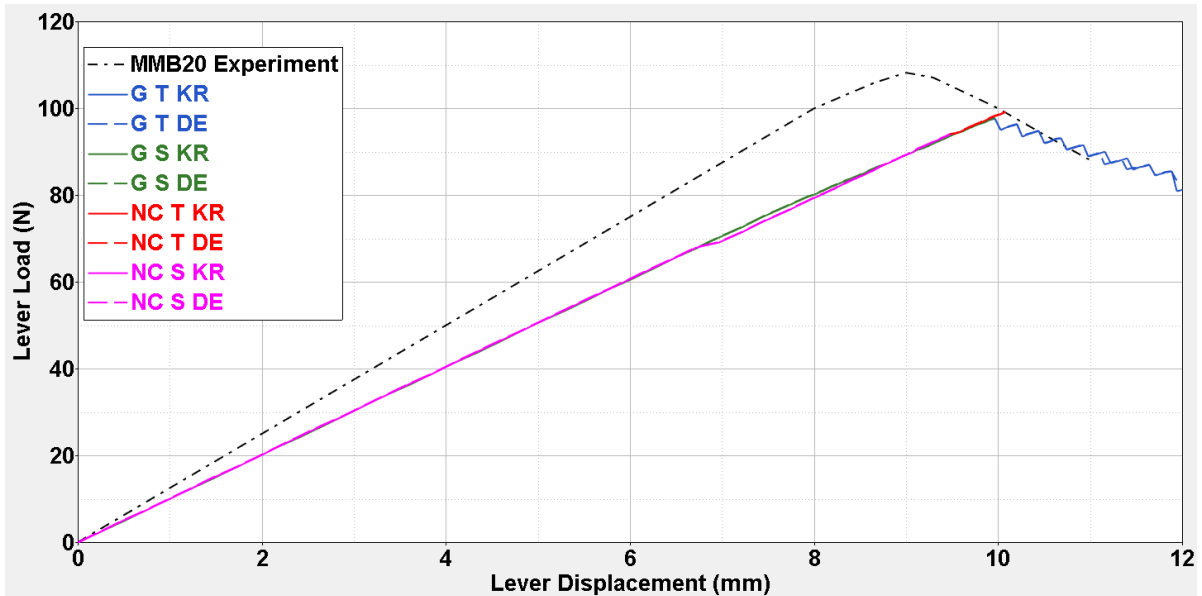
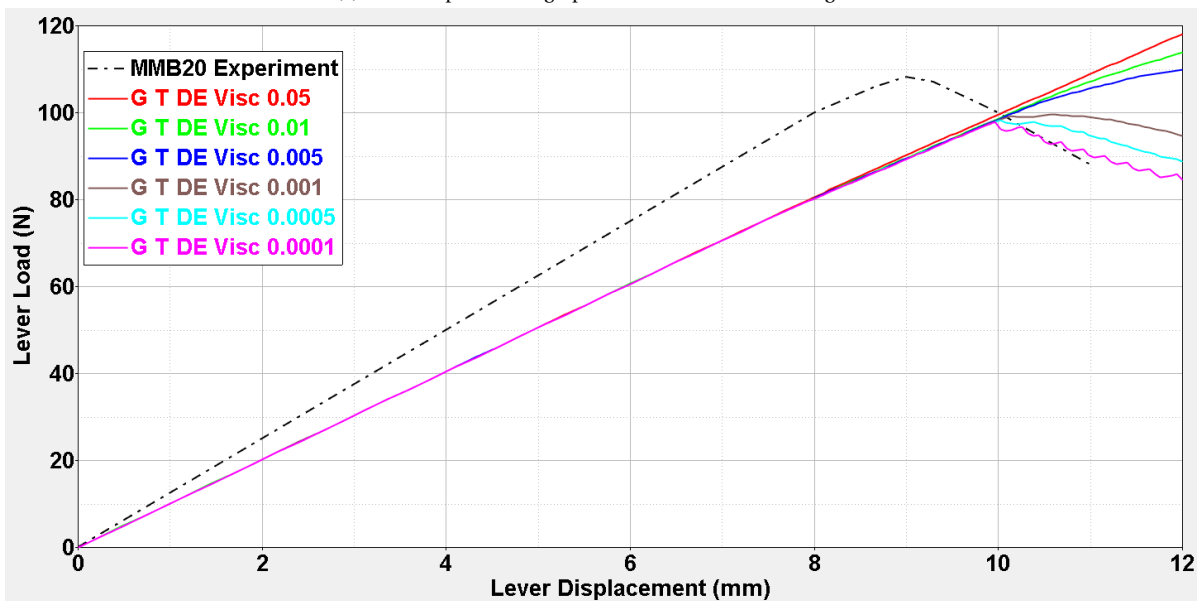


Figure A.13: Results of the 20% fracture mode setup for 3D simulations 1 through 8 with varying cohesive zone model settings.



(a) Load-Displacement graph of 3D simulations 1 through 8.



(b) Load-Displacement graph of 3D simulations 9 through 14: Viscosity factor results.

Figure A.14: Results of the 20% fracture mode setup for 3D simulations 1 through 14 with varying cohesive zone model settings.

Sim	Time Step Size [s]	$G_{c,I}$ [ $kJ/m^2$ ]	$G_{c,II}$ [ $kJ/m^2$ ]	$T_{m,I}$ [MPa]	$T_{m,II}$ [MPa]	Max. Load [N]	Exp. Load [N]	Error [%]	Comp. Time [s]
Turon	0.005	0.969	1.719	80	100	99.3	108.1	-8.14	-
15	0.05	0.969	1.719	80	100	96.4	108.1	-10.82	378
16	0.01	0.969	1.719	80	100	97.8	108.1	-9.53	215
17	0.005	0.969	1.719	80	100	97.8	108.1	-9.53	306
18	0.001	0.969	1.719	80	100	97.9	108.1	-9.44	591
19	0.0005	0.969	1.719	80	100	97.9	108.1	-9.44	904
20	0.0001	0.969	1.719	80	100	97.9	108.1	-9.44	3487

Table A.8: Results from the 20% fracture mode ratio for 3D simulations 15 through 20 with varying time step sizes.

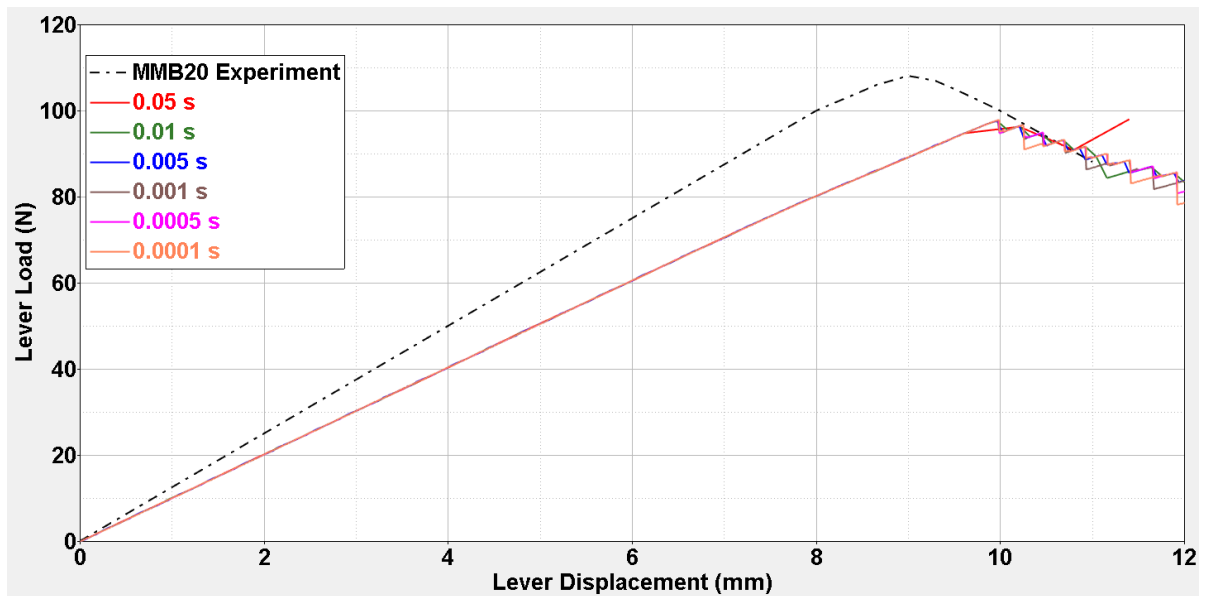


Figure A.15: Results from the 20% fracture mode for 3D simulations 15 through 20 with varying time step sizes.

Sim	Integ. Scheme	Stiffness Mtx. Method	CZE De-act./Kept	Visc. Factor	Max. Load [N]	Exp. Load [N]	Error [%]	Comp. Time [s]
Turon	G	T	-	-	263.9	275.3	-4.2	-
1	G	S	K	-	277.9	275.3	0.94	354
2	G	S	D	-	277.9	275.3	0.94	362
3	G	T	K	-	277.9	275.3	0.94	371
4	G	T	D	-	277.9	275.3	0.94	372
5	NC	S	K	-	295.4	275.3	7.30	524
6	NC	S	D	-	295.4	275.3	7.30	520
7	NC	T	K	-	295.5	275.3	7.34	338
8	NC	T	D	-	295.5	275.3	7.34	335
9	G	T	D	0.05	344.5	275.3	25.14	8
10	G	T	D	0.01	334.5	275.3	21.50	11
11	G	T	D	0.005	325.7	275.3	18.31	15
12	G	T	D	0.001	290.6	275.3	5.56	42
13	G	T	D	0.0005	283.5	275.3	2.98	70
14	G	T	D	0.0001	278.8	275.3	1.27	179

Table A.9: Results from the 50% fracture mode ratio for 2D simulations 1 through 14 with varying cohesive zone model settings.

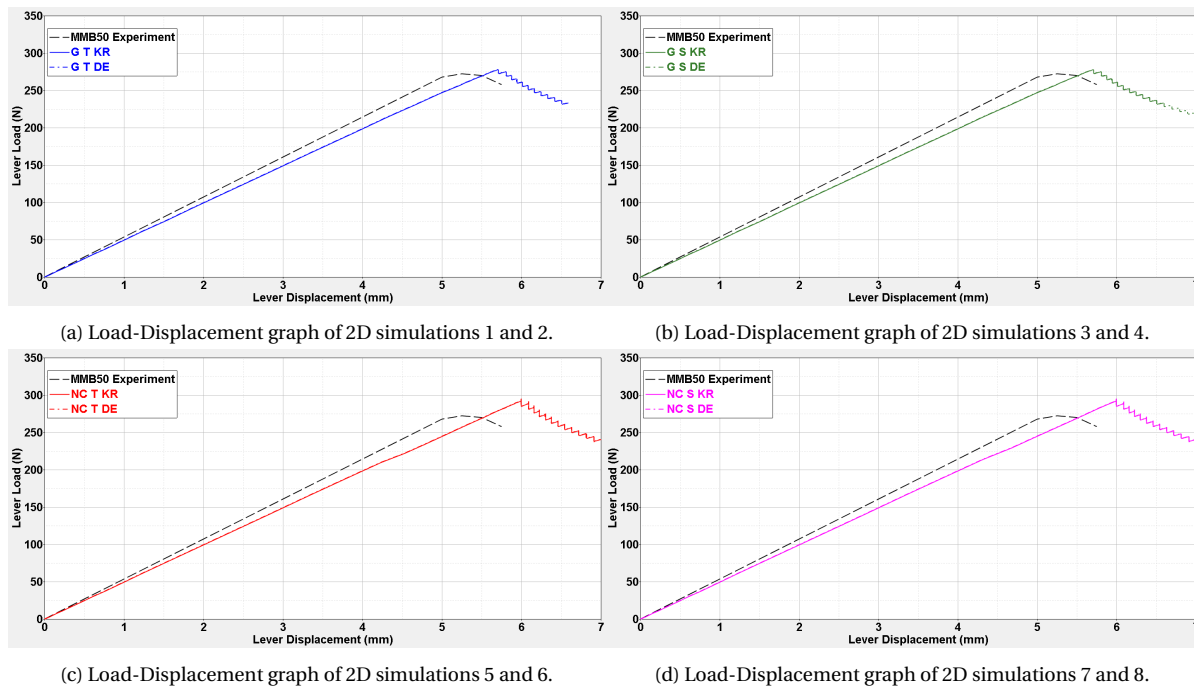
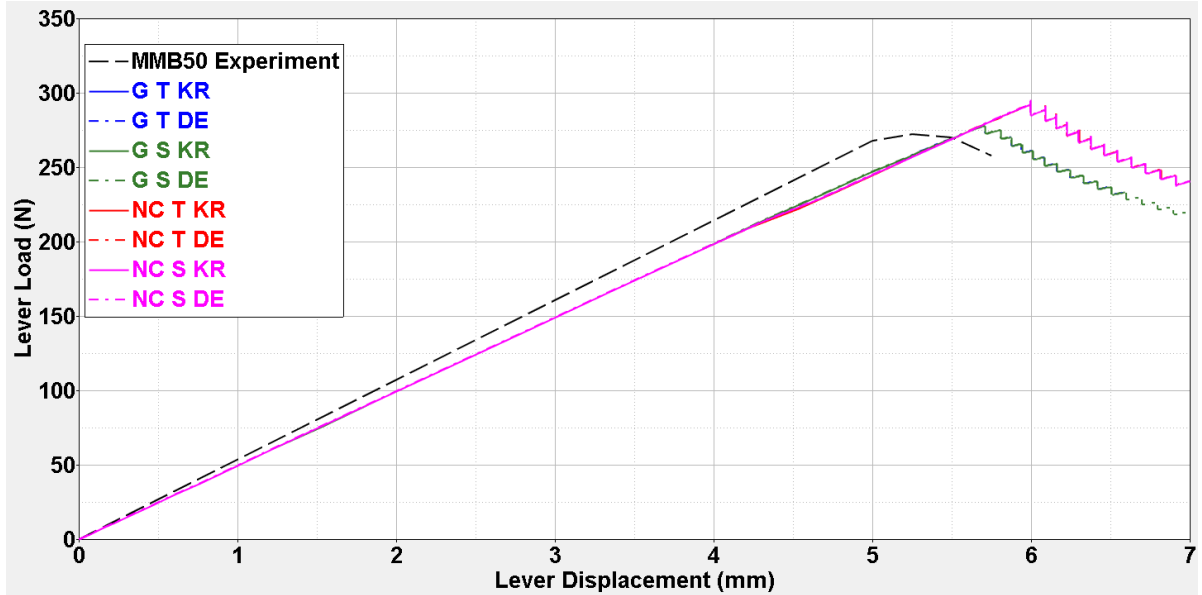
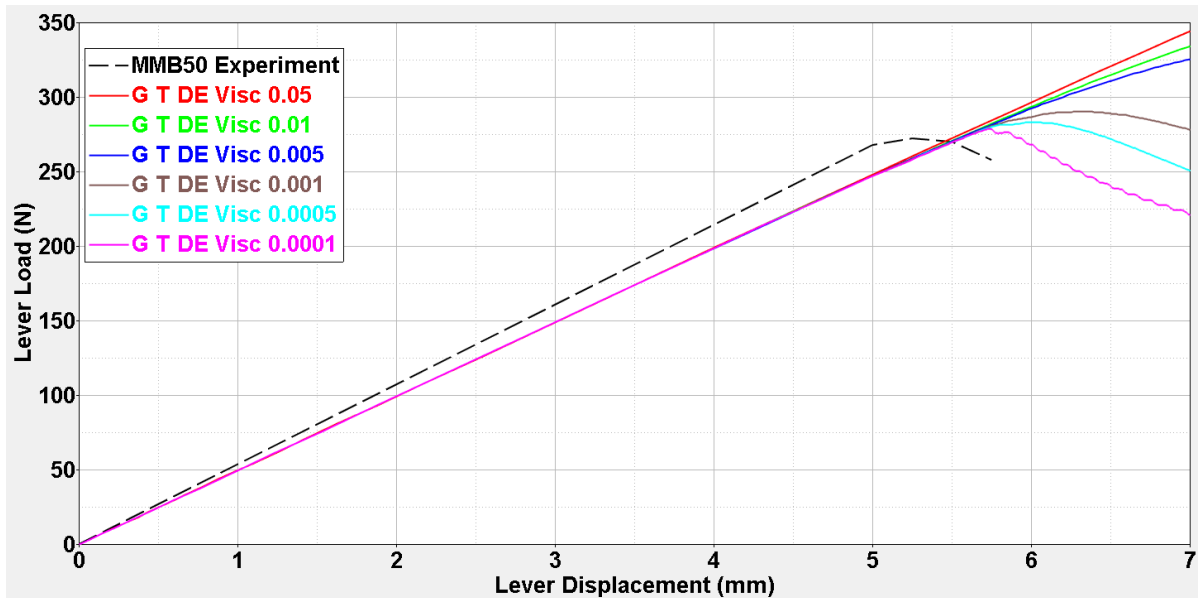


Figure A.16: Results of the 50% fracture mode setup for 2D simulations 1 through 8 with varying cohesive zone model settings.



(a) Load-Displacement graph of 2D simulations 1 through 8.



(b) Load-Displacement graph of 2D simulations 9 through 14: Viscosity factor results.

Figure A.17: Results of the 50% fracture mode setup for 2D simulations 1 through 14 with varying cohesive zone model settings.

Sim	Integ. Scheme	Stiffness Mtx. Method	CZE De-act./Kept	Visc. Factor	Max. Load [N]	Exp. Load [N]	Error [%]	Comp. Time [s]
Turon	G	T	-	-	263.9	275.3	-4.2	-
1	G	S	K	-	275.8	275.3	0.18	376
2	G	S	D	-	275.8	275.3	0.18	375
3	G	T	K	-	276.2	275.3	0.33	209
4	G	T	D	-	276.2	275.3	0.33	213
5	NC	S	K	-	293.4	275.3	6.57	373
6	NC	S	D	-	293.4	275.3	6.57	373
7	NC	T	K	-	281.3	275.3	2.18	420
8	NC	T	D	-	281.3	275.3	2.18	419
9	G	T	D	0.05	284.9	275.3	3.49	113
10	G	T	D	0.01	327.7	275.3	19.03	111
11	G	T	D	0.005	315.9	275.3	14.75	125
12	G	T	D	0.001	287.3	275.3	4.36	134
13	G	T	D	0.0005	281	275.3	2.07	143
14	G	T	D	0.0001	276	275.3	0.25	203

Table A.10: Results from the 50% fracture mode ratio for 3D simulations 1 through 14 with varying cohesive zone model settings.

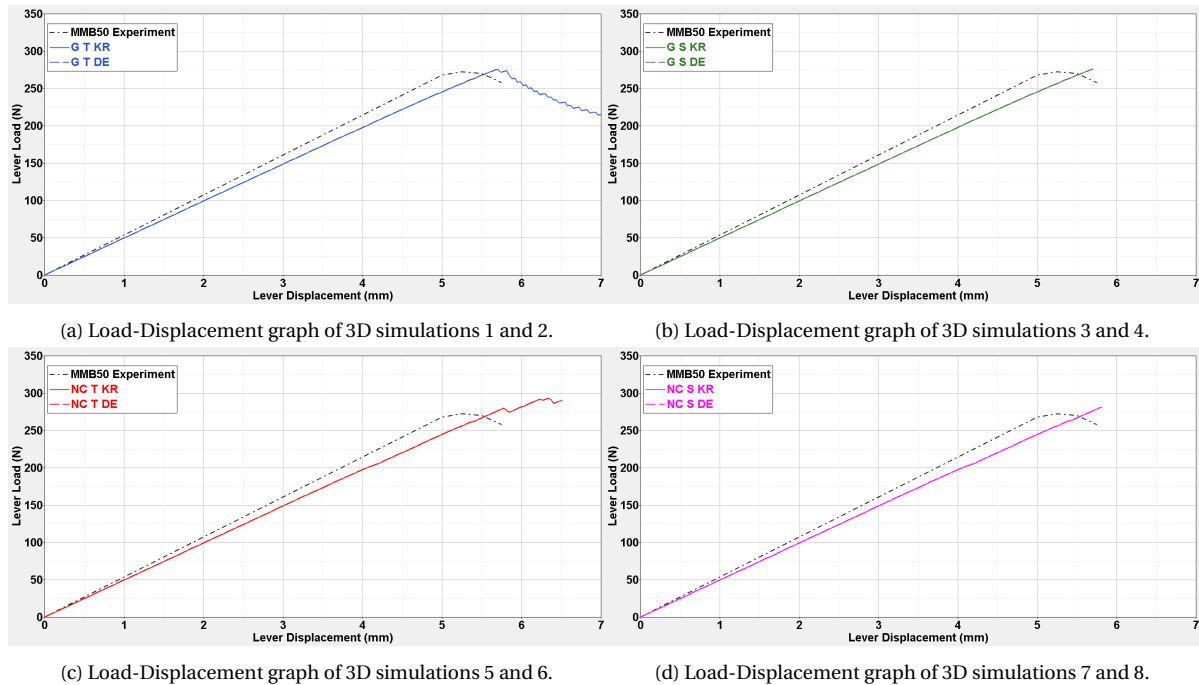
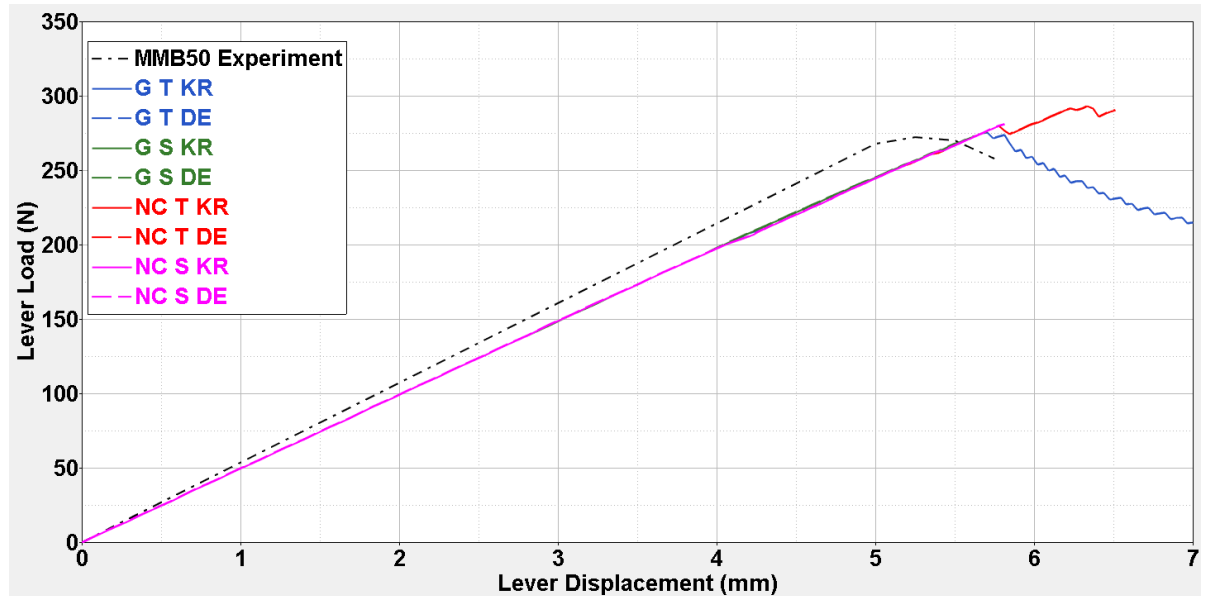
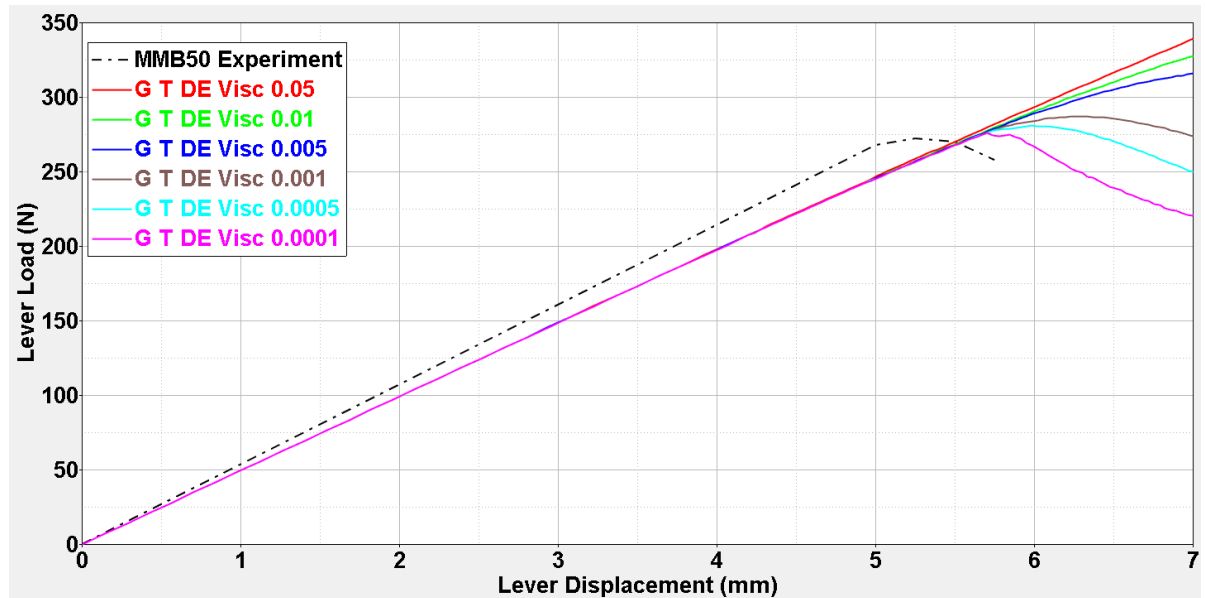


Figure A.18: Results of the 50% fracture mode setup for 3D simulations 1 through 8 with varying cohesive zone model settings.



(a) Load-Displacement graph of 3D simulations 1 through 8.



(b) Load-Displacement graph of 3D simulations 9 through 14: Viscosity factor results.

Figure A.19: Results of the 50% fracture mode setup for 3D simulations 1 through 14 with varying cohesive zone model settings.

Sim	Time Step Size [s]	$G_{c,I}$ [ $kJ/m^2$ ]	$G_{c,II}$ [ $kJ/m^2$ ]	$T_{m,I}$ [MPa]	$T_{m,II}$ [MPa]	Max. Load [N]	Exp. Load [N]	Error [%]	Comp. Time [s]
Turon	0.005	0.969	1.719	80	100	263.9	275.3	-4.2	-
15	0.05	0.969	1.719	80	100	271.8	275.3	-1.27	73
16	0.01	0.969	1.719	80	100	274.8	275.3	-0.18	146
17	0.005	0.969	1.719	80	100	275.8	275.3	0.18	192
18	0.001	0.969	1.719	80	100	276.7	275.3	0.51	441
19	0.0005	0.969	1.719	80	100	277.0	275.3	0.62	757
20	0.0001	0.969	1.719	80	100	276.1	275.3	0.29	3435

Table A.11: Results from the 50% fracture mode ratio for 3D simulations 15 through 20 with varying time step sizes.

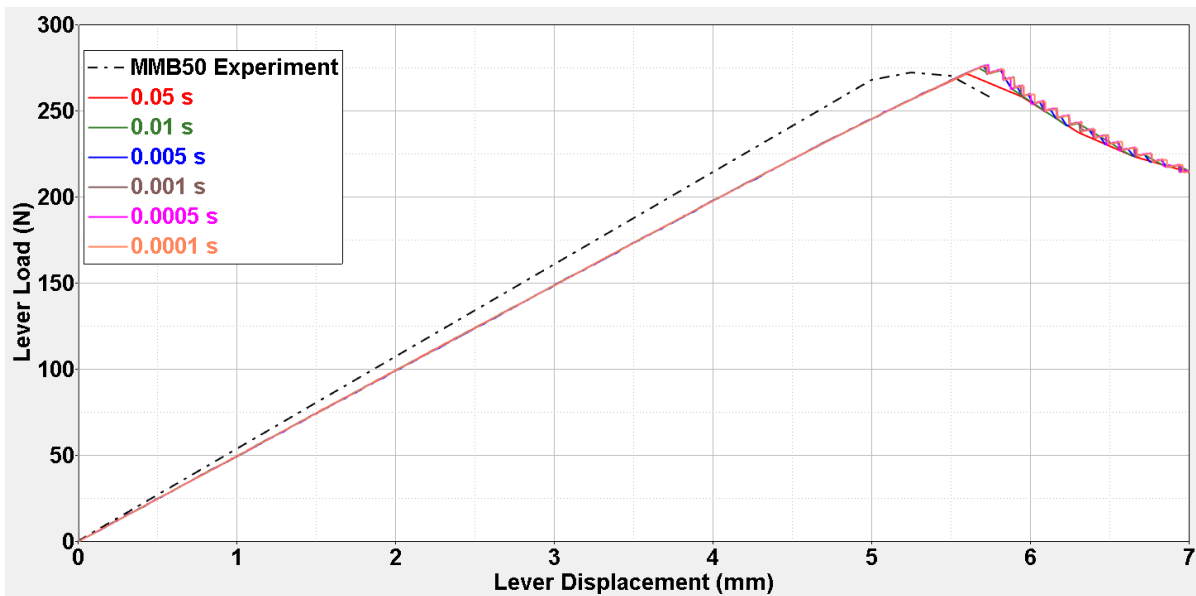


Figure A.20: Results from the 50% fracture mode for 3D simulations 15 through 20 with varying time step sizes.

Sim	Integ. Scheme	Stiffness Mtx. Method	CZE De-act./Kept	Visc. Factor	Max. Load [N]	Exp. Load [N]	Error [%]	Comp. Time [s]
Turon	G	T	-	-	496.9	518.7	-4.20	-
1	G	S	K	-	490.6	518.7	-5.42	347
2	G	S	D	-	490.6	518.7	-5.42	334
3	G	T	K	-	490.2	518.7	-5.49	274
4	G	T	D	-	490.2	518.7	-5.49	274
5	NC	S	K	-	489.4	518.7	-5.65	354
6	NC	S	D	-	489.4	518.7	-5.65	355
7	NC	T	K	-	489.3	518.7	-5.67	372
8	NC	T	D	-	489.3	518.7	-5.67	372
9	G	T	D	0.05	-	518.7	-	5
10	G	T	D	0.01	-	518.7	-	9
11	G	T	D	0.005	575.8	518.7	11.01	13
12	G	T	D	0.001	512.7	518.7	-1.16	35
13	G	T	D	0.0005	501.7	518.7	-3.28	61
14	G	T	D	0.0001	492.8	518.7	-4.99	151

Table A.12: Results from the 80% fracture mode ratio for 2D simulations 1 through 14 with varying cohesive zone model settings.

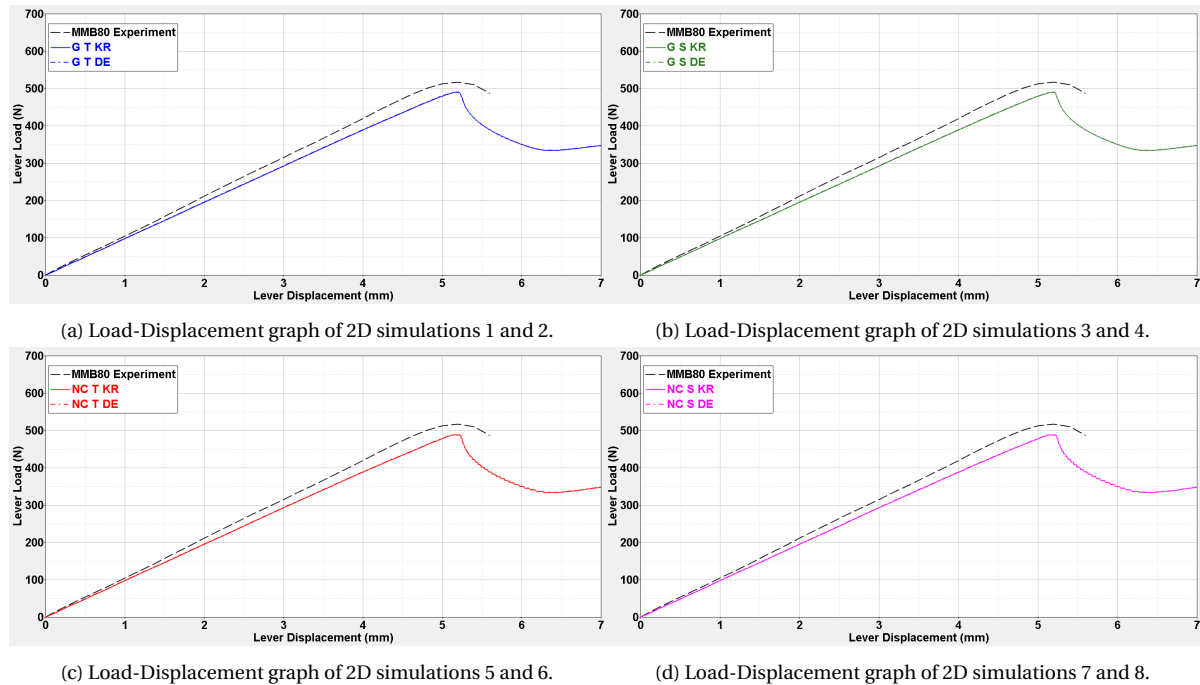
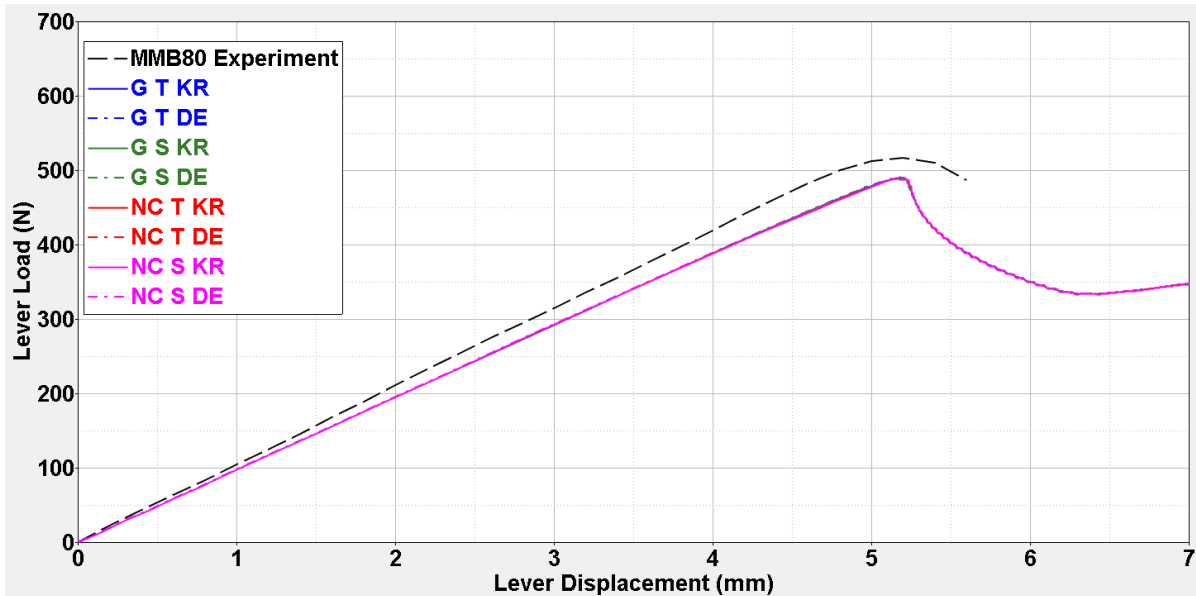
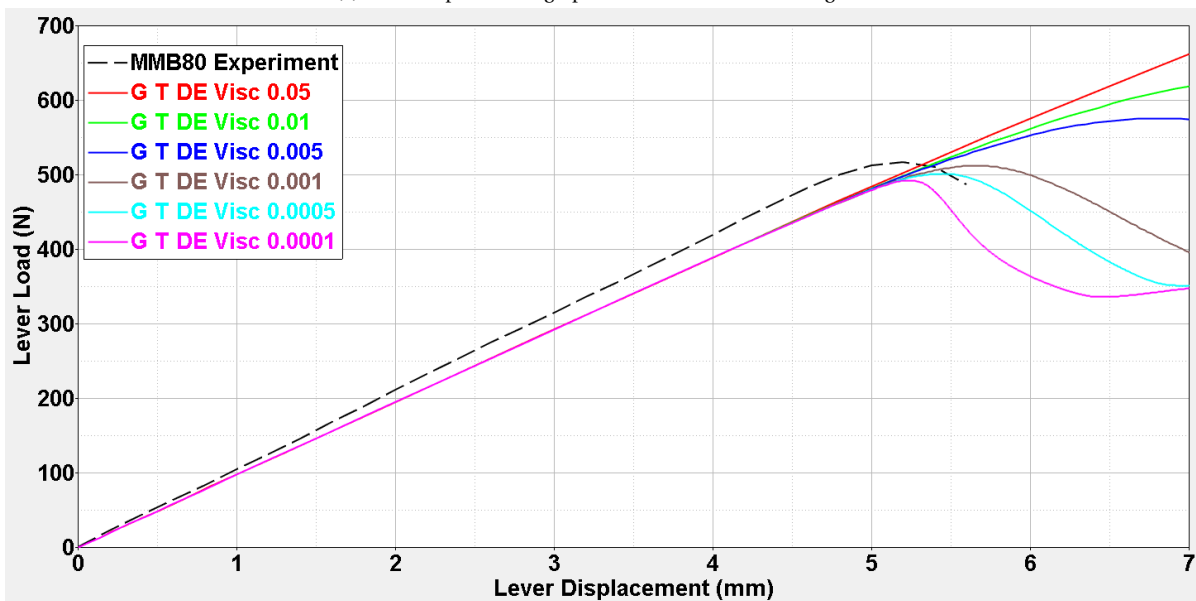


Figure A.21: Results of the 80% fracture mode setup for 2D simulations 1 through 8 with varying cohesive zone model settings.



(a) Load-Displacement graph of 2D simulations 1 through 8.



(b) Load-Displacement graph of 2D simulations 9 through 14: Viscosity factor results.

Figure A.22: Results of the 80% fracture mode setup for 2D simulations 1 through 14 with varying cohesive zone model settings.

Sim	Integ. Scheme	Stiffness Mtx. Method	CZE De-act./Kept	Visc. Factor	Max. Load [N]	Exp. Load [N]	Error [%]	Comp. Time [s]
Turon	G	T	-	-	496.9	518.7	-4.20	-
1	G	S	K	-	490.7	518.7	-5.40	1531
2	G	S	D	-	490.7	518.7	-5.40	1520
3	G	T	K	-	491.6	518.7	-5.22	243
4	G	T	D	-	491.6	518.7	-5.22	243
5	NC	S	K	-	485.7	518.7	6.36	357
6	NC	S	D	-	485.7	518.7	6.36	371
7	NC	T	K	-	470.8	518.7	9.23	466
8	NC	T	D	-	470.8	518.7	9.23	411
9	G	T	D	0.05	-	518.7	-	125
10	G	T	D	0.01	-	518.7	-	133
11	G	T	D	0.005	563.1	518.7	8.56	145
12	G	T	D	0.001	508.3	518.7	-2.01	172
13	G	T	D	0.0005	499	518.7	-3.80	179
14	G	T	D	0.0001	492.1	518.7	-5.13	202

Table A.13: Results from the 80% fracture mode ratio for 3D simulations 1 through 14 with varying cohesive zone model settings.

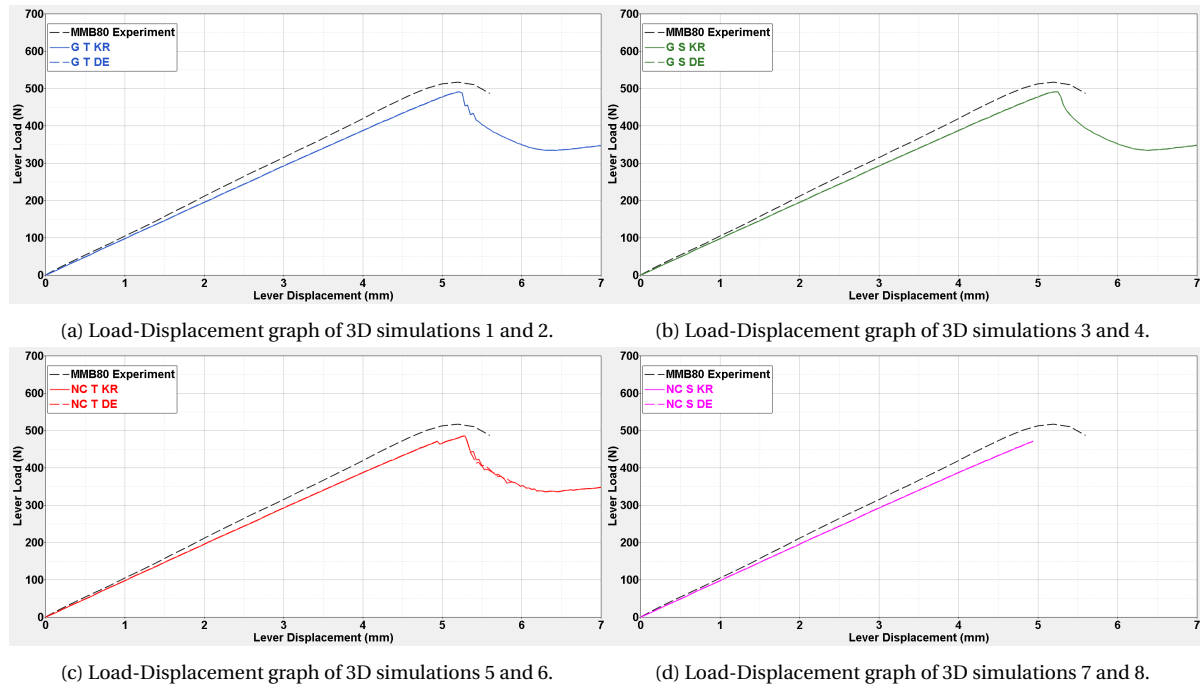
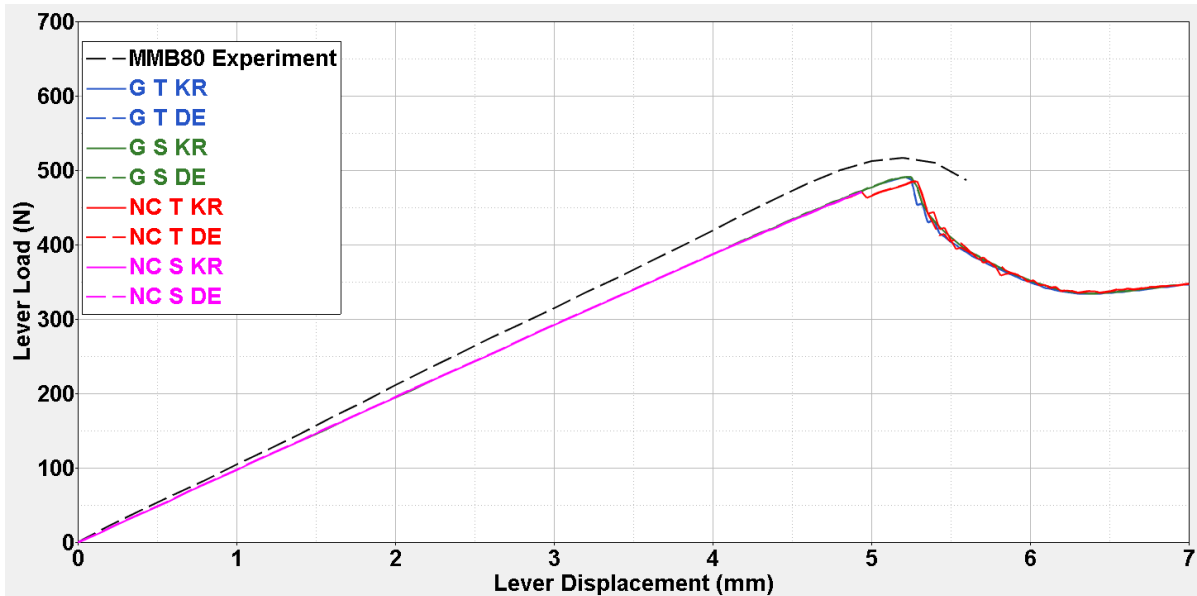
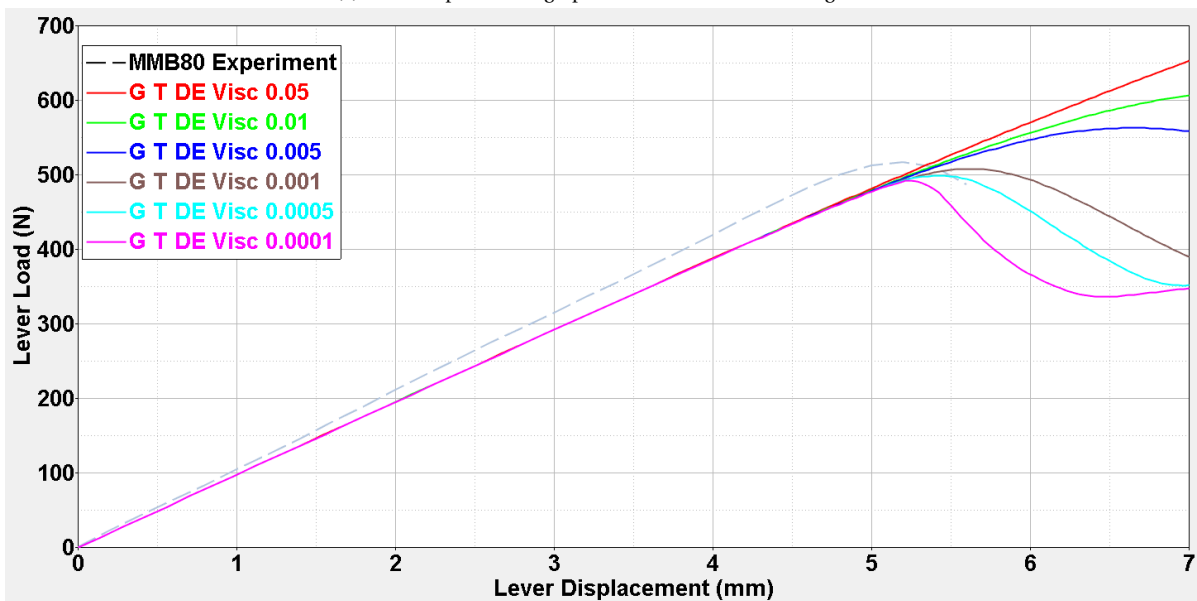


Figure A.23: Results of the 80% fracture mode setup for 3D simulations 1 through 8 with varying cohesive zone model settings.



(a) Load-Displacement graph of 3D simulations 1 through 8.



(b) Load-Displacement graph of 3D simulations 9 through 14: Viscosity factor results.

Figure A.24: Results of the 80% fracture mode setup for 3D simulations 1 through 14 with varying cohesive zone model settings.

Sim	Time Step Size [s]	$G_{c,I}$ [ $kJ/m^2$ ]	$G_{c,II}$ [ $kJ/m^2$ ]	$T_{m,I}$ [MPa]	$T_{m,II}$ [MPa]	Max. Load [N]	Exp. Load [N]	Error [%]	Comp. Time [s]
Turon	0.005	0.969	1.719	80	100	496.9	518.7	-4.20	-
15	0.05	0.969	1.719	80	100	479.8	518.7	-7.50	67
16	0.01	0.969	1.719	80	100	489.7	518.7	-5.59	149
17	0.005	0.969	1.719	80	100	490.7	518.7	-5.40	208
18	0.001	0.969	1.719	80	100	491.4	518.7	-5.26	484
19	0.0005	0.969	1.719	80	100	491.8	518.7	-5.19	788
20	0.0001	0.969	1.719	80	100	489.6	518.7	-5.61	3452

Table A.14: Results from the 80% fracture mode ratio for 3D simulations 15 through 20.

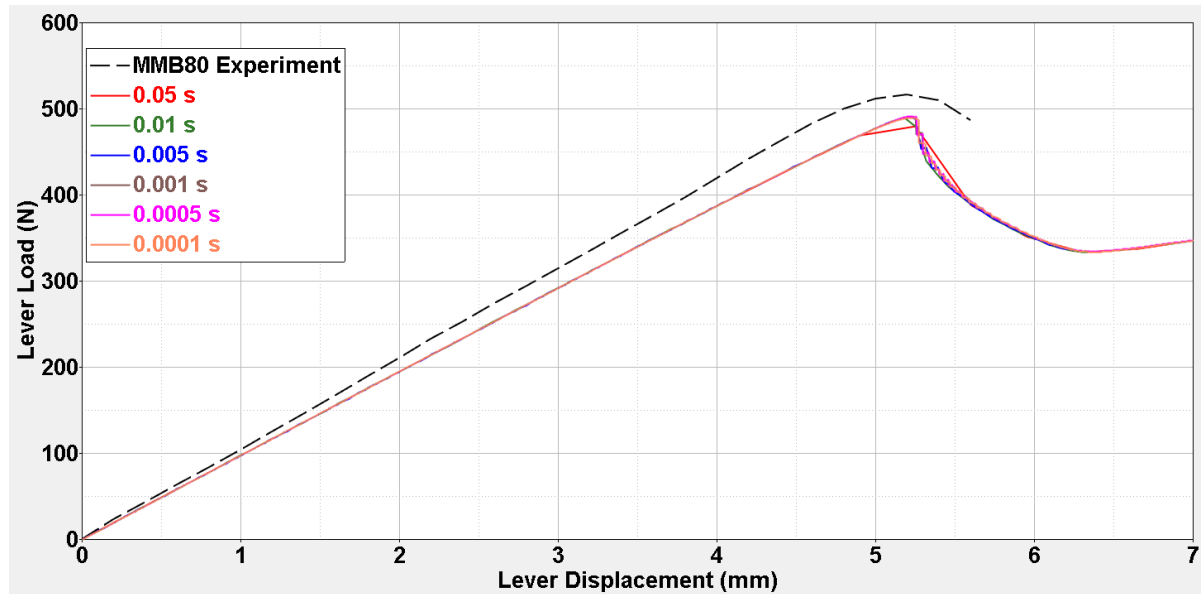


Figure A.25: Results from the 80% fracture mode for 3D simulations 15 through 20 with varying time step sizes.

Sim	Integ. Scheme	Stiffness Mt. Method	CZE De-act./Kept	Visc. Factor	Max. Load [N]	Exp. Load [N]	Error [%]	Comp. Time [s]
Turon	G	T	-	-	697.1	748.4	-6.9	-
1	G	S	K	-	710.6	748.4	-5.05	155
2	G	S	D	-	710.6	748.4	-5.05	150
3	G	T	K	-	710.6	748.4	-5.05	17
4	G	T	D	-	710.6	748.4	-5.05	19
5	NC	S	K	-	709.2	748.4	-5.24	153
6	NC	S	D	-	709.2	748.4	-5.24	157
7	NC	T	K	-	709.7	748.4	-5.17	19
8	NC	T	D	-	709.7	748.4	-5.17	21
9	G	T	D	0.05	-	748.4	-	16
10	G	T	D	0.01	829.6	748.4	10.85	16
11	G	T	D	0.005	773.1	748.4	3.30	15
12	G	T	D	0.001	721	748.4	-3.66	19
13	G	T	D	0.0005	715.9	748.4	-4.34	20
14	G	T	D	0.0001	711.5	748.4	-4.93	21

Table A.15: Results from the 100% fracture mode ratio for 2D simulations 1 through 14 with varying cohesive zone model settings.

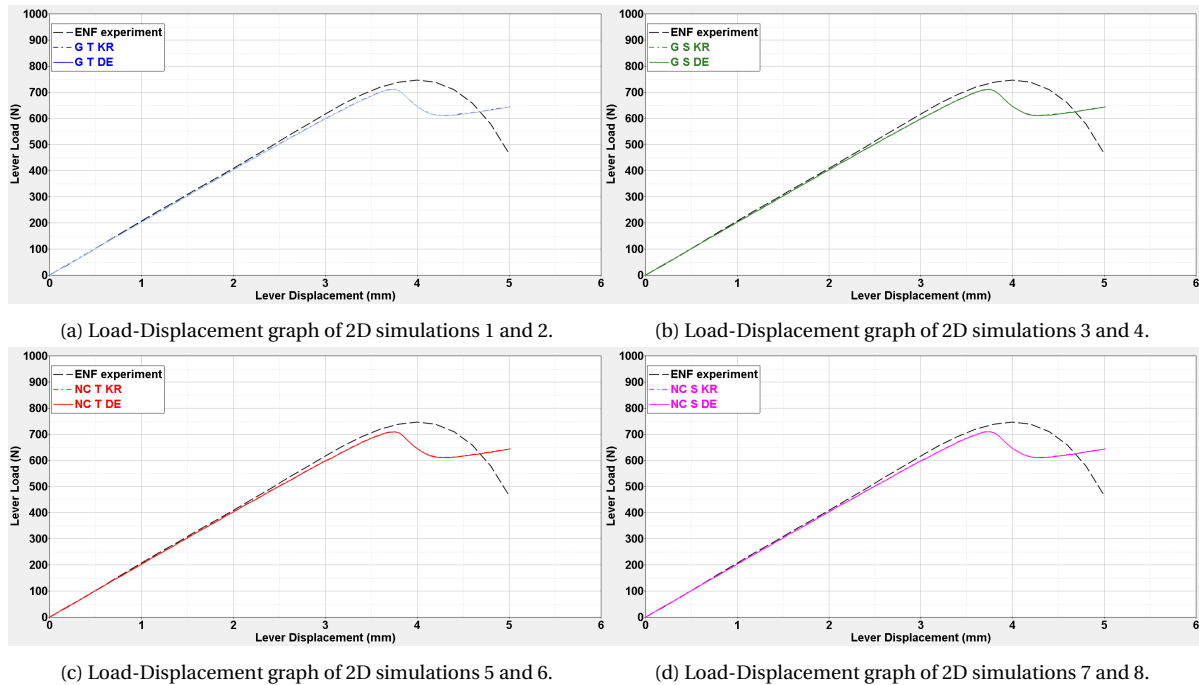
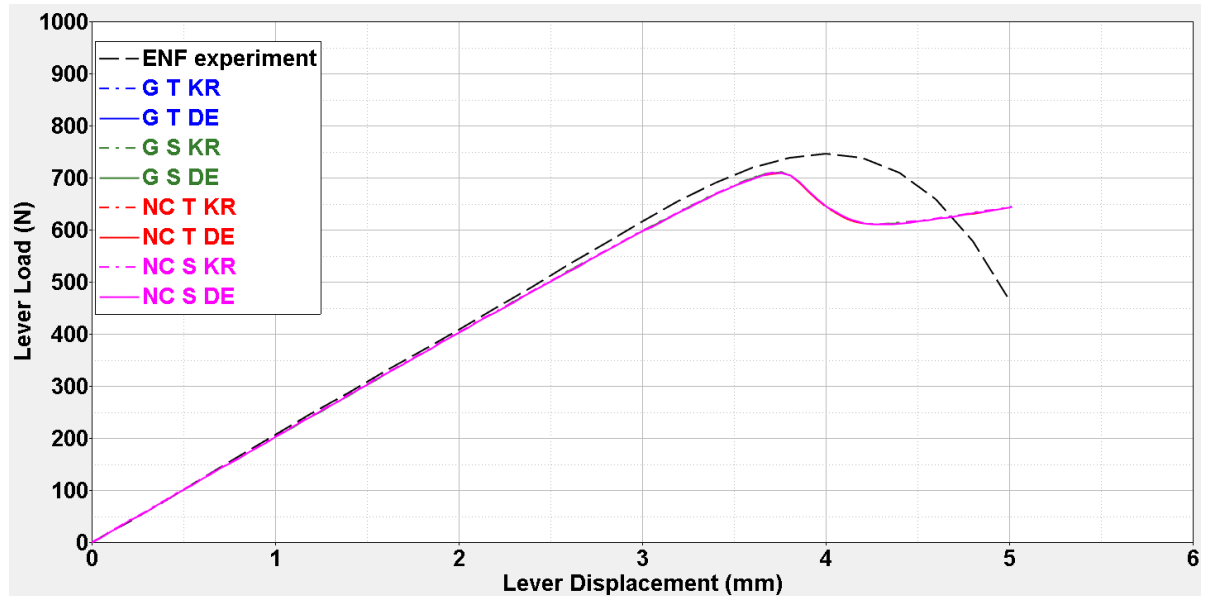
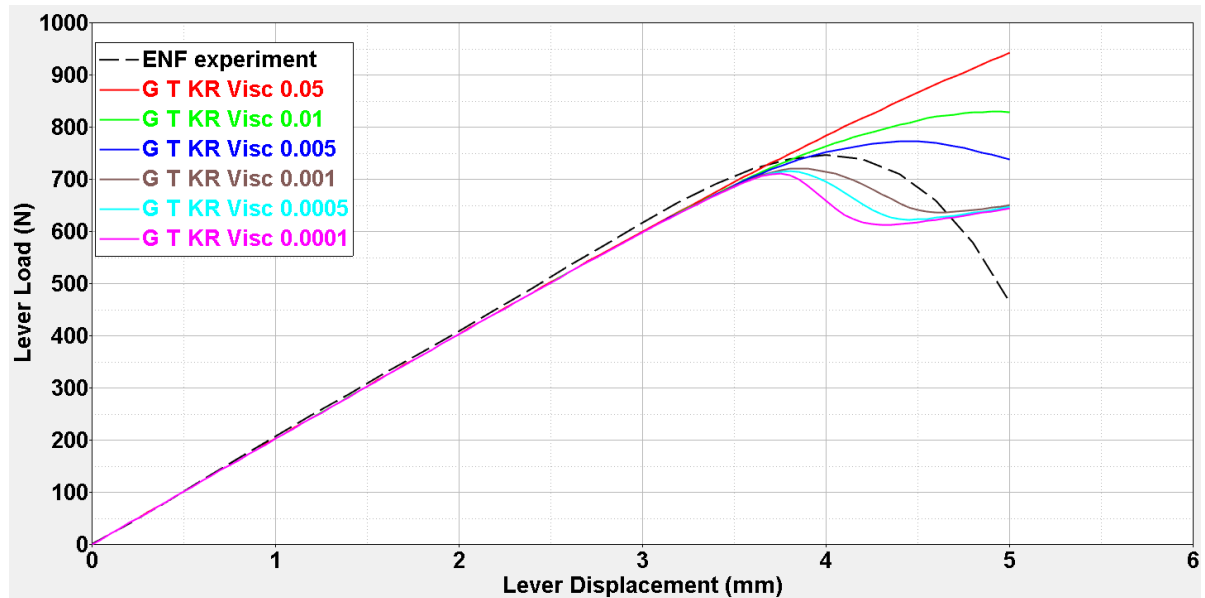


Figure A.26: Results of the 100% fracture mode setup for 2D simulations 1 through 8 with varying cohesive zone model settings.



(a) Load-Displacement graph of 2D simulations 1 through 8.



(b) Load-Displacement graph of 2D simulations 9 through 14: Viscosity factor results.

Figure A.27: Results of the 100% fracture mode setup for 2D simulations 1 through 14 with varying cohesive zone model settings.

Sim	Integ. Scheme	Stiffness Mtx. Method	CZE De-act./Kept	Visc. Factor	Max. Load [N]	Exp. Load [N]	Error [%]	Comp. Time [s]
Turon	G	T	-	-	697.1	748.4	-6.9	-
1	G	S	K	-	713.3	748.4	-4.69	478
2	G	S	D	-	713.3	748.4	-4.69	477
3	G	T	K	-	714.6	748.4	-4.52	341
4	G	T	D	-	714.6	748.4	-4.52	297
5	NC	S	K	-	699.5	748.4	-6.53	558
6	NC	S	D	-	699.5	748.4	-6.53	565
7	NC	T	K	-	700	748.4	-6.47	292
8	NC	T	D	-	700	748.4	-6.47	296
9	G	T	D	0.05	851.4	748.4	13.76	278
10	G	T	D	0.01	741.4	748.4	-0.94	345
11	G	T	D	0.005	726.3	748.4	-2.95	345
12	G	T	D	0.001	716.2	748.4	-4.30	258
13	G	T	D	0.0005	714.9	748.4	-4.48	260
14	G	T	D	0.0001	714	748.4	-4.60	269

Table A.16: Results from the 100% fracture mode ratio for 3D simulations 1 through 14 with varying cohesive zone model settings.

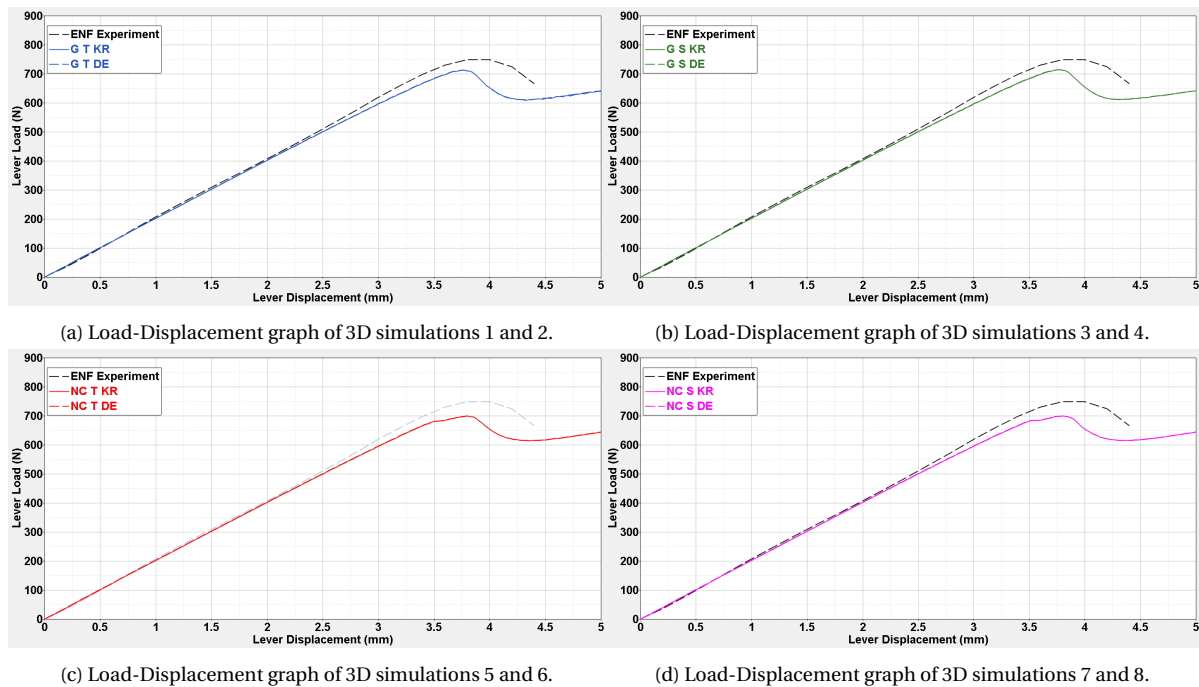
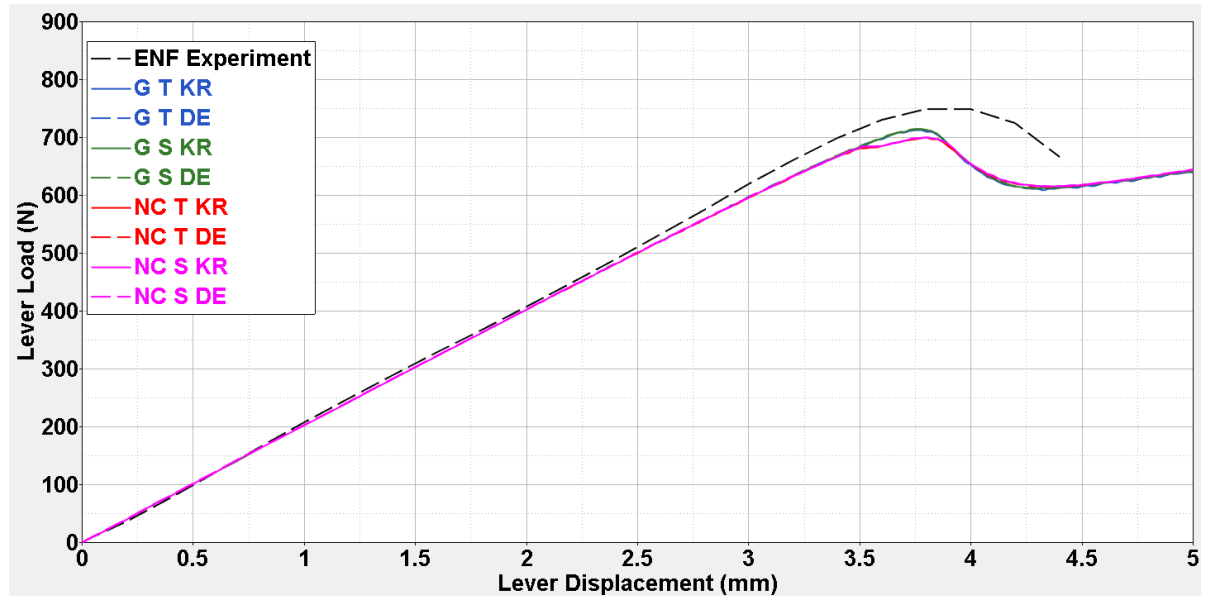
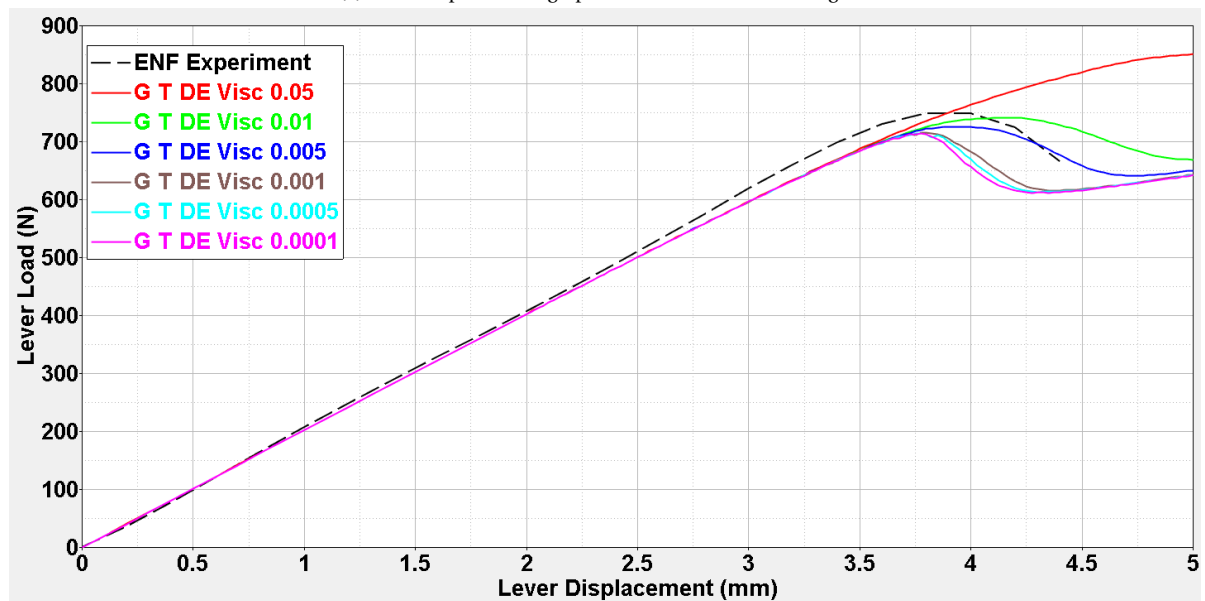


Figure A.28: Results of the 100% fracture mode setup for 3D simulations 1 through 8 with varying cohesive zone model settings.



(a) Load-Displacement graph of 3D simulations 1 through 8.



(b) Load-Displacement graph of 3D simulations 9 through 14: Viscosity factor results.

Figure A.29: Results of the 100% fracture mode setup for 3D simulations 1 through 14 with varying cohesive zone model settings.

Sim	Time Step Size [s]	$G_{c,I}$ [ $kJ/m^2$ ]	$G_{c,II}$ [ $kJ/m^2$ ]	$T_{m,I}$ [MPa]	$T_{m,II}$ [MPa]	Max. Load [N]	Exp. Load [N]	Error [%]	Comp. Time [s]
Turon	0.005	0.969	1.719	80	100	697.1	748.4	-6.9	-
15	0.05	0.969	1.719	80	100	712.4	748.4	-4.81	69
16	0.01	0.969	1.719	80	100	713.5	748.4	-4.66	166
17	0.005	0.969	1.719	80	100	712.7	748.4	-4.77	243
18	0.001	0.969	1.719	80	100	712.5	748.4	-4.80	1325
19	0.0005	0.969	1.719	80	100	708.6	748.4	-5.32	3655
20	0.0001	0.969	1.719	80	100	708.1	748.4	-5.38	19600
21	0.001	0.500	1.719	80	100	709.9	748.4	-5.14	1340
22	0.001	1.000	1.719	80	100	712.5	748.4	-4.80	1306
23	0.001	1.500	1.719	80	100	710	748.4	-5.13	1279
24	0.001	2.000	1.719	80	100	710.8	748.4	-5.02	1316
25	0.001	0.969	1.250	80	100	614.7	748.4	-17.86	1271
26	0.001	0.969	1.750	80	100	715.4	748.4	-4.41	1308
27	0.001	0.969	2.250	80	100	866.8	748.4	15.82	1030
28	0.001	0.969	2.750	80	100	906.8	748.4	21.17	1083
29	0.001	0.969	1.719	60	100	711.1	748.4	-4.98	1257
30	0.001	0.969	1.719	80	100	712.5	748.4	-4.80	1241
31	0.001	0.969	1.719	100	100	710.1	748.4	-5.12	1344
32	0.001	0.969	1.719	120	100	710.5	748.4	-5.06	1226
33	0.001	0.969	1.719	80	80	697.5	748.4	-6.80	1266
34	0.001	0.969	1.719	80	100	712.5	748.4	-4.80	1240
35	0.001	0.969	1.719	80	120	720.6	748.4	-3.71	1313
36	0.001	0.969	1.719	80	140	728.9	748.4	-2.61	1346

Table A.17: Results from the 100% fracture mode ratio for 3D simulations 15 through 36 with varying time step sizes,  $G_{c,I}$ ,  $G_{c,II}$ ,  $T_{m,I}$  and  $T_{m,II}$ .

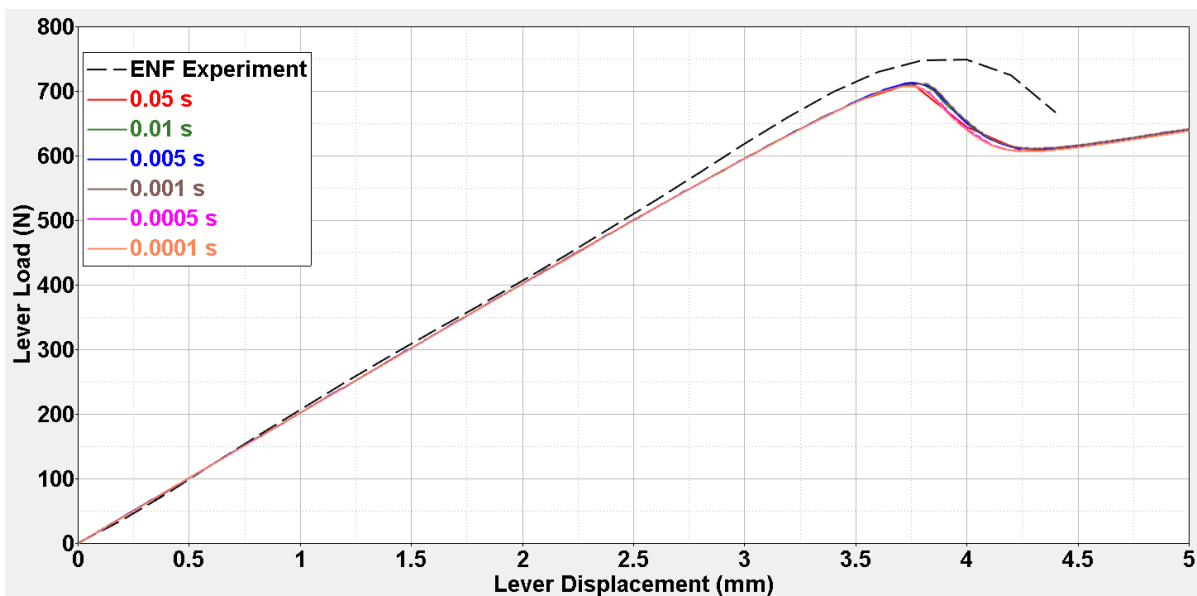
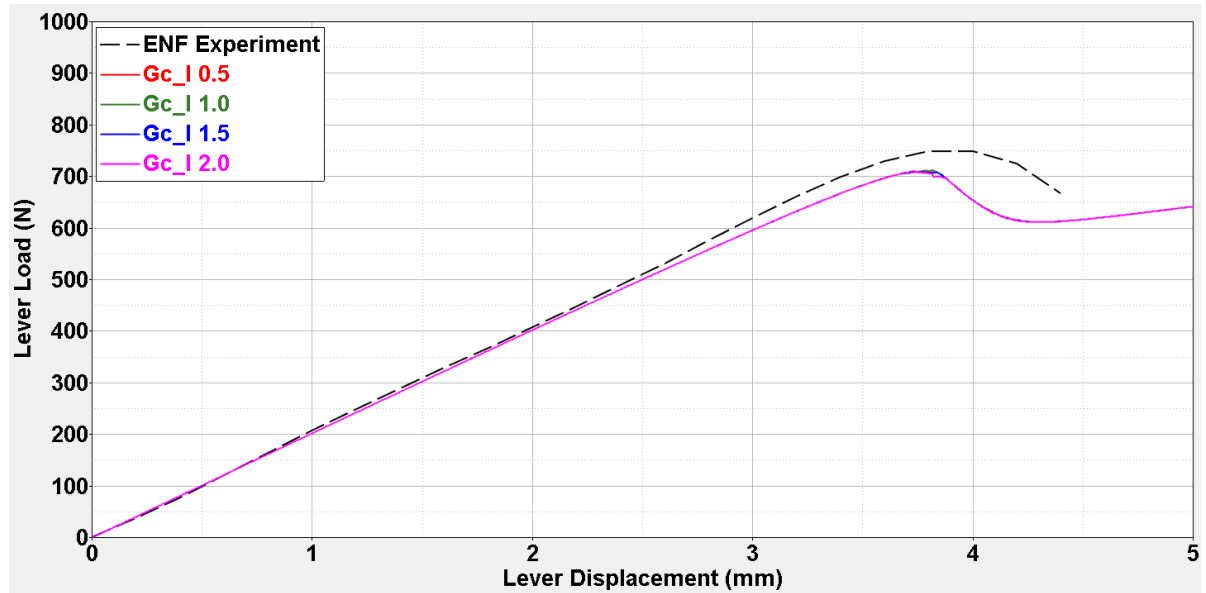


Figure A.30: Results from the 100% fracture mode for 3D simulations 15 through 20 with varying time step sizes.

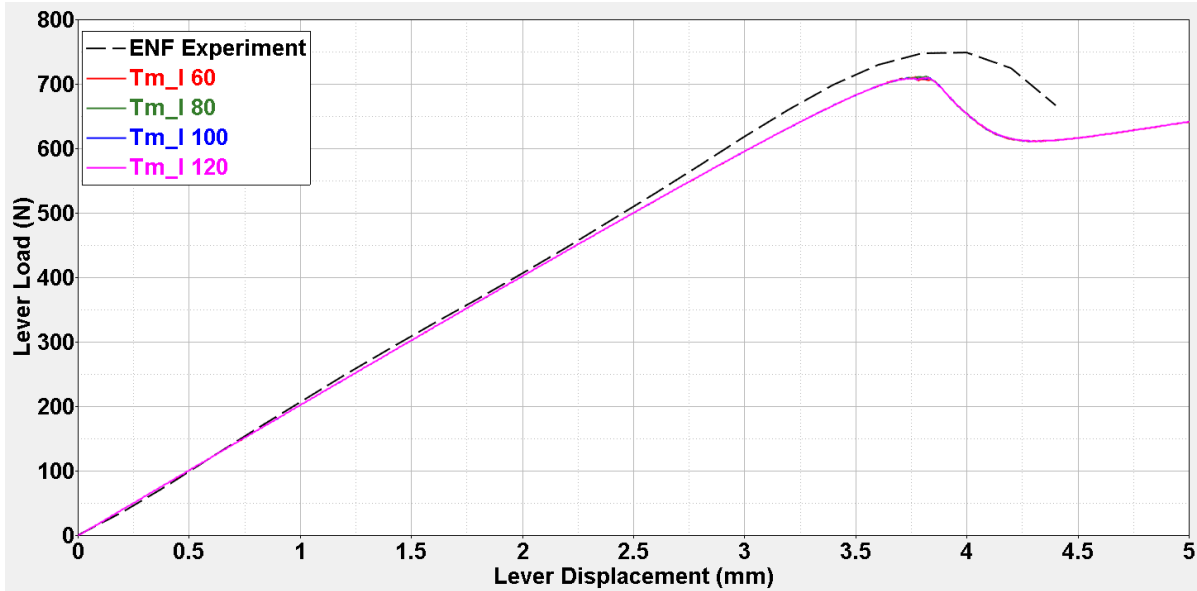


(a) Load-Displacement graph of 3D simulations 21 through 24.

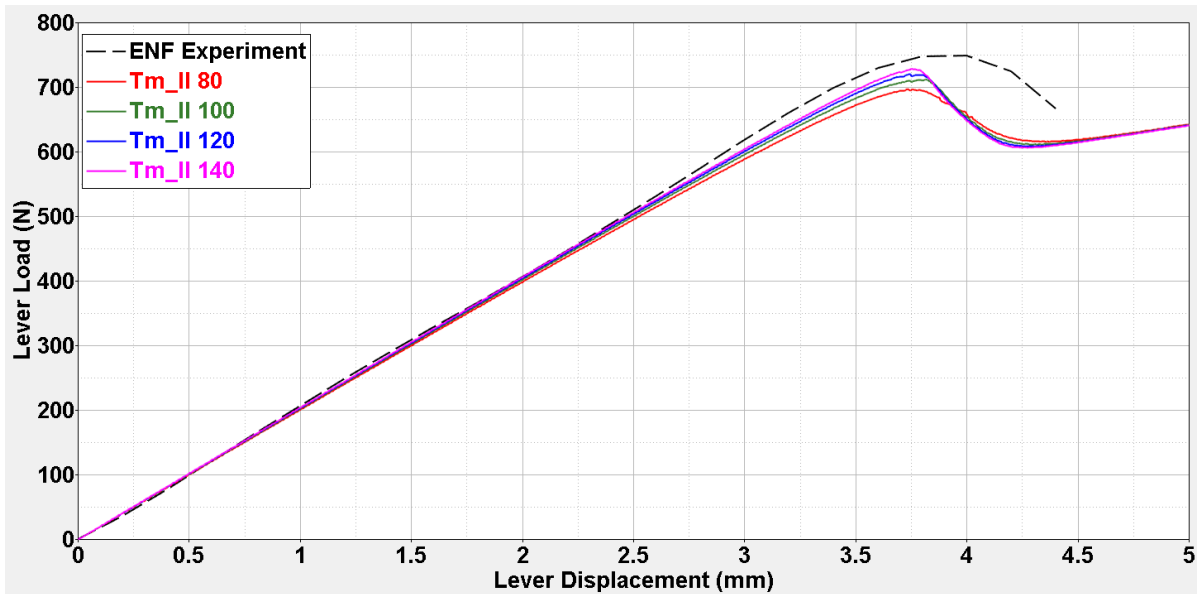


(b) Load-Displacement graph of 3D simulations 25 through 28.

Figure A.31: Results of the 100% fracture mode setup for 3D simulations 21 through 28 with varying  $G_{c,I}$  and  $G_{c,II}$ .



(a) Load-Displacement graph of 3D simulations 29 through 32.



(b) Load-Displacement graph of 3D simulations 33 through 36.

Figure A.32: Results of the 100% fracture mode setup for 3D simulations 29 through 36 with varying  $T_{m,I}$  and  $T_{m,II}$ .



# B

## CLS MODEL & SIMULATIONS

### B.1. FULL DETAILS MODELLING

Information regarding element types and sizes can be found in Table B.1.

Models	Part of Model/Region	Element Size	No. Elements	Element Type	Element Class
CLS	Strap (bulk)	2.5 by 2.5 by 2.5		149	Hex 8 - Composite
CLS	Strap (single ply)	2.5 by 2.5 by 0.125	2200	149	Hex 8 - Composite
CLS	Lap	2.5 by 2.5 by 3	1400	149	Hex 8 - Composite
CLS	Foot	2.5 by 2.5 by 3	400	149	Hex 8 - Composite
CLS	Bondline Main Part	2.5 by 2.5 by 0.3	1320	188	Hex 8 - Interface
CLS	Bondline Trigger Part	2.5 by 0.0625 by 0.3	80	192	Penta 6 - Interface
CLS	Bondline Foot Part	2.5 by 0.0625 by 0.3	400	192	Hex 8 - Interface
CLS	Interlaminar Adhesive	2.5 by 2.5 by 0	2200	188	Hex 8 - Interface

Table B.1: Element information.

The contact table for the contact conditions is found in Figure B.1.

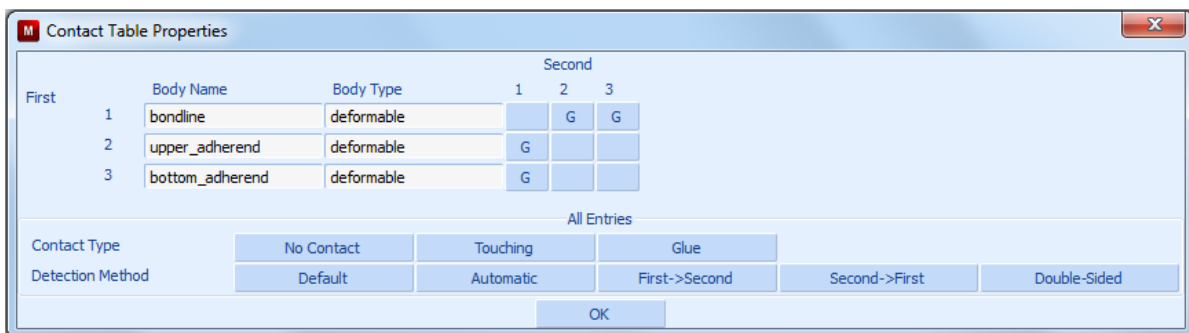


Figure B.1: Contact table for CLS specimen.

Technical drawing as in Figure B.2.

Figure B.3 shows a multi ply region definition as in MSC.Marc, used for the bulk and lap region which models an element to have multiple plies within instead of having separate multiple ply layers.

Material and failure properties as given in Figure B.4.

### B.2. TIME STEP EVALUATION

A time step evaluation is held to assess what time step will be used in the main simulation of the CLS specimen. The simulations have a displacement of 2.5 mm over a total of 1 second. The model is the same model

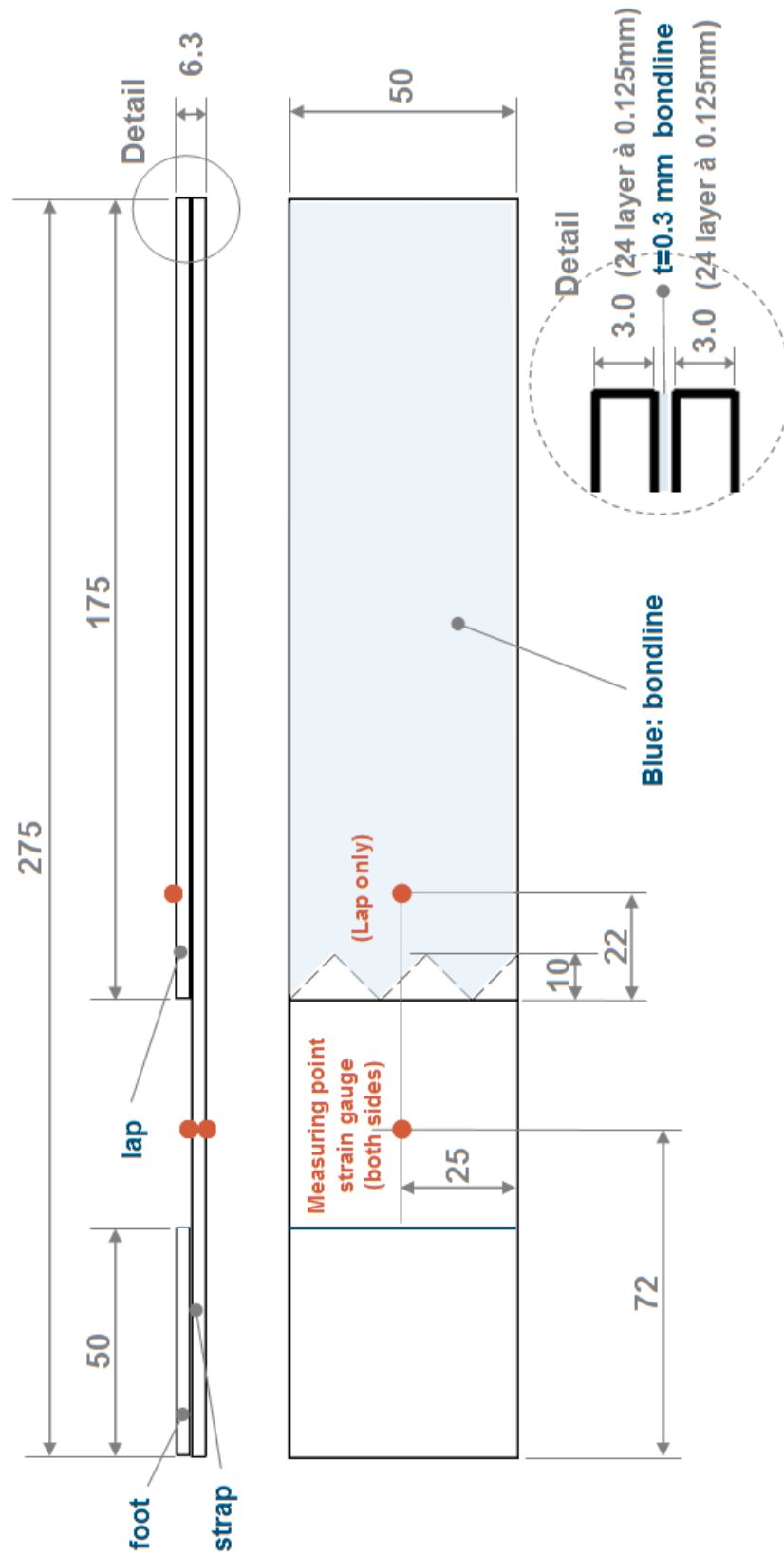


Figure B.2: Technical drawing of CLS specimen.

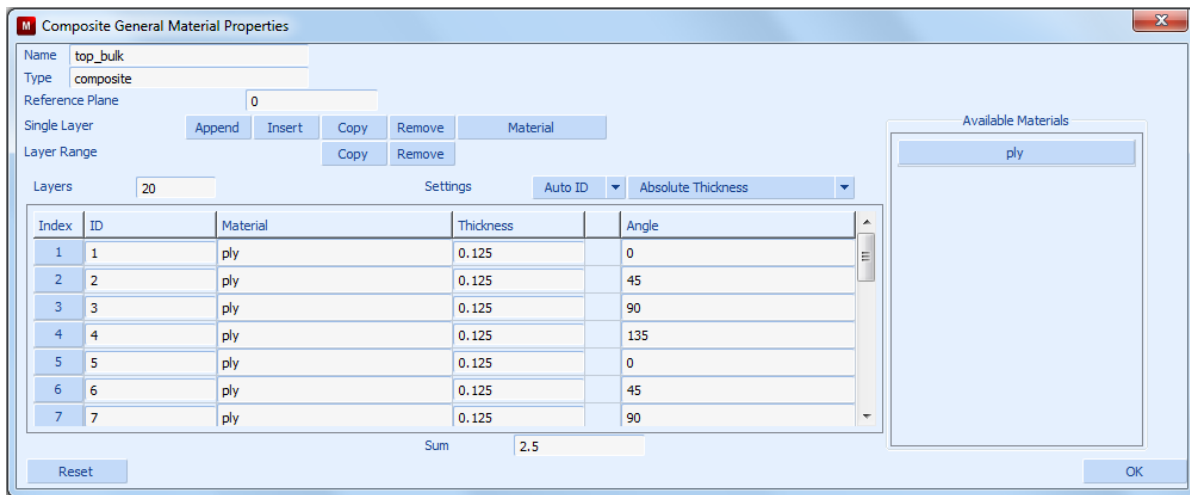


Figure B.3: Material property defining of a composite region.

as in Table B.1. Table B.2 shows the simulations with different time step sizes and their wall times that were needed to complete them.

Sim	Time Step Size [ms]	Time Step #	Wall Time [s]
1	10	10	679
2	1	100	4710
3	0.5	200	8548
4	0.2	500	17740
5	0.1	1000	30953
6	0.05	2000	52230

Table B.2: Simulation setup for CLS model.

Figure B.5 shows the results of the different time steps used. There is a significant difference in what time step is used. For the first part, the linear part, the time step sizes don't seem to make a difference. This is useful since the use of a large time step has a lower wall time, which can speed up the simulation. For the non-linear part though, the smaller the time step gets the more accurate the results become by converging at a certain point. The drawback is the very large wall times of the small time steps. This way, a trade-off has to be made: a small enough time step size with reasonable accuracy and a long wall time or a very small time step size with great accuracy at the cost of nearly a full day's worth.

It was chosen to take a time step size of 0.05 ms for non-linear parts and not smaller, to compensate for an even larger wall time.

### B.3. FIGURES OF RESULTS

stiffness		
E11t	160000 N/mm <sup>2</sup>	E11c = 140000
E22t	9000 N/mm <sup>2</sup>	E22c = 10000
E33t	9000 N/mm <sup>2</sup>	
G12	4500 N/mm <sup>2</sup>	
G13	4500 N/mm <sup>2</sup>	
G23	3215 N/mm <sup>2</sup>	= E22/(2*(1+v <sub>23</sub> ))
v <sub>12</sub>	0.32	v <sub>12c</sub> = 0.36
v <sub>13</sub>	0.32	
v <sub>23</sub>	0.40	
α <sub>11</sub>	-1.7e-6 1/K	
α <sub>22</sub>	3.1e-5 1/K	

(a) Material properties.

strength	
F <sub>11,t</sub>	2500 N/mm <sup>2</sup>
F <sub>11,c</sub>	2000 N/mm <sup>2</sup>
F <sub>22,t</sub>	65 N/mm <sup>2</sup>
F <sub>22,c</sub>	285 N/mm <sup>2</sup>
τ <sub>12</sub>	85 N/mm <sup>2</sup>
τ <sub>13</sub>	50 N/mm <sup>2</sup>
τ <sub>23</sub>	50 N/mm <sup>2</sup>

(b) Failure strengths.

Figure B.4: Properties of the laminates of the CLS specimen.

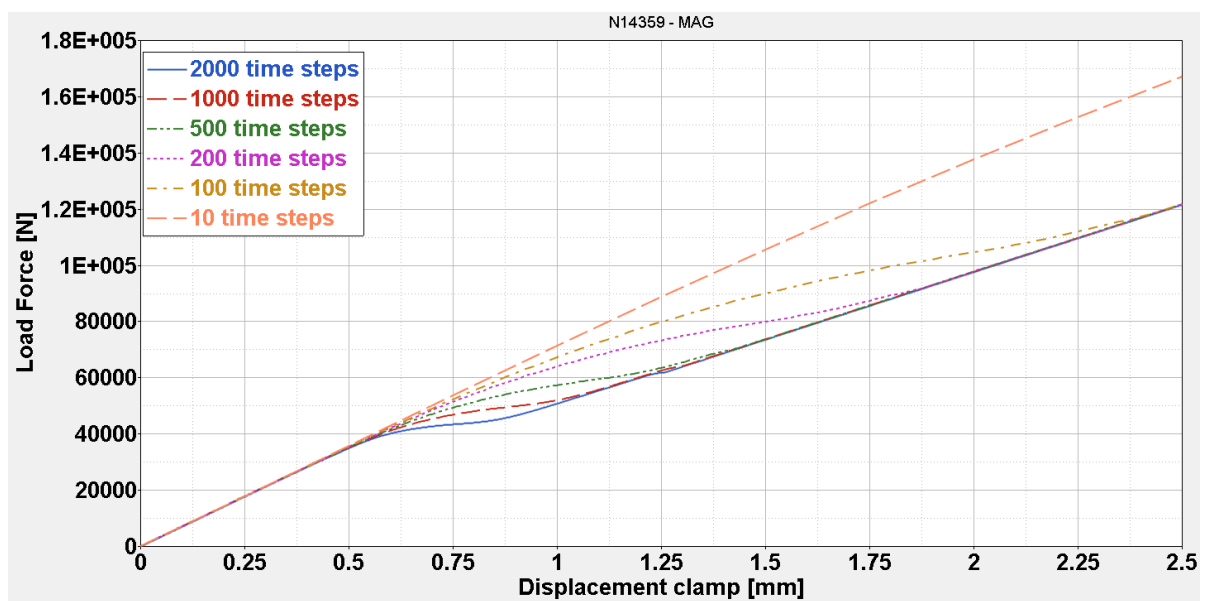
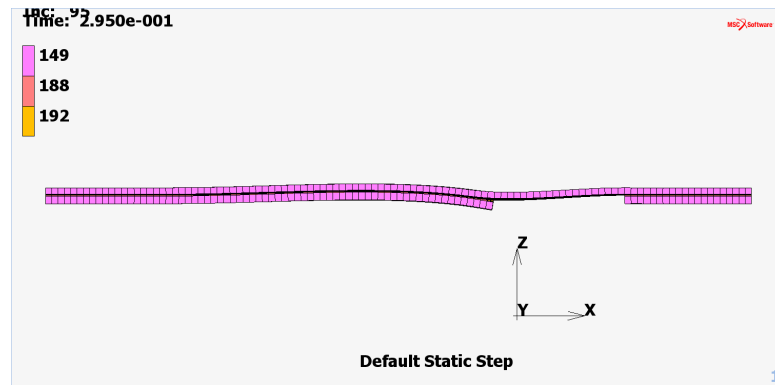
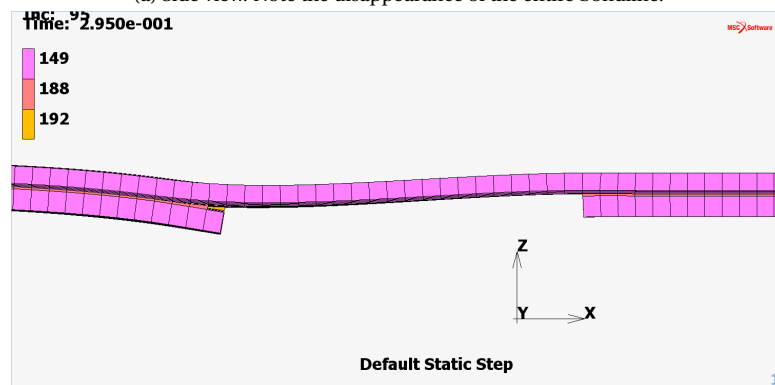


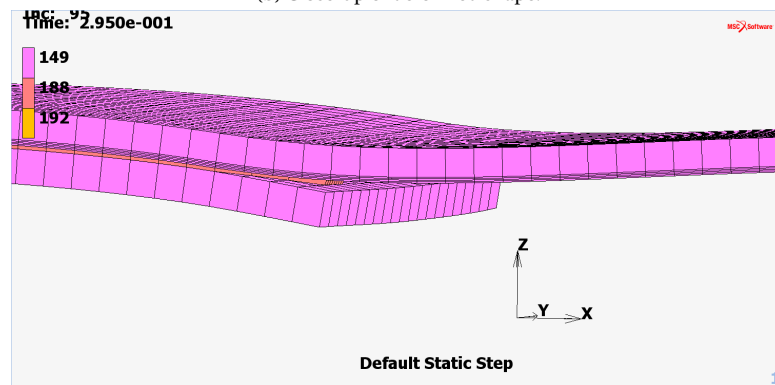
Figure B.5: Comparison of time step sizes.



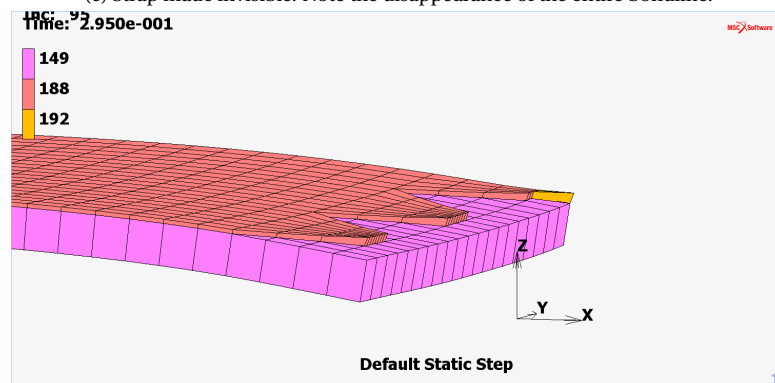
(a) Side view. Note the disappearance of the entire bondline.



(b) Close-up of deformed shape.

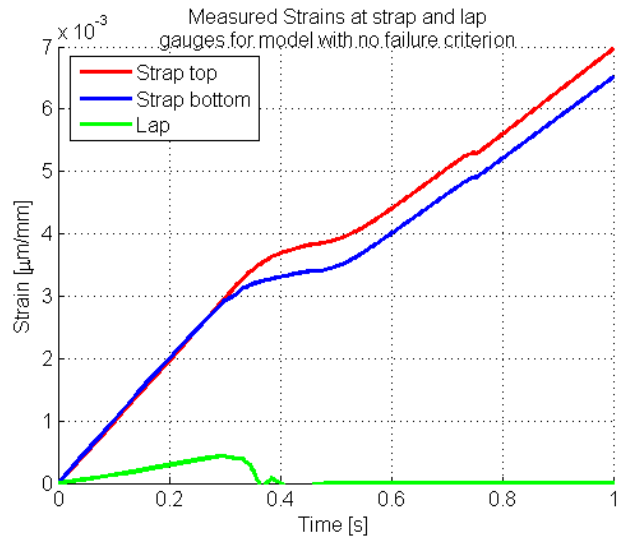


(c) Strap made invisible. Note the disappearance of the entire bondline.

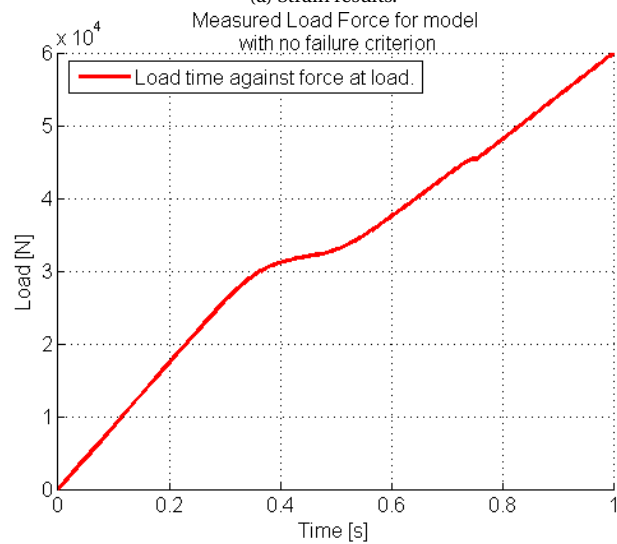


(d) Damage results for the 135° ply.

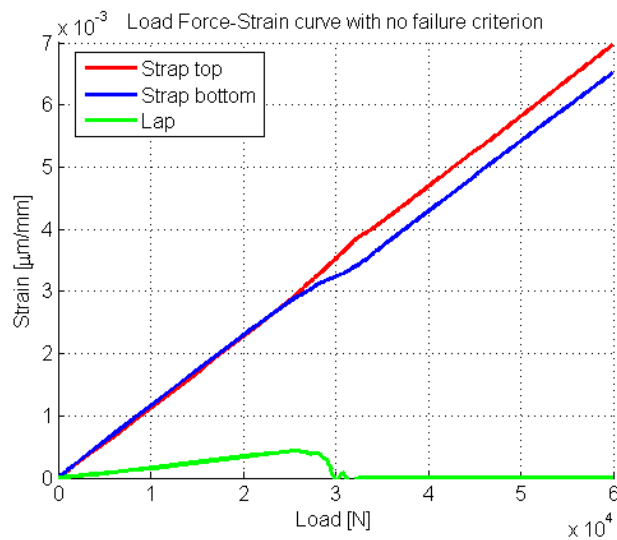
Figure B.6: First few CZE disappearing, or failing, in the bondline.



(a) Strain results.

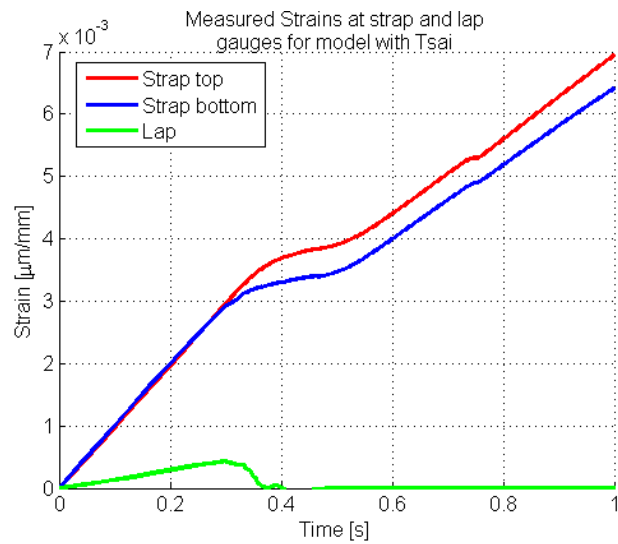


(b) Load results.

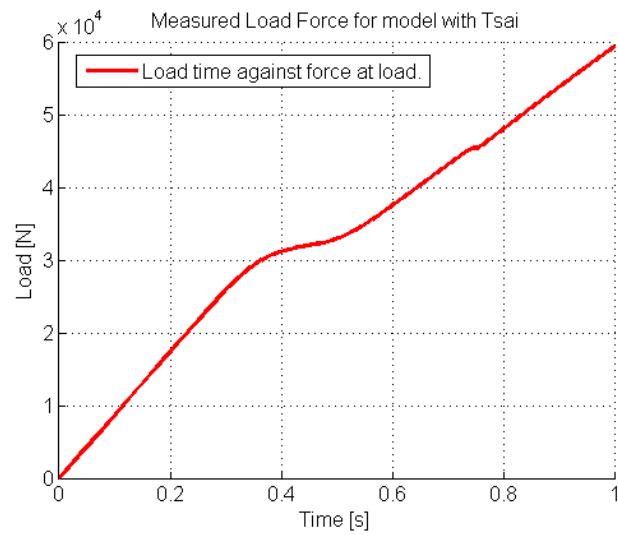


(c) Strain-Load results.

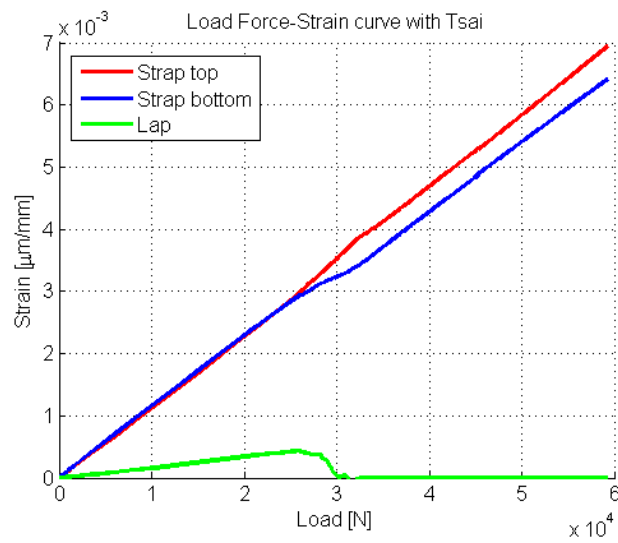
Figure B.7: The strain and load results of the simulation without failure criteria.



(a) Strain results.

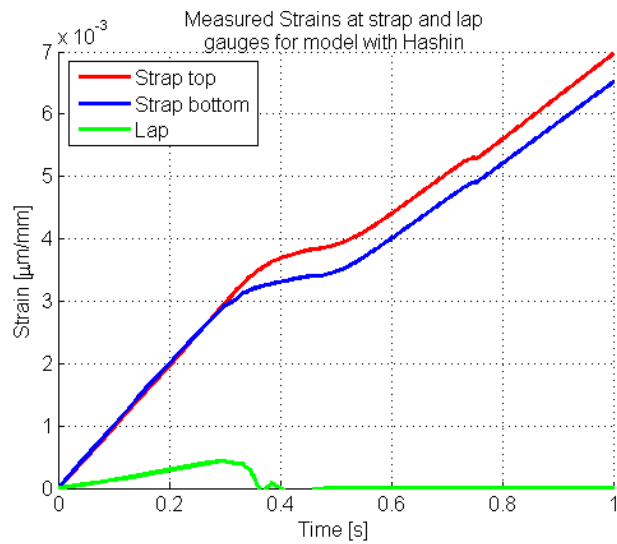


(b) Load results.

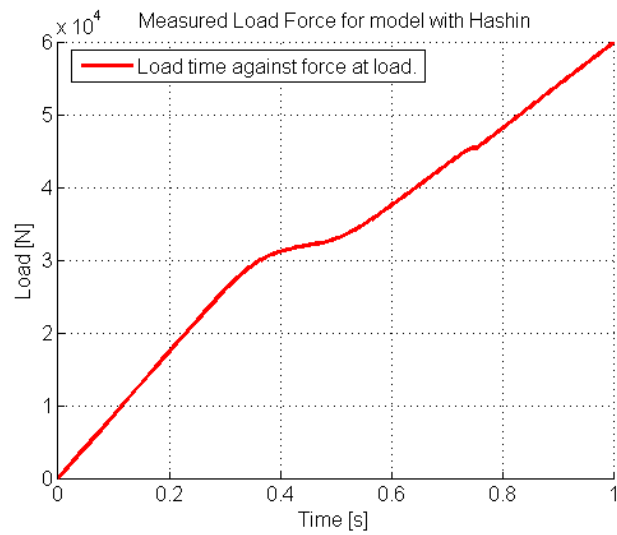


(c) Strain-Load results.

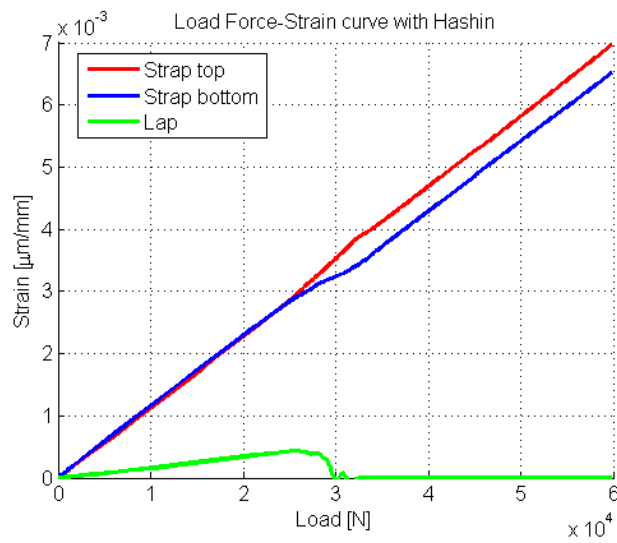
Figure B.8: The strain and load results of the simulation with Tsai-Wu failure criterion.



(a) Strain results.

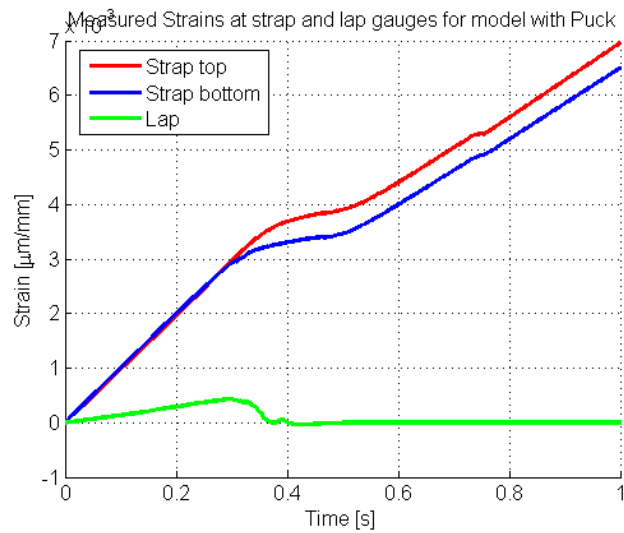


(b) Load results.

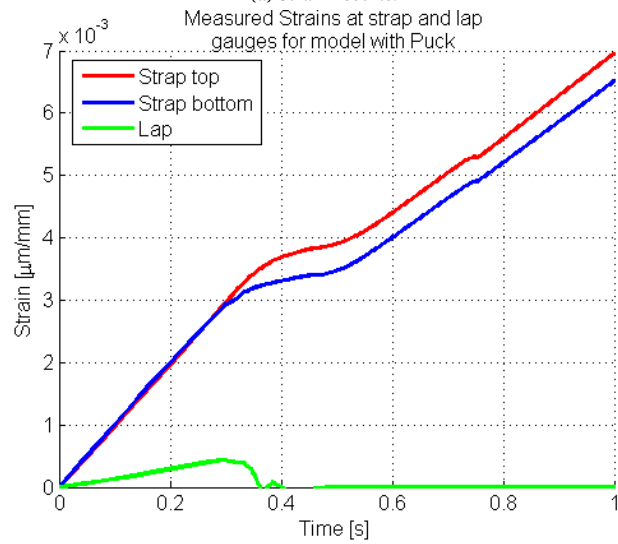


(c) Strain-Load results.

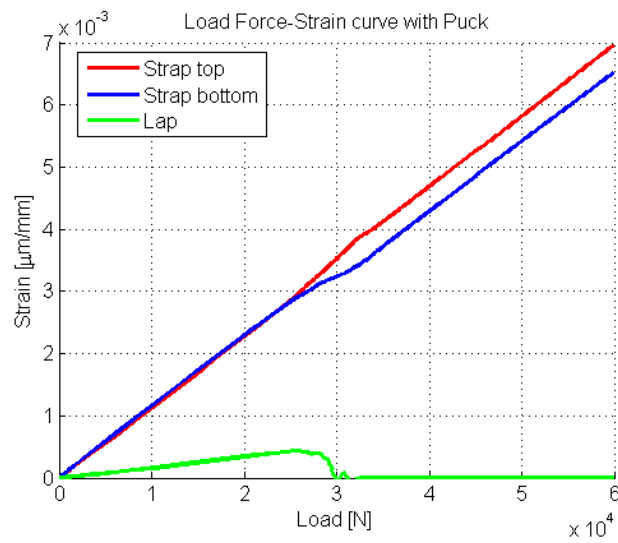
Figure B.9: The strain and load results of the simulation with Hashin failure criterion.



(a) Strain results.

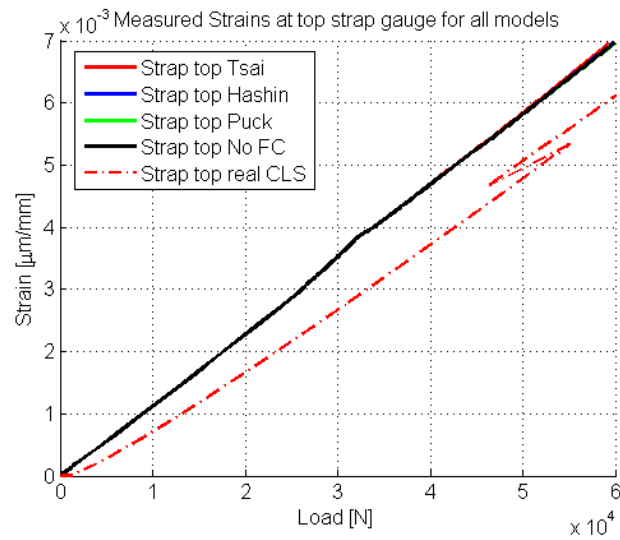


(b) Load results.

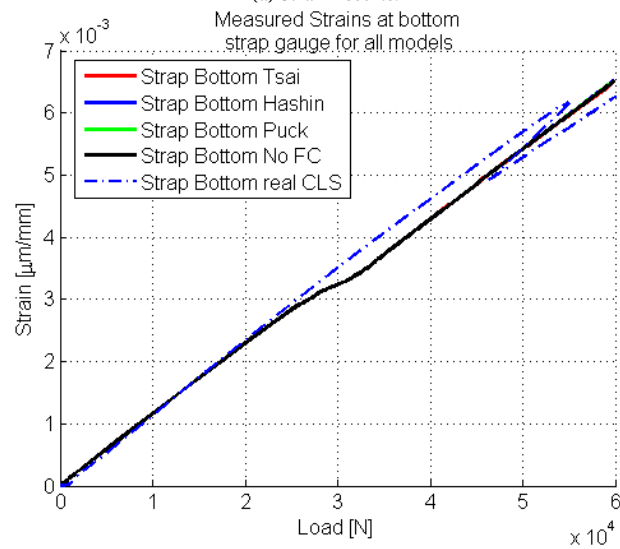


(c) Strain-Load results.

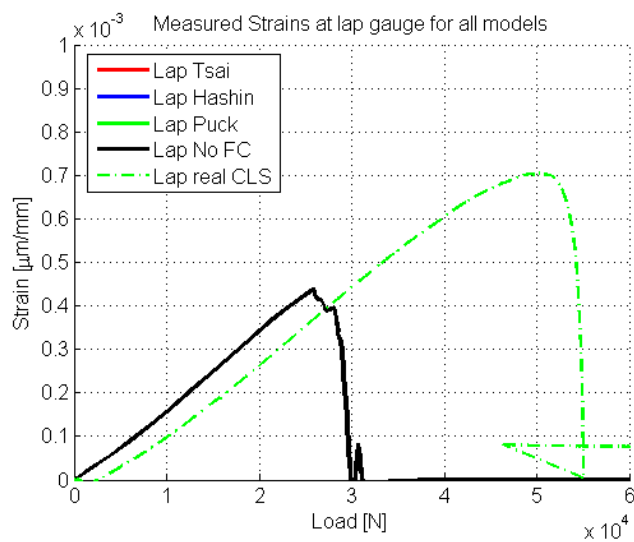
Figure B.10: The strain and load results of the simulation with Puck failure criterion.



(a) Strain results.

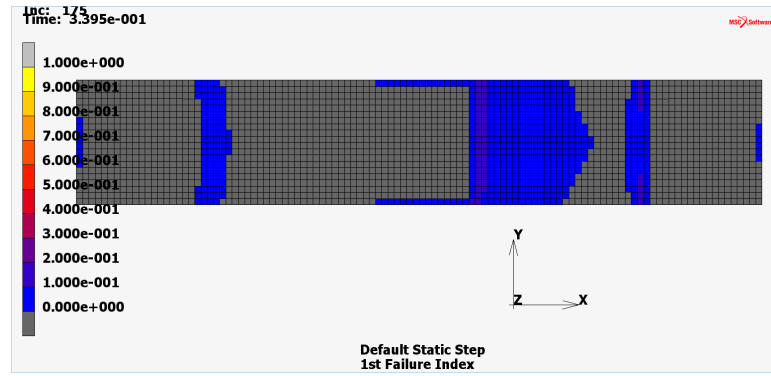


(b) Load results.

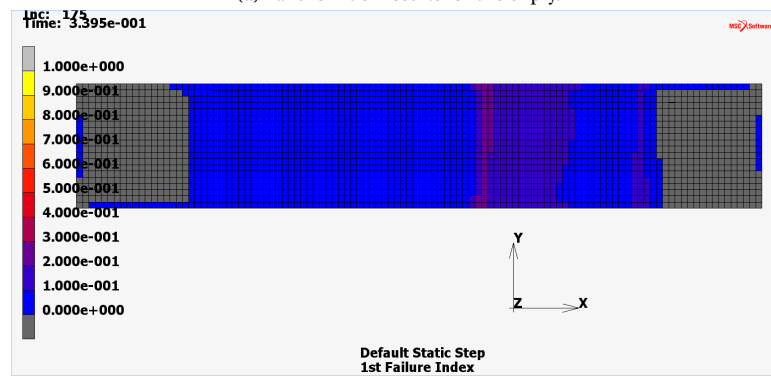


(c) Strain-Load results.

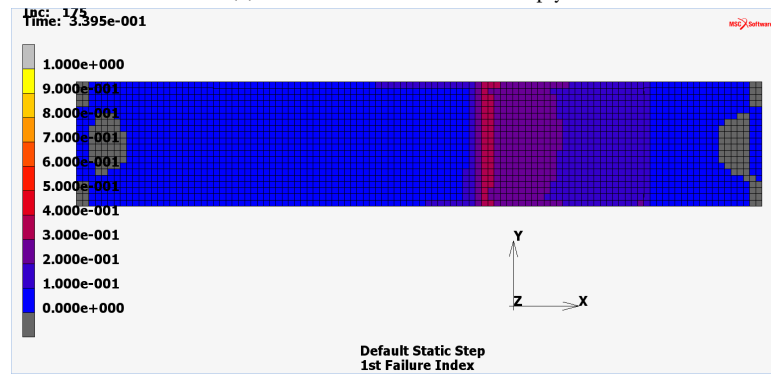
Figure B.11: The strain and load results at the gauges for all models and real CLS.



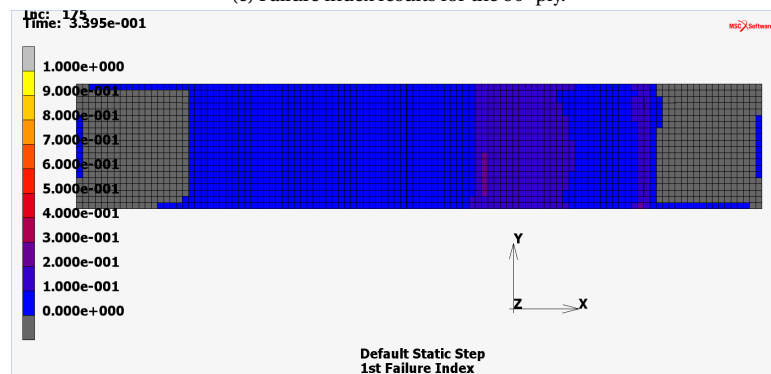
(a) Failure index results for the 0° ply.



(b) Failure index results for the 45° ply.

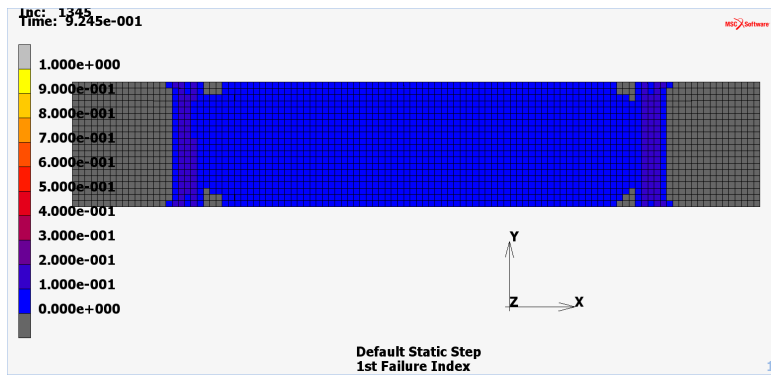


(c) Failure index results for the 90° ply.

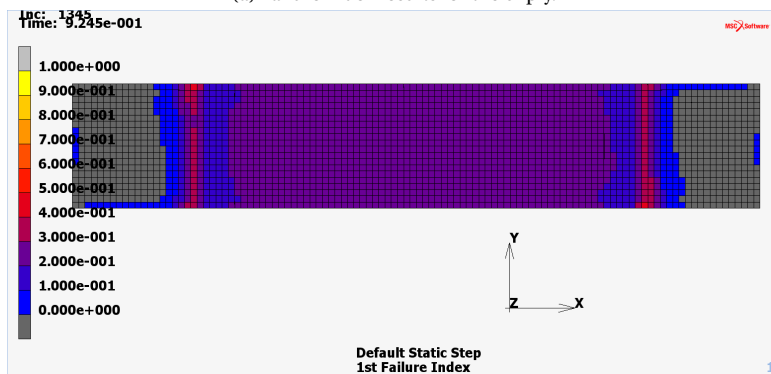


(d) Failure index results for the 135° ply.

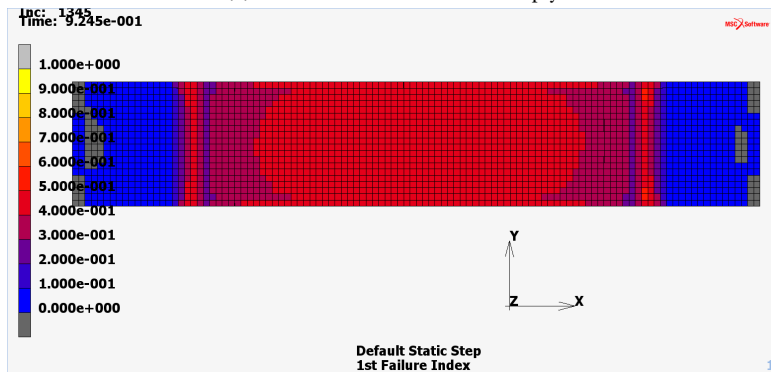
Figure B.12: The highest failure index results in the single ply region of the Tsai-Wu model at  $F = 25.6\text{ kN}$  ( $t = 0.3395$ ).



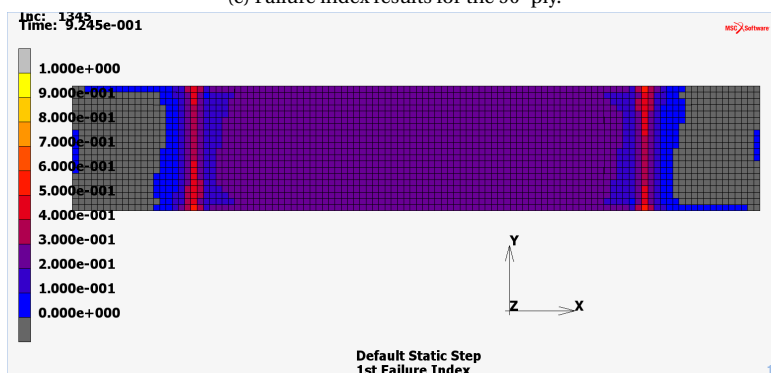
(a) Failure index results for the 0° ply.



(b) Failure index results for the 45° ply.

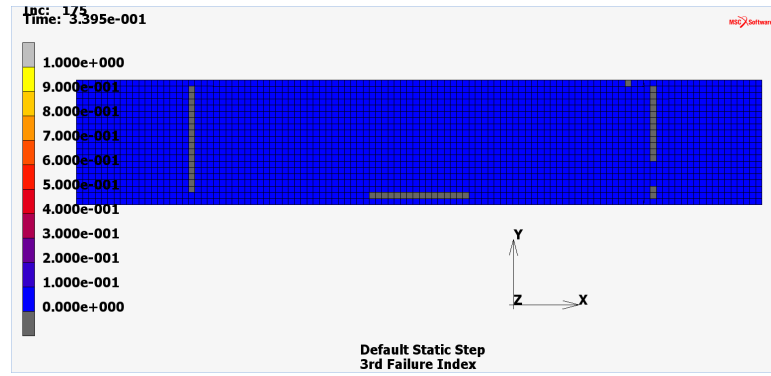


(c) Failure index results for the 90° ply.

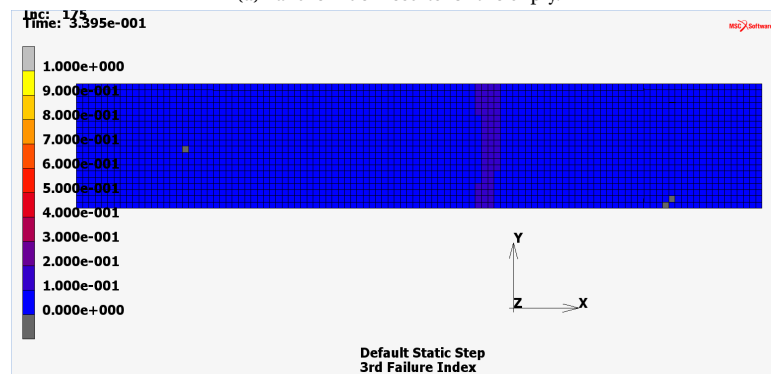


(d) Failure index results for the 135° ply.

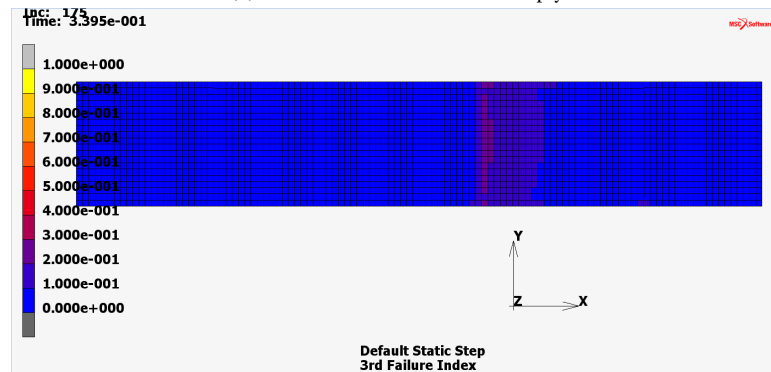
Figure B.13: The highest failure index results in the single ply region of the Tsai-Wu model at  $F = 55kN$  ( $t = 0.9245$ ).



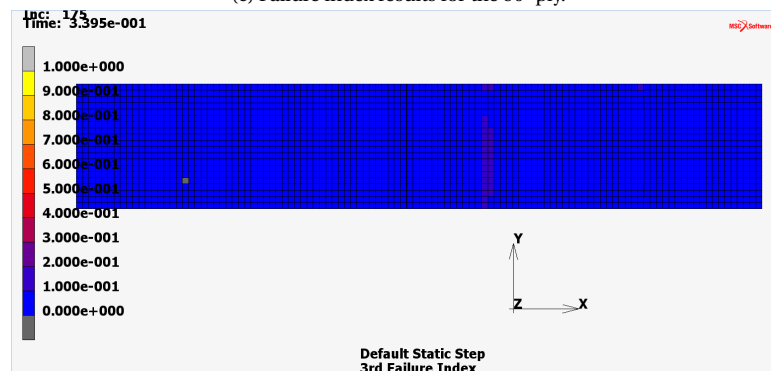
(a) Failure index results for the 0° ply.



(b) Failure index results for the 45° ply.

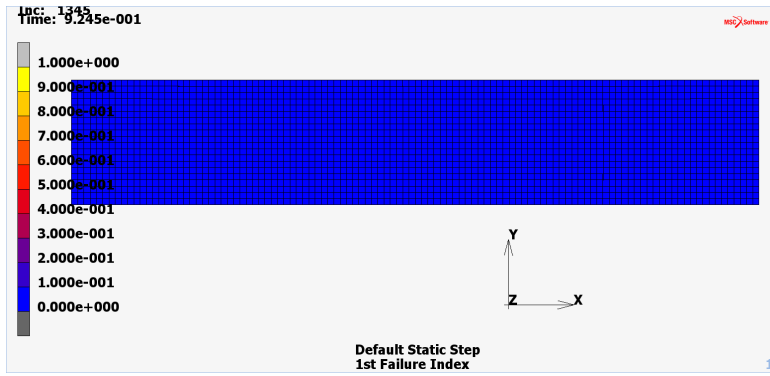


(c) Failure index results for the 90° ply.

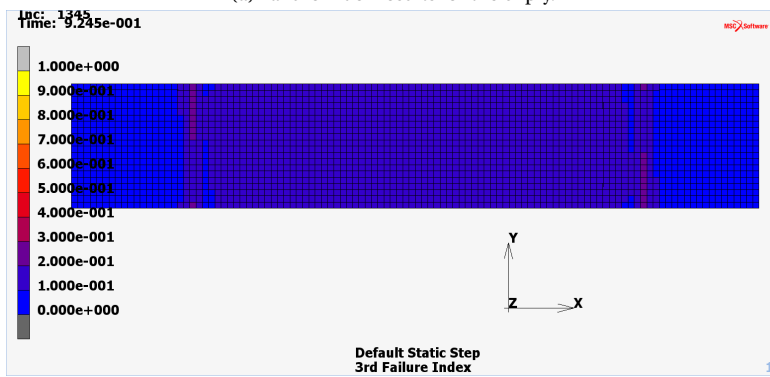


(d) Failure index results for the 135° ply.

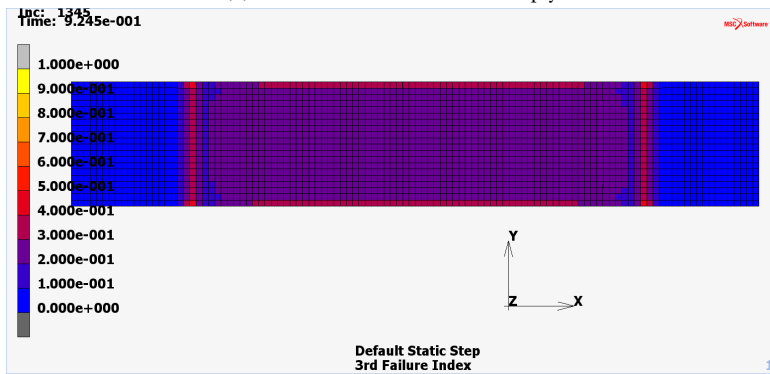
Figure B.14: The highest failure index results in the single ply region of the Hashin model at  $F = 25.6\text{ kN}$  ( $t = 0.3395$ ).



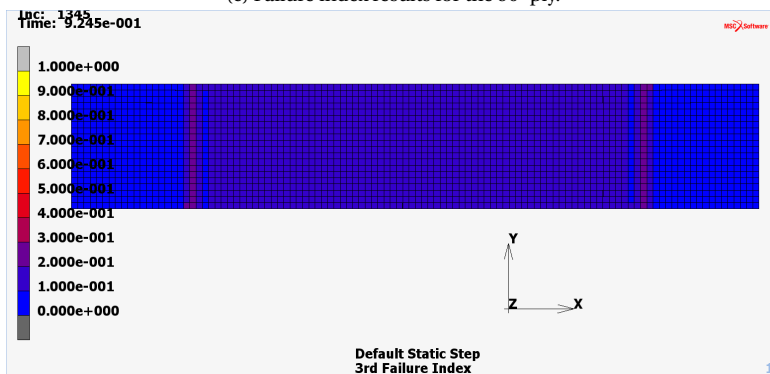
(a) Failure index results for the 0° ply.



(b) Failure index results for the 45° ply.

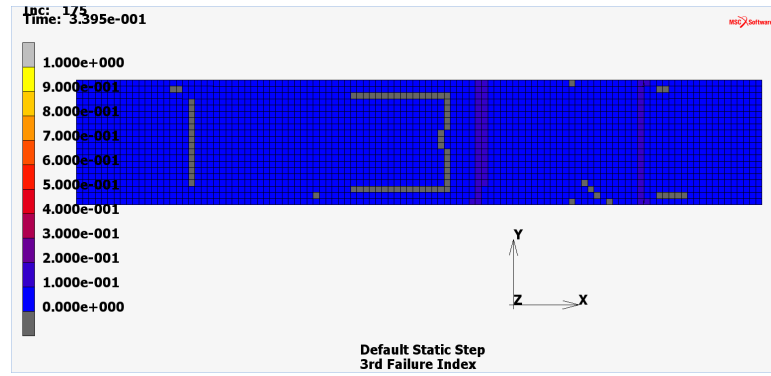


(c) Failure index results for the 90° ply.

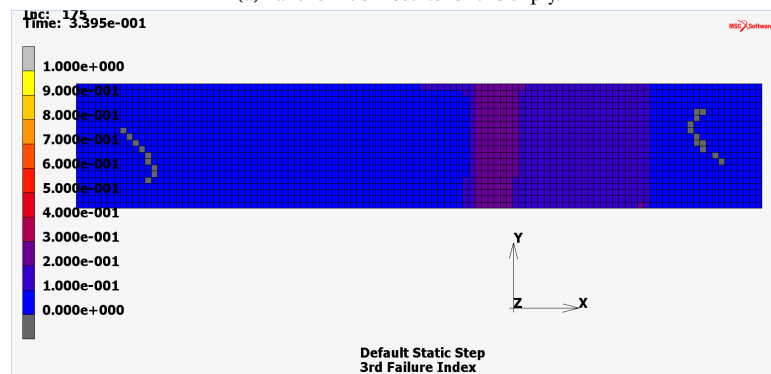


(d) Failure index results for the 135° ply.

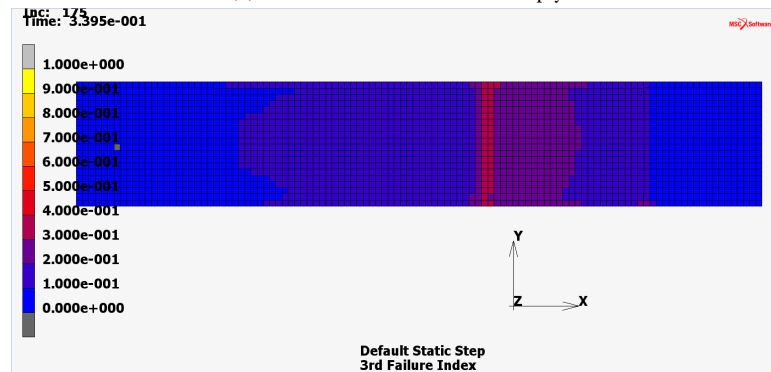
Figure B.15: The highest failure index results in the single ply region of the Puck model at  $F = 55\text{ kN}$  ( $t = 0.9245$ ).



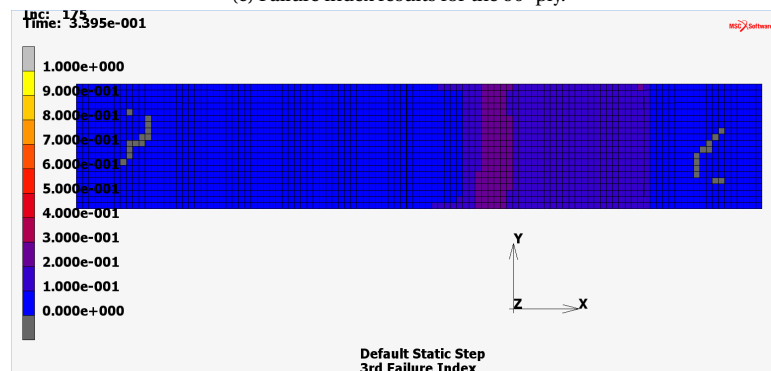
(a) Failure index results for the 0° ply.



(b) Failure index results for the 45° ply.

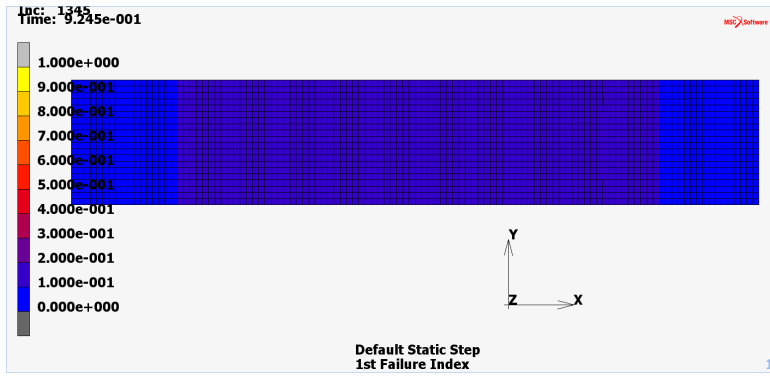


(c) Failure index results for the 90° ply.

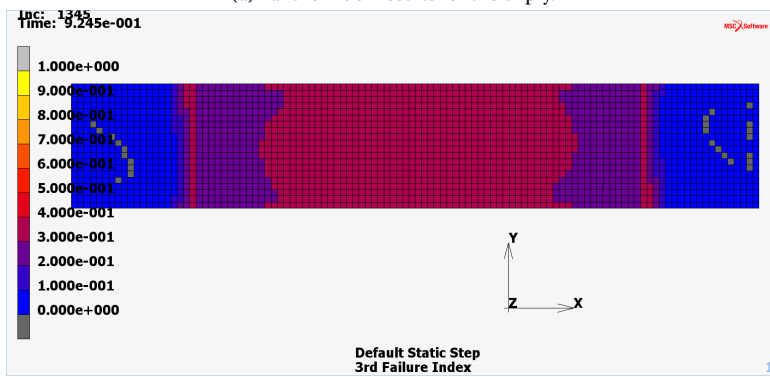


(d) Failure index results for the 135° ply.

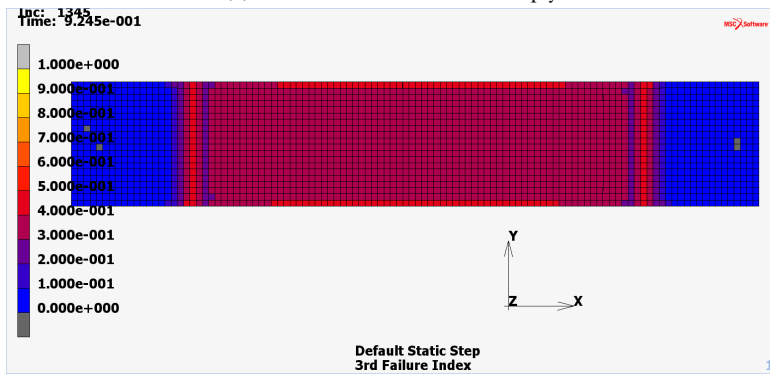
Figure B.16: The highest failure index results in the single ply region of the Puck model at  $F = 25.6kN$  ( $t = 0.3395$ ).



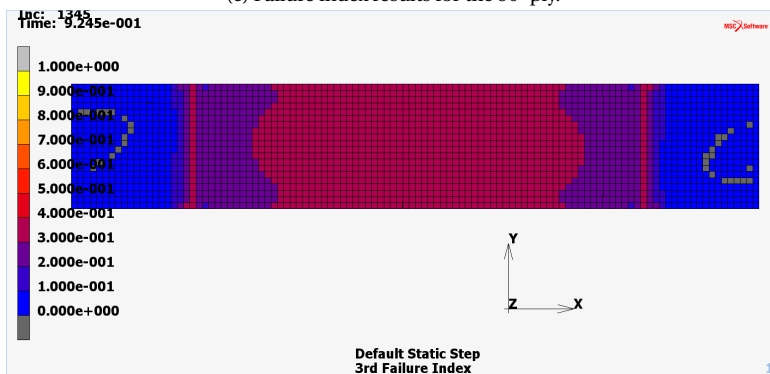
(a) Failure index results for the 0° ply.



(b) Failure index results for the 45° ply.

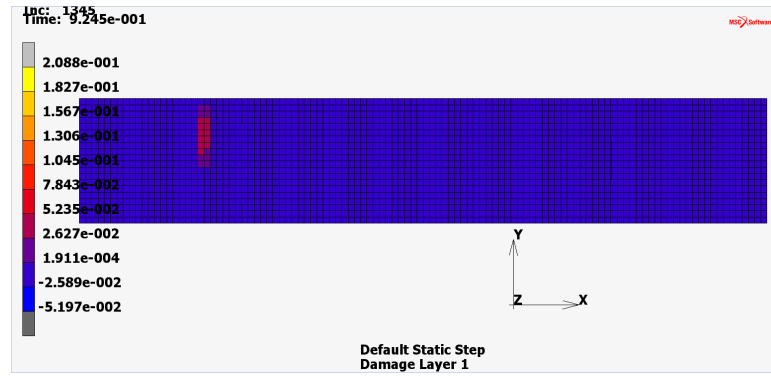


(c) Failure index results for the 90° ply.

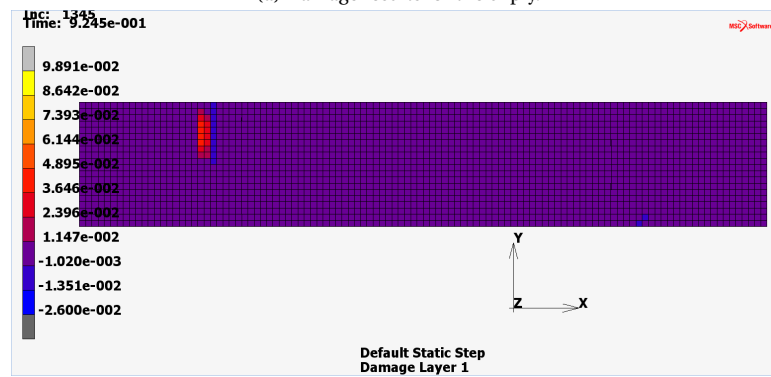


(d) Failure index results for the 135° ply.

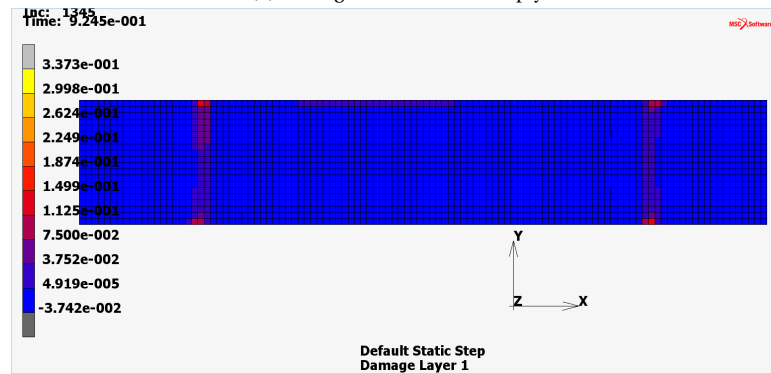
Figure B.17: The highest failure index results in the single ply region of the Puck model at  $F = 55\text{ kN}$  ( $t = 0.9245$ ).



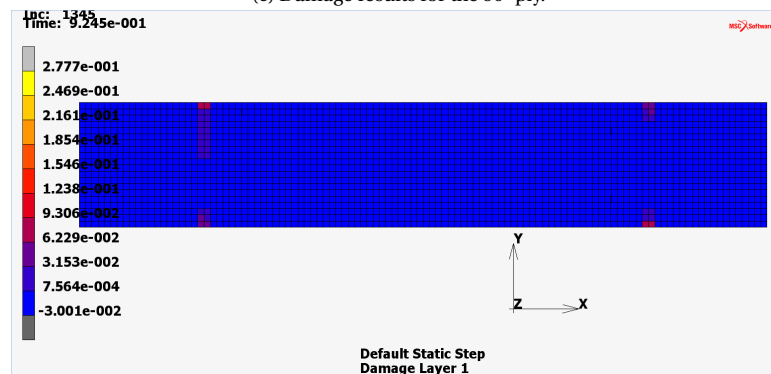
(a) Damage results for the 0° ply.



(b) Damage results for the 45° ply.

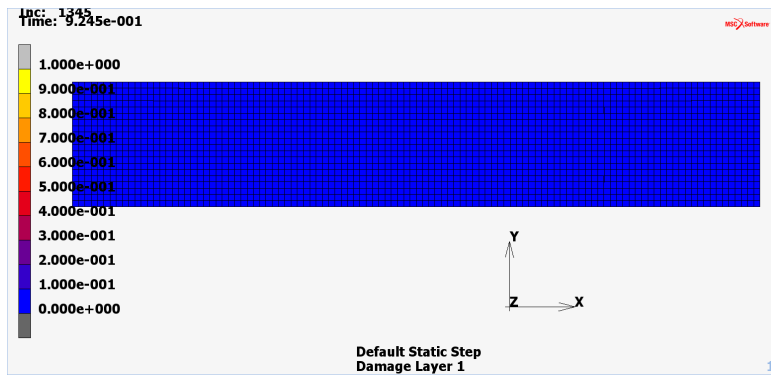


(c) Damage results for the 90° ply.

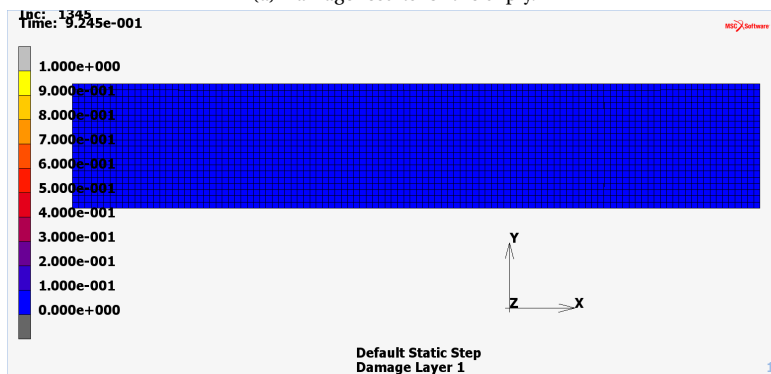


(d) Damage results for the 135° ply.

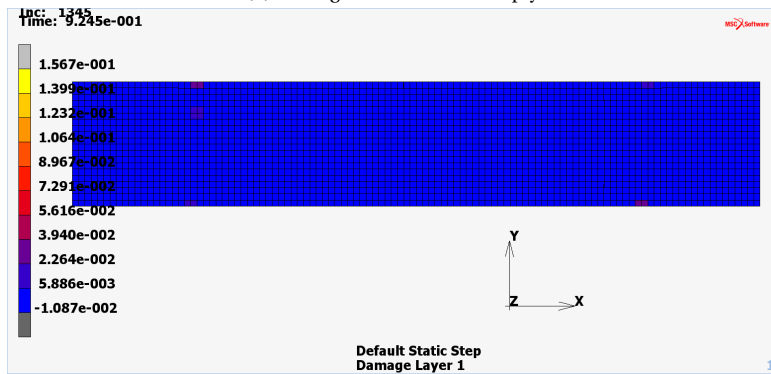
Figure B.18: The highest damage results in the single ply region of the Tsai-Wu model at  $F = 55kN$  ( $t = 0.9245$ ).



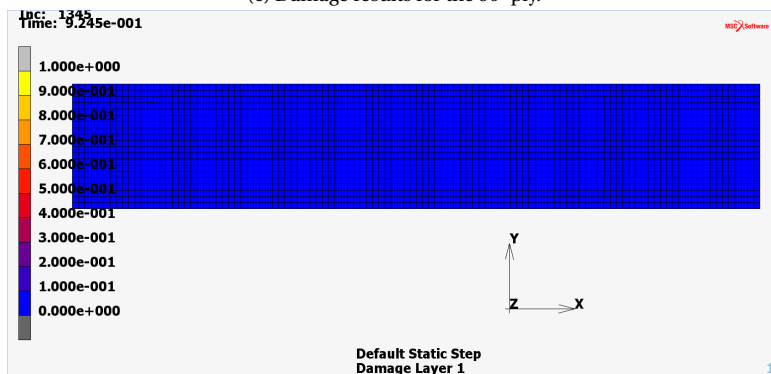
(a) Damage results for the 0° ply.



(b) Damage results for the 45° ply.

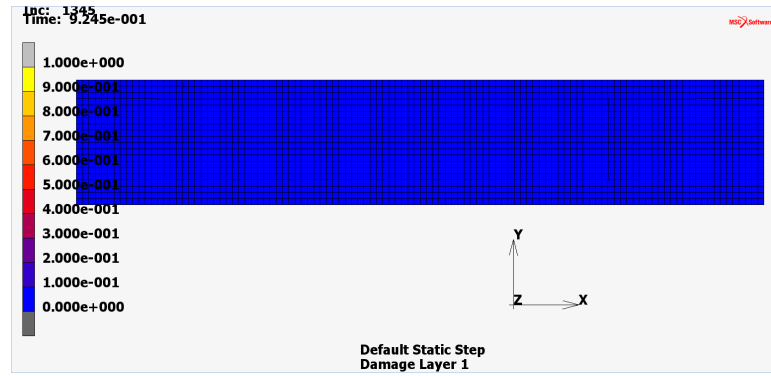


(c) Damage results for the 90° ply.

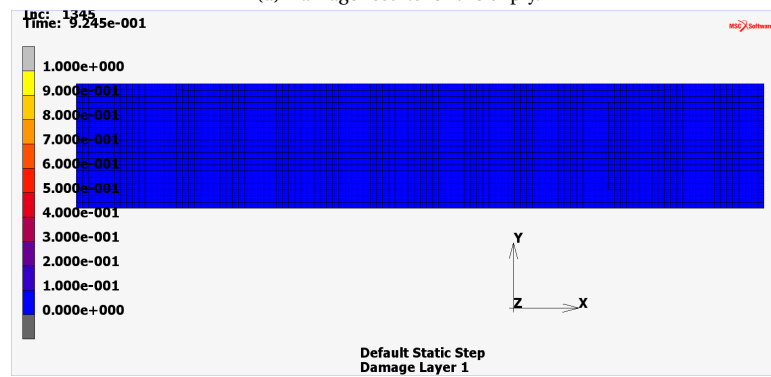


(d) Damage results for the 135° ply.

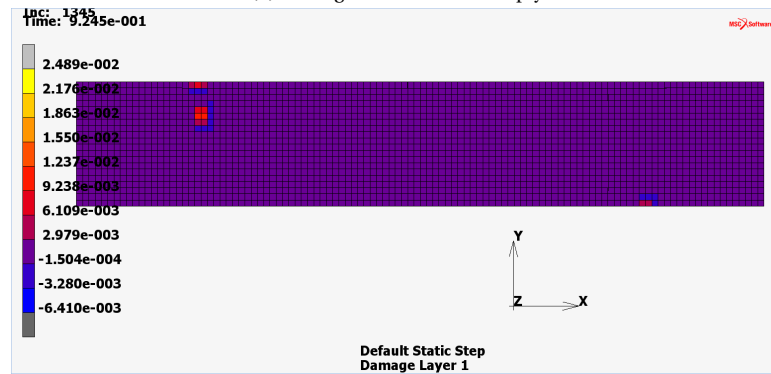
Figure B.19: The highest damage results in the single ply region of the Puck model at  $F = 55\text{ kN}$  ( $t = 0.9245$ ).



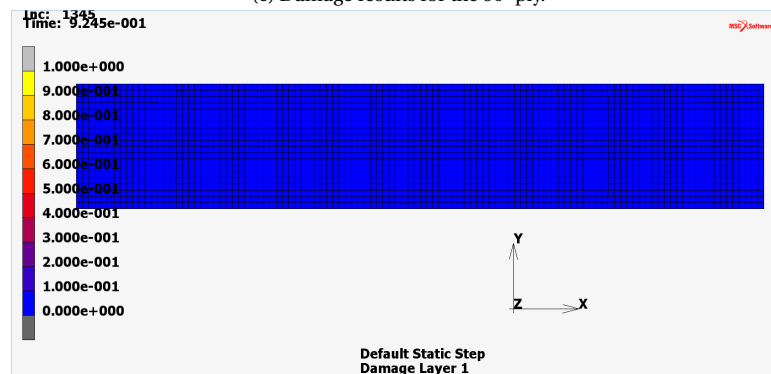
(a) Damage results for the 0° ply.



(b) Damage results for the 45° ply.



(c) Damage results for the 90° ply.



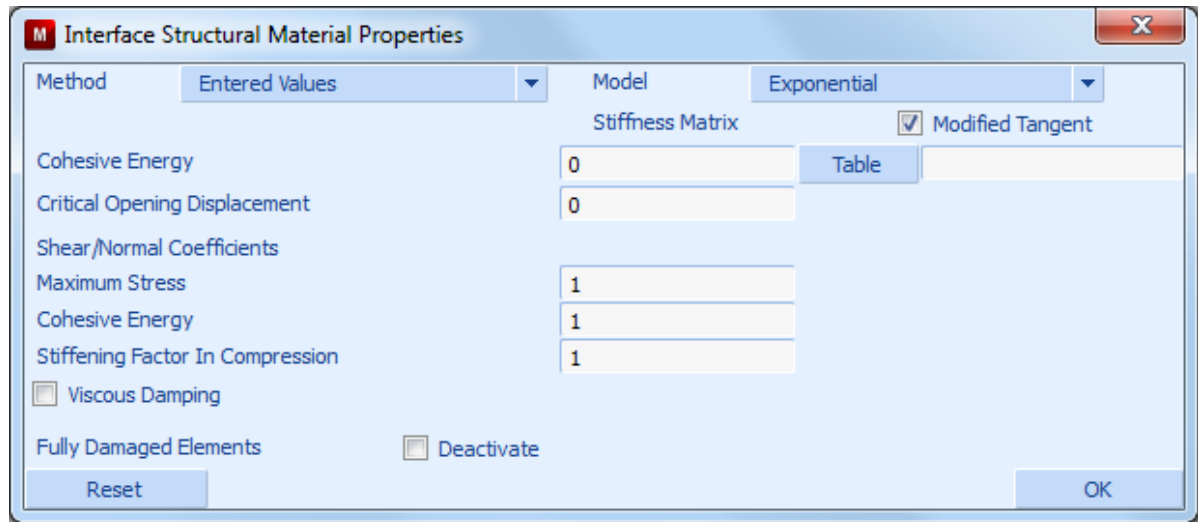
(d) Damage results for the 135° ply.

Figure B.20: The highest damage results in the single ply region of the Puck model at  $F = 55\text{ kN}$  ( $t = 0.9245$ ).

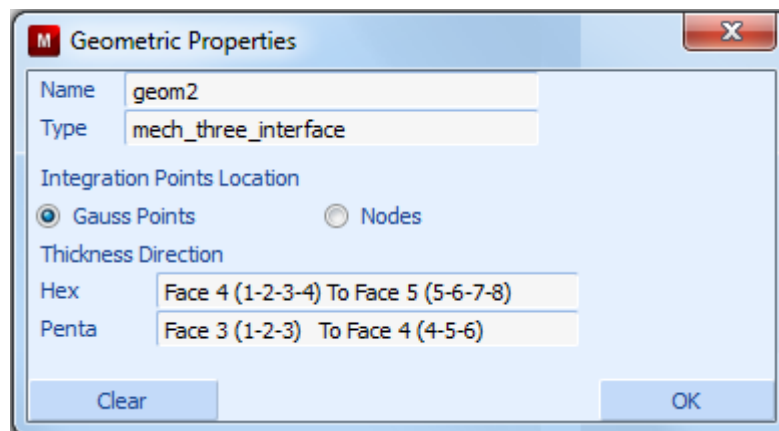
# C

## GUI OF MSC.MARC WINDOWS AND OPTIONS

Here several GUI windows of options in MSC.Marc can be found for user's ease to understand and visualise the input windows.



(a) Geometric property window for cohesive elements.



(b) Material property window for cohesive elements.

Figure C.1: Mentat GUI windows for defining cohesive properties.

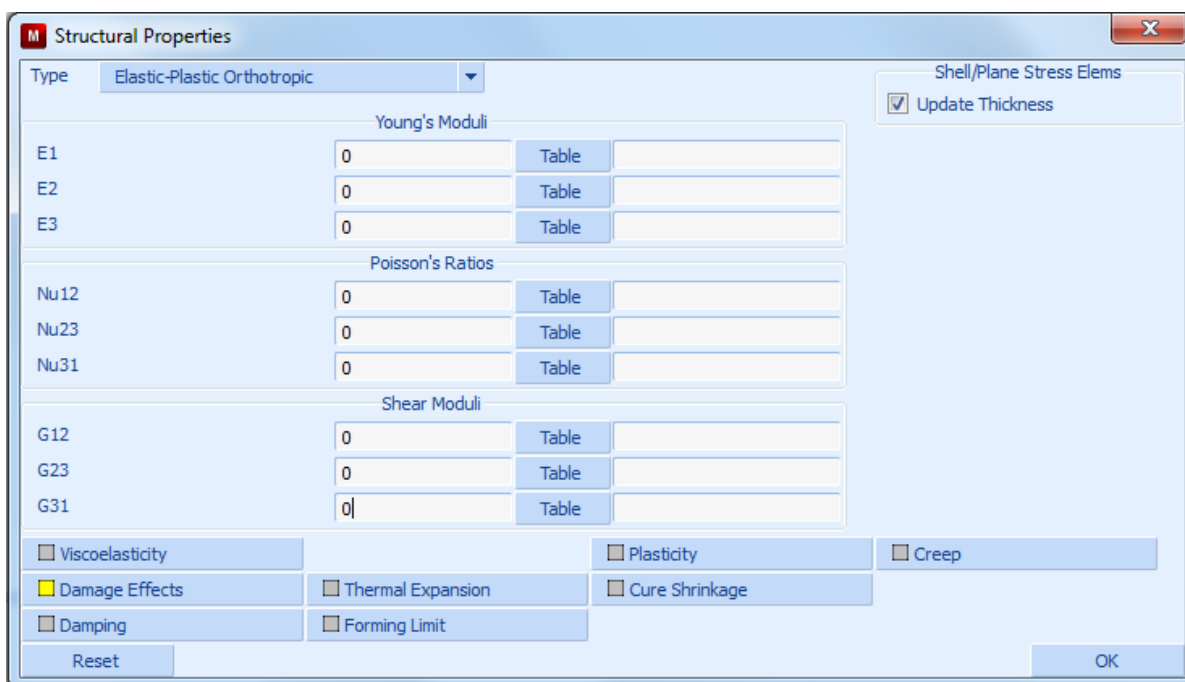


Figure C.2: Material property window for solids in Mentat.

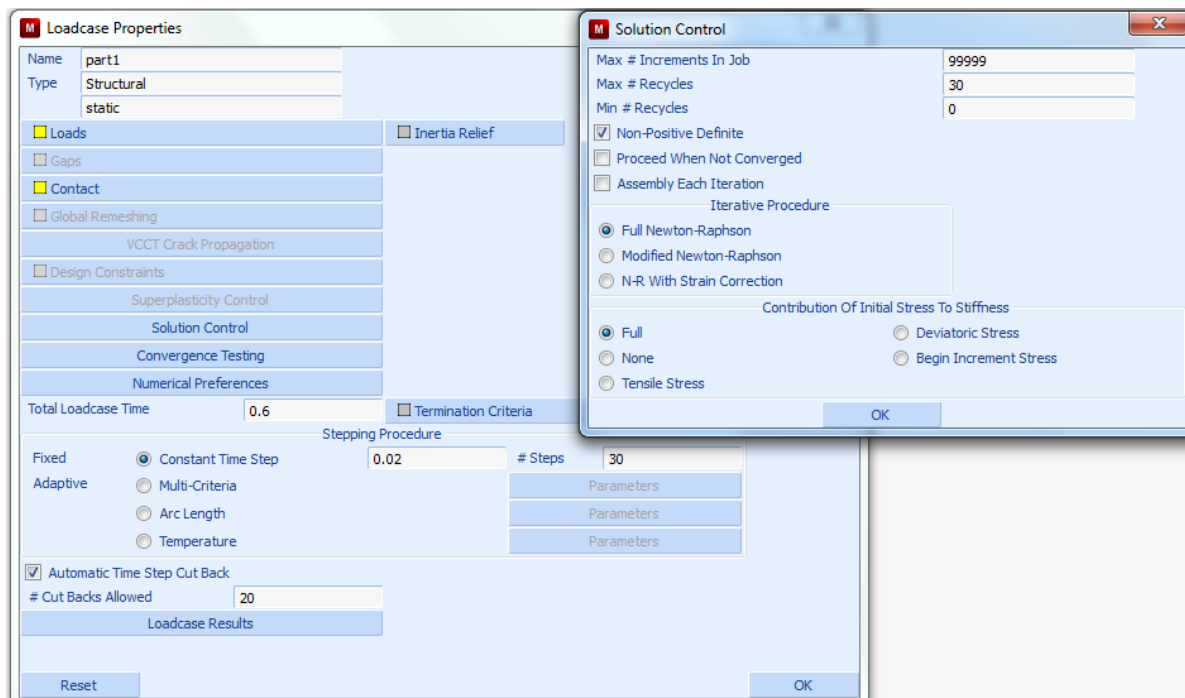


Figure C.3: Loadcase property with solution control.

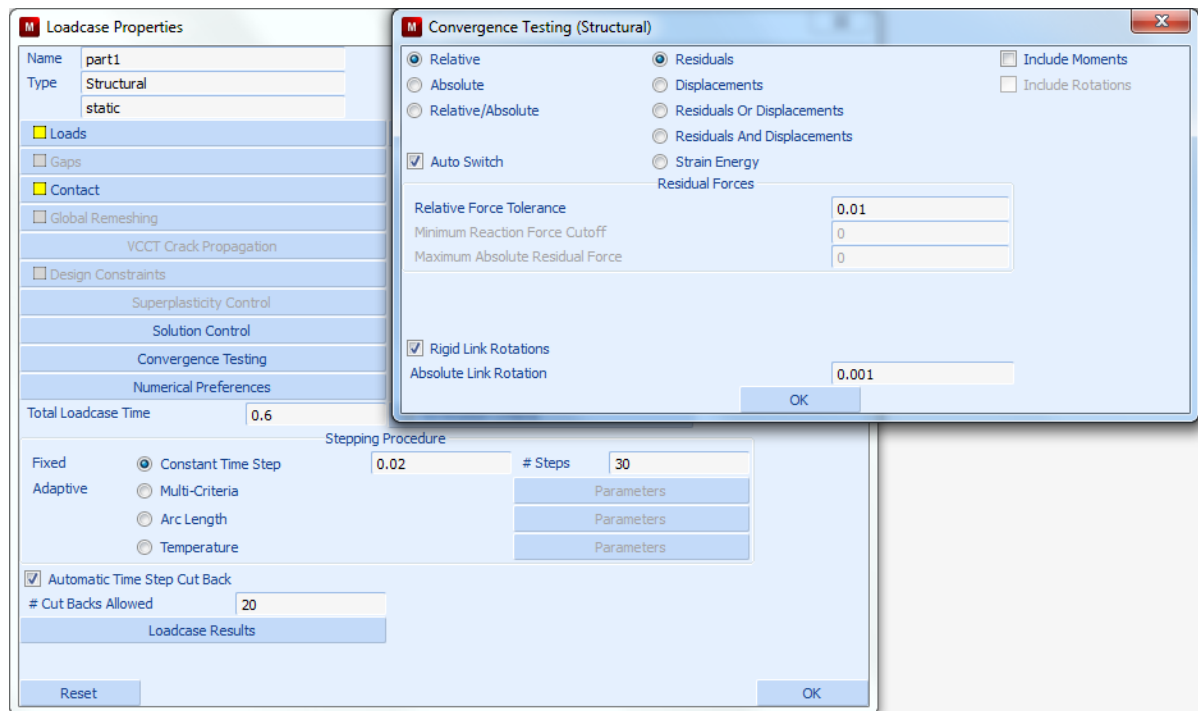
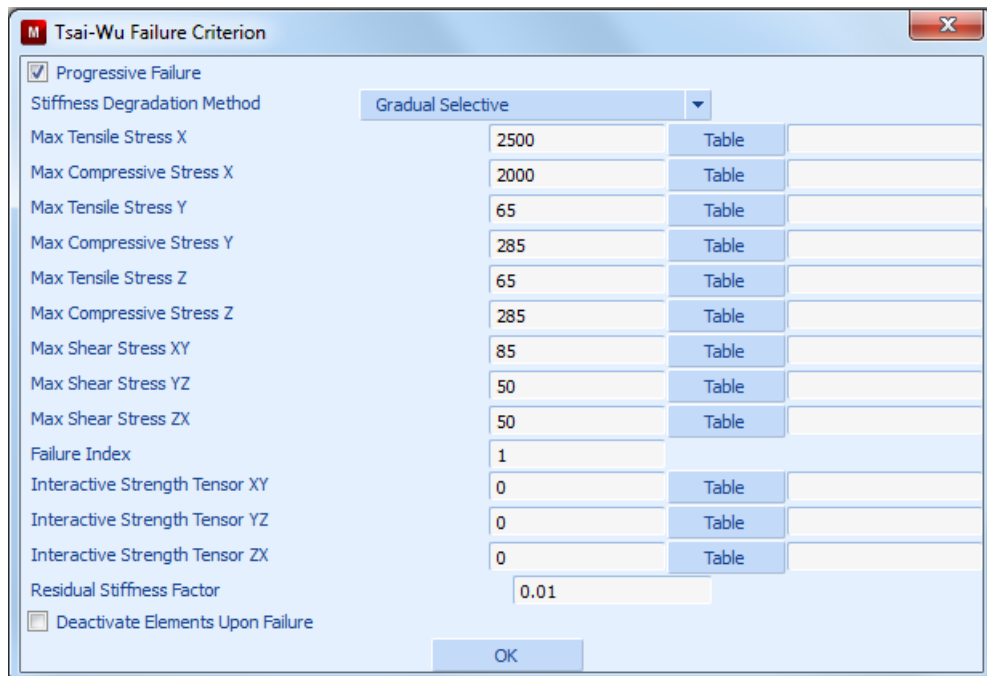


Figure C.4: Loadcase property with convergence testing.



(a) Tsai-Wu failure criteria window under 'Damage Effects' in the 'Structural' window of the material property for solids, with input parameters.

(b) Puck failure criteria window under 'Damage Effects' in the 'Structural' window of the material property for solids, with input parameters.

(c) Hashin failure criteria window under 'Damage Effects' in the 'Structural' window of the material property for solids, with input parameters.

Figure C.5: Failure criteria options.



# D

## MATLAB CODES

In this appendix one can find the MatLab codes used in this thesis work.  
Traction laws used for Ch. 3.1.1:

```
1 %% Bilinear, trapezoidal, exponential traction laws
2
3 clear all
4 clc
5 close all
6
7 % Properties law
8 GcI = 1;
9 tc = 1;
10 dcEXP = GcI/(exp(1)*tc);
11
12 GcI2 = 0.75;
13 tc2 = 1;
14 dcEXP2 = GcI2/(exp(1)*tc2);
15
16 GcI3 = 0.5;
17 tc3 = 1;
18 dcEXP3 = GcI3/(exp(1)*tc3);
19
20 GcI4 = 0.25;
21 tc4 = 1;
22 dcEXP4 = GcI4/(exp(1)*tc4);
23
24 % Pure modes EXP
25 dn = [0:0.001:5];
26 zerodn = zeros(1, length(dn));
27 ntract = GcI.*dn/dcEXP^2.*exp(-dn/dcEXP);
28 ntract2 = GcI2.*dn/dcEXP2^2.*exp(-dn/dcEXP2);
29 ntract3 = GcI3.*dn/dcEXP3^2.*exp(-dn/dcEXP3);
30 ntract4 = GcI4.*dn/dcEXP4^2.*exp(-dn/dcEXP4);
31
32 figure(1)
33 hold on
34 area(dn,ntract,'Facecolor',[0 1 1])
35 plot(dcEXP,tc,'o','MarkerSize',7,'MarkerFaceColor','k','MarkerEdgeColor','k')
36 ylim([0 1.25])
37 xlabel('\Delta (mm)')
38 ylabel('T (N/mm^2)')
39 text(0.5,0.2,'G_c')
40 text((dcEXP),(tc+0.05),['\Delta_c,T_{max}'])
41 plot([0 dcEXP],[tc tc],'--k',[dcEXP dcEXP],[0 tc],'--k')
42 title('Exponential Law')
43
44 figure(8)
45 hold on
46 p1 = area(dn,ntract,'Facecolor',[0 1 1])
```

```

47 plot(dcEXP,tc,'o','MarkerSize',7,'MarkerFaceColor','k','MarkerEdgeColor','k')
48 p2 = area(dn,ntract2,'Facecolor',[0 1 0.8])
49 plot(dcEXP2,tc2,'o','MarkerSize',7,'MarkerFaceColor','k','MarkerEdgeColor','k')
50 p3 = area(dn,ntract3,'Facecolor',[0 1 0.6])
51 plot(dcEXP3,tc3,'o','MarkerSize',7,'MarkerFaceColor','k','MarkerEdgeColor','k')
52 p4 = area(dn,ntract4,'Facecolor',[0 1 0.4])
53 plot(dcEXP4,tc4,'o','MarkerSize',7,'MarkerFaceColor','k','MarkerEdgeColor','k')
54 ylim([0 1.5])
55 xlabel('\Delta (mm)')
56 ylabel('T (N/mm^2)')
57 text(0.5,0.3,'G_c')
58 text((dcEXP),(tc+0.05),['\Delta_c,T_{max}'])
59 plot([0 dcEXP],[tc tc],'--k',[dcEXP dcEXP],[0 tc],'--k')
60 % legend([p1 p2 p3 p4],{'Max T_{max} = 1 (N/mm^2)','Max T_{max} = 0.75 (N/mm^2)',...
61 % 'Max T_{max} = 0.5 (N/mm^2)','Max T_{max} = 0.25 (N/mm^2)'})
62 legend([p1 p2 p3 p4],{'G_c = 1 (N/mm^2)','G_c = 0.75 (N/mm^2)',...
63 % 'G_c = 0.5 (N/mm^2)','G_c = 0.25 (N/mm^2)'})
64 title('Exponential Law with different max tractions')
65 %%
66 % Pure modes BIL
67 dnormalBIL = 2*GcI/tc;
68 dcnormalBIL = 0.5;
69 dn1 = [0:0.001:dcnormalBIL];
70 ntract1 = 2*GcI/dnormalBIL.*dn1/dcnormalBIL;
71 dn2 = [dcnormalBIL:0.001:dnormalBIL];
72 ntract2 = 2*GcI/dnormalBIL.*(dnormalBIL-dn2)/(dnormalBIL-dcnormalBIL);
73
74 figure(2)
75 hold on
76 area([dn1 dn2],[ntract1 ntract2],'Facecolor',[0 1 1])
77 plot(dcnormalBIL,tc,'o','MarkerSize',7,'MarkerFaceColor','k','MarkerEdgeColor','k')
78 plot([0 dcnormalBIL],[tc tc],'--k',[dcnormalBIL dcnormalBIL],[0 tc],'--k')
79 ylim([0 1.25])
80 xlabel('\Delta (mm)')
81 ylabel('T (N/mm^2)')
82 text(0.8,0.2,'G_c')
83 text((dcnormalBIL),(tc+0.05),['\Delta_c,T_{max}'])
84 title('Bilinear Law')
85
86 figure(5)
87 hold on
88 area([dn1],[ntract1],'Facecolor',[0 1 1])
89 area([dn2],[ntract2],'Facecolor',[0 0 1])
90 plot(dcnormalBIL,tc,'o','MarkerSize',7,'MarkerFaceColor','k','MarkerEdgeColor','k')
91 plot([0 dcnormalBIL],[tc tc],'--k',[dcnormalBIL dcnormalBIL],[0 tc],'--k')
92 ylim([0 1.25])
93 xlabel('\Delta (mm)')
94 ylabel('T (N/mm^2)')
95 text(0.3,0.2,'(1)')
96 text(0.8,0.2,'(2)')
97 text((dcnormalBIL),(tc+0.05),['\Delta_c,T_{max}'])
98 title('Bilinear Law')
99
100 figure(6)
101 hold on
102 plot([dn1 dn2],[ntract1 ntract2],'b','linewidth',2)
103 plot(dcnormalBIL,tc,'o','MarkerSize',7,'MarkerFaceColor','k','MarkerEdgeColor','k')
104 plot([0 dcnormalBIL],[tc tc],'--k',[dcnormalBIL dcnormalBIL],[0 tc],'--k')
105 ylim([0 1.25])
106 xlabel('\Delta (mm)')
107 ylabel('T (N/mm^2)')
108 text(0.3,0.2,'(1)')
109 text(0.8,0.2,'(2)')
110 text((dcnormalBIL),(tc+0.05),['\Delta_c,T_{max}'])
111 title('Bilinear Law')
112
113 % Pure modes Trap
114 dcnormalTRAP1 = 0.5;
115 dcnormalTRAP2 = 0.95;
116 dnormalTRAP = ...
    2*(GcI-1/2*dcnormalTRAP1-(dcnormalTRAP2-dcnormalTRAP1)*tc)/tc+dcnormalTRAP2;

```

```

117 dn4 = [0:0.001:dcnormalTRAP1];
118 ntract4 = 2*(GcI)/dmnormalBIL.*dn4/dcnormalTRAP1;
119 dn5 = [dcnormalTRAP1:0.001:dcnormalTRAP2];
120 ntract5 = dn5./dn5 * tc
121 dn6 = [dcnormalTRAP2:0.001:dmnormalTRAP];
122 %ntract3 = 2*(GcI)/dmnormalTRAP.*((dmnormalTRAP-dn3)/(dmnormalTRAP-dcnormalTRAP2));
123 ntract3 = (-tc/(dmnormalTRAP-dcnormalTRAP2)).*...
124     dn6-dmnormalTRAP.*(-tc/(dmnormalTRAP-dcnormalTRAP2));
125 title('Trapezoidal Law')
126
127 figure(3)
128 %plot(dn4,ntract4,'b',dn5,ntract5,'b',dn6,ntract3,'b')
129 hold on
130 area([dn4 dn5 dn6],[ntract4 ntract5 ntract3],'Facecolor',[0 1 1])
131 plot([dcnormalTRAP1 dcnormalTRAP2],[tc tc],'o','MarkerSize',7,...
132     'MarkerFaceColor','k','MarkerEdgeColor','k')
133 plot([0 dcnormalTRAP2],[tc tc],'--k',[dcnormalTRAP1 dcnormalTRAP1],...
134     [0 tc],'--k',[dcnormalTRAP2 dcnormalTRAP2],[0 tc],'--k')
135 ylim([0 1.25])
136 xlabel('\Delta (mm)')
137 ylabel('T (N/mm^2)')
138 text(0.75,0.2,'G_c')
139 text((dcnormalTRAP1),(tc+0.05),['\Delta_{c1},T_{max}'])
140 text((dcnormalTRAP2),(tc+0.05),['\Delta_{c2},T_{max}'])
141 title('Trapezoidal Law')
142
143 figure(4)
144 hold on
145 plot(dn,ntract,'b','linewidth',2)
146 plot([dn1 dn2],[ntract1 ntract2],'r','linewidth',2)
147 plot(dn4,ntract4,'g',dn5,ntract5,'g',dn6,ntract3,'g','linewidth',2)
148 plot([0 dcnormalTRAP2],[tc tc],'--k')
149 ylim([0 1.25])
150 xlabel('\Delta (mm)')
151 ylabel('T (N/mm^2)')
152 text((dcnormalTRAP2+0.1),(tc),'T_{max}')
153 legend('Exponential law','Bilinear law','Trapezoidal law')
154
155 % figure(5)
156 % hold on
157 % area(dn,ntract,'Facecolor',[0 1 1])
158 % area([dn1 dn2],[ntract1 ntract2],'Facecolor',[0 1 1])
159 % area([dn4 dn5 dn6],[ntract4 ntract5 ntract6],'Facecolor',[0 1 1])
160 % ylim([0 1.25])
161 % xlabel('\Delta (mm)')
162 % ylabel('T (N/mm^2)')
163
164 %%
165 clc
166 clear all
167 close all
168 % Properties law
169 GcI = 1;
170 tc = 1;
171 dcEXP = GcI/(exp(1)*tc);
172 beta1 = 0.6
173 beta2 = 0.9
174 tcshear = tc*beta1;
175 GcII = GcI*beta2;
176 dcEXPshear = GcII/(exp(1)*tcshear);
177
178 % Pure modes EXP
179 dn = [0:0.001:5];
180 zerodn = zeros(1, length(dn));
181 ntract = GcI.*dn/dcEXP^2.*exp(-dn/dcEXP);
182 stract = GcII.*dn/dcEXPshear^2.*exp(-dn/dcEXPshear);
183
184 figure(1)
185 hold on
186 area(dn,ntract,'Facecolor',[0 1 1])
187 area(dn,stract,'Facecolor',[0 0 1])

```

```

188 legend('Pure mode 1', 'Pure mode 2')
189 plot(dcEXP, tc, 'o', 'MarkerSize', 7, 'MarkerFaceColor', 'k', 'MarkerEdgeColor', 'k')
190 plot(dcEXPShear, tcShear, 'o', 'MarkerSize', 7, 'MarkerFaceColor', 'k', 'MarkerEdgeColor', 'k')
191 ylim([0 1.25])
192 xlabel('\Delta (mm)')
193 ylabel('T (N/mm^2)')
194 text(0.4, 0.8, 'G_{c,I}')
195 text(0.9, 0.2, 'G_{c,II}')
196 text((dcEXP), (tc+0.05), '[\Delta_{c,I}, T_{max,I}]')
197 text((dcEXPShear), (tcShear+0.05), '[\Delta_{c,II}, T_{max,II}]')
198 plot([0 dcEXP], [tc tc], '--k', [dcEXP dcEXP], [0 tc], '--k')
199 plot([0 dcEXPShear], [tcShear tcShear], '--k', [dcEXPShear dcEXPShear], [0 tcShear], '--k')
200 title('Exponential Law with \beta_1 = 0.6 and \beta_2 = 0.9')

```

3D exponential traction law with mixed-mode surface, used in Ch. 3.1.3 and Ch. 5.2:

```

1 %% How the mixed mode works in MARC - Exp
2
3 clear all
4 close all
5 clc
6
7 % Properties law - You can change these 4 first ones for additional effects!
8 GcI = 0.32;
9 dcnormal = 2.5;
10 beta2 = 0.5/0.32; % ratio normal-to-shear energy (Gii = beta2*Gi)
11 normal_crit = 64 %GcI/(exp(1)*dcnormal); % max normal stress
12 betal = 35/64; % ratio normal-to-shear stress (tau = betal*sigma)
13
14 dcnormal = GcI/(exp(1)*normal_crit);
15 shear_crit = normal_crit*betal; % max shear stress
16 GcII = GcI*beta2;
17 dcshear = GcII/(exp(1)*shear_crit); % dependent on ratio
18
19 radius = dcnormal; % crit opening displacemnt (of fracture stress) based on normal stress
20 xCenter = 0;
21 yCenter = 0;
22 theta = 0:0.005:1/2*pi;
23
24 % dc line with ratio change
25 x = radius * cos(theta) + xCenter; % normal crit displacement
26 y = dcshear * sin(theta) + yCenter; % sqrt(beta)*shear crit displacement
27 z = (shear_crit - normal_crit)/dcshear*y+normal_crit; % max traction
28
29 % Pure modes
30 dn = [0:0.0004:.02];
31 ds = [0:0.0004:.025];
32 zerodn = zeros(1, length(dn));
33 zerods = zeros(1, length(ds));
34 ntract = GcI.*dn/dcnormal^2.*exp(-dn/dcnormal);
35 stract = GcII.*ds/dcshear^2.*exp(-ds/dcshear);
36
37 % Mixed mode graph based on orthogonality xy-plane
38 n = 120;
39 mlx = dn;
40 alpha = y(n)/x(n);
41 mly = alpha*dn;
42 if GcI < GcII
43     Gcm = sin(atan(alpha))*(GcII-GcI)+GcI
44 else
45     Gcm = GcI - sin(atan(alpha))*(GcI-GcII)
46 end
47 mlc = Gcm/(exp(1)*z(n));
48 mlv = sqrt(mlx.^2+mly.^2);
49 mtract1 = Gcm.*mlv/(mlc)^2.*exp(-mlv/mlc);
50
51 % 3D meshed
52 dN = [0:0.0004:.02];

```

```

53 dS = [0:0.0004:0.025];
54 [X,Y] = meshgrid(dN,dS);
55 MX = X;
56 ALPHA = Y ./ X;
57 MY = ALPHA .* X;
58 R = (dcshear*dcnormal)./sqrt((dcshear.*cos(atan(ALPHA))).^2+(dcnormal.*...
59     sin(atan(ALPHA))).^2); %varying radius ellipse of COD for mixed mode
60 YC = sin(atan(ALPHA)).*R;
61 Z = (shear_crit - normal_crit)./dcshear.*YC+normal_crit; % max traction
62 if GcI < GcII
63     GcM = sin(atan(ALPHA))*(GcII-GcI)+GcI
64 else
65     GcM = GcI - sin(atan(ALPHA))*(GcI-GcII)
66 end
67 MC = GcM ./ (exp(1).*Z); % crit displ
68 MV = sqrt(X.^2+(Y).^2); % displ
69 MTRACT = GcM .* MV./(MC).^2.*exp(-MV./MC);
70
71 figure(1)
72 hold on
73 plot(y, z);
74 plot([0],[normal_crit],'ko','MarkerSize',7,'MarkerFaceColor','k','MarkerEdgeColor','k')
75 text([0],[normal_crit+1],['\Delta_{n,c},T_{n,max}'])
76 plot(y(end),z(end),'ko','MarkerSize',7,'MarkerFaceColor','k','MarkerEdgeColor','k')
77 text(y(end),[z(end)+1],['\Delta_{s,c},T_{s,max}'])
78 f1 = plot(ds,stract,'r--','colorspec',[0 0 0.5],'LineWidth',1);
79 plot([0 dcshear],[shear_crit shear_crit],'--k',[dcshear dcshear],[0 shear_crit],'--k')
80 text(5,2,'G_{cII}')
81 axis square;
82 xlim([0 20]);
83 ylim([0 20]);
84 grid on;
85 xlabel('Shear displacement \Delta_s')
86 ylabel('Traction T')
87 legend('Linear relation between max traction Mode I and II','Pure mode II response')
88 title('Linear relation between maximum traction Pure Mode I and II, on the plane ...
      [\Delta_s;T]')
89
90 grey = [0.5 0.5 0.5];
91 figure(2)
92 hold on
93 p3 = plot3(x, y, z,'Color',grey) %,'LineStyle','--','LineWidth',2);
94 fill3([dn dn(end)],[zerodn 0],[ntract 0],grey);
95 fill3([zerods 0],[ds ds(end)],[stract 0],grey);
96 fill3([mlx mlx(end)],[mly mly(end)],[mtract1 0],'y');
97 xlim([0 20]);
98 ylim([0 25]);
99 zlim([0 10]);
100 grid on;
101 xlabel('normal displ')
102 ylabel('shear displ')
103 zlabel('traction')
104
105 figure(3)
106 hold on
107 set(gca,'FontSize',12)
108 p3 = plot3(x, y, z,'Color',grey) %,'LineStyle','--','LineWidth',2);
109 f1 = fill3([dn dn(end)],[zerodn 0],[ntract 0],grey,'LineWidth',1) %,'colorspec',[0 0 ...
      0.5],'LineWidth',1);
110 f2 = fill3([zerods 0],[ds ds(end)],[stract 0],grey,'LineWidth',1);
111 f3 = fill3([mlx mlx(end)],[mly mly(end)],[mtract1 0],'c','LineWidth',1.5);
112 s = surf(X,Y,MTRACT)
113 plot3([0 0 0],[dcshear dcshear 0],[0 shear_crit shear_crit],'k--','LineWidth',1.5)
114 plot3([dcnormal dcnormal 0],[0 0 0],[0 normal_crit normal_crit],'k--','LineWidth',1.5)
115 plot3([dcnormal],[0],[normal_crit],'ko','MarkerSize',7,'MarkerFaceColor','k',...
      'MarkerEdgeColor','k')
116 plot3([0],[dcshear],[shear_crit],'ko','MarkerSize',7,'MarkerFaceColor','k',...
      'MarkerEdgeColor','k')
117 text([dcnormal],[0],[normal_crit+1],['\Delta_{n,c},T_{n,max}'])
118 text([0],[dcshear],[shear_crit+1],['\Delta_{s,c},T_{s,max}'])
119
120 xlim([0 0.02]);

```

```

122 ylim([0 0.025]);
123 zlim([0 65]);
124 zlim([0 125]);
125 grid on;
126 xlabel('\Delta_n[mm]')
127 ylabel('\Delta_s [mm]')
128 zlabel('traction T [N/mm^2]')
129 %title('Mixed-mode response for \beta_1=0.75 and \beta_2=1.0')
130 title('Mixed-mode response for the bondline')
131 view(115,30)
132 set(s,'facecolor','yellow','FaceAlpha',0.75,'edgealpha',0.1)
133
134
135 % figure(4)
136 % hold on
137 % f1 = area(dn,ntract)%, 'colormap', [0 0 0.5], 'LineWidth',1);
138 % plot([0 dcnormal],[normal_crit normal_crit], '--k', [dcnormal dcnormal], [0 ...
    normal_crit], '--k')
139 % set(f1,'facecolor','c')
140 % xlim([0 20]);
141 % ylim([0 10]);
142 % grid on;
143 % text(dcnormal, (normal_crit+0.5), '\Delta_{c,normal}, T_{max,normal}', ...
144 % 'BackgroundColor',[1 1 1])
145 % xlabel('\Delta_n')
146 % ylabel('traction T')
147 % title('Pure mode I response for \beta_1=0.75 and \beta_2=1.0')
148 % text(4,2,'G_{cI}')
149 %
150 % figure(5)
151 % hold on
152 % f1 = area(ds,stract)%, 'colormap', [0 0 0.5], 'LineWidth',1);
153 % plot([0 dcshear],[shear_crit shear_crit], '--k', [dcshear dcshear], [0 shear_crit], '--k')
154 % set(f1,'facecolor','c')
155 % text(dcshear, (shear_crit+0.5), '\Delta_{c,shear}, T_{max,shear}', ...
156 % 'BackgroundColor',[1 1 1])
157 % xlim([0 25]);
158 % ylim([0 10]);
159 % grid on;
160 % xlabel('\Delta_s')
161 % ylabel('traction T')
162 % title('Pure mode II response for \beta_1=0.75 and \beta_2=1.0')
163 % text(5,2,'G_{cII}')
164 %
165 % figure(6)
166 % hold on
167 % f1 = plot(dn,ntract,'linewidth',2)%, 'colormap', [0 0 0.5], 'LineWidth',1);
168 % xlim([0 25]);
169 % ylim([0 10]);
170 % grid on;
171 % xlabel('\Delta_n')
172 % ylabel('traction T')
173 % title('Pure mode I response')

```

Code for creating recreating the data points from the real experiment strain gauge results and how to interpolate the load to even equalised point by time.

```

1 % Strain gauge data to graph conversion
2
3 clc
4 clear all
5 close all
6
7 % Test
8 Test = importdata('Testgauge.txt')
9
10 figure(1)
11 hold on

```

```

12 plot(Test(:,1),Test(:,2),'r')
13 xlabel('Time [s]')
14 ylabel('Strain [\num/mm]')
15 title('Strain Gauge Test')
16
17
18 MeasuredStrain = importdata('converterStrain-time.txt');
19 figure(2)
20 hold on
21 set(gca,'FontSize',12)
22 plot(MeasuredStrain(:,1),MeasuredStrain(:,2),'r','Linewidth',2.5)
23 plot(MeasuredStrain(:,1),MeasuredStrain(:,3),'b','Linewidth',2.5)
24 plot(MeasuredStrain(:,1),MeasuredStrain(:,4),'g','Linewidth',2.5)
25 legend('Strap top','Strap bottom','Lap bottom')
26 xlabel('Time [s]')
27 ylabel('Strain [\num/mm]')
28 grid on
29 title('Measured Strains')
30
31 MeasuredForce2 = importdata('converterForce-time.txt');
32 MeasuredForce2(:,1) = MeasuredForce2(:,1)/(2/60);
33 figure(3)
34 hold on
35 set(gca,'FontSize',12)
36 plot(MeasuredForce2(:,1),MeasuredForce2(:,2),'r')
37 legend('Machine displacement against force')
38 xlabel('Time [s]')
39 ylabel('Load [N]')
40 grid on
41 title('Measured Load Force')
42
43 MeasuredForce = importdata('converterForce-time.txt');
44 MeasuredForce(:,1) = MeasuredForce(:,1)/(2/60); % convert to seconds
45 % scale for strain results :
46 for i = 1:length(MeasuredForce(5919:end,1))
47     MeasuredForce(5918+i,1) = ...
48     MeasuredForce(5918+i,1)+i/length(MeasuredForce(5919:9617,1))*4.46;
49 end
50 for i = 1:length(MeasuredForce(1:5917,1))
51     MeasuredForce(i,1) = MeasuredForce(i,1)-(length(MeasuredForce(1:5917,1))-i+1) ...
52     length(MeasuredForce(5919:9617,1))*4.46;
53 end
54 MeasuredForce(:,1) = MeasuredForce(:,1)+23.08; % scale for strain results
55 MeasuredForce(1:6,2) = mean(MeasuredForce(1:6,2)); % average values at multiple same ...
56     time results
57 MeasuredForce(1:5,:) = []; % remove same valued rows
58 MeasuredForce(2:19,2) = mean(MeasuredForce(2:19,2)); % average values at multiple same ...
59     time results
60 MeasuredForce(2:18,:) = []; % remove same valued rows
61 MeasuredForce(16064:end,:) = []; % remove excess rows
62 MeasuredForceq(:,1) = 0.02:0.02:400;
63 MeasuredForceq(:,2) = ...
64     interp1(MeasuredForce(:,1),MeasuredForce(:,2),MeasuredForceq(:,1),'linear');
65 A = find(MeasuredStrain(:,1) == 400)
66 MeasuredStrainq = MeasuredStrain(1:A,:);
67
68 figure(4)
69 hold on
70 set(gca,'FontSize',12)
71 %plot(MeasuredForce(:,1),MeasuredForce(:,2),'r')
72 plot(MeasuredForceq(:,1),MeasuredForceq(:,2),'b','Linewidth',2.5)
73 legend('Converted force load results against time')
74 xlabel('Time [s]')
75 ylabel('Load [N]')
76 grid on
77 title('Measured Load Force')
78
79 figure(5)
80 hold on
81 set(gca,'FontSize',12)
82 p1 = plot(MeasuredForceq(1:12548,2),MeasuredStrainq(1:12548,2),'r','Linewidth',2.5)

```

```

79 p12 = plot(MeasuredForceq([12548 12560],2),MeasuredStrainq([12548 ...
12560],2), 'r', 'Linewidth',2.5)
80 p2 = ...
    plot(MeasuredForceq(12560:16066,2),MeasuredStrainq(12560:16066,2), 'r', 'Linewidth',2.5)
81 p3 = plot (MeasuredForceq(1:12548,2),MeasuredStrainq(1:12548,3), 'b', 'Linewidth',2.5)
82 p34 = plot (MeasuredForceq([12548 12560],2),MeasuredStrainq([12548 ...
12560],3), 'b', 'Linewidth',2.5)
83 p4 = ...
    plot (MeasuredForceq(12560:16066,2),MeasuredStrainq(12560:16066,3), 'b', 'Linewidth',2.5)
84 p5 = plot (MeasuredForceq(1:12548,2),MeasuredStrainq(1:12548,4), 'g', 'Linewidth',2.5)
85 p56 = plot (MeasuredForceq([12548 12560],2),MeasuredStrainq([12548 ...
12560],4), 'g', 'Linewidth',2.5)
86 p6 = ...
    plot (MeasuredForceq(12560:16066,2),MeasuredStrainq(12560:16066,4), 'g', 'Linewidth',2.5)
87 legend([p1 p3 p5],{'Strap top','Strap bottom','Lap bottom'})
88 xlabel('Load [N]')
89 ylabel('Strain [\mum/mm]')
90 axis([0 80000 0 8000])
91 grid on
92 title('Measured Strains against Load')
93
94
95
96
97
98 %%
99 % Strain gauge data to graph conversion
100
101 clc
102 clear all
103 close all
104
105
106 DEStrainStrapTop = importdata('DE_strain_strap_top.txt');
107 DETime = DEStrainStrapTop(:,1);
108 DEStrainStrapBottom = importdata('DE_strain_strap_bottom.txt'); % Bottom is lap-side
109 DEStrainLap = importdata('DE_strain_lap.txt');
110
111 figure(2)
112 hold on
113 set(gca, 'FontSize',12)
114 plot (DETime,DEStrainStrapTop(:,2), 'r', 'Linewidth',2.5)
115 plot (DETime,DEStrainStrapBottom(:,2), 'b', 'Linewidth',2.5)
116 plot (DETime,DEStrainLap(:,2), 'g', 'Linewidth',2.5)
117 legend('Strap top','Strap bottom','Lap')
118 xlabel('Time [s]')
119 ylabel('Strain [\mum/mm]')
120 grid on
121 title('Measured Strains at strap and lap gauges for model with no failure criterion')
122
123 DEForce = importdata('DE_load.txt');
124 figure(3)
125 hold on
126 set(gca, 'FontSize',12)
127 plot (DETime,DEForce(:,2), 'r', 'Linewidth',2.5)
128 legend('Load time against force at load.')
129 xlabel('Time [s]')
130 ylabel('Load [N]')
131 grid on
132 title('Measured Load Force for model with no failure criterion')
133
134 figure(4)
135 hold on
136 set(gca, 'FontSize',12)
137 plot (DEForce(:,2),DEStrainStrapTop(:,2), 'r', 'Linewidth',2.5)
138 plot (DEForce(:,2),DEStrainStrapBottom(:,2), 'b', 'Linewidth',2.5)
139 plot (DEForce(:,2),DEStrainLap(:,2), 'g', 'Linewidth',2.5)
140 legend('Strap top','Strap bottom','Lap')
141 xlabel('Load [N]')
142 ylabel('Strain [\mum/mm]')
143 grid on

```

```
144 title('Load Force-Strain curve with no failure criterion')
```



# E

## RECOMMENDATIONS FOR WHEN USING MSC.MARC

Many problems arose during this thesis work. Most of them were based around getting to know and to work with the finite element package MSC.Marc, which costed a severe amount of time. What follows is a list of recommendations to prevent any of the problems that were once encountered, and to save a lot of time.

### When should you use MSC.Marc?

- For solving analyses of structures with cohesive zone modelling
- For solving analyses of structures with the aid of progressive failure
- For coupon level based structures

### Modelling with MSC.Marc

- It is able to import several file types, including ACIS, IGES, STL, Nastran Bulk Data, Patran and other. Experience has learned that it is paired with many importing errors though, so it's safer to model within MSC.Mentat, the default pre- and postprocessing program.
- It is possible to model the geometry and elements in another FE or modelling program, although importing can be dangerous since MSC.Marc imports all settings which may not be default settings according to MSC.Marc. Patran geometry imports seem to work.
- Keep attention to what exact input parameter is asked for i.e. a material property.  $\nu_{31} \neq \nu_{13}$  and a calculation should be made beforehand to use the correct input parameter.
- If one encounters limitations of several options due to licensing problems, find a way to circumvent this. I.e. to create solid elements, one can first create a surface mesh, and use the 'Expand' command to expand the surface mesh to a 3D solid mesh. Creating CZE in a local approach, e.g. zero thickness, can be tedious and arduous. There are three ways to create CZE:
  - What's recommendable if you want to create 2D or 3D CZE, is to create a surface or solid first, assign them cohesive element type and other properties, and use the 'Move' command to forcibly move nodes to coincide with each other.
  - Similar to the previous option, one can also first create a curve or surface and use the 'Expand' command with thickness 0, automatically creating a planar or solid element with thickness 0.
  - Another, more practical, way is to use the 'Matching Boundaries' option, where one can select a plane in or between an element region and create CZE directly inbetween those elements on the specified plane.
  - Another option is to use the 'Delamination' option to create CZE 'on the fly' during an analysis. This has the advantage of having lesser elements in the model, although it can get confusing once you want to visualise and analyse certain element groups, since these newly created CZE are not assigned to an element set. Another disadvantage is that the CZE are activated by another criterion, which use is blackbox and currently still unknown.

- Create element sets while in preprocessing, because in postprocessing there is no way to save element sets and retain them for all increments. This is very useful for when checking certain layers and element groups in postprocessing. To define a flat CZE set, reduce the element size in 'View'>'Plot Control'>'Element Settings' to get a reduced view of element, making flat CZE easier to select.
- Contact bodies need to be defined delicately. For unknown reason, MSC.Marc assigns a priority order based on what contact body was defined first. The former created contact body acts as a slave contact body for all other defined bodies beneath in the list. Using the 'Glued' contact option makes the first created contact bodies follow the rest, and not vice versa. Example: if the bondline in the CLS specimen was defined as the third contact body instead of the first, coincidental nodes would not follow the lap and strap nodes and element surface.

### Solving with MSC.Marc

- If one has a simulation with a large model and a large amount of increments, loading and retrieving of results can be arduous and the amount of space taken up on the hard drive incredibly large. To reduce this, make MSC.Marc only get a result every x increment during the analysis. To do this, go to Jobs>Properties>Job Results and within this window is a smaller window which says 'Post File' with the option 'Increment Frequency'. This option enables MSC.Marc to collect and store data during the analysis at the given frequency, reducing the amount of increments saved and saving space and result loading times.
- Never, ever, use another preprocessing programme with using MSC.Marc as a solver. Often the default settings within other preprocessing FE packages are completely different from MSC.Mentat, which may lead to faulty simulation results or even none at all.
- It was recommended by Per Nordlund, lead designer of MSC.Marc, to use a residual force convergency of a factor 10 less, e.g. 0.01, instead of 0.1, as Dr. Nordlund deems this as not accurate enough.
- The default setting within defining loadcases are still alright to use.
- Make sure to select what postprocessing parameters need to be retrieved. Once a simulation has started and results are in, there is no way to retrieve a parameter which was not selected in the 'Job Results' window unless by restarting the simulation with the parameter selected. For composite plies, make sure to select the 'List' option next to the input parameter in the 'Select Element Quantities' window (the default option is 'Default'), and select which ply results must be taken. For example, if you want the results of ply 1 and 24, type [1 24] in the field next to it, without the brackets.

### Postprocessing with MSC.Marc

- If one needs to average, sum or subtract nodal information from each other, it is best to use MSC.Mentat. MSC.Marc's postprocessing program has the advantage of using functions for multiple curves, like averaging, multiplying, adding etc.
- Use MSC.Mentat to quickly extract simple data like load-displacement curves. One can also quickly create graphs with different nodal values from different nodes with each other, i.e. the displacement of node 3 on the x-axis against the strain of node 1 on the y-axis.
- Checking the 'Damage' parameter needs to be done with 'Nodal Averaging' off and extrapolation option 'Translate', found in 'Settings'.
- MSC.Marc only retrieves nodal information, no element information. One can use HyperWorks for element information extraction, but HyperWorks has been unable to collect 3D CZE information. The reason for this is that Altair, HyperWorks' head company, has MSC.Marc on a low priority list, resulting in less updates and support for MSC.Marc results.
- Models with large elements can be problematic when retrieving results: use MSC.Mentat's option to retrieve only a set of increments to save loading time.

# F

## USED SOFTWARE AND HARDWARE

The software used to perform this thesis are the following:

- Texmaker 4.0.4  $\LaTeX$  Editor, compiled with Qt 5.1.0 and Poppler 0.22.5. Copyright (c) 2003-2013 by Pascal Brachet
- Typesetting system MiKTeX
- Marc Mentat 2012.1.0 (64bit). Copyright (c) 1994-2014 by MSC.Software Corporation
- HyperView, Altair HyperWorks Version 12.0 (64bit). Copyright (c) 1986-2014 by Altair Engineering Inc.
- MatLab 2011b (7.13.0.564) (64bit). Copyright (c) 1984-2011 by The MathWorks Inc.
- Mendeley Desktop Version 1.10.1. Copyright (c) 2008-2013 by Mendeley Ltd.
- MS Paint
- Windows 7 Professional 64bit, Service Pack 1. Copyright (c) 2009 by MicroSoft Corporation.

The hardware used to perform this thesis and all the simulations are the following:

- CPU: AMD Phenom(tm) II X4 965 Processor, 3.40 GHz
- RAM: 4,00 GB
- GPU: NVIDIA GeForce 8800 GT
- MB: ACPI x64



## BIBLIOGRAPHY

- [1] *Space engineering: Adhesive Bonding Handbook*, ESA-ESTEC (2011).
- [2] R. E. Zwinderman, *Analysis of Adhesively Bonded Composite Joints Employing a P-Finite Element Method.*, Diploma thesis, Technical University of Delft. (2013).
- [3] G. Kelly, *Joining of carbon fibre reinforced plastics for automotive applications.*, Technical Report (Royal Insitiute of Technology, 2004).
- [4] D. M. Gleich, M. J. L. Van Tooren, and A. Beukers, *Analysis and evaluation of bondline thickness effects on failure load in adhesively bonded structures.* J. Adhesive Science and Technology. **15**, 1091 (2001).
- [5] L. F. M. da Silva and R. D. S. G. Campilho, *Advances in Numerical Modelling of Adhesive Joints.*, Springer-Briefs in Applied Sciences and Technology (Springer, 2012).
- [6] R. Cuntze, *Strength failure conditions of transversely-isotropic material (ud-material).* (2013).
- [7] R. Krueger, *The virtual crack closure technique: history, approach and applications.*, Contractor Report (NASA., 2002) cR-2002-211628.
- [8] A. Puck and H. Schürmann, *Failure analysis of frp laminates by means of physically based phenomenological models.* Composites Science and Technology **58**, 1045 (1998).
- [9] R. Kregting, *Cohesive zone models towards a robust implementation of irreversible behaviour.*, Tech. Rep. (Philips Applied Technologies., 2005).
- [10] M. J. Bosch, P. J. G. Schreurs, and M. G. D. Geers, *On the development of a 3d cohesive zone element in the presence of large deformations.* Computational Mechanics **42**, 171 (2007).
- [11] H. Khoramishad, A. Crocombe, K. B. Katnam, and I. A. Ashcroft, *Predicting fatigue damage in adhesively bonded joints using a cohesive zone model.* Int. J. Fatigue. **32**, 1146 (2010).
- [12] *Marc 2010 Volume A: Theory and User Information*, MSC.Software Corporation (2010).
- [13] A. Turon, P. Camanho, and J. Costa, *An interface damage model for the simulation of delamination under variable-mode ratio in composite materials.*, Technical Memorandum NASA/TM-2004-213277 (NASA., 2004).
- [14] L. F. M. da Silva, P. J. C. das Neves, R. D. Adams, and J. K. Spelt, *Analytical models of adhesively bonded joints—part i: literature survey.* Int. J. Adhesion and Adhesives. **29**, 319 (2009).
- [15] L. J. Hart-Smith, *Adhesive-bonded single-lap joints.*, Contract Report CR-112236 (NASA, 1973).
- [16] M. Davis and J. Tomblin, *Best practice in adhesive-bonded structures and repairs.*, Technical note DOT/FAA/AR-TN06/57 (National Institute for Aviation Research, 2007) federal Aviation Association.
- [17] T. K. O'Brien, G. B. Murri, and S. A. Salpekar, *Interlaminar shear fracture toughness and fatigue thresholds for composite material.* Composite Materials: Fatigue and Fracture, ASTM STP **1012**, 225 (1989).
- [18] D. S. Dugdale, *Yielding of steel sheets containing slits.* J. the Mechanics and Physics of Solids. **8**, 100 (1960).
- [19] G. Barenblatt, *The mathematical theory of equilibrium cracks in brittle fracture.* Adv. Applied Mechanics **7**, 55 (1962).
- [20] A. Hillerborg, M. Modeer, and P. E. Petersson, *Analysis of crack formation and crack growth in concrete by means of fracture mechanics and finite elements.* Cement and Concrete Research. **6**, 773 (1976).

- [21] C. H. Wang and A. Gunnion, *Design methodology for scarf repairs to composite structures.*, Technical report dsto-rr-0317 (Australian Government, Department of Defence., 2006).
- [22] A. Objois, Y. Gilbert, and B. Fargette, *Theoretical and experimental analysis and design of high-performance frp-composite structural elements.* J. Adhesion **70**, 13 (1999).
- [23] M. Dawood, *Bond characteristics and environmental durability of cfrp materials for strength-ening steel bridges and structures.*, Technical report (Graduate Faculty of North Carolina State University, 2007).
- [24] X. Zhao, R. D. Adams, and L. F. M. da Silva, *Single lap joints with rounded adherend corners: experimental results and strength prediction.* J. Adhesive Science and Technology. **25**, 837 (2011).
- [25] A. Baker, S. Dutton, and D. Kelly, *Composite Materials for Aircraft Structures.* (American Institute of Aeronautics and Astronautics, 2004).
- [26] ASTM, *Standard Practice for Classifying Failure Modes in Fiber-Reinforced-Plastic (FRP) Joints.*, Tech. Rep. D-5573-99 (American Society for Testing and Materials, 2012).
- [27] R. B. Heslehurst and L. Hart-Smith, *The science and art of structural adhesive bonding.* Society of Material and Process Engineering Journal. **38**, 60 (2002).
- [28] R. R. Talreja and C. V. Singh, *Damage and Failure of Composite Materials.* (Cambridge University Press, 2012).
- [29] V. D. Ingenieure, *Development of Fibre-Reinforced Plastics components.*, Technical Guidelines ICS 59.100, 83.140.20 (VDI., 2006).
- [30] R. D. Adams and J. A. Harris, *Strength prediction of bonded single lap joints by nonlinear finite element methods.* Int. J. Adhesion and Adhesives. **7**, 55 (1984).
- [31] M. L. Williams, *The stresses around a fault or crack in dissimilar media.* Bulletin of the Seismological Society of America. **49**, 199 (1959).
- [32] R. D. Adams, J. Comyn, and W. C. Wake, *Structural Adhesive Joints in Engineering.*, 2nd ed. (Chapman & Hall, 1997).
- [33] L. F. M. da Silva, G. W. Critchlow, and M. A. V. Figueiredo, *Parametric study of adhesively bonded single lap joints by the taguchi method.* J. Adhesive Science and Technology. **22**, 1477 (2008).
- [34] J. D. Clarke and I. J. McGregor, *Ultimate tensile stress over a zone: a new failure criterion for adhesive joints.* J. Adhesion. **42**, 227 (1993).
- [35] L. Greenwood, *The Strength of a Lap Joint.*, edited by D. Alner, Aspects of Adhesion-5 (University of London Press, 1969).
- [36] S. J. John, A. J. Kinloch, and F. L. Matthews, *Measuring and predicting the durability of bonded fibre/epoxy composite joints.* Composites. **22**, 121 (1991).
- [37] S. J. Lee and D. G. Lee, *Development of a failure model for the adhesively bonded tubular single lap joint.* J. Adhesion. **40**, 1 (1992).
- [38] L. F. M. da Silva, R. J. C. Carbas, G. W. Critchlow, M. A. V. Figueiredo, and K. Brown, *Effect of material, geometry, surface treatment and environment on the shear strength of single lap joints.* Int. J. Adhesion and Adhesives. **29**, 621 (2009).
- [39] J. D. Clarke and I. J. McGregor, *Global yielding as a failure criteria for bonded joints.* Int. J. Adhesion and Adhesives. **9**, 145 (1989).
- [40] R. D. Adams and V. Mallick, *A method for the stress analysis of lap joints.* J. Adhesion. **38**, 199 (1992).
- [41] L. F. M. da Silva, P. J. C. das Neves, R. D. Adams, and J. K. Spelt, *Analytical models of adhesively bonded joints—part ii: comparative study.* Int. J. Adhesion and Adhesives. **29**, 331 (2009).

- [42] R. D. Adams and J. A. Harris, *The influence of local geometry on the strength of adhesive joints*. Int. J. Adhesion and Adhesives. **7**, 69 (1987).
- [43] A. A. Griffith, *The phenomena of rupture and flow in solids*. Philosophical Transaction of the Royal Society of London. **221**, 163 (1921).
- [44] G. R. Irwin, *Analysis of stresses and strains near the end of a crack traversing a plate*. J. Applied Mechanics. **24**, 361 (1957).
- [45] D. R. Moore, *The value of fracture mechanics to industry*. Prospects in Fracture. **8-9** (2003).
- [46] J. R. Reeder and J. H. Crews, *Mixed-mode bending method for delamination testing*. AIAA Journal. **28**, 1270 (1990).
- [47] C. Fan, P. Y. B. Jar, and J. J. R. Cheng, *Cohesive zone with continuum damage properties for simulation of delamination development in fibre composites and failure of adhesive joints*. Engineering Fracture Mechanics. **75**, 3866 (2008).
- [48] K. Shahin and F. Taheri, *The strain energy release rates in adhesively bonded balanced and unbalanced specimens and lap joints*. Int. J. Solids and Structures. **45**, 6284 (2008).
- [49] H. L. Groth, *Stress singularities and fracture at interface corners in bonded joints*. Int. J. Adhesion and Adhesives. **8**, 107 (1988).
- [50] J. Q. Xu, Y. H. Liu, and X. G. Wang, *Numerical methods for the determination of multiple stress singularities and related stress intensity coefficients*. Engineering Fracture Mechanics. **63**, 775 (1999).
- [51] A. A. Wells, *Application of fracture mechanics at and beyond general yielding*. British Welding Research Association. (1963).
- [52] J. R. Rice and G. F. Rosengren, *Plane strain deformation near a crack tip in a powerlaw hardening material*. J. the Mechanics and Physics of Solids. **16**, 1 (1968).
- [53] J. W. Hutchinson, *Singular behavior at the end of a tensile crack in a hardening material*. J. the Mechanics and Physics of Solids. **16**, 13 (1968).
- [54] W. Ramberg and W. R. Osgood, *Description of stress-strain curves by three parameters.*, Technical Note 902 (National Advisory Committee for Aeronautics., 1948).
- [55] G. Fernlund, M. Papini, M. McCammond, and J. K. Spelt, *Fracture load predictions for adhesive joints*. Composite Science and Technology **51**, 587 (1994).
- [56] N. Choupani, *Interfacial mixed-mode fracture characterization of adhesively bonded joints*. Int. J. Adhesion and Adhesives. **28**, 267 (2008).
- [57] B. F. Soerensen and T. K. Jacobsen, *Determination of cohesive laws by the j integral approach*. Engineering Fracture Mechanics. **70**, 1841 (2003).
- [58] Z. Chen, R. D. Adams, and L. F. M. da Silva, *The use of the j-integral to analyse adhesive bonds with and without a crack*. Int. J. Adhesion and Adhesives. **31**, 48 (2011).
- [59] A. Turon, *Simulation of delamination in composites under quasi-static and fatigue loading using cohesive zone models.*, Ph.D. thesis, Universitat de Girona (2006).
- [60] T. Belytschko and T. Black, *Elastic crack growth in finite elements with minimal remeshing*. J. Fracture Mechanics **45**, 601 (1999).
- [61] N. Sukumar, N. Moës, B. Moran, and T. Belytschko, *Extended finite element method for three-dimensional crack modeling*. Int. J. Numerical Methods in Engineering. **48**, 1549 (2000).
- [62] C. Daux, N. Moës, J. Dolbow, N. Sukumark, and T. Belytschko, *Arbitrary branched and intersecting cracks with the extended finite element method*. Int. J. Numerical Methods in Engineering. **48**, 1741 (2000).

- [63] T. Elguedj, A. Gravouil, and A. Combescure, *Appropriate extended functions for x-fem simulation of plastic fracture mechanics*. Computational Methods in Applied Mechanical Engineering. **195**, 501 (2006).
- [64] N. Moës and T. Belytschko, *Extended finite element method for cohesive crack growth*. Engineering Fracture Mechanics. **69**, 813 (2002).
- [65] J. Dolbow, N. Moës, and T. Belytschko, *An extended finite element method for modeling crack growth with frictional contact*. Finite Element Analysis in Analysis and Design. **36**, 235 (2000).
- [66] A. R. Khoei and M. Nikbaht, *Contact friction modeling with the extended finite element method (x-fem)*. J. Materials Processing Technology. **177**, 58 (2006).
- [67] M. Fagerström and R. Larsson, *Theory and numerics for finite deformation fracture modelling using strong discontinuities*. Int. J. Numerical Methods in Engineering. **66**, 911 (2006).
- [68] Y. Xu and H. Yuan, *Computational analysis of mixed-mode fatigue crack growth in quasi-brittle materials using extended finite element methods*. Engineering Fracture Mechanics. **76**, 165 (2009).
- [69] S. Mohammadi, *Extended Finite Element Method for Fracture Analysis of Structures*. (Blackwell Publishing, 1998).
- [70] R. D. S. G. Campilho, M. D. Banea, F. J. P. Chaves, and L. F. M. da Silva, *extended finite element method for fracture characterization of adhesive joints in pure mode i*. Computational Material Science. **50**, 1543 (2011).
- [71] R. D. S. G. Campilho, M. D. Banea, A. M. G. Pinto, L. F. M. da Silva, and A. M. P. de Jesus, *Strength prediction of single- and double-lap joints by standard and extended finite element modelling*. Int. J. Adhesion and Adhesives. **31**, 363 (2011).
- [72] J. Lemaitre and R. Desmorat, *Engineering Damage Mechanics*. (Springer, 2005).
- [73] K. Song, Y. Li, and C. Rose, *Continuum Damage Mechanics Models for the Analysis of Progressive Failure in Open-Hole Tension Laminates.*, Tech. Rep. (AIAA., 2011).
- [74] C. Scheucker and H. E. Pettermann, *Fiber reinforced laminates: Progressive damage modeling based on failure mechanisms*, Computational Methods in Engineering. **15**, 163 (2008).
- [75] X. Xu and A. Needleman, *Numerical simulations of fast crack growth in brittle solids*. J. Mechanics and Physics of Solids. **42**, 1397 (1994).
- [76] G. T. Camacho and M. Ortiz, *Computational modelling of impact damage in brittle materials*. Int. J. Solids and Structures. **33**, 2899 (1996).
- [77] M. Cavalli and M. Thouless, *The effect of damage nucleation on the toughness of an adhesive joint*. J. Adhesion. **76**, 75 (2001).
- [78] P. P. Camanho, C. G. Davila, and M. F. de Moura, *Numerical simulation of mixed-mode progressive delamination in composite materials*. J. Composite Materials. **37**, 1415 (2003).
- [79] S. Li, M. D. Thouless, A. Waas, J. A. Schroeder, and P. D. Zavattieri, *Use of mode-i cohesive-zone models to describe the fracture of an adhesively-bonded polymer-matrix composite*. J. Composites Science and Technology. **65**, 281 (2005).
- [80] S. Li, M. D. Thouless, A. Waas, J. A. Schroeder, and P. D. Zavattieri, *Mixed-mode cohesive-zone models for fracture of an adhesively-bonded polymer-matrix composite*. Engineering Fracture Mechanics. **72**, 64 (2006).
- [81] A. Turon, P. Camanho, J. Costa, and C. G. Davila, *A damage model for the simulation of delamination in advanced composites under variable-mode loading*. Mechanics of Materials. **38**, 1072 (2006).
- [82] B. R. K. Blackman, H. Hadavinia, A. J. Kinloch, and J. G. Williams, *The use of a cohesive zone model to study the fracture of fibre composites and adhesively-bonded joints*. Int. J. Fracture **119**, 25 (2003).

- [83] C. Sun, M. D. Thouless, A. M. Waas, J. A. Schroeder, and P. D. Zavattieri, *Ductile–brittle transitions in the fracture of plastically-deforming, adhesively-bonded structures. part i: Experimental studies*. Int. J. Solids and Structures. **45**, 3059 (2008).
- [84] R. D. S. G. Campilho, M. F. S. F. de Moura, A. M. G. Pinto, J. J. L. Morais, and J. J. M. S. Domingues, *Modelling the tensile fracture behaviour of cfrp scarf repairs*. Int. J. Adhesion and Adhesives. **40**, 149 (2009).
- [85] R. D. S. G. Campilho, M. F. S. F. de Moura, D. A. Ramantani, J. J. L. Morais, and J. J. M. S. Domingues, *Buckling behaviour of carbon-epoxy adhesively-bonded scarf repairs*. J. Adhesion Science and Technology. **23**, 1493 (2009).
- [86] P. A. Gustafson and A. M. Waas, *The influence of adhesive constitutive parameters in cohesive zone finite element models of adhesively bonded joints*. Int. J. Solids and Structures. **46**, 2201 (2009).
- [87] P. W. Harper and S. R. Hallett, *Cohesive zone length in numerical simulations of composite delamination*. Engineering Fracture Mechanics. **75**, 4774 (2008).
- [88] S. Mohammad, *A self-adaptive cohesive zone model for interfacial delamination.*, Ph.D. thesis, Eindhoven University of Technology (2011).
- [89] M. S. Kafkalidis and M. D. Thouless, *The effects of geometry and material properties on the fracture of single lap-shear joints*. Int. J. Solids and Structures. **39**, 4367–4383 (2002).
- [90] R. D. S. G. Campilho, M. F. S. F. de Moura, D. A. Ramantani, J. J. L. Morais, and J. J. M. S. Domingues, *Buckling strength of adhesively-bonded single and double-strap repairs on carbon-epoxy structures*. Composites Science and Technology. **70**, 371 (2010).
- [91] P. J. G. Schreurs, *Fracture Mechanics.*, Lecture notes (Eindhoven Technical University of Technology, 2011).
- [92] M. Elices, G. V. Guinea, J. Gómez, and J. Planas, *The cohesive zone model : advantages , limitations and challenges*. Engineering Fracture Mechanics **69**, 137 (2002).
- [93] M. Hinton, S. Kaddour, and P. Soden, *Failure Criteria in Fibre Reinforced Polymer Composites: The World-Wide Failure Exercise* (Elsevier Ltd, 2004).
- [94] M. Hinton, S. Kaddour, P. Smith, S. Li, and P. Soden, *Failure criteria in fibre reinforced polymer composites: Can any of the predictive theories be trusted?.*, International Association of the Engineering Modelling, Analysis and Simulation Community (NAFEMS, 2011).
- [95] P. P. Camanho, *Failure Criteria for Fibre-Reinforced Polymer Composites.*, Tech. Rep. (Faculdade de Engenharia da Universidade do Porto, 2002).
- [96] C. G. Davila, C. C. Camanho, and C. A. Rose, *Failure criteria for frp laminates*. J. Composite Materials. **39** (2005).
- [97] S. W. Tsai and E. M. Wu, *General theory of strength for anisotropic materials*. J. Composite Materials. **5**, 58 (1971).
- [98] Z. Hashin and A. Rotem, *A fatigue failure criterion for fiber reinforced materials. journal of composite materials*. J. Composite Materials. **7**, 448–464 (1973).
- [99] Z. Hashin, *Failure criteria for unidirectional fiber composites*. J. Applied Mechanics. **47**, 329 (1980).
- [100] L. Greve and A. K. Picket, *Modelling damage and failure in carbon/epoxy non-crimp fabric composites including effects of fabric pre-shear*, Composites: Part A. **37**, 1983 (2006).
- [101] M. Knops and C. Bögle, *Gradual failure in fibre/polymer laminates*. Composites Science and Technology. **66**, 616–625 (2006).
- [102] G. Alfano, *On the influence of the shape of the interface law on the application of cohesive-zone models*. Composites Science and Technology **66**, 723 (2006).

- [103] P. Feraren and H. M. Jensen, *Cohesive zone modelling of interface fracture near flaws in adhesive joints*. Engineering Fracture Mechanics **71**, 2125 (2004).
- [104] U. Mi, M. A. Crisfield, and G. A. O. Davies, *Progressive delamination using interface elements*. J. Composite Materials. **32**, 1246 (1998).
- [105] J. P. M. Gonçalves, M. F. S. F. de Moura, P. T. de Castro, and A. T. Marques, *Interface element including point-to-surface constraints for three-dimensional problems with damage propagation*. Engineering Computations. **17**, 28 (2000).
- [106] P. P. Camanho, C. G. Davila, and S. Pinho, *Fracture analysis of composite co-cured structural joints using decohesion elements*. Fatigue and fracture of engineering materials and structures. **27**, 745 (2004).
- [107] V. Tvergaard and J. W. Hutchinson, *The relation between crack growth resistance and fracture process parameters in elastic-plastic solids*. J. Mechanics and Physics of Solids. **40**, 1377 (1992).
- [108] *Marc 2010 Volume C: Program Input*, MSC.Software Corporation (2010).